5-2023

Time-Resolved FTIR Difference Spectroscopy for The Study of Quinones in Photosynthetic Protein Binding Sites

Neva Agarwala

Time-Resolved FTIR Difference Spectroscopy for The Study of Quinones in Photosynthetic Protein Binding Sites

by

Neva Agarwala

Under the Direction of Gary Hastings, PhD

A Dissertation Submitted in Partial Fulfillment of the Requirements for the Degree of

Doctor of Philosophy

in the College of Arts and Sciences

Georgia State University

2023

ABSTRACT

Time–resolved Fourier transform infrared difference spectroscopy has been used to study photosystem I (PSI) photosynthetic reaction centers from *Synechocystis* sp. PCC 6803 (*S6803*) at cryogenic temperature (77 K) with a series of native and non-native quinones incorporated in the A_1 binding site. LED-based pump-probe spectroscopy was used to study the $P700^+(F_{A/B}^-/A_{1A}^-)$ state recombination at room temperature (298 K). "Foreign minus native" double difference spectra (DDS) were constructed by subtracting TR FTIR DS for native PSI from corresponding spectra of non-native quinones. To help assess and assign bands, density functional theory based vibrational frequency calculations for quinones in solvent, or in the presence of a single asymmetric H–bond to either a water molecule or a peptide backbone NH group, were undertaken.

In the study of four high-potential naphthoquinones (2-chloro-, 2-bromo-, 2,3-dichloro- and 2,3-dibromo-1,4-naphthoquinone), we conclude that the mono-substituted NQs (2ClNQ and 2BrNQ) can occupy the binding site in different orientations, with the C_3 hydrogen atom being both ortho and meta to the H-bonded C_4=O group.

In PSI complexes at 298 K electron transfer from A_1^- to F_X is an order of magnitude faster on the B-branch compared to the A-branch. One factor that might contribute to this branch asymmetry in time constants is TrpB673, which is located between A_{1B} and F_X. In the study of the TrpB673Phe mutant (WB673F mutant - mutation of TrpB673 to Phe) cells, photoaccumulated FTIR DS for WB673F mutant cells indicate changes in amide I and II protein vibrations upon mutation, indicating the protein environment near F_X is altered upon mutation. In the WB673F mutant light sensitive PSI samples, the phylloquinone molecule is likely doubly protonated following long periods of repetitive flash illumination at 298K which can be restored by incubating the light treated mutant PSI samples in the presence of added phylloquinone.

In cyanobacteria, PSI is found mainly in trimeric and slightly in monomeric form [26]. Previous x-ray structural studies indicate there are no significant differences between them. In this study, we investigated whether they are kinetically different, and we conclude that they are very similar in this aspect as well.

INDEX WORDS: Photosynthesis, Photosystem I (PS I), Electron Transfer (ET), P700, Fourier transform infrared (FTIR), *Synechocystis* sp. PCC 6803 (*S. 6803*), Time-resolved spectroscopy, A_1, Phylloquinone, Density Functional Theory (DFT)

Time-Resolved FTIR Difference Spectroscopy for The Study of Quinones in Photosynthetic Protein Binding Sites

by

Neva Agarwala

Committee Chair: Gary Hastings

Committee: Murad Sarsour

Samer Gozem

Gennady Cymbalyuk

Viacheslav Sadykov

Electronic Version Approved:

Office of Graduate Studies

College of Arts and Sciences

Georgia State University

May 2023

ACKNOWLEDGMENTS

My sincere gratitude goes to Dr. Gary Hastings for his invaluable guidance and support in completing my MS and Ph.D. work, for his patience during times when my progress was slow, and for his trust in me. I would never have been able to finish my dissertation without his guidance.

My gratitude also goes to my lab mates, past and present: Dr. Hiroki Makita for this guidance, time, and training; Aranyo Mitra for his enormous amount of help during my first year of Ph.D.; Daniel Ranke for being a great researcher to work with and his contributions mainly on the first published article and being my tennis coach; Komalpreet Singh for his hard works, support, and contributions of multiple projects; Michael Nelson and Julia Kirpich for their time and help. Dr. Leyla Rohani is acknowledged especially for her help in training on the vibrational frequency calculations and her work on the potential energy distribution calculations and being part of some project. I cannot imagine of finishing this work without their support.

Special thanks to my committee members, Dr. Samer Gozem who always supported me whenever I needed his guidance; Dr. Murad Sarsour, Dr. Gennady Cymbalyuk, and Dr. Viacheslav Sadykov for helpful suggestions and support.

I would also like to thank the remarkable teachers at Georgia State University, including, but not limited to, Dr. Gary Hastings, Dr. Mark Stockman, Dr. Steven Manson, ad Dr. Vadym Apalkov.

Thanks, are also due to numerous others in the Physics and Astronomy community: Peter Walker at the Physics Shop, Justin Cantrell and Jeremy M. Simmons for their technical support, Carola Butler, and Felicia Watts and all the staff at the Physics and Astronomy office who have helped with administrative dealings.

I would like to thank all our collaborators who have their contributions of this works. Financial support for this research came through research grants from Department of Energy (DE -SC0012991). The support is gratefully acknowledged.

I would like to acknowledge the Molecular Basis of Disease program at Georgia State University for providing me with a research fellowship over the past three years.

I would also like to thank all my friends for their support and encouragements.

Most significantly, my best friend Dr. Ruaa Al Juboori for her great tolerance during my period of mental breakdown, giving me hope, accepting and supporting me at every single moment of this Ph.D. journey including driving thousands of miles to meet research professors at different schools. She encouraged me to finish and achieve my goals, being one of the most important persons of my life, and kept me in her prayer. Special thanks to my very close friend Nicole Mishra who always prays for me and helps me in improving my English skills; brother Shyju Sathyanesan and sister-in-law Rina Sathyanesan for their enormous amount of support, prayer, and delicious meals. I could not finish this work without support.

Most importantly, I would like to express my ultimate gratitude to my parents and my grandmother for their unconditional love, support, understanding and patience. Their love provides me inspiration and encouragement. I cannot imagine myself at this position without their love and concern, whatever I am today is just because of them. I would also like to thank all my aunts and uncles, my sister, brother-in-law, brother, and sister-in-law who have been very supportive throughout my life.

TABLE OF CONTENTS

LIST OF TABLES

LIST OF FIGURES

LIST OF ABBREVIATIONS

µs	microsecond
2BrNQ	2-bromo-1,4-naphthoquinone
2ClNQ	2-chloro-1,4-naphthoquinone
2MNQ	2-methyl-1,4-naphthoquinone
Asc	sodium ascorbate
Blastochloris viridis	*Bl. viridis*
BQ	1,4-benzoquinone
Br_2NQ	2,3-dibromo-1,4-naphthoquinone
C. reinhardtii	*Chlamydomonas reinhardtii*
C=O	carbonyl
CaF_2	calcium fluoride
Chl-*a*	chlorophyll-*a*
Cl_2NQ	2,3-dichloro-1,4-naphthoquinone
cyt	cytochrome
DAS	decay-associated spectrum, spectra
DDS	double difference spectrum, spectra
DFT	density functional theory
DMNQ	2,3-dimethyl-1,4-naphthoquinone
DMSO	dimethyl sulfoxide
DS	difference spectrum, spectra, spectroscopy
EPR	electron paramagnetic resonance
ET	electron transfer
Fd	ferredoxin
FNR	ferredoxin-$NADP^+$ oxidoreductase
FTIR	Fourier transform infrared
FWHM	full width at half maximum
H-bond	hydrogen bond
IR	infrared
Lhc	light harvesting complex
LT	low temperature (77 K)
MIR	mid-infrared
MM	molecular mechanical
ms	millisecond
NIR	near-infrared
NQ	1,4-naphthoquinone
ns	nanosecond
ONIOM	our own n-layered integrated molecular orbital and molecular mechanics
OPD	optical pathlength difference
pbRC	purple bacterial reaction center
Pc	plastocyanin
PED	potential energy distribution
PhQ	phylloquinone (2-methyl-3-phytyl-1,4-naphthoquinone)
PMS	phenazine methosulfate

PQ, PQ_9, PQ-9	plastoquinone, plastoquinone-9
PQH_2	plastoquinol
ps	picosecond
PSI	photosystem I
PSII	photosystem II
QM	quantum mechanical
Rb. sphaeroides	*Rhodobacter sphaeroides*
RC	reaction center
RT	room temperature (~298 K)
*S*6803	*Synechocystis* sp. PCC6803
T. elongatus	*Thermosynechococcus elongatus*
THF	tetrahydrofuran
TR	time-resolved
TRRS	time-resolved rapid-scan
TRSS	time-resolved step-scan
WT	wild type
ZPD	zero path difference

LIST OF PUBLICATIONS

Parts of the work presented in this dissertation have been published.

1. Agarwala, N.; Makita, H.; Hastings, G.; "Time-Resolved FTIR Difference Spectroscopy for the Study of Photosystem I with High Potential Naphthoquinones Incorporated into the A_1 Binding Site", *Biochimica et Biophysica Acta (BBA) - Bioenergetics*, USA. Vol. 1864, Issue 1, Jan. 2023.

2. Agarwala, N.; Rohani, L.; Hastings, G.; "Experimental and Calculated Infrared Spectra of Disubstituted Naphthoquinones", *Spectrochimica Acta Part A: Molecular and Biomolecular Spectroscopy*, USA. Vol. 268, Issue 5, Nov. 2021.

3. Agarwala, N.; Makita, H.; Luo, L.; Xu, W.; Hastings, G.; "Reversible inhibition and reactivation of electron transfer in photosystem I", *Photosynthesis Research,* USA. Vol. 145, Issue 2, 97-109, May 2020.

4. Agarwala, N.; Ranke, D.; Hastings, G.; "Calculated and Experimental Infrared spectra of substituted naphthoquinones" *Front. Sci. Technol. Eng. Math.,* USA. Vol. 3, Issue 2, Nov. 2019.

1 INTRODUCTION

1.1 Photosynthesis

Mankind continues increasing, and according to the United Nation (UN), the population reached 8 billion by November 15, 2022, and is projected to reach to 10.4 billion in 2080s [2]. This increasing global population also brings increasing demand for fossil fuels, and dwindling supplies, which creates a global energy crisis. One way to solve this crisis is to harness and convert only a small portion of the $1.8x10^{17}$ W of solar radiation striking the earth's surface [3, 4], which is just one hour of radiation to satisfy the energy needs of mankind for one year [5]. Photosynthesis organisms can easily harness solar energy and use it for a synthesis of chemical products, which serve as the source for most of food and energy consumed by humanity [6]. The quantum efficiency of light conversion during the initial stages of photosynthesis is close to 100%. Such a high efficiency of transformation without destruction or harmful side effects is achieved by the fine-turning of the pigments bound properties in large protein complexes called photosystems [7].

Photosynthetic process can be classified into two categories, oxygenic and anoxygenic photosynthesis. Oxygenic photosynthesis takes place in high plants, algae, and cyanobacteria where water and atmospheric CO_2 is used to synthesize carbohydrates in the presence of sunlight while releasing oxygen [8-10]. Anoxygenic photosynthetic organisms, like purple bacteria, green sulfur bacteria, and heliobacteria use solar energy to create organic compounds but do not produce oxygen. Oxygenic photosynthesis process is traditionally divided into two distinct phases called the light reactions and the dark reactions. In the light reaction for the oxygenic photosynthesis process, solar energy is captured and converted independently with high efficiency and cooperatively by two systems called photosystem I and II (PSI and PSII) [11]. Fig. 1.1 shows the

schematic representation of the protein complexes that engage in photosynthesis embedded in the thylakoid membrane which, in plants and algae, is organized in chloroplasts [12].

In both PSI and PSII, large numbers of chlorophyll molecules are found embedded in large pigment-protein arrays called light harvesting complexes (Lhca 1-4 for PSI in Fig. 1.1), which are called antenna pigments with very large cross sections for solar photon absorption. The captured solar energy is rapidly transferred to a pigment protein complex called the reaction center (RC), where the primary photochemistry occurs [13] which is then transferred to a special pigment (or group of pigments), called the primary electron donor. The primary electron donor in PSI/PSII is called P700 and P680 (Fig. 1.1), respectively. Upon light excitation of the primary electron donor an electron is transferred via a series of acceptors across the thylakoid membrane to a terminal acceptor species that is either an iron-sulfur cluster (F_A/F_B in Fig. 1.1) or a quinone (Q_B in Fig. 1.1) which creates a charge separation across the membrane with a net negative charge on the stromal side and net positive on the lumenal side. The energy in the gradient is captured or harnessed by the ATP synthase and used to generate ATP. Finally, $NADP^+$ is reduced to NADPH by the ferredoxin $NADP^+$ oxidoreductase. The dark reaction uses these molecules to reduce CO_2 to carbohydrates.

This dissertation focuses on PSI from oxygenic photosynthetic organisms from cells from *Synechocystis* sp. PCC 6803 (*S6803*) because in PSI, the photochemical quantum yield is exceptionally high and is reported to be approaching unity [11, 12]. For this reason, PSI has been well investigated in the literature for many years by researchers and scientists of different specialities for the development of a bio-hybrid solar energy conversion device, which is highly efficient and cost-effective [14]. Even after such long-term research, many of the molecular and thermodynamic properties of PSI are still unknown [15]. As a result, it is very important to

understand the mechanisms of efficient energy conversion reactions to develop efficient artificial solar cells. For this reason, this dissertation focuses on an explanation of the molecular mechanisms underlying the highly efficient solar energy conversion processes in PSI.

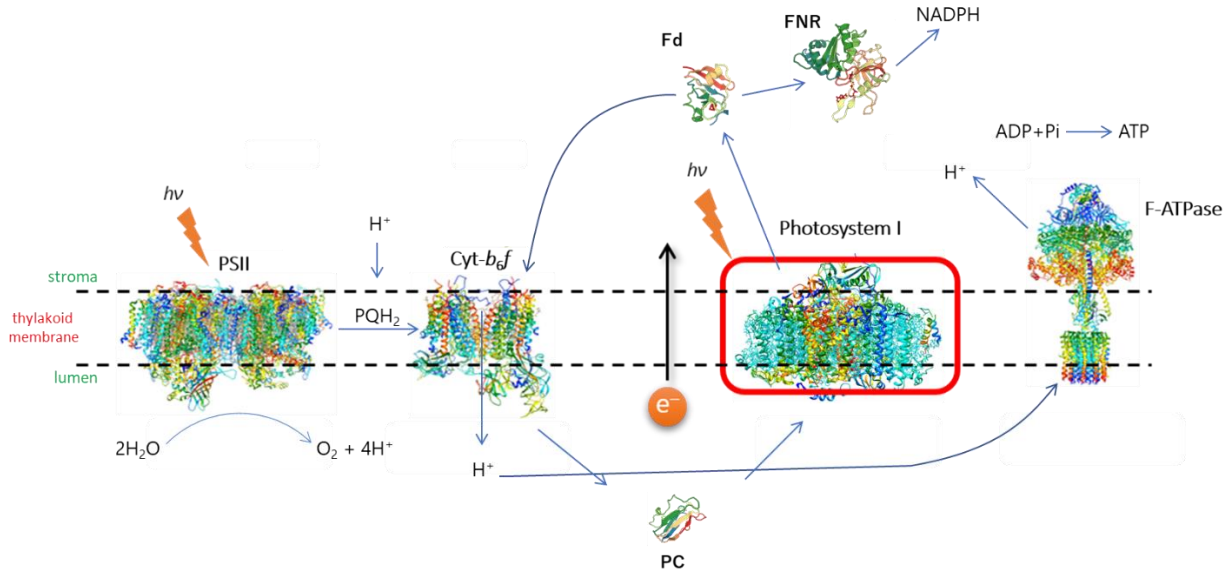

Figure 1.1 Schematic model of the main photosynthetic complexes engaged in oxygenic photosynthesis situated within the higher plant/green algal thylakoid membrane. The four complexes are photosystem II (PSII), cytochrome b_6f complex (Cyt b_6f), photosystem I (PSI), and ATP synthase [3].

1.2 Photosystem I

Fig. 1.2 shows the structure of PSI, that is derived from the 2.5 Å X–ray crystal structure of cyanobacterial PSI and isolated from *Thermosynechococus elongatus (T. elongatus)* (PDB 1JB0 [16]). The isolated cyanobacteria PS I exists as a trimer. And each PS I monomer (Fig. 1.2A) is composed of 12 protein subunits, 96 chlorophylls (Chl), 22 carotenoids, 3 iron-sulfur clusters, 2 phylloquinones (PhQ), and 4 lipids [16, 17]. The number of subunits and the molecules vary slightly between different cyanobacterial species. In cyanobacterial PSI which is isolated from *Synechocystis* sp. PCC6803 (*S*6803), 11 protein subunits, 24 carotenoids, 3 iron-sulfur clusters, 2 PhQ, and 17 lipids are found [18]. In higher plants and algae, a functional unit called light-

harvesting complex (Lhc) forms a super complex with PSI [19], where Lhc serves as an antenna to collect incident light and transfer energy to PSI. In cyanobacteria, Lhc is lacking and chlorophyll and carotenoid molecules in PSI serve as antenna pigments. ET occurs in a centralized pigment–protein complex called a reaction center (RC). The organization of the ET cofactors in the PSI RC are outlined in Fig. 1B, which are bound in three protein subunits: heterodimeric PsaA, PsaB units at the stromal side and a PsaC unit at the lumenal side [17]. The cofactors that participate in ET are termed P700, A_0, A_1, F_X, F_A, and F_B [17]. P700 is a heterodimeric chlorophyll–*a*/ chlorophyll–*a'* (Chl–*a*/Chl–*a*') species. Chl–*a*' is a 13^2 epimer of Chl–*a* [16]. The Chl-*a* and Chl-*a*' are bound to PsaB and PsaA and are referred as P_B and P_A, respectively. A_0 is a monomeric Chl–*a* molecule. In PSI, the secondary electron acceptor, A_1, is a phylloquinone molecule (PhQ, 2–methyl–3-phytyl–NQ). F_X, F_A, and F_B are iron sulfur [4Fe−4S] clusters where F_x is positioned between PsaA, PsaB, and PsaC and the other two electron acceptors are in PsaC. In PSI, the cofactors are arranged two near symmetrical "branches," termed the A– and B–branches. And the cofactors on either branch are indicated by a subscript in Fig. 1B (e.g. A_{1A}/A_{1B}).

In native PSI, following light excitation, an electron is transferred forming the secondary radical pair state, $P700^+A_1^-$ within ~50 picoseconds (ps) [20, 21] (Fig. 1.3). Reported estimates of the relative utilization of the two branches show variations, but in most cases the use of A-branch is favored over the B-branch [22-26]. $P700^+A_1^-$ undergoes forward ET to form $P700^+F_X^-$ in ~20 and ~300 nanoseconds (ns) at room temperature (RT, ~293 K). These time constants are thought to represent intrinsic lifetimes of ET on the B and A branches, respectively [27, 28]. Forward ET from F_X^- to the terminal electron acceptors, F_A and F_B occurs on a sub–µs timescale [29]. In isolated cyanobacterial PSI particles, the $P700^+F_{A/B}^-$ terminal radical pair state recombines *via* repopulation of A_{1A}^- with a time constant of ~50−100 ms [30-35] shown in Fig. 1.3.

At 77 K, ET in PSI becomes heterogeneous. $P700^+A_1^-$ charge recombination occurs in ~35 % of the PSI particles, while ~20% undergoes $P700^+F_X^-$ charge recombination [22, 36]. Both recombination reactions occur almost exclusively through A_{1A} [37]. In the remainder of the PSI particles, the $P700^+F_{A/B}^-$ formation is irreversible, resulting in a loss of signal amplitude in repetitive flash experiments [22, 36]. At 77 K, in native cyanobacterial PSI, the $P700^+A_{1A}^-$ state recombines with a time constant of ~350 μs [36, 38]. For PSI with low potential NQs incorporated with $P700^+A_{1A}^-$ recombines (at 77 K) in less than 100 μs [22, 35].

In this dissertation, although much of the experimental work was performed on PSI isolated from *S*6803, the numbering scheme for the molecules in PSI was based on the *Thermosynechococus elongatus (T. elongatus)* structure. Fig. 1C shows the structure of PhQ in the protein environment of the A_{1A} binding site, highlighting the possible quinone-protein interactions derived from the 2.5 Å X–ray crystal structure of cyanobacterial PSI isolated from *T. elongatus* (PDB 1JB0 [16]). Similar structures are obtained from plant and algae PSI [17, 39-42]. For the secondary acceptor A_1, the indole ring of tryptophan (TrpA697 for the A_{1A} binding site) seems to be π-stacked with the ring plane of PhQ, the cofactor in the binding site. Neutral PhQ in PSI is asymmetrically hydrogen bonded (H-bonded) to the backbone N–H group of leucine residue (LeuA722). H–bonding is to the C_4=O carbonyl group that is adjacent (ortho) to the phytyl chain while the other carbonyl group (C_1=O) is likely not H-bonded. The N···O distance is 2.67 Å. Electron paramagnetic resonance (EPR) data supports this asymmetric H–bonding idea for the semiquinone anion [43], as do FTIR studies [44]. The FTIR studies suggest that this H–bond is especially strong, at least for PhQ^- [44]. Despite that, many of the underlying PhQ pigment–protein interactions, including the exact role of this asymmetric H–bonding are still not well understood [15].

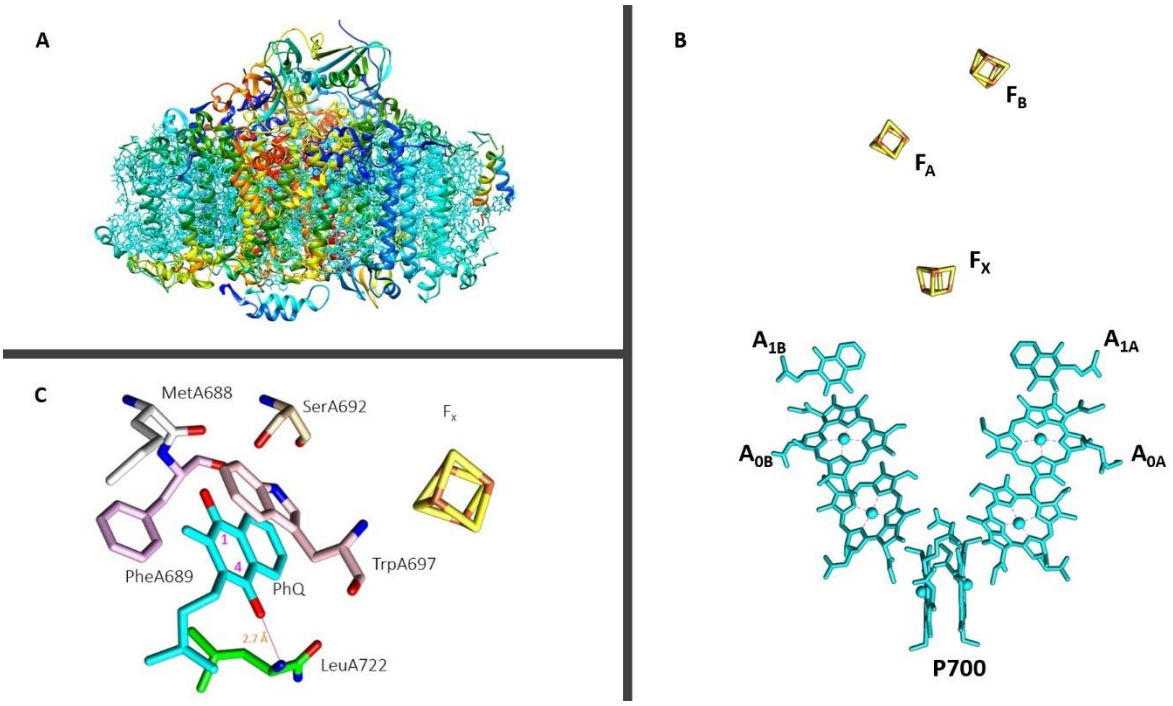

Figure 1.2 Structure derived from the 2.5 Å X−ray crystal structure of PSI from *T. elongatus* (PDB file 1JB0 [16]). (A) Side view of the arrangement of all protein in one monomer of PSI. (B) Arrangement of ET cofactors in PSI. Subscripts A and B refer to the ET branch. (C) View of PhQ in the A_{1A} binding site. Possible H-bonding interactions are indicated (*solid, orange*). The numbering scheme for quinonic ring is indicated in magenta. Atom coloring: cyan: carbon atoms of A_1, light khaki: carbon atoms of Ser, desert sand: carbon atoms of Trp, magenta: carbon atoms of Phe, beige: carbon atoms of Met, green: carbon atoms of Leu, red: oxygen, blue: nitrogen, yellow: sulfur, dark yellow: iron. Hydrocarbon chain of PhQ and Chl molecules are truncated for clarity in A and B.

1.3 The Energetics of Electron Transfer in PSI

Fig. 1.3 shows an outline of the overall light induced energetics of ET reactions in PSI are mostly thermodynamically downhill, with an exception to the excitation of P700 [45]. The left axis gives the redox potential for each radical pair [45]. P700 has some very unique redox properties, which is species-dependent and is approximately ~+450 mV for *S*6803 [46]. The lowest excited singlet state of P700 (P700*) has a negative redox potential of ~ -1300 mV, which makes P700* one of the most reducing species in nature.

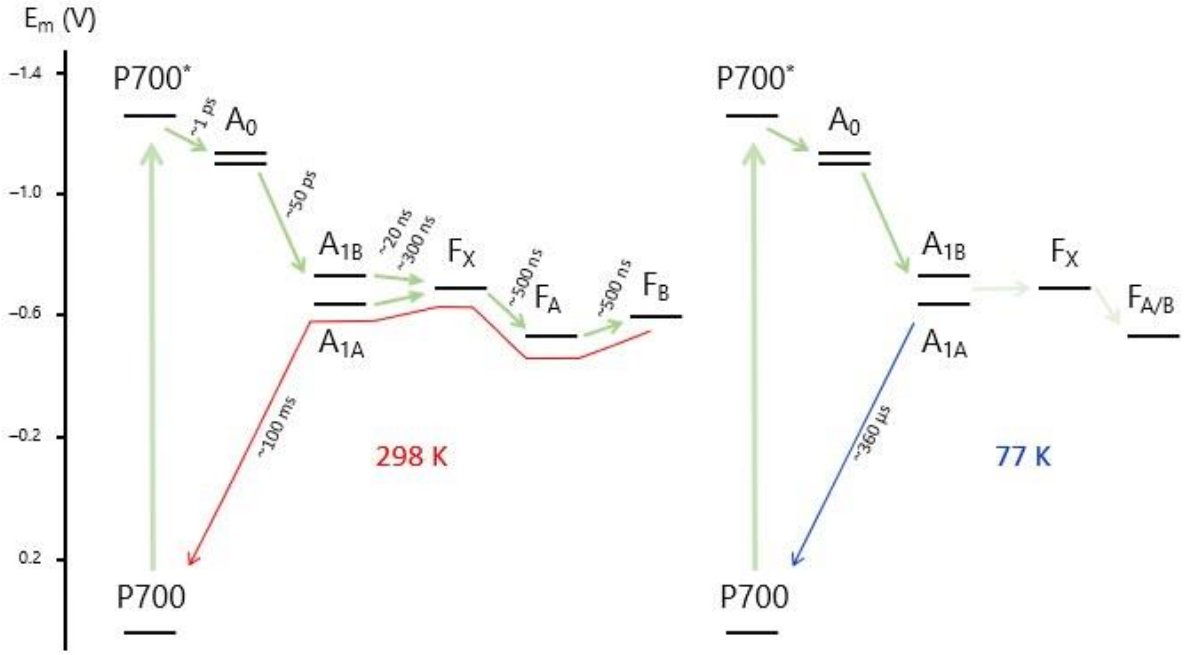

Figure 1.3 The kinetics of charge separation in PSI ET at 298 K (*left*) and 77 K (*right*). Approximate redox properties are gauged on left axis. The $P700^{+}F_{B}^{-}$ charge recombination through A_{1A} at 298 K is highlighted in red, and the $P700^{+}A_{1A}^{-}$ charge recombination pathway at 77 K is indicated in blue. The lighter arrows for a 77 K diagram refer to inhibited or blocked ET pathways.

For A_1, it is not possible to estimate redox potential directly, so multiple indirect methods are used in past to get an estimation which gave a wide range of values ranging from -810 mV to -530 mV [47-52]. The lowest potential reported would suggest the ET from A_1^{-} to F_X is a highly exergonic, or a thermodynamically downhill reaction, while the highest reported value would indicate that the same process is highly endergonic, or thermodynamically uphill. So, due to its downhill nature at low redox potential, at room temperature, it is hard to study $P700^{+}A_1^{-}$ charge recombination as it is very short lived, which becomes possible for the ones that have high redox potential. Therefore, this is one of the main objectives of this study (chapter 4). The redox potentials of F_A and F_B are in the range of ~-520 mV and ~-550 mV, respectively, and the estimate for A_0 is in the -1100 mV range [34]. A range of values has been reported for the redox potential of F_X, but a consensus value is in the range of -680 mV [15].

Next, charge recombination reactions can be observed if the forward electron transfer to the next series of electron acceptors is blocked. For example, electron transfer from A_0^- to A_1 can be blocked by removal or pre-reduction of A_1. In this case the $P700^+A_0^-$ decays by charge recombination with the half-life of ~30ns to form the triplet state, $^3P700$ [32, 53, 54]. The triplet state then decays to the ground state on the micro to millisecond timescale [32, 53, 54]. Similarly, charge recombination of the secondary radical pair state, $P700^+A_1^-$, occurs when F_X, F_A and F_B are either removed or pre-reduced [32]. The best way so far to study this $P700^+A_1^-$ charge recombination reactions is to incorporate the high potential Quinones in the A_1 bonding site of PSI (Chapter 4). Finally, if none of the acceptors are modified, the recombination lifetime of the terminal radical pair state, $P700^+F_{A/B}^-$, is ~80-100 ms [1, 32, 53, 54].

1.4 Protein-Quinone Interactions using Native and Non-Native Quinones

The functional and structural properties of the PSI RC can be investigated by inducing mutations. Multiple mutagenesis methods were applied in the past to the study of PSI which successfully introduced modifications to the function and structure of specific cofactors, ET chains, antenna pigments, and protein subunits. To investigate the molecular properties of PhQ in the A_1 binding site in PSI (and for quinones in protein binding sites in general) one possible way is to study PSI where the native quinone is replaced with a foreign one. This process of foreign quinone incorporation has been simplified with the generation of so–called *menB*$^-$ mutant cells where PhQ biosynthesis has been disrupted. In this study, we used cyanobacterial cells from *Synechocystis* sp. PCC 6803 (*S6803*) in which the *menB* gene is inactivated. In these mutant cells a plastoquinone (PQ) molecule is recruited into the A_1 binding site instead of PhQ [55]. PQ is weakly bound and is easily displaced by incubating PSI particles in the presence of a large molar excess of different NQs [35, 43, 56], including the high potential NQs that are the subject of the

study in chapter 4. This is an ideal, minimally disruptive incorporation method and *menB*$^{-}$ PSI samples with different quinones incorporated have been used in a number of spectroscopic studies [43, 44, 57-62]. These studies have shown that for all non–native incorporated quinones the position and orientation of the C=O groups is essentially the same as it is for PhQ [44].

Recent time resolved step scan (TRSS) FTIR DS studies of PSI with foreign quinones incorporated, together with QM/MM vibrational frequency calculations, have allowed a more detailed understanding of the vibrational properties of quinones in the A_1 binding site in both the neutral and reduced states [44, 63, 64]. One suggestion from these studies is that asymmetric H–bonding to the C_4=O of PhQ is stronger in the anion state compared to the neutral state [44].

Most of the previous FTIR studies focused on the vibrational properties of (relatively) low potential NQs incorporated into PSI. In this dissertation, we focus on studies of PSI with a series of high potential halogenated NQs in solution (chapter 2) and incorporated into the PSI binding site (chapter 4). There are many reasons for this, one of them being that it is, or will be, possible to study PSI at RT, as microsecond $P700^{+}A_1^{-}$ recombination is still the dominant decay pathway at RT in PSI with high potential NQs incorporated [22]. In preparation for these future TRSS FTIR studies we first present here studies at 77 K, focusing on the quinones in the reduced states [1, 57, 63, 65, 66]. Research has also been done with three methyl substituted 1,4-naphthoquinones (NQs) in solution (see chapter 2). Chapter 4 focuses on the study of isolated PSI complexes from wild type and TrpB673Phe mutant (WB673F mutant) cells from *Synechocystis* sp. PCC *6803*. The study of trimeric and monomeric cyanobacterial photosystem I (PSI) samples isolated from *Synechocystis* sp. PCC *6803* is stated in chapter 6. Structures of quinones of interest are shown in Fig. 1.4.

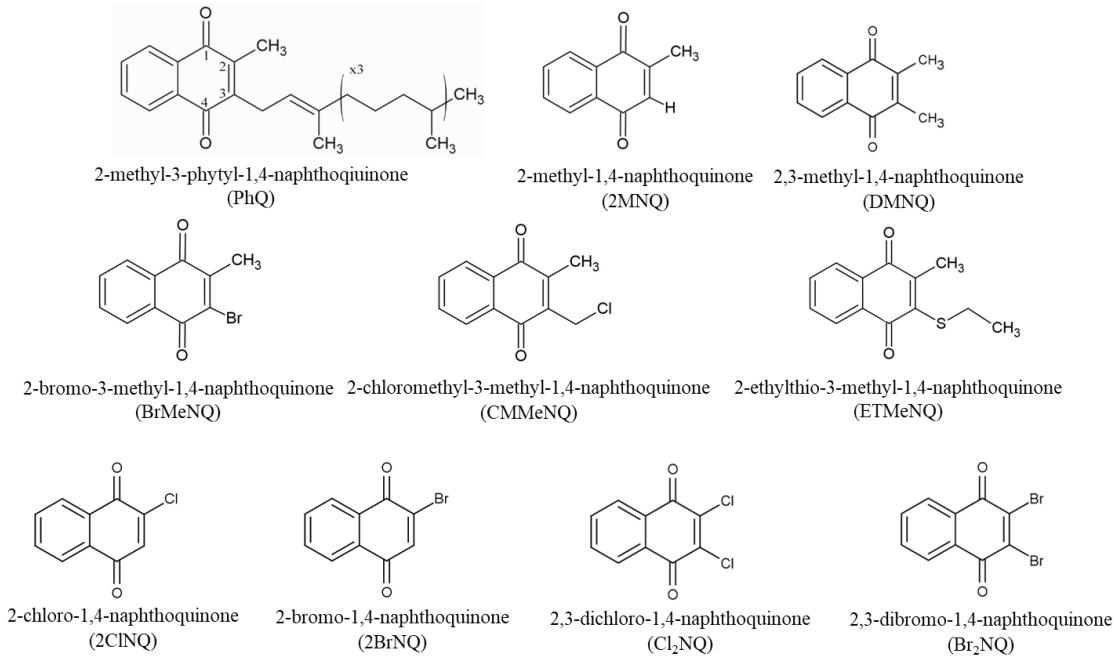

Figure 1.4 Structure of 2-methyl-3-phytyl-1,4-naphthoquinone (PhQ), 2-methyl-1,4-naphthoquinone (2MNQ), and 2,3-dimethyl-1,4-naphthoquinone (DMNQ) (*top* : *left to right*); 2-methyl-3-bromo-1,4-naphthoquinone (BrMeNQ), 2-methyl-3-chloromethyl-1, 4-naphthoquinone (CMMeNQ) and 2-methyl-3-ethylthio-1,4-naphthoquinone (ETMeNQ) (*middle* : *left to right*); 2-chloro-1,4-naphthoquinone (2ClNQ), 2-bromo-1,4-napthpquinone (2BrNQ), (2,3-dichloro-1,4-NQ (Cl_2NQ), and 2,3-dibromo-1,4-NQ (Br_2NQ) (*bottom* : *left to right*) considered in this dissertation. The numbers in the quinonic rings indicate the carbon numbering schemes.

1.5 Fourier Transform Infra-Red (FTIR) Spectroscopy

Infrared (IR) spectroscopy is a useful method for determining the structure of small molecules, as well as large biological systems. IR spectra is used to monitor vibrations in molecules that have specific frequencies at which they rotate or vibrate corresponding to discrete energy levels. It also provides information about chemical structure, bond, angle parameters, hydrogen bonding and electric fields.

IR spectroscopy is one of the best spectroscopic techniques that offers many advantages to study biological systems. First and foremost, IR spectroscopy can determine the positions of hydrogen atoms, van der Waals force, electrostatic intermolecular interactions, and H bonding

which is not possible to determine in crystal structures of biological system. Additionally, IR spectroscopy has the capability to study both the small biomolecules and large complex biological system, which is not possible with nuclear magnetic resonance (NMR) spectroscopy. Another advantage is that this technique can be used for samples in solid, liquid, powder forms, or polymers [67, 68].

An IR spectrum is a plot of the incident IR radiation that passing through a sample which provides the absorption bands in an IR spectrum relate to specific vibrational modes of specific molecular bonds. These vibrational modes are solely dependent on the molecular bonding geometry of the sample that is specific for specific samples. Therefore, IR spectroscopy is a tool that can be used to establish a unique fingerprint or signature for a given molecular sample.

1.5.1 Normal Modes

A molecule of N atoms has total of 3N degrees of freedom, of which three correspond to transitional degrees of freedom and two or three correspond to rotational degrees of freedom. For non-linear and linear molecules with *N* atoms, molecules have 3*N*-6 or 3N-5 degrees of freedom respectively for vibrational motions. These vibrational motions are called normal modes. In each normal mode, all atoms of a molecule are vibrating in same phase and frequency which are unique to each molecule and susceptible to environmental effect. The frequency of this periodic motion is known as vibration frequency. A stretching vibrational mode can be identified if a change in the bond length is experienced and bending mode can be identified if a bond angle is modified. Stretching modes can be symmetrical or asymmetrical, whereas bending movement includes scissoring, rocking, wagging, and twisting. For the simplest case of a diatomic molecule, the vibrational frequency ($\tilde{\upsilon}$) can be calculated using the equation:

$\tilde{\upsilon} = \frac{1}{2\pi c}\sqrt{\frac{k}{\mu}}$, where k is the force constant (spring constant) and μ is the reduced mass. The reduced mass is given by

$\mu = \frac{m_1 m_2}{m_1 + m_2}$, where m_1 and m_2 are the component masses of the two atoms forming the chemical bond.

The vibrational frequency equation provides simple link that relates the frequency of light that a molecule will absorb to the reduced mass of the interacting atoms and the strength of the covalent bond between the two atoms. An isotope labeling of an atom can be determined from the dependence on mass, which modifies the atomic mass, and will induce a shift in the frequency. The force constant dependence suggests that a bond order and bond length will impact the vibrational frequency. Finally, the ionization state of a molecule modifies the force constant. That is, anion and cation formation of a molecule will cause changes in molecular electronic structure. Such frequency shifts are easily observed in IR spectra. These sensitivities make IR spectroscopy a great tool to understand molecular details such as chemical structure, bond, angle, orientation parameters, and intramolecular interactions.

1.5.2 Working Principle of FTIR

The center of FTIR spectroscopy is the Michelson interferometer that is shown in Fig. 1.5 (A). It consists of two-beam interferometer that divides a source light into two paths with different pathlengths but equal intensity. The divided beams are reflected off mirrors oriented perpendicularly to each other, and then recombined via the beam splitter. The recombining beams experience interference due to the pathlength difference. In a conventional FTIR spectrometer, one of the mirrors is fixed while the other mirror is scanning and moving continuously at constant velocity. The moving mirror creates a difference in optical pathlength, and the recombining beams

produces a constructively or destructively interference pattern depending on the optical path difference. The helium neon laser is applied to measure the optical path difference and align accessories. When the pathlengths are same distance meaning that the two light beams have zero path difference (ZPD), two beams are in phase and produce constructive interference for light at all wavelengths; however, if these two split lights travel different distance, meaning they have optical pathlength difference (OPD), it produces interferences where some are constructive and some are destructive. The resulting interference pattern of the recombined beams is known as an interferogram, and a plot of light intensity versus optical path difference is obtained by IR spectroscopy as is shown in Fig. 1.5 (B). Since an interferogram contains information of all the wavelengths in it, separation of light is not required: each time a measurement is made, data on all the wavelengths are collected simultaneously. This multiplexity is one of the major advantages of FTIR spectrometry over dispersive spectrometry (Fellgett's advantage) [69]. Additionally, the slits used in a dispersive spectrometer for a selection of wavelength is not required in an FTIR spectrometer, so more light can be delivered to the detector. This advantage is known as the throughput or Jacquinot's advantage. Instead of slit widths, an OPD determines a spectral resolution for an FTIR spectrometer. Although an interferogram contains information of all the spectral region, a relationship between intensity and OPD is of little use. For polychromatic radiation, the interferogram is a sum of monochromatic waves. The intensity of interferogram falling in the detector, I (δ), is

$I(\delta) = \int_{-\infty}^{+\infty} B(\tilde{\nu})\,(\cos 2\pi\tilde{\nu}\delta)\,d\tilde{\nu}$, where δ is the path difference between two beams, $\tilde{\nu}$ is the wavenumber, and B is the spectral power density.

The Fourier transformation mathematic method is applied to transform the digitized information on the interferogram into spectrum. The intensity of light can be represented as a

function of wavenumber as follows: $B(\tilde{\nu}) = \int_{-\infty}^{+\infty} I(\delta)\,(\cos 2\pi\tilde{\nu}\delta)\,d\delta$, where $B(\tilde{\nu})$ is the intensity of the light detected as a function of wavelength and is called a single beam spectrum. The Fourier-transformed interferogram in the last equation gives an intensity as a function of frequency, $\tilde{\nu}$. The processed spectrum of intensity *vs.* frequency is known as a single-beam spectrum that is shown in Fig. 1.5 (C). Calculation of an absorption spectrum (Fig. 1.5 (D)) from the single-beam spectrum is similar to other absorption spectroscopy and follows the Beer-Lambert law [70, 71], which is as follows:

$A = \log(\frac{I_0}{I}) = \varepsilon c l$, where A is absorbance; I_0 is the intensity of incident radiation; I is the intensity after passing through the sample; ε is the molar extinction coefficient or absorptivity; c is the concentration; and l is the path length. Vibrations from different chemical functional groups in the molecule give rise to infrared bands of different intensities due to difference in the change in dipole moment upon light excitation or absorptivity ε.

Fig. 1.5 (D) shows an infrared absorption spectrum for trimeric PSI particles from cyanobacterium *S.6803* where the binding site is occupied by one of the halogenated NQs and only a few broad and intense bands are observed. The prominent bands of the spectrum can be determined based on the functional group frequencies where the intensity of an absorption band depends on the concentration of the absorbing chromophore and the path length of the sample. In the PSI protein sample, there are many thousands of functional groups contributing to each band in the absorption spectrum and much information is hidden under the broad, featureless absorption bands. As a result, specific molecular bond information cannot be extracted from this absorption spectrum. Oftentimes, contribution from the system is many orders of magnitude greater than an absorption by a target molecule. As shown in the Fig. 1.5 (D) in a biological system (inset is the pics of a FTIR cell), the major contributions in the higher region are due to water in the

environment and the amino acid. The repetitive unit of the peptide backbone gives rise to large characteristic absorption bands around 1650 and 1550 cm^{-1}, two of which are known as amide I and amide II respectively. To study the vibrational properties of the target cofactor, the absorption by the cofactor of interest must be selectively extracted. Therefore, to obtain specific molecular level information from such a complicated sample difference spectroscopy (DS) is required.

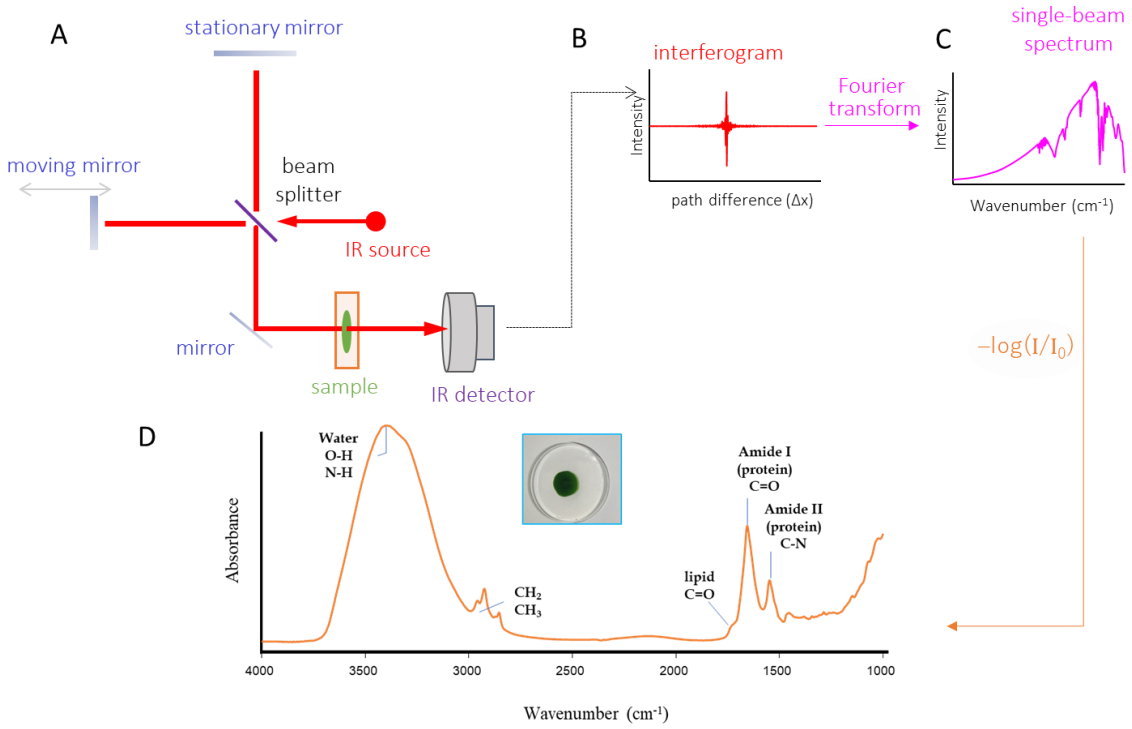

Figure 1.5 (A) A schematic of core components of an FTIR spectrometer, (B) Interferogram, as an IR intensity against optical pathlength difference (OPD), (C) A typical single-beam spectrum, and (D) An absorption spectrum of a biological system (*inset* is an FTIR cell).

1.5.3 Difference Spectrum (DS) and Double Difference Spectrum (DDS)

Light-induced IR DS is constructed by subtracting one absorbance spectrum from another that has been changed slightly due to some perturbation, in other words, it can be calculated from spectra recorded before and after illumination. The DS only display contributions from those groups undergoing molecular change, meaning a shift in frequency during the illumination, and all the bands that remain unchanged cancel each other out. This gives the information of the

absorption for two different states of the molecule/bond/interaction of interest. Most widely the measured states include cation/anion, changes in oxidation state, and formation/dissociation of a bond. The intensity of a difference band depends on the shift induced upon the excited state formation, the smaller the shift, and the lower the intensity of the difference band. The magnitude of a difference band shift gives a measure of the change in electron density distributed in the molecular bond. The intensity of a difference band therefore effectively reveals how electron density within a bond is modified by the perturbation. As a result, the absorption bands due cofactor of interest can be revealed by removing contributions from the environment.

The main issue with the IR DS is that specific band assignments for specific molecular structure are hard to be determined even when the unwanted protein and water absorption are removed. To solve this problem, the construction of double difference spectrum (DDS) is required. By subtracting one difference spectrum of one species from difference spectrum of another species in the same environment, a double difference spectrum (DDS) can be generated. Based on DS, site-directed mutagenesis and isotopic labeling of ligands, cofactors and amino acids can be used to assign different signals to individual molecular groups. The changes are aimed to shift frequencies of specific vibrational modes of molecular bonds. By producing DDS, all the unaffected modes disappear and only the modes shifted by the introduced change will be visible.

In order to produce DS, two different states such as ground and excited states need to be produced, which is facilitated if a second state is triggered by an actinic light that can be controlled simply by on/off of the actinic light source. As mentioned in the earlier section, the reactions in photosynthetic RCs are light-activated. Light-induced FTIR DS is applied as a photoaccumulation experiment for photosynthetic RCs. During this experiment, absorption spectra are measured before, during, and after an exposure to actinic light, with a duration of the exposure ranging on a

second to minute timescale. Continuous exposure to the actinic light accumulates a static, photo−accumulated [$P700^+$ – P700] radical pair state and allows for its spectrum to be measured and averaged on a sub-minute to minute timescale. This type of DS before and after the light-activation is free from absorption bands and suitable for the environmental effect. Many of the FTIR DS for the primary donors are collected by this method. In this study, static photo−accumulated [$P700^+$ – P700] FTIR DS were obtained at 77K as described previously using a Bruker Vertex80 FTIR spectrometer equipped with a MCT detector (Bruker Optics, Billerica, MA) [72-75]. Illumination was provided by a 20-mW helium neon laser, expanded to a spot size of ~1 cm at the sample.

However, A_1 is shortly lived and sometimes the states cannot be accumulated; that time static (steady-state), photoaccumulated (light-dark) technique fails to capture the information of the cofactors in the PSI RCs as it does not monitor the temporal evolution of the spectra. Here comes FTIR DS where the DS technique must be applied in a time-resolved fashion.

1.5.4 Time-resolved step-scan Fourier Transform infrared DS and decay associated spectra (DAS)

To study a cofactor like A_1 which decays in a µs time scale, a measurement technique with much faster temporal resolution is required. To achieve µs time resolution, the interferometer must scan in discrete “steps” instead of in a continuous motion as in rapid-scan mode. Such a technique is called time-resolved step-scan (TRSS) FTIR difference spectroscopy. Here, the transient absorption kinetics is measured at a distinct mirror position, while the scanning mirror is held still which is then “stepped” slightly in OPD to the next position, and the kinetic measurement is repeated. Once these light beams recombined at beam splitter after having either constructive or destructive (ZPD or OPD) interference, time-resolved interferograms can be re-constructed.

In the TRSS FTIR measurement, the data acquisition is on the temporal axis and the spectral profile is computed by the data analysis which is opposite to the steady-state or rapid scan techniques where a data acquisition in on the spectral axis and a product of post-acquisition data analysis is visible on the temporal axis.

In this measurement technique, as the mirror is moved in discrete steps instead of continuous moving mirror, the speed of the scanning mirror is not applicable any more to the temporal resolution. The time resolution is determined by the detector response time, the width of actinic light source, and the analog-to-digital converter. A few noteworthy steps must be followed to collect reliable data. Firstly, to reproduce an interferogram, the mirror steps are often in the range of 500 to 1000 and at least one kinetic measurement must be made at each step. Secondly, multiple measurements are coadded (10 to 20) at each step to have a better signal-to-noise ratio, which means the reaction must be repeatable (~20 – 60 times) and averaged. Variations in any step of the measured reaction as well as in the sample state will produce spectral and/or kinetic artifacts as each experimental steps needs tens to hundreds of thousands of repeated reactions.

The reaction timescale, number of repetitions required, and the number of steps required to complete an interferogram determine the duration of the step-scan experiment. Reaction kinetics generated by the previous actinic flash must be decayed 100% before a new one can be sent. The timescale of the reaction kinetics, therefore, sets the maximum repetition rate at which the actinic pulse can triggered. With a repetition rate of 10 Hz, with 20 coadditions per step and 60 individually averaged data, an entire set of experiments would take approximately (120 x number of steps) seconds which is more than 30 hours of continuous collection of data.

For the studies in this dissertation (chapter 4-6), time−resolved step−scan (TRSS) FTIR DS were collected in a manner similar to that described previously [73-76], using the same Bruker

Vertex 80 FTIR spectrometer equipped with a MCT detector. TRSS FTIR DS were collected with the temporal resolution which was 6 μs over a 3.5 ms time window at 77 K, and 590 time slices are measured per kinetic trace (36 points before the actinic flash). 20 coadditions are made per stepping point, and the experiment is usually repeated 40-60 times. At least three independently prepared PSI samples (with the different quinones incorporated) were used, and the result of ~120 full step-scan acquisitions were averaged. Data were collected at 4 cm^{-1} spectral resolution and 946 stepping points, which corresponds to the spectral range of 2106.39 to 1065.54 cm^{-1}. Light above 1950 cm^{-1} was blocked by placing 2000−1000 cm^{-1} bandpass filters both before the sample and in front of the MCT detector. The latter also blocks stray laser illumination from reaching the detector. Light below ~1100 cm^{-1} was also blocked by the CaF_2 sample windows and the windows on the cryostat shroud. Sample excitation was provided by 532 nm laser flash of 5 ns duration from a Minilite Nd:YAG laser (Continuum, San Jose, CA) operating at 10 Hz. Laser flashes with a power of ~0.785 mJ/cm^2 (1 mJ per pulse spread over a circle of diameter of ~1 cm at the sample) were used. The standard error of the three independent spectra obtained for each sample is taken as a measure of experimental variability (noise level) in the measurements and is indicated as error bars on the spectra.

The complete TRSS FTIR DS data set was globally analyzed using Glotaran software [77]. The TRSS FTIR DS were fitted globally to multi−exponential functions and decay−associated spectra (DAS) were constructed. This was done in part to separate spectral features associated with a sample heating artifact caused by the actinic laser flashes used to initiate photochemistry [44].

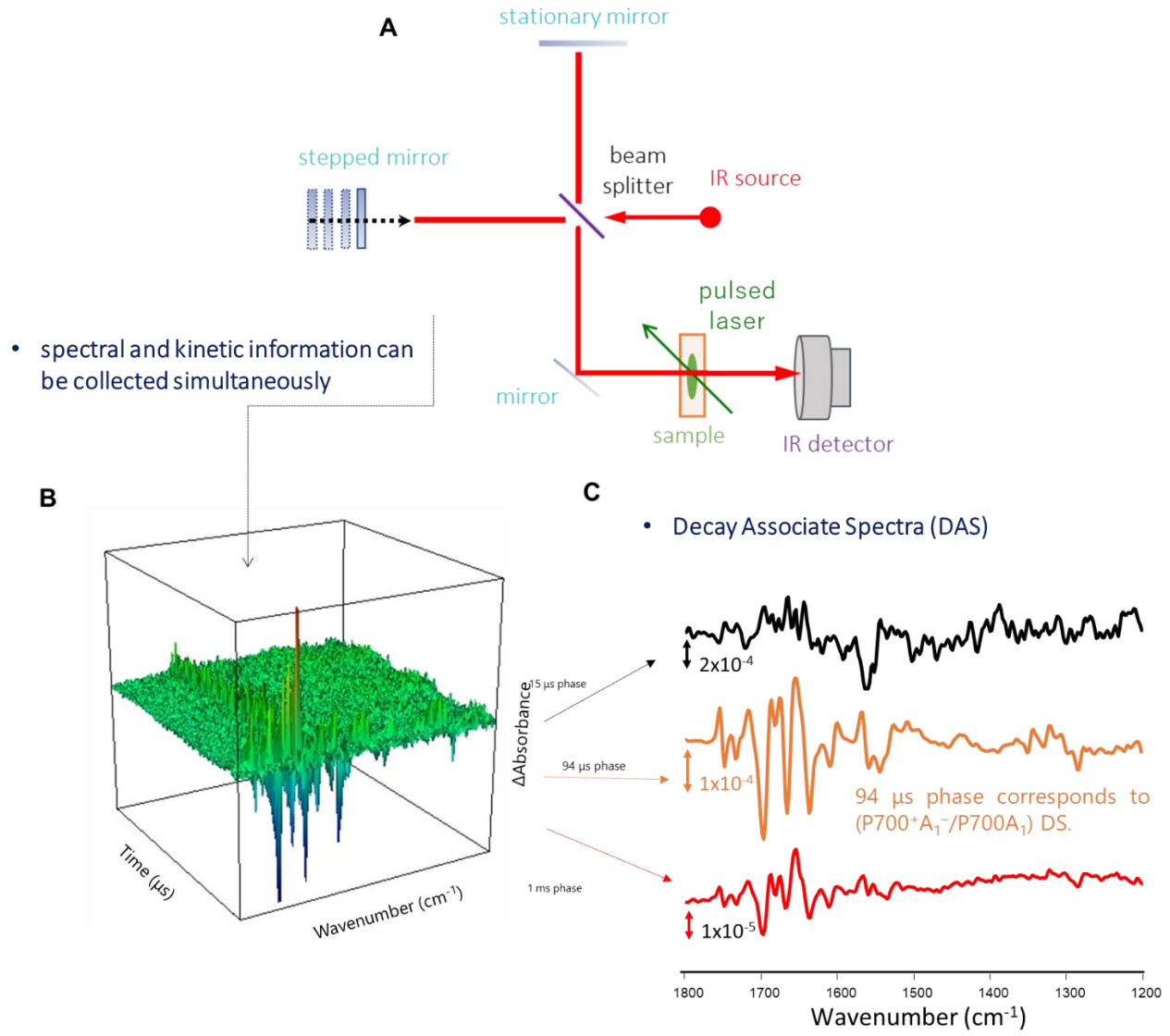

Figure 1.6 (A) A schematic of core components of an TRSS FTIR spectrometer, (B) 3D spectral and kinetics information, (C) Decay Associated Spectra (DAS).

1.6 Computational Methods for Spectral Analysis

To aid in the analysis and interpretation of the bands from the experimental data, DFT−based molecular geometry optimization and harmonic normal−mode vibrational frequency calculations were undertaken for the different neutral and semiquinone anions in THF (Fig. 1.7 (A)) as described previously [78], using Gaussian16 software (Gaussian Inc. Wallingford, CT) [79]. The phytyl tail of PhQ was truncated to a 5−carbon unit [$CH_2CHC(CH_3)_2$]. Asymmetric

H−bonded quinone models were constructed starting from the 2.5 Å X−ray crystal structure of PSI from *T. elongatus*. To construct this model for the other NQs, PhQ in the A_{1A} binding site was modified without altering the position and orientation of the quinonic ring atoms.

DFT calculations were performed using the B3LYP functional in combination with the 6−31+G(d) basis set [80]. For the anion state of the quinone of interest, the overall charge was assigned as −1 which is 0 for neutral state. The solvent (THF) was considered using the integral equation formalism of the polarizable continuum model [81], using default parameters in Gaussian16 software. Harmonic, normal mode vibrational frequency calculations result in "stick spectra" (intensities at given frequencies). These stick spectra are convolved with Gaussian functions of 4 cm^{-1} half−width to produce more realistic looking absorption spectra.

For each molecular model a single scaling factor was calculated by taking the ratio of the calculated and experimental frequencies of the main $C_1 \cdots O$ mode of PhQ^- (at 1495 cm^{-1} [44]) for anion state (chapter 4) and $C_1 = O$ mode of PhQ (at 1662 cm^{-1}) [82-84] for neutral state (chapter 2 and 3). Such a scale factor is in the range of that expected for the functional and basis sets used in our calculations. These scaling factors are purely for ease of comparison and are largely irrelevant as it is primarily the shift in the vibrational frequencies for the different quinones that are of interest, and this shift does not depend significantly on the scaling factor.

An assignment of calculated frequencies to molecular groups was based on visual inspection of the calculated atomic displacements associated with the normal modes. The atomic displacements were visualized using GaussView 6 software (Gaussian, Wallingford, CT).

For the isolated quinones in solution, potential energy distributions (PEDs) associated with the normal modes are calculated using VEDA [85]. PEDs provide a percentage estimate of how much a specific molecular group contributes to a normal mode (chapter 2 and 3).

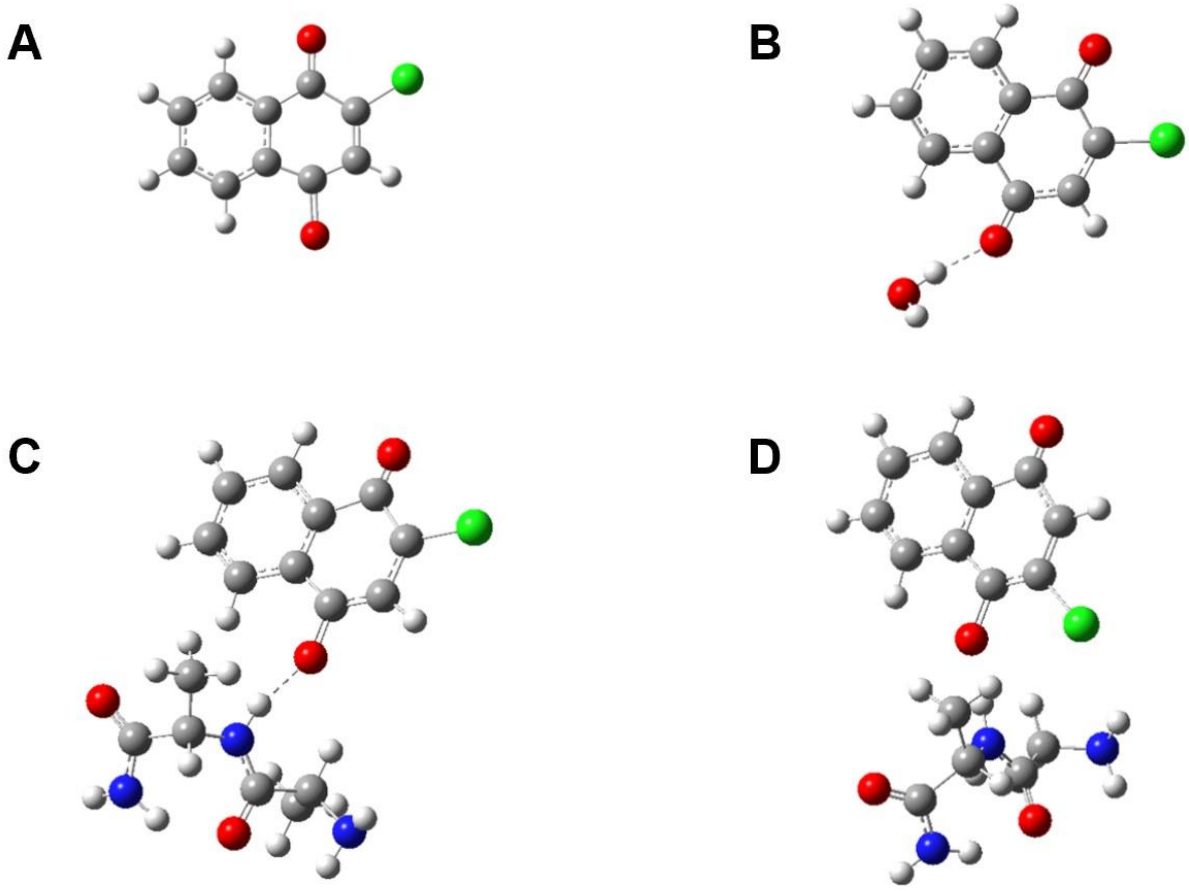

Figure 1.7 Computational models for the vibrational frequency calculations. (A) No specific interaction (in solution), Asymmetrical H-bonding is provided to a carbonyl group of quinone by a water molecule in (B) Q+H_2O model, by amino acid residues cutout from the A_{1A} binding site in (C) Q+Leu model, in (D) flipped model. Parameters for the optimized geometry (bond lengths and angles) are listed in Table 4.5 (2ClNQ in these illustrations).

For quinones in the binding site for the reduced state, calculations for the semiquinones H−bonded to either a water molecule (Fig. 1.7 (B) and 4.9) or to the amide backbone N−H group of a Leu residue (Fig. 1.7 (C)/4.5/4.10) were undertaken. The different molecular models are referred to as follows: (Q^-+H_2O) for the semiquinones H-bonded to a water molecule (Fig. 1.7 (B); (Q^-+Leu) for the model shown in the inset in Fig. 1.7 (C)/4.5 for the semiquinones H-bonded to a peptide N−H group of a truncated Leu residue which indicates the molecular model also

includes a portion of the backbone from Ala721 and Ser723. When necessary, we will refer to this as (Q^{-}+Leu, model 1 (m_1)). A slightly simpler model with a reduced number of atoms in the protein backbone is considered in Fig 4.10. When necessary, we will refer to this simpler model as (Q^{-}+Leu, model 2 (m_2)). Comparison of the data in Fig. 4.5 and 4.10-4.14 indicate very similar spectra are calculated for the m_1 and m_2 models.

A model termed (flipped Q^{-}+Leu (f-m_1)) is also considered (Fig. 1.7 (D)), where the semiquinone is rotated ~180^{o} along the axis perpendicular to the line joining the C=O groups (quinone is "flipped"). For the three mono substituted NQs, the quinones are "flipped" simply by interchanging the positions of groups attached at C_2 and C_3. Calculated spectra for the "flipped" monosubstituted NQs are shown as *dotted* lines in Fig. 4.5 and 4.10. Composite spectra that are the average of the spectra obtained using the flipped and non-flipped models are also shown in Fig. 4.5 (*grey dotted lines*).

In this study, for PSI with non-native NQs incorporated, we will refer to the H–bonded C=O group as the C_4=O group. We will also refer to the substitutions at C_3 and C_2 as being ortho or meta to the H–bonded C_4=O group, respectively. In some instances, this numbering scheme is not in keeping with IUPAC numbering, but it will make it simpler to compare normal modes for the different incorporated NQs.

1.7 Motivation for this Research

Recent studies started to reveal the functionality of the quinone in the A_1 binding site along with how the structural properties may relate to the thermodynamic and energetic properties of the pigment in the A_1 binding site [1, 86-88]. However, there are many unanswered questions on how different pigment-protein interactions may modulate the functionality of the quinones as ET cofactors in the A_1 binding site [15].

In recent years there has been a growing interest to investigate the molecular properties of PhQ in the A_1 binding site in photosystem I (PSI) photosynthetic protein complexes (and for quinones in protein binding sites in general). One possible way is to study PSI where the native quinone is replaced with a foreign one. Therefore, this interest in part stems from the considerably altered bioenergetics of electron transfer that occur in PSI with such substitutions. This became the focus of this dissertation which is on elucidation of the molecular mechanisms underlying the highly efficient solar energy conversion processes in PSI by studying the protein-quinone interaction through FTIR difference spectroscopy.

The second goal of this dissertation is to establish a way to study the PSI at RT in the future which has never been done before by studying vibrational properties of (relatively) low potential NQs incorporated into PSI, since the microsecond $P700^+A_1^-$ recombination is still the dominant decay pathway at RT in PSI with high potential NQs incorporated [22].

In cyanobacteria, PSI is found mainly in trimeric and slightly in monomeric form [89]. Recent studies reported that PSI also appears in a tetrameric form in some filamentous cyanobacterial species [90, 91]. In mesophilic *Synechocystis* 6803, both trimeric and monomeric structure of PSI have been resolved at atomic level [92, 93]. It seems there are no critical structural changes in monomeric and trimeric PSI. However, the ratio of PSI trimer and monomer varies under different growth conditions, such as light intensity, temperature, and nutrients, etc. [94, 95]. As such, it remains unknown how trimeric PSI is kinetically different than monomeric PSI which can only be probed by using flash induced/photo-accumulated PSI samples followed by biophysical interrogations. Therefore, the third goal is to investigate if there are PSI oligomerization states associated with differences in electron transfer kinetics by using TRSS FTIR.

FTIR is a molecular specific probe and can measure all infrared-active vibrational modes of the pigments involved in ET. In the ET process in the RC, A_1 is the key pigment to study as it is involved in both the forward and backward ET reactions. To study this short-lived A_1, time-resolved technique is used that can provide the kinetics and spectral information simultaneously. To fulfill all the above-mentioned aims, highly-resolved FTIR DS and "foreign – native" DDS are constructed for the A_1 cofactors, and to identify and assign the vibrational modes due to native and nom-native NQs in the A_1 binding site using DFT based vibrational frequency calculations for the different quinones in solvent or in the presence of a single asymmetric H–bond. Specifically, the effect of asymmetrical H-bonding to the quinone and the orientation of mono-substituted halogenated NQs in the binding site are investigated.

1.8 Dissertation Overview

This chapter introduces the background information on photosynthesis and photosystem I, on the structure, function, and energetics in PSI. Brief introductions to the FTIR spectroscopy, DFT based vibrational frequency calculations are summarized here as well.

In chapter 2, we present FTIR absorbance spectra for 2-chloro-1,4-naphthoquinone (2ClNQ), 2-bromo-1,4-naphthoquinone (2BrNQ), 2,3-dichloro-1,4-naphthoquinone (Cl_2NQ), and 2,3-dibromo-1,4-naphthoquinone (Br_2NQ) in tetrahydrofuran (THF). These spectra are compared to that obtained for PhQ (and DMNQ) and 2MNQ in THF. In addition, in order to help assign bands in the experimental spectra, density functional theory (DFT) based vibrational frequency calculations were undertaken. By calculating normal mode potential energy distributions unambiguous, quantitative band assignments were made. The calculated and experimental spectra make several predictions about what might be observed in time resolved FTIR difference spectra obtained using PSI with the different quinones incorporated.

Chapter 3 mainly focuses on studying three disubstituted NQs, all of which also have a methyl group substitution. According to the IUPAC numbering scheme the methyl group is at the 3-position for some of these disubstituted NQs (Fig.3.1). For ease of comparison and discussion, we will adopt a numbering scheme for all the quinones where the methyl group is at the 2-position. The substituted NQs therefore differ only in the substitution at the 3-position, and our goal here is to try to parse out subtle features in the FTIR absorption spectra that may be related to the substitution at the 3-position. In this study FTIR absorbance spectra for BrMeNQ, CMMeNQ and ETMeNQ in tetrahydrofuran (THF) are obtained. These spectra are compared to spectra for 2MNQ, DMNQ and PhQ (all in THF) that have been obtained previously. Like the chapter 2, density functional theory (DFT) based vibrational frequency calculations are also undertaken here for all the quinones in THF. From these calculations, calculated FTIR absorption spectra are produced and compared to the experimental spectra.

Chapter 4 is one of the main attractions of this dissertation. Most of the previous FTIR studies focused on the vibrational properties of (relatively) low potential NQs incorporated into PSI. In this part of the study, we focus on studies of PSI with a series of high potential halogenated NQs incorporated. There are many reasons for this, one of them being that it is, or will be, possible to study PSI at RT, as microsecond $P700^{+}A_1^{-}$ recombination is still the dominant decay pathway at RT in PSI with high potential NQs incorporated [22]. In preparation for these future TRSS FTIR studies we first present here studies at 77 K, focusing on the quinones in the reduced states [1, 57, 63, 65, 66].

In chapter 4, we further probe the vibrational properties of four different high potential NQs incorporated into the A_1 protein binding site by obtaining [$P700^{+}A_1^{-}$ – $P700A_1$] and [A_1^{-} – A_1] FTIR DS and “foreign − native” DDS. We show that bands in the DS are unmasked and more

easily visualized when multiple DDS can be compared. To aid in spectral interpretation of the demasked bands we also used DFT based vibrational frequency calculations for the different quinones in solvent or in the presence of a single asymmetric H−bond.

In Chapter 5, we use time-resolved step-scan (TRSS) FTIR difference spectroscopy (DS) at 77 K to study a PSI mutant from S6803 in which TrpB673 was changed to Phe. In this PSI mutant, spectral contributions from both $P700^{+}A_{1}^{-}$ and $^{3}P700$ are found. Adjusting the PSI samples' exposure to actinic illumination at RT, prior to freezing, resulted in different ratio of $P700^{+}A_{1}^{-}$ and $^{3}P700$ states formed. Furthermore, $^{3}P700$ state formation was quenched in actinic light exposed PSI mutant samples incubated in the presence of PhQ. This study indicates that the TrpB673 mutation likely disturbs the group of water molecules in the environment near the aromatic ring of PhQ, leading to light-induced phylloquinol ($PhQH_2$) formation, presumably through a double-protonation event induced by the disturbed water molecules. Added PhQ in the buffer is able to displace $PhQH_2$ in the A_1 binding site.

In chapter 6, we isolated and investigated cyanobacterial PSI (*Synechocystis* sp. PCC 6803 (*S6803*) using µs time-resolved step-scan FTIR difference spectroscopy (TRSS FTIR DS) at 77 K. The investigation was for both the neutral and anion states with three different PSI complexes Comparisons have been performed between trimeric and monomeric native and non-native PSI (mutant cells, hereafter called *menB*$^{-}$ PSI). For wild type (WT) trimeric and monomeric PSI, phylloquinone (PhQ) (2-methyl-3-phytyl-1,4-naphthoquinone) molecule is occupied in the A_1 binding site and for the trimeric *menB*$^{-}$ PSI in which the *menB* gene is inactivated, PhQ synthesis is inhibited, and a plastoquinone molecule (PQ) (2,3-dimethyl-1,4-benzoquinone) is found to occupy the A_1 binding site instead of PhQ [55] (see Fig. 6.1 for molecular structures). In addition, we investigated the $P700^{+}F_{A/B}^{-}$ radical pair recombination time constant at RT and $P700^{+}A_{1}^{-}$

radical pair recombination time constant at LT for monomeric and trimeric PSI with PhQ incorporated at 298 K and compared the data with previous studies on trimeric PSI with PhQ and PQ incorporated. Previously studies are conducted on all these PSI complexes but to clarify some ambiguities on some bands in both neutral and anion spectral regions and comparisons have been made between WT trimeric and monomeric PSI and trimeric *menB*$^{-}$ PSI complexes from same *Synechocystis* sp. PCC 6803 (*S.6803)*. For observing bands associated to $P700^{+}$/P700 and neutral and reduced quinone bands, [$P700^{+}$ – P700]FTIR DS, [$P700^{+}A_1^{-}$ – $P700A_1$] DS and [A_1^{-} – A_1] FTIR DS are calculated.

2 CALCULATED AND EXPERIMENTAL INFRARED SPECTRA OF SUBSTITUTED NAPHTHOQUINONES

ABSTRACT

In recent years there has been interest in incorporating high-potential, halogenated 1,4-naphthoquinones (NQs) into the A_1 binding site in photosystem I (PSI). This interest in part stems from the considerably altered bioenergetics of electron transfer that occur in PSI with such a substitution. FTIR studies of PSI complexes with halogenated NQs incorporated are also being undertaken. With this in mind it is necessary to consider FTIR absorption spectra of these halogenated quinones in solution, and here we present FTIR absorbance spectra for 2-chloro-1,4-naphthoquinone (2ClNQ), 2-bromo-1,4-naphthoquinone (2BrNQ), 2,3-dichloro-1,4-naphthoquinone (Cl_2NQ) and 2,3-dibromo-1,4-naphthoquinone (Br_2NQ) in tetrahydrofuran (THF). The FTIR spectra of the substituted naphthoquinones (NQs) were compared to FTIR spectra of 2-methyl-3-phytyl-1,4-naphthaquinone (phylloquinone (PhQ)) and 2-methyl-naphthoquinone (2MNQ). To aid in the assignment of bands in the experimental spectra, density functional theory (DFT) based vibrational frequency calculations for all the substituted NQs were undertaken. The calculated and experiment spectra agree well. By calculating normal mode potential energy distributions unambiguous, quantitative band assignments were made. The calculated and experimental spectra make several predictions about what might be observed in time resolved FTIR difference spectra obtained using PSI with the different quinones incorporated.

2.1 Introduction

The redox properties of quinones allow them to be utilized in a wide range of functions in different biological systems [96]. In photosynthetic reaction centers (RCs), quinones are well known cofactors in electron transport (ET). In type II RCs, which includes photosystem II (PSII)

of oxygen evolving organisms and purple, non-sulfur bacteria, quinones function as terminal electron acceptors in the so-called Q_A and Q_B binding sites [97, 98]. Even although the Q_A and Q_B binding sites may be occupied by the same quinone (such as plastoquinone in PSII [99]) their functions are quite different, where the Q_A quinone is an intermediary in ET while the Q_B quinone is involved in proton-coupled ET [100]. In type I RCs, which have iron sulfur clusters as terminal electron acceptors, and includes photosystem I (PSI) from plants and algae, quinones function as an intermediary in transferring electrons from A_0 to F_x [101].

In native PSI a phylloquinone (PhQ) molecule occupies the A_1 binding site [30]. PhQ is a di-substituted 1,4-naphthaquinone (NQ) (2-methyl,3-phtyl-NQ) (also known as Vitamin K_1). Menaquinones (MQs) are identical to PhQ except in the degree of saturation of the hydrocarbon tail, [102] and MQs are found in the Q_A binding site in type II purple bacterial reaction centers from *Blastochloris viridis* and *Chloroflexus aurantiacus* [103]. MQs (and PhQ) can also be substituted into the Q_A binding site in purple bacterial reaction centers from *Rhodobacter sphaeroides* [98]. The function of substituted NQs in both type I and II RCs is therefore of some interest [104]. In particular, exactly how the substituent groups of the NQs can alter or modulate their redox properties of quinones in protein binding sites is of considerable interest [57].

In recent years it has become possible to substitute a range of different NQs into the A_1 binding site in PSI [1, 98]. These PSI particles with different NQs incorporated into the A_1 binding site are now being studied using FTIR difference spectroscopy, [44, 105] and of particular interest for the purposes of this manuscript is PSI with different halogenated NQs incorporated. The overall goal in FTIR studies of PSI with different NQs incorporated is the identification of bands in the spectra that are associated with the neutral and reduced states of the incorporated NQs. These bands will provide information on pigment protein interactions that may help modulate the

redox properties of the incorporated quinones [30, 64, 99, 105]. Study of halogenated NQs in the A_1 binding site is very interesting, not only in terms of the FTIR difference spectra, but also in terms of the bioenergetics, which are very different. Halogenated NQs intrinsically have a very high redox potential, and even in the A_1 binding site in PSI, the $P700^+A_1^-$ radical pair state is considerably lower in energy than the $P700^+F_X^-$ state, making uphill ET from A_1^- to F_X essentially impossible. Therefore, the $P700^+A_1^-$ state decays by radical pair recombination, which occurs on a tens to hundreds of microsecond timescale at both 298 and 77 K [57, 106]. This simplifies the collection of highly-sensitive time resolved (TR) FTIR DS [107].

When considering bands in TR FTIR DS obtained using PSI with different NQs incorporated, the starting point is to first obtain and interpret the FTIR spectrum of the NQ in solution. Such an interpretation invariably involves (more recently) the use of quantum chemical computational methods to simulate the experimental spectra. These suggested initial steps are the subject of this manuscript.

In this manuscript FTIR absorbance spectra for 2-chloro-1,4-naphthoquinone (2ClNQ), 2-bromo-1,4-naphthoquinone (2BrNQ), 2,3-dichloro-1,4-naphthoquinone (Cl_2NQ), and 2,3-dibromo-1,4-naphthoquinone (Br_2NQ) in tetrahydrofuran (THF) are obtained. These spectra are compared to that obtained for PhQ (and DMNQ) and 2MNQ in THF. In addition, in order to help assign bands in the experimental spectra density functional theory (DFT) based vibrational frequency calculations are undertaken.

2.2 Materials and Methods

All quinones and solvents used here were obtained from Sigma-Aldrich Inc. (St Louis, MO), and used as received. 2ClNQ was obtained from Pure-Chemistry Scientific (Burlington, MA) and used as received.

FTIR absorption spectra of the NQs were measured using a Varian 600 UMA FTIR microscope (Varian Inc., MA, USA), utilizing a mercury cadmium telluride detector. Spectra were collected at 4 cm^{-1} resolution. The different NQs were dissolved in tetrahydrofuran (THF) at various concentrations, and a small drop (<5 μL) was deposited on a zinc selenide window. An FTIR spectrum of pure THF was obtained and interactively subtracted.

Calculations were undertaken using Gaussian16 software.[108] (Gaussian Inc. Wallingford, CT). The phytyl tail of PhQ was truncated to a 5-carbon unit [$CH_2CHC(CH_3)_2$]. DFT calculations were performed using the B3LYP functional in combination with the 6-31+G(d) basis set [80]. The solvent was considered using the integral equation formalism (IEF) of the polarizable continuum model (PCM),[109] as it is implemented in Gaussian16. Harmonic, normal mode vibrational frequency calculations result in "stick spectra", which we convolve with Gaussian functions of 4 cm^{-1} half-width, to produce more realistic looking calculated spectra.

Assignment of calculated vibrational frequencies to molecular groups is often based on the calculation of potential energy distributions (PEDs) associated with the normal modes. PEDs are calculated using VEDA [85]. PEDs provide an estimate of how much a specific molecular group vibration contributes to a normal mode.

2.3 Results and Discussions

Fig. 2.1 shows the structure and numbering for the six quinones considered in this study. PhQ is the same as 2MNQ except that the phytyl chain is replaced with a hydrogen atom. Fig. 2.2 shows FTIR absorption spectra in the 1750-1200 cm^{-1} spectral region for PhQ, 2MNQ, 2ClNQ, 2BrNQ, Cl_2NQ, and Br_2NQ in THF. A spectrum for PhQ cast in a film of hexane has been obtained previously, and is very similar to that presented in Fig. 2.2 [110]. A spectrum for 2,3-dimethyl-1,4-naphthaquinone (DMNQ) in CCl_4 has also been obtained [63]. DMNQ is the same as PhQ

except the phytyl chain has been replaced with a methyl group, and it is found that the FTIR absorption spectra of PhQ and DMNQ (in the 1680-1580 cm^{-1} region) are nearly identical.

Fig. 2.3 shows DFT calculated FTIR spectra for the six quinones considered in this study. The PEDs associated with the normal modes that give rise to the most intense bands in the spectra in Fig. 2.3 are listed in Table 2.1. The calculated and experimental spectra clearly display similarities in both peak positions and in relative band intensities. How the calculated and experimental bands are associated is indicated in Table 2.1. In this manuscript calculated frequencies are scaled by 0.978 [111], which is arbitrarily chosen so that the observed band at 1662 cm^{-1} for neutral PhQ matches the frequency for the calculated band.

Modes of the phytyl chain of PhQ. PhQ in THF (Fig. 2.2A) displays bands at 1469 and 1377 cm^{-1} that are absent in the spectra of the other NQs (Fig. 2.2). These bands are therefore likely to be associated with the hydrocarbon phytyl chain of PhQ. The calculations support this notion, and show that the 1469 cm^{-1} band is due to CH_2 bending modes [$\delta(CH_2)$] of the phytyl-tail, while the 1377 cm^{-1} band is due to both $\delta(CH_2)$ and $\delta(CH_3)$ modes of the phytyl-tail (Table 2.1). This conclusion also agrees with previous studies [44, 112]. These assignments indicate the appropriateness of the computational methods used here.

Quinone C=O vibrations. For PhQ in THF the most intense absorption band is found at 1662 cm^{-1}, and calculations indicate that this band is due to the antisymmetric stretching vibration of both C=O groups (C_1=O, 54% and C_4=O, 30%) (Table. 2.1). For 2MNQ in THF a similar intense peak is observed at 1666 cm^{-1} with a weak shoulder near 1670 cm^{-1} (Fig. 2.2B). Computationally the intense 1666 cm^{-1} band is also assigned to an antisymmetric stretching vibration of both C=O groups (C_1=O, 52% and C_4=O, 32%) (Table. 2.1). Similarly, for Cl_2NQ and Br_2NQ in THF intense

bands are observed at 1686 and 1684 cm^{-1}, respectively. This is an upshift of 26 and 22 cm^{-1} relative to the same band of PhQ. Importantly, the observed upshift is very similar to that predicted computationally (26 and 24 cm^{-1}). In addition, the normal mode giving rise to the intense bands at 1686 and 1684 cm^{-1} for Cl_2NQ and Br_2NQ is again calculated to be an antisymmetric coupled vibration of both the C_1=O and C_4=O groups (For Cl_2NQ: C_1=O, 44% and C_4=O, 44%. For Br_2NQ: C_1=O, 44% and C_4=O, 45%) (Table. 2.1).

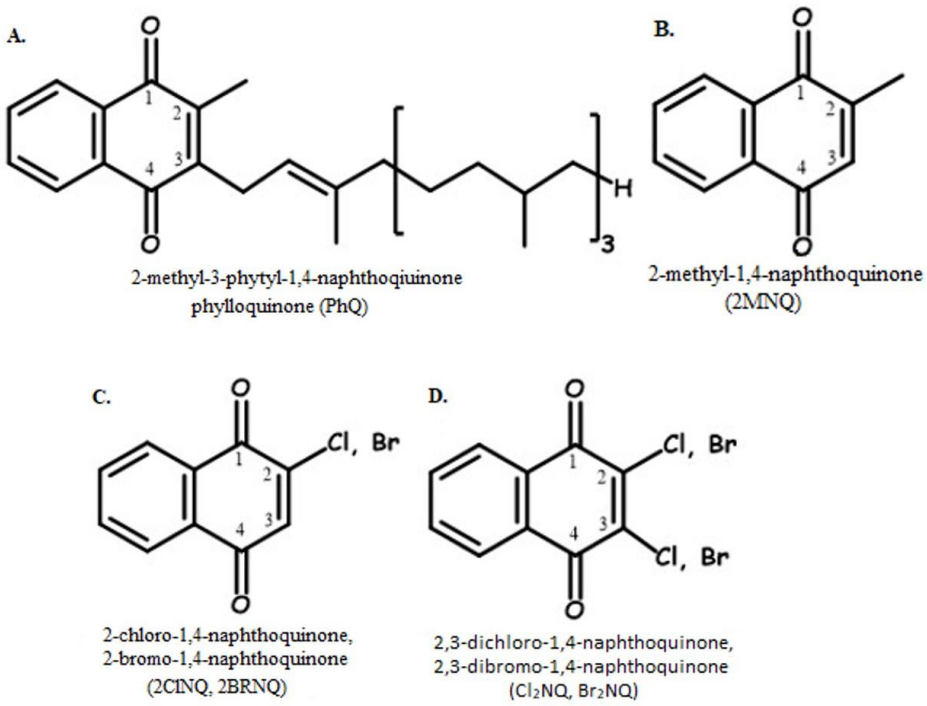

Figure 2.1 Structure and numbering of the different NQs considered here.

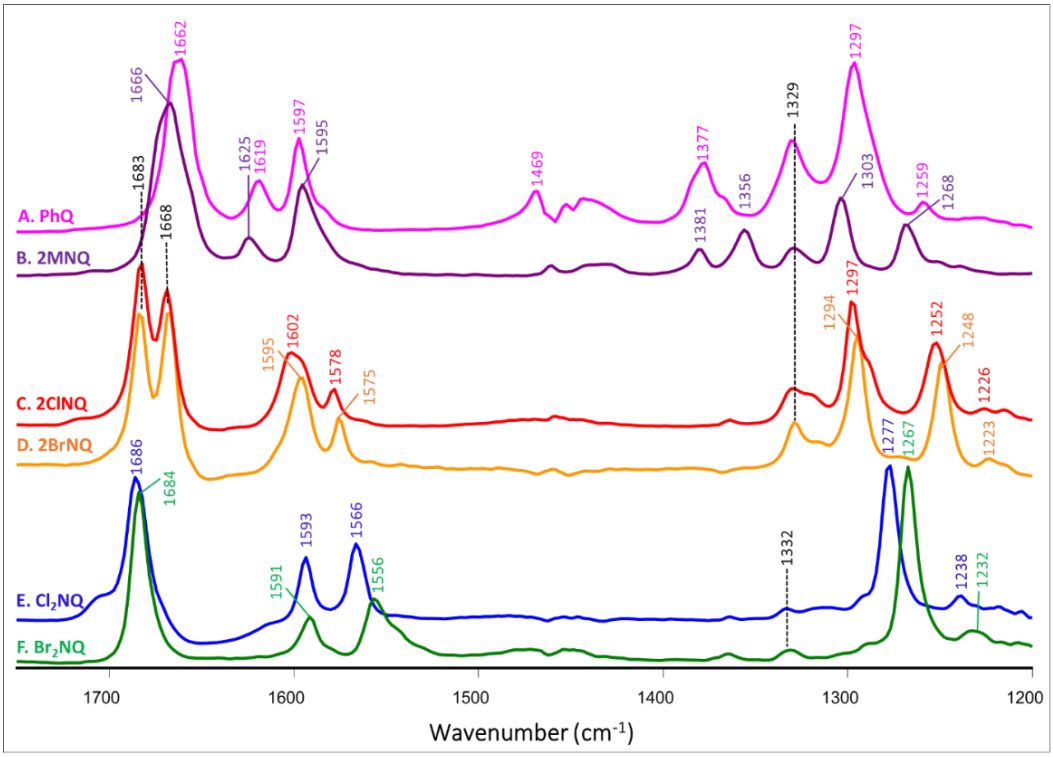

Figure 2.2 Experimental FTIR absorption spectra for (A) PhQ, (B) 2MNQ, (C) 2ClNQ, (D) 2BrNQ, (E) Cl_2NQ, and (F) Br_2NQ in THF. The spectra were scaled (1695-1640 cm^{-1}) so that the intensities of the bands around 1684 cm^{-1} are similar.

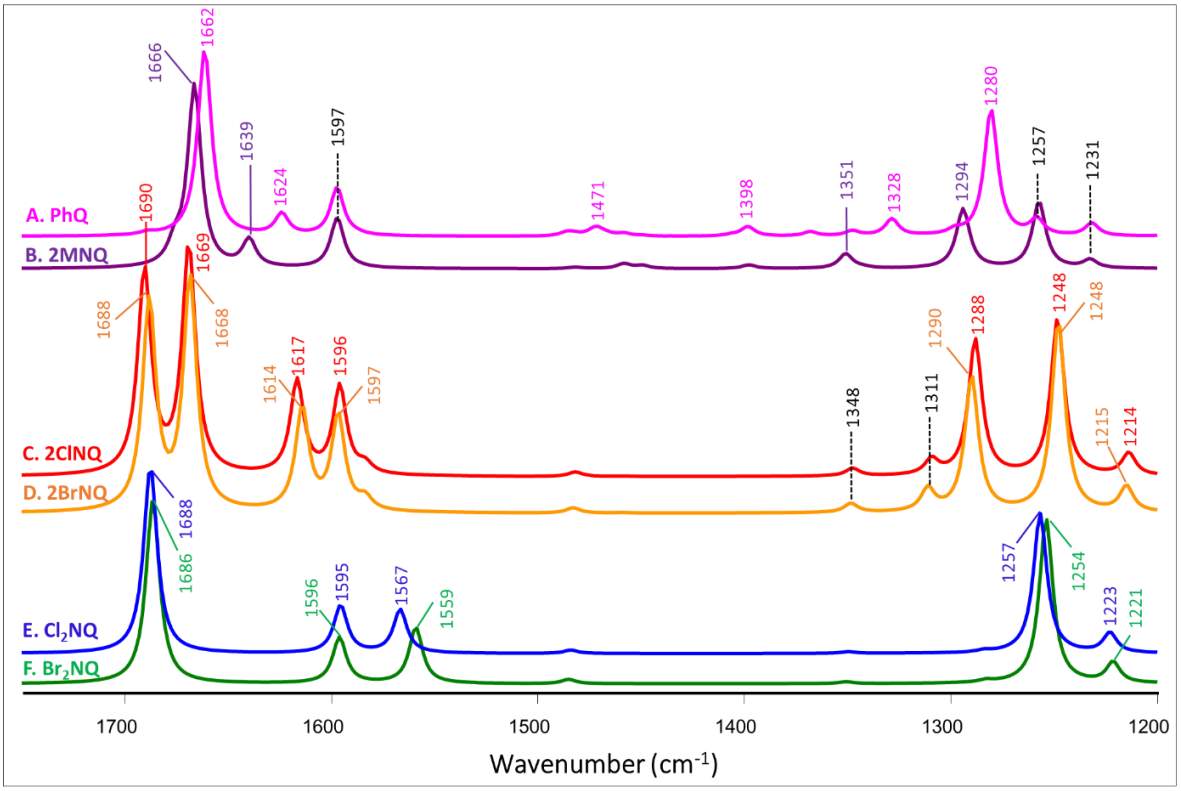

Figure 2.3 Calculated IR absorption spectra for (A) PhQ, (B) 2MNQ, (C) 2ClNQ, (D) 2BrNQ, (E) Cl_2NQ, and (F) Br_2NQ in THF. Frequencies are scaled by 0.978 [111]. Spectra were scaled so that the intensities of the bands between 1688-1662 cm^{-1} are similar. The actual intensities (in km/mol) are indicated in Table 2.1.

Table 2.1 Calculated normal mode vibrational frequencies (in cm^{-1}) and intensities (in km/mol) for the six NQs in THF. Only the most intense normal modes are listed. Frequencies are scaled by 0.978 to compare to experimental band frequencies, which are also listed. Potential energy distributions (PED) (in %) are also listed. Only molecular groups with PED above 10% are included. *Abbreviations*: *v*, bond stretching; *δ*, bending vibration; a, aromatic part of NQ ring; *q*, quinonic part of NQ ring; H*, hydrogen atom attached at position C_3; AS, antisymmetric.

Experimental frequencies (in THF) (cm^{-1})	Calculated frequencies (in THF) (cm^{-1})	Intensity (km/mol)	Potential Energy Distribution (%)
PhQ			
1662	1662	765.7	$[\nu(C_1{=}O)\ 54\% + \nu(C_4{=}O)\ 30\%]_{CAS}$
1619	1624	90.8	$\nu(C_2{=}C_3)\ 68\%$
1597	1597	204.7	$\nu(C\text{-}C)_a\ 64\%$
1469	1471	26.7	$\delta(CH_2)_{Methyl\text{-}tail}\ 49\% + \delta(CH_2)_{tail}\ 27\%$
1377	1398	71.8	$\delta(CH_2)_{tail}\ 85\%$
1297	1280	540.5	$\nu(C\text{-}C)_a\ 10\% + \nu(C\text{-}C)_q\ 39\%$
2MNQ			
1666	1666	765.9	$[\nu(C_1{=}O)\ 52\% + \nu(C_4{=}O)32\%]_{AS}$
1625	1639	114.6	$\nu(C_2{=}C_3)\ 68\%$
1595	1597	210.6	$\nu(C\text{-}C)_a\ 65\%$

1356	1351	61.9	ν(C-C)$_a$ 10% + ν(C-C)$_q$ 10%+ δ(CCH*) 17%+ δ(CCH)$_a$ 12%
1303	1294	249.6	ν(C-C)$_q$ 71%
1268	1257	278.9	ν(C-C)$_q$ 16% + δ(CCH)$_a$ 22%
2ClNQ			
1683	1690	403.8	ν(C$_1$=O) 86%
1668	1669	450.1	ν(C$_4$=O) 83%
1602	1617	185.6	ν(C$_2$=C$_3$) 72%
1578	1596	174.7	ν(C-C)$_a$ 63%
1297	1288	269.7	ν(C-C)$_q$ 32% +δ(CCH)$_q$ 12%+δ(CCH)$_a$ 14%
1252	1248	310.5	ν(C-C)$_q$ 10% +δ(CCH)$_a$ 25%
1226	1214	43.9	ν(C-C)$_q$ 28% +δ(CCH)$_a$ 10% + δ(CCH*) 17%
2BrNQ			
1683	1688	396.5	ν(C$_1$=O) 85%
1668	1668	437.9	ν(C$_4$=O) 82%
1595	1614	194.1	ν(C$_2$=C$_3$) 71%
1575	1597	180.2	ν(C-C)$_a$ 63%
1329	1311	42.3	ν(C-C)$_q$ 13% +δ(CCC)$_q$ 14%+ δ(CCH*) 36%
1294	1290	257.2	ν(C-C)$_q$ 34%+ δ(CCH)$_a$ 16%
1248	1248	361.2	ν(C-C)$_q$ 11%+ δ(CCH)$_a$ 25%
1223	1215	48.0	ν(C-C)$_q$ 28%+ δ(CCH)$_a$ 26%
Cl_2NQ			
1686	1688	789.8	[ν(C$_1$=O) 44%+ ν(C$_4$=O)44%]$_{AS}$
1593	1595	153.0	ν(C-C)$_a$ 68%
1566	1567	188.9	ν(C$_2$=C$_3$) 73%
1277	1257	607.9	ν(C-C)$_a$ 11% + ν(C-C)$_q$ 42%
1238	1223	86.2	ν(C-C)$_q$ 23% + δ(CCH)$_a$ 27%
Br_2NQ			
1684	1686	755.8	[ν(C$_1$=O) 44%+ ν(C$_4$=O)45%]$_{AS}$
1591	1596	153.1	ν(C-C)$_a$ 66%
1556	1559	233.1	ν(C$_2$=C$_3$) 68%
1267	1254	688.8	ν(C-C)$_q$ 52%
1232	1221	85.2	ν(C-C)$_q$ 25% + δ(CCH)$_a$ 29%

For 2ClNQ and 2BrNQ in THF the main intense peak discussed above is split into two separate peaks at 1683 and 1668 cm^{-1} (Fig. 2.2C, D). Such a clear (15 cm^{-1}) splitting is in agreement with calculations, which indicate intense bands at 1688-1690 and 1668-1669 cm^{-1} (Fig. 2.3C, D). The 1683 and 1668 cm^{-1} bands for 2ClNQ and 2BrNQ in THF are predicted to be due to C$_1$=O (86%) and C$_4$=O (83%) vibrations (Table. 2.1). This is an interesting result, as it is not observed or calculated for 2MNQ, which one might anticipate having spectra more similar to that of 2ClNQ or 2BrNQ than that for Cl_2NQ or Br_2NQ.

Quinonic and aromatic ring C=C vibrations. For PhQ in THF an absorption band is observed at 1619 cm^{-1} (Fig. 2.2A). A similar band is calculated at 1624 cm^{-1} (Fig. 2.3A), and is predicted to

be mainly due to a C_2=C_3 stretching vibration ($\nu(C_2=C_3)$, 68%) (Table. 2.1). For 2MNQ in THF the corresponding band is upshifted 6 cm^{-1} compared to PhQ to 1625 cm^{-1} ($\nu(C_2=C_3)$, 68%) (Table. 2.1). However, the calculated upshift is 15 cm^{-1} (Table 2.1).

For PhQ in THF an absorption band is observed at 1597 cm^{-1} (Fig. 2.2A). A similar band is calculated at the same frequency (Fig. 2.3A), and is predicted to be mainly due to a C=C stretching associated with the aromatic part of the NQ ring ($\nu(C=C)_a$, 64%) (Table. 2.1). For 2MNQ in THF the corresponding band is downshifted 2 cm^{-1} compared to PhQ at 1595 cm^{-1} ($\nu(C=C)_a$, 65%) (Table. 2.1). This agrees with calculations which predict the $\nu(C=C)_a$ mode to be at the same frequency for both 2MNQ and PhQ (Table 2.1).

For PhQ and 2MNQ the $\nu(C_2=C_3)$ vibration is at a higher frequency than the $\nu(C=C)_a$ vibration. This appears to be true for 2BrNQ and 2ClNQ, although the reverse is calculated to be true for Cl_2NQ and Br_2NQ.

For 2ClNQ and 2BrNQ in THF bands are observed at 1602 and 1595 cm^{-1}, respectively. Corresponding bands appear to be calculated ~15 cm^{-1} higher in frequency at 1617 and 1614 cm^{-1}, however. These bands are due to the $\nu(C_2=C_3)$ vibration. The corresponding bands for Cl_2NQ and Br_2NQ in THF (at least from a visual inspection of the spectra) are observed at 1593 and 1591 cm^{-1}, respectively. Corresponding bands appear to be calculated at very similar frequencies (1595 and 1596 cm^{-1}). These bands are due to the $\nu(C=C)_a$ vibration, however.

For 2ClNQ and 2BrNQ in THF bands are observed at 1578 and 1575 cm^{-1}, respectively (Fig. 2.2). Corresponding bands appear to be calculated at 1596 and 1597 cm^{-1}. These bands are due to the $\nu(C=C)_a$ vibration. The corresponding bands for Cl_2NQ and Br_2NQ in THF (at least from a visual inspection of the spectra) are observed at 1566 and 1556 cm^{-1}, respectively.

Corresponding bands appear to be calculated at very similar frequencies (1567 and 1559 cm^{-1}). These bands are due to the $\nu(C_2=C_3)$ vibration, however.

In summary, all the experimental and calculated spectra show three or four bands in the 1550-1690 cm^{-1} region. The highest frequency bands are due to $C_1=O$ and $C_4=O$ vibrations, or an antisymmetric combination of both. The next two lower intensity bands are due to $\nu(C_2=C_3)$ and $\nu(C=C)_a$ vibrations, with the $\nu(C_2=C_3)$ vibration being higher in frequency than the $\nu(C=C)_a$ vibration for PhQ, 2MNQ, 2ClNQ and 2BrNQ, and lower for Cl_2NQ and Br_2NQ. One noteworthy point is that for Cl_2NQ in THF the FTIR spectrum in Fig. 2.2E displays shoulders on the high frequency sides of some of the above discussed absorption bands. These shoulders are of unknown origin at present. A second noteworthy point is that the relative intensities of the three (or four) bands in the experimental spectra overall agree reasonably well with the calculated spectra.

PhQ in THF displays an intense band at 1297 cm^{-1}, which is at least as intense as the 1662 cm^{-1} band (Fig. 2.2A). Such an intense band is calculated at 1280 cm^{-1}, and is predicted to be due to $\nu(C\text{-}C)_a$ (10%) and $\nu(C\text{-}C)_q$ stretching (39%). Most TR FTIR DS experiments of native PSI have focused on a spectral region above 1400 cm^{-1}. However, the calculated and experimental spectra presented here indicate that extending work to lower frequency (to ~ 1200 cm^{-1}) might be useful for the identification of a band of neutral PhQ in the A_1 binding site. Prior to undertaking this experiment, however, it will off course be useful to calculate spectra for $PhQ^{\square}$ to establish how and if this band is altered upon anion formation.

The PhQ band calculated at 1280 cm^{-1} in Fig. 2.3A is found downshifted ~15 cm^{-1} to 1257-1254 cm^{-1} for Cl_2NQ and Br_2NQ (Fig. 2.3E, F). This calculated result suggests the bands at 1277 and 1267 cm^{-1} in the Cl_2NQ and Br_2NQ FTIR spectra in Fig. 2.2E and F correspond to the 1297 cm^{-1} band for PhQ. This result, suggesting an intense band of neutral PhQ near 1295 cm^{-1}, and

corresponding bands of neutral Cl_2NQ and Br_2NQ ~20-30 cm^{-1} lower in frequency, may be extremely useful and help in the identification of bands in future TR FTIR DS obtained using PSI with neutral Cl_2NQ and Br_2NQ incorporated. The value of this result is even greater when one considers that in the past it has proven very difficult to unambiguously identify absorption bands associated with the neutral quinones incorporated into PSI.

It appears that the calculated band of PhQ at 1280 cm^{-1} is split into two bands for 2ClNQ and 2BrNQ. Such a splitting is also found in the 2MNQ calculated spectra. For 2ClNQ and 2BrNQ bands are found at 1290-1288 and 1248 cm^{-1}. The former band is upshifted ~9 cm^{-1} (relative to the 1280 cm^{-1} band of PhQ) and is due to [$\nu(C\text{-}C)_q$ (32%) + $\delta(CCH)_q$ (12%) + $\delta(CCH)_a$ (14%)]. The latter band is downshifted 32 cm^{-1} and is due to [$\nu(C\text{-}C)_q$, (10%) + $\delta(CCH)_a$ (25%)]. These calculated spectra suggest that the bands at 1290-1288 and 1248 cm^{-1} could correspond to the bands at 1297-1294 and 1252-1248 cm^{-1} in the experimental spectra for 2ClNQ and 2BrNQ in THF. Again, the calculated and experimental spectra presented here predict that bands of neutral 2BrNQ and 2ClNQ may be found at ~1295 and ~1250 cm^{-1} in TR FTIR DS obtained using PSI with 2BrNQ and/or 2ClNQ incorporated into the A_1 binding site. We will certainly be on the lookout for such features in the TR FTIR DS when they become available.

2.4 Conclusions

FTIR absorption spectra for six NQs in THF are presented. Corresponding calculated spectra are also presented, and indicate detailed normal mode assignments for the bands in the experimental spectra. For PhQ in THF a band is observed at 1469 cm^{-1}, which is absent in FTIR spectra for the other quinones, indicating that this band is due to vibrations associated with the phytyl tail of PhQ.

Neutral PhQ/2MNQ/Cl_2NQ/Br_2NQ in THF gives rise to an intense absorption band at 1662/1666/1686/1684 cm^{-1}, respectively, that calculations indicate is due to the antisymmetric coupled vibration of both C=O groups. For 2ClNQ/2BrNQ in THF this band is split into two bands, the higher/lower frequency band being due to the C_1=O/C_4=O stretching vibration, respectively.

FTIR spectra of PhQ/Cl_2NQ/Br_2NQ in THF display an intense absorption band at 1297/1277/1267 cm^{-1}, respectively, that calculations indicate is due to a C-C stretching of both the aromatic and quinonic parts of the NQ ring. For 2MNQ/2ClNQ/2BrNQ in THF this band is split into two. The spectra presented here suggest or lead to predictions about the location of quinone bands that may be found in TR FTIR DS.

3 EXPERIMENTAL AND CALCULATED INFRARED SPECTRA OF DISUBSTITUTED NAPHTHOQUINONES

ABSTRACT

In recent years there has been interest in incorporating substituted 1,4-naphthoquinones (NQs) into the A_1 binding site in photosystem I (PSI) photosynthetic protein complexes. This interest in part stems from the considerably altered bioenergetics of electron transfer that occur in PSI with such substitutions. Time resolved FTIR studies of PSI complexes with disubstituted NQs incorporated have and currently are being undertaken, and with this in mind it is worth considering FTIR absorption spectra of these disubstituted NQs in solution. Here we present FTIR absorbance spectra for 2-bromo-3-methyl-1,4-naphthoquinone (BrMeNQ), 2-chloromethyl-3-methyl-1,4-naphthoquinone (CMMeNQ) and 2-ethylthio-3-methyl-1,4-naphthoquinone (ETMeNQ) in tetrahydrofuran (THF). The FTIR spectra of these di-substituted naphthoquinones (NQs) were compared to FTIR spectra of 2-methyl-3-phytyl-1,4-naphthoquinone [phylloquinone (PhQ)]c, 2,3-dimethyl-1,4-naphthoquinone (DMNQ), and 2-methyl-1, 4-naphthoquinone (2MNQ). To aid in the assignment of bands in the experimental spectra, density functional theory (DFT) based vibrational frequency calculations for all the substituted NQs in solution were undertaken. The calculated and experiment spectra agree well. By calculating normal mode potential energy distributions, unambiguous quantitative band assignments were made. The calculated and experimental spectra together make predictions about what may be observable in time resolved FTIR difference spectra obtained using PSI with the different NQs incorporated. Time resolved FTIR difference spectra are presented that support these predictions.

3.1 Introduction

The redox properties of quinones are a critical factor that allow them to be utilized in a wide range of functions in different biological systems [113]. In photosynthetic reaction centers (RCs)[1], quinones are key cofactors in electron transport (ET) [114]. Quinones bound in photosynthetic RCs are of the 1,4-benzoquinone (BQ) and 1,4-naphthoquinone (NQ) variety [113, 115, 116].

In type II RCs, which includes photosystem II (PSII) of oxygen evolving organisms (plants, algae and cyanobacteria) and purple, non-sulfur bacteria (anoxygenic photosynthetic RCs), quinones function as terminal electron acceptors in the so-called Q_A and Q_B binding sites [117, 118]. The quinones in the Q_A and Q_B binding sites have very different functions. This is in spite of the fact that the same quinone often occupies the different binding sites. For example, in PSII plastoquinone (a BQ analogue) occupies both the Q_A and Q_B binding sites [119], while in purple bacterial reaction centers (PBRCs) from *Rhodobacter sphaeroides*, a ubiquinone occupies both sites [120].

In photosystem I (PSI) of oxygen evolving organisms, a phylloquinone (PhQ) molecule occupies the A_1 binding site and functions as the intermediary in ET from A_0 to the iron-sulfur cluster F_x [30, 121, 122]. PhQ is a disubstituted NQ (2-methyl-3-phtyl-1,4-NQ) which is also known as Vitamin K_1 (see structure and numbering in Fig. 3.1). For PhQ occupying the A_1 binding site in PSI, the role that the methyl, phytyl and carbonyl substituents play in modulating the overall

[1]***Abbreviations*:** BQ, 1,4-benzoquinone; BrMeNQ, 2-bromo-3-methyl-1,4-naphthoquinone; CMMeNQ, 2-chloromethyl-3-methyl-1,4-naphthoquinone; DFT, density functional theory; DMNQ, 2,3-dimethyl-1,4-naphthoquinone; ET, electron transfer; ETMeNQ, 2-ethylthio-3-methyl-1,4-naphthoquinone; FTIR, Fourier transform infrared; H-bond, hydrogen bond; MCT, mercury cadmium telluride; MQ, menaquinone; 2MNQ, 2-methyl-1, 4-naphthoquinone; NQ, 1,4-naphthoquinone; PSI, photosystem I; PhQ, phylloquinone (2-methyl-3-phytyl-1,4-naphthoqiuinone); PED, potential energy distribution; PBRCs, purple bacterial reaction centers; THF, tetrahydrofuran; TR, time resolved.

functionality of the cofactor in ET is not well understood, and continues to be a subject of considerable interest [115].

Menaquinone (MQ) is identical to PhQ except in the degree of saturation of the hydrocarbon tail [123] and MQs are found in the Q_A binding site in type II PBRCs from *Blastochloris viridis* [124], *Chromatium vinosum* [103] and *Chloroflexus aurantiacus* [103]. In PBRCs from *Rhodobacter sphaeroides* the native ubiquinone can be removed from the Q_A binding site and other quinones including MQ and PhQ can be incorporated via incubation [118]. Given the very different properties of the same PhQ molecule in the Q_A and A_1 binding sites, comparison of the properties of PhQ in the different binding sites is of some interest [104]. Even a comparison of the properties of MQ or PhQ in the Q_A binding sites in PBRC's from *Rhodobacter sphaeroides* and *Blastochloris viridis* is of considerable interest [1, 57, 125].

Substituting a range of different NQs into the A_1 binding site in PSI has become possible in recent years [1]. PSI with these NQs incorporated have been studied using EPR spectroscopy [58], and now also using FTIR difference spectroscopy (DS) [44, 59, 65, 126].

The overall goal in FTIR DS studies of PSI with different NQs incorporated into the A_1 binding site is the identification of bands in the spectra that are associated with both the neutral and reduced states of the incorporated NQs. These bands will provide information on pigment protein interactions that may help modulate the redox properties of the incorporated quinones [30, 64, 116, 119]. Study of these NQs in the A_1 binding site is also important in terms of the bioenergetics of ET in PSI, which can vary significantly depending on the NQs incorporated [1, 35]. The bioenergetics in PSI can also be used to assess the redox properties of the quinones incorporated into the A_1 binding site [127].

As a first level of interpretation of experimental time resolved (TR) FTIR DS obtained using PSI with different quinones incorporated into the A_1 binding site, it is useful to have an understanding of both experimental and calculated FTIR absorption spectra for the corresponding quinones in solution. Such an interpretation invariably involves (more recently) the use of quantum chemical computational methods to simulate the experimental spectra. These suggested initial steps are the subject of this manuscript.

In our previous studies we have focused on PSI with mainly substituted NQs incorporated. All these NQs have a methyl group at the 2-position, such as PhQ, DMNQ and 2MNQ (Fig. 3.1). In the present study we focus on three disubstituted NQs, all of which also have a methyl group substitution. According to the IUPAC numbering scheme the methyl group is at the 3-position for some of these disubstituted NQs (Fig.3.1). For ease of comparison and discussion in this manuscript we will adopt a numbering scheme for all the quinones where the methyl group is at the 2-position. The substituted NQs therefore differ only in the substitution at the 3-position, and our goal here is to try to parse out subtle features in the FTIR absorption spectra that may be related to the substitution at the 3-position.

In this manuscript FTIR absorbance spectra for BrMeNQ, CMMeNQ and ETMeNQ in tetrahydrofuran (THF) are obtained. These spectra are compared to spectra for 2MNQ, DMNQ and PhQ (all in THF) that have been obtained previously.

Density functional theory (DFT) based vibrational frequency calculations are also undertaken for all the quinones in THF. From these calculations, calculated FTIR absorption spectra are produced and compared to the experimental spectra.

3.2 Materials and Methods

All quinones and solvents were obtained from Sigma-Aldrich (St Louis, MO) and used as received. FTIR absorption spectra of the NQs were measured using a Varian 600 UMA FTIR microscope (Varian Inc., MA, USA) utilizing a mercury cadmium telluride (MCT) detector. Spectra were collected at 4 cm^{-1} resolution. The different NQs were dissolved in THF at various concentrations, and a small drop (< 5 μL) was deposited on a zinc selenide window. An FTIR spectrum of THF was obtained and interactively subtracted. No special effort was taken to keep the solvent dry. This seemed reasonable given that the IR spectrum for different quinones in different (hygroscopic and non-hygroscopic) solvents is similar.

Photo-accumulated [$P700^+ - P700$] FTIR DS and time resolved [$P700^+A_1^- - P700A_1$] FTIR DS at 77 K were obtained as described previously using a Bruker Vertex80 FTIR spectrometer equipped with MCT detector (Bruker Optics, Billerica, MA) [73-76]. The time resolved FTIR DS data block was globally analyzed using Glotaran software [77] and fitted to multi-exponential functions from which decay-associated spectra (DAS) were constructed. The [$P700^+A_1^- - P700A_1$] DAS are presented in Fig. 3.4.

DFT calculations were undertaken using Gaussian 16 software (Gaussian Inc. Wallingford, CT) [128]. The phytyl tail of PhQ was truncated to a 5-carbon unit [$CH_2CHC(CH_3)_2$]. The B3LYP functional was used in combination with the 6-31+G(d) basis set [80]. The solvent was considered using the integral equation formalism (IEF) of the polarizable continuum model (PCM) [109] as implemented in Gaussian 16 using default parameters. Normal mode vibrational frequency calculations result in “stick spectra”, which we convolve with Gaussian functions of 4 cm^{-1} half-width to produce more realistic looking IR absorption spectra.

To estimate to what extent different molecular groups contribute to the calculated vibrational modes potential energy distributions (PEDs) associated with the normal modes were calculated using VEDA software [85].

The quinone structures were created using Advanced Chemistry Development (ACD)/ChemSketch Freeware [129] and the Van der Waals spheres (Fig. 3.3) were generated using Avogadro software [130].

3.3 Results and Discussions

Fig. 3.1 shows the structure and numbering for the six NQs considered in this study. To simplify comparison, we will use a numbering scheme in which the methyl group is at the 2-position for all the different quinones, as it is for PhQ. PhQ has a phytyl tail at the 3-position, while 2MNQ/DMNQ has a hydrogen atom/methyl group, respectively. BrMeNQ, CMMeNQ, and ETMeNQ have a bromine atom, chloromethyl, and ethylthio substituent at the 3-position, respectively.

Fig. 3.2 shows FTIR absorption spectra in the 1800−1200 cm^{-1} region for five NQs in THF. A FTIR spectrum for PhQ in hexane has been obtained previously, and is similar to that presented in Fig. 3.2A [131]. A spectrum for 2,3-dimethyl-1,4-naphthaquinone (DMNQ) in CCl_4 has also been obtained [118]. The spectra for PhQ and DMNQ are near identical (in the 1680−1580 cm^{-1} region) [65], and so a spectrum for DMNQ is not included in Fig. 3.2.

Fig. 3.3 shows DFT calculated IR absorption spectra for the six NQs considered in this study. The PEDs associated with the normal modes that give rise to the most intense bands in the spectra are listed in Table 3.1. The calculated and experimental spectra clearly display similarities in both peak positions and in relative band intensities. How the calculated and experimental bands are associated is indicated in Table 3.1. In this manuscript calculated frequencies are scaled by

0.978, which is arbitrarily chosen so that the observed band at 1662 cm^{-1} for neutral PhQ matches the frequency for the calculated band. Such a scale factor is in the range of that expected for the functional and basis sets used in our calculations [82-84].

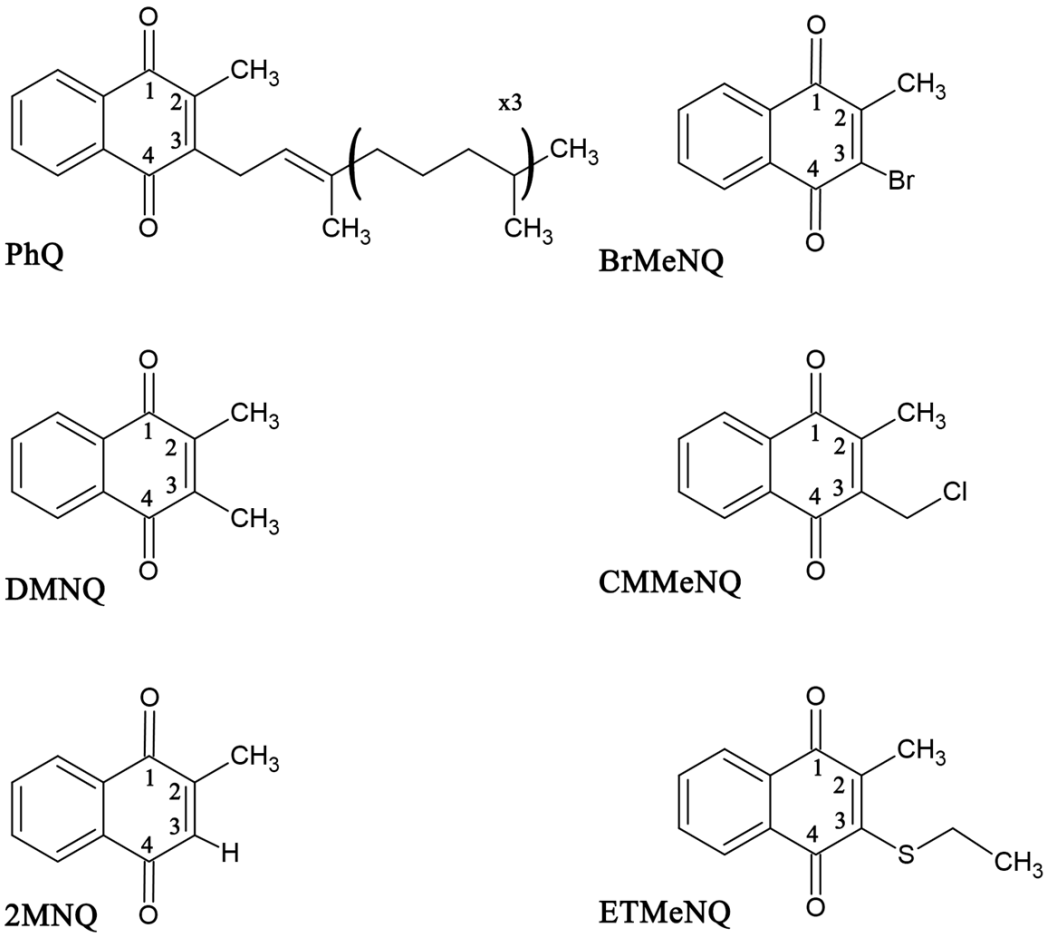

Figure 3.1 Structure and partial numbering for 2-methyl-3-phytyl-1,4-naphthoqiuinone (PhQ), 2,3-dimethyl-1,4-naphthoquinone (DMNQ), 2-methyl-1,4-naphthoquinone (2MNQ), 2-methyl-3-bromo-1,4-naphthoquinone (BrMeNQ), 2-methyl-3-chloromethyl-1, 4-naphthoquinone (CMMeNQ) and 2-methyl-3-ethylthio-1,4-naphthoquinone (ETMeNQ). For ease of comparison, for all the quinones we chose the methyl group to be at the 2-position. Such numbering is inconsistent with IUPAC numbering for BrMeNQ, CMMeNQ and ETMeNQ.

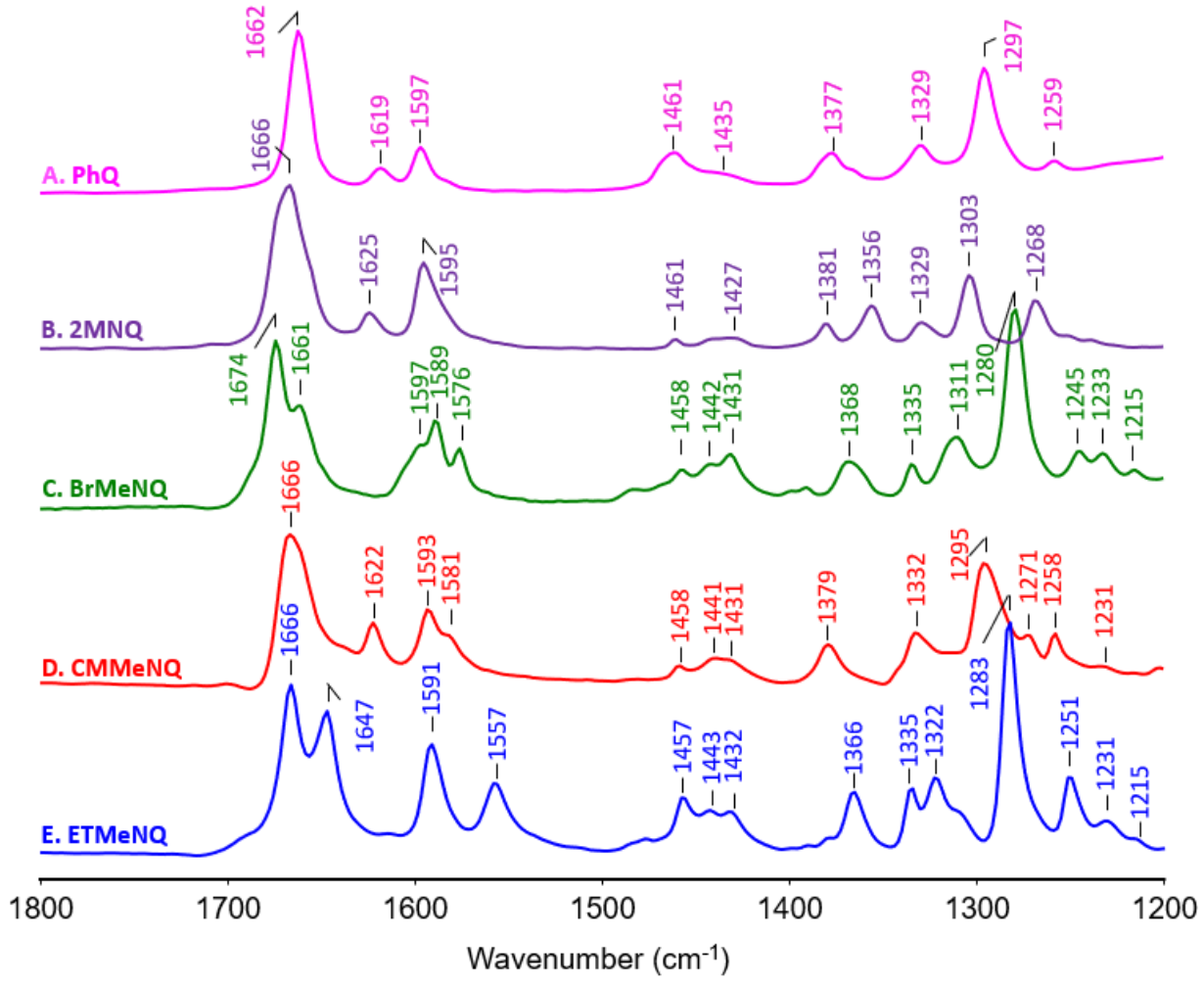

Figure 3.2 Experimental FTIR absorption spectra for (A) PhQ, (B) 2MNQ, (C) BrMeNQ, (D) CMMeNQ, and (E) ETMeNQ in THF. The spectra were arbitrarily scaled so that the intensities of the bands in the ~1666 cm^{-1} are similar.

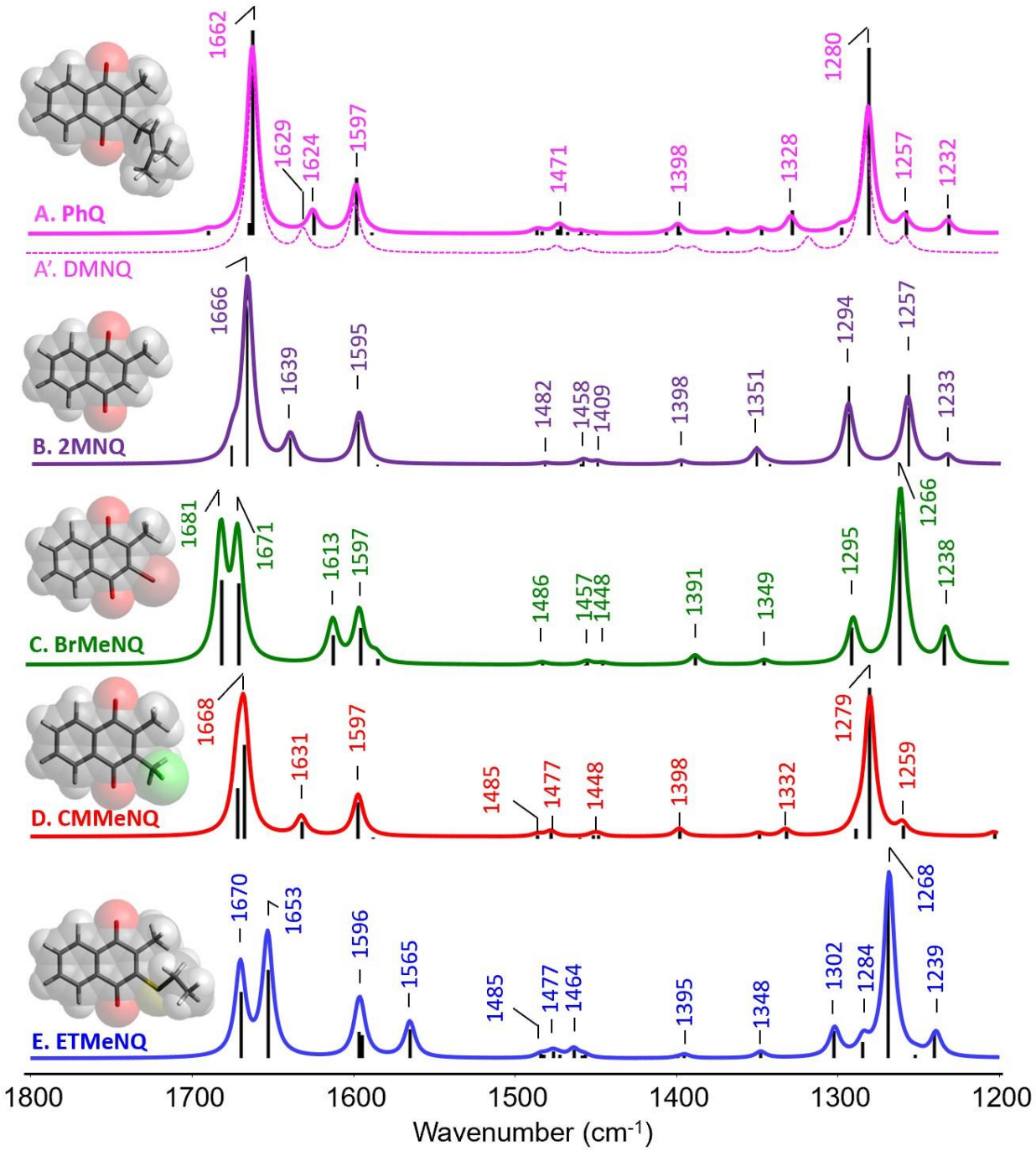

Figure 3.3 Calculated IR spectra for (A) PhQ, (A') DMNQ, (B) 2MNQ, (C) BrMeNQ, (D) CMMeNQ, and (E) ETMeNQ in THF. Frequencies are scaled by 0.978 [83, 84, 132]. Intensities (in km/mol) are listed in Table 3.1. Insets show the quinone structures with van der Waals surfaces. The calculated normal modes are shown as (black) vertical lines.

Table 3.1 Calculated normal mode vibrational frequencies (in cm^{-1}) and intensities (in km/mol) for the neutral NQs in THF. Frequencies are scaled by 0.978. Mode assignments and associated PEDs (in parenthesis, in %) were calculated using VEDA. The methyl group is taken to be at the 2-position for all quinones in the normal mode descriptions.

Abbreviations: ***ν***, bond stretching; ***δ***, bending vibration; ***θ***, torsion. **a**, aromatic ring; ***q***, quinonic ring; **AS**, antisymmetric coupling; **S**, symmetric coupling; **M**, methyl; **T**, Tail.

Calculated Frequency (Intensity)	PED (%)	Experimental Frequency
PhQ		
1662 (766)	$[\nu(C_1{=}O)\ (54) + \nu(C_4{=}O)\ (30)]_{AS}$	1662
1624 (91)	$\nu(C_2{=}C_3)\ (68)$	1619
1597 (205)	$\nu(C{-}C)_a\ (64)$	1597
*1473 (14) *1471 (27)	$\delta(CH_2)_T\ (55)$ $\delta(CH_2)_T\ (68)$	1461
1398 (34)	$\delta(CH_2)_M\ (85)$	1377
1328 (72)	$\nu(C{-}C)_q\ (10) + \delta(C_1C_2C_3)\ (13) +$ $\delta(HCC)_T\ (16)$	1329
1281 (541)	$\nu(C{-}C)_a\ (10) + \nu(C{-}C)_q\ (39)$	1297
1257 (67)	$\nu(C{-}C)_a\ (10) + \delta(HCC)_a\ (37)$	1259
DMNQ		
1660 (761)	$[\nu(C_1{=}O)\ (57) + \nu(C_4{=}O)\ (22)]_{AS}$	–
1629 (95)	$\nu(C_2{=}C_3)\ (67)$	–
1597 (215)	$\nu(C{-}C)_a\ (62)$	–
1473 (31)	$\delta(CH_2)_M\ (46)$	–
1398 (28)	$\delta(CH_2)_M\ (84)$	–
1317 (65)	$\nu(C{-}C)_q\ (27) + \delta(C_2C_3C_4)\ (20)$	–
1282 (535)	$\nu(C{-}C)_a\ (11) + \nu(C{-}C)_q\ (48)$	–
1258 (63)	$\nu(C{-}C)_a\ (22) + \delta(HCC)_a\ (37)$	
2MNQ		
1666 (766)	$[\nu(C_1{=}O)\ (52) + \nu(C_4{=}O)\ (32)]_{AS}$	1666
1640 (115)	$\nu(C_2{=}C_3)\ (68)$	1625
1597 (211)	$\nu(C{-}C)_a\ (65)$	1595
1351 (62)	$\nu(C{-}C)_a\ (10) + \nu(C{-}C)_q\ (10) +$ $\delta(CCH^*)\ (17) + \delta(CCH)_a\ (12)$	1356
1294 (250)	$\nu(C{-}C)_q\ (71)$	1330
1257 (279)	$\nu(C{-}C)_q\ (16) + \delta(CCH)_a\ (22)$	1268
BrMeNQ		
1681 (413)	$\nu(C_4{=}O)\ (87)$	1674
1671 (395)	$\nu(C_1{=}O)\ (83)$	1661
1613 (137)	$\nu(C_2{=}C_3)\ (64)$	1597
1597 (170)	$\nu(C{-}C)_a\ (61)$	1589
1586 (26)	$\nu(C_2{=}C_3)\ (15) + \nu(C{-}C)_a\ (26) +$ $\delta(CCC)_a\ (11)$	1576
1457 (12)	$\nu(C{-}C)_a\ (10) + \delta(CCC)_a\ (51)$	1458
1391 (30)	$\delta(CH_2)_M\ (89)$	1368
1349 (14)	$\nu(C{-}C)_a\ (77)$	1335
1295 (141)	$\nu(C{-}C)_q\ (18)$	1311
1266 (562)	$\nu(C{-}C)_q\ (33) + \delta(HCC)_a\ (15)$	1280

1238 (110)	$\nu(\mathrm{C{-}C})_{\mathrm{q}}(14) + \delta(\mathrm{HCC})_{\mathrm{a}}(23) + \delta(\mathrm{CCC})_{\mathrm{q}}(15)$	1245
CMMeNQ		
1672 (271)	$\nu(\mathrm{C_1{=}O})\ (74)$	
1667 (507)	$\nu(\mathrm{C_4{=}O})\ (79)$	1666
1632 (86)	$\nu(\mathrm{C_2{=}C_3})\ (69)$	1622
1597 (186)	$\nu(\mathrm{C{-}C})_{\mathrm{a}}(62)$	1593
1485 (13)	$\delta(\mathrm{HCC})_{\mathrm{a}}(43)$	1458
1477 (26)	$\delta(\mathrm{CH_2})_{\mathrm{M}}(31) + \delta(\mathrm{CH_2})_{\mathrm{T}}(42)$	1441
*1451 (12) *1448 (12)	$\delta(\mathrm{CH_2})_{\mathrm{M}}(73) + \theta(\mathrm{HCCC})\mathrm{q}\ (20)$ $\delta(\mathrm{CH_2})_{\mathrm{M}}(33) + \delta(\mathrm{CH_2})_{\mathrm{T}}(36)$	1431
1398 (36)	$\delta(\mathrm{CH_2})_{\mathrm{M}}(75)$	1379
1332 (32)	$\nu(\mathrm{C{-}C})_{\mathrm{a}}(10) + \delta(\mathrm{CCC})_{\mathrm{q}}(16)$	1332
1279 (626)	$\nu(\mathrm{C{-}C})_{\mathrm{a}}(13) + \nu(\mathrm{C{-}C})_{\mathrm{q}}(39)$	1295
1259 (51)	$\delta(\mathrm{HCC})_{\mathrm{a}}(40)$	1271
ETMeNQ		
1670 (362)	$\nu(\mathrm{C_4{=}O})\ (84)$	1666
1653 (481)	$\nu(\mathrm{C_1{=}O})\ (81)$	1647
*1597 (134) *1595 (114)	$\nu(\mathrm{C{-}C})_{\mathrm{a}}(49)$ $\nu(\mathrm{C{-}C})_{\mathrm{a}}(40)$	1591
1565 (141)	$\nu(\mathrm{C_2{=}C_3})\ (81)$	1557
1485 (12)	$\delta(\mathrm{HCC})_{\mathrm{a}}(43)$	1457
1477 (25)	$\delta(\mathrm{CH_2})_{\mathrm{T}}(15) + \delta(\mathrm{CH_2})_{\mathrm{M}}(18) + \delta(\mathrm{CCO})_{\mathrm{q}}(12)$	1443
1464 (36)	$\delta(\mathrm{CH_2})_{\mathrm{T}}(15) + \delta(\mathrm{CH_2})_{\mathrm{M}}(18) + \delta(\mathrm{CCO})_{\mathrm{q}}(12)$	1432
1395 (15)	$\delta(\mathrm{CH_2})_{\mathrm{M}}(93)$	1366
1302 (113)	$\nu(\mathrm{C{-}C})_{\mathrm{a}}(13) + \delta(\mathrm{CCO})_{\mathrm{q}}(12)$	1322
1268 (724)	$\nu(\mathrm{C{-}C})_{\mathrm{q}}(36) + \delta(\mathrm{HCC})_{\mathrm{a}}(11)$	1283
1239 (94)	$\delta(\mathrm{HCS})\ (27) + \theta(\mathrm{HCSC})\ (44)$	1251

*Similar vibrational modes were calculated at multiple frequencies.
**Hydrogen at the 3-position of 2MNQ.

The calculated and experimental spectra display similarities in both peak positions and in relative band intensities. Interestingly, in the experimental spectra in Fig. 3.2, PhQ, 2MNQ and CMMeNQ display one intense band in the 1675−1662 cm^{-1} region, while BrMeNQ and ETMeNQ display two distinct bands. This observation is confirmed in the calculated spectra and is one indication of the appropriateness of the calculations. There are hints in the experimental spectra for PhQ, 2MNQ, and CMMeNQ that the band in the 1675−1662 cm^{-1} region contains contributions from more than a single mode, and this is also indicated in the calculations in Fig. 3.3, where the single intense band is in fact due to two vibrational modes that are close in frequency (see stick spectra in Fig. 3.3).

Frequencies of the calculated and experimental bands are listed in Table 3.1, where the calculated frequencies are scaled by 0.978 . This scale factor is arbitrarily chosen so that the experimental band at 1662 cm^{-1} for neutral PhQ matches the frequency for the calculated band.

3.3.1 Modes of the phytyl chain of PhQ and the methyl group of NQs

The spectrum for PhQ in THF (Fig. 3.2A) displays a band at 1461 cm^{-1} which is considerably less intense in the 2MNQ spectrum. This 1461 cm^{-1} band of PhQ is therefore likely associated with the phytyl tail of PhQ. This 1461 cm^{-1} feature is less obvious in the calculated PhQ spectrum, although a weak band is observed near 1471 cm^{-1} (Fig. 3.3). This weak band is calculated to be associated with $\delta(CH_2)$ bending vibrations of molecular groups of the phytyl chain of PhQ (Table 3.1). Bear in mind that for calculations the phytyl chain of PhQ is truncated to just the first five carbon atoms.

The experimental spectra for the three disubstituted NQs show a trio of bands in the 1460-1430 cm^{-1} region, at ~1457/~1442/~1431 cm^{-1}. A trio of bands are also observed in the 2MNQ spectrum albeit with reduced intensity and such a grouping is also probably present in the PhQ

spectrum. Since these NQs have a methyl group this trio of bands is likely associated with the methyl substitution at the 2-position. This idea is further supported by the observation that bands are not observed at these frequencies in the experimental spectra for 2ClNQ, 2BrNQ, Cl_2NQ or Br_2NQ [78], all of which lack a methyl group [78].

This trio of bands in the experimental spectra are relatively intense. However, such bands are much weaker in the calculated spectra. A set of bands in the 1485−1464 cm^{-1} region is most obvious in the calculated ETMeNQ spectrum, where these modes are associated with C_2−methyl group and $\delta(CH_2)$ bending vibrations of the hydrocarbon tail at the 3-position (Table 3.1).

In *all* experimental spectra in Fig. 3.2, a band is found at 1381−1366 cm^{-1}. Such a band is also found in spectra for DMNQ in CCl_4 [63]. This is again an indication that it could be associated with the methyl group substitution. In all the calculated spectra in Fig. 3.3 a weak band is found near 1397 cm^{-1}, and this band is indeed due to a methyl $\delta(CH_2)$ bending vibration (Table 3.1). In further support of this proposed assignment is the observation that none of the experimental spectra of NQs that lack a methyl group substitution display a band near ~1370 cm^{-1} [78].

3.3.2 NQ C=O vibrations

For PhQ in THF the most intense IR absorption band in the spectrum is found at 1662 cm^{-1} (Fig. 3.2A). Calculations indicate that this band is due to the antisymmetric stretching vibration of both C=O groups (C_1=O, 54% and C_4=O, 30%) (Table 3.1). For 2MNQ in THF a similar intense band is observed at 1666 cm^{-1} with a weak shoulder near 1670 cm^{-1} (Fig. 3.2B). The intense 1666 cm^{-1} band in the 2MNQ spectrum is also assigned to an antisymmetric stretching vibration of both C=O groups (C_1=O, 52% and C_4=O, 32%) (Table 3.1), as is the 1662 cm^{-1} band for DMNQ (C_1=O, 57% and C_4=O, 22%) (Fig. 3.3A’ and Table 3.1).

For BrMeNQ in THF two intense bands are observed at 1674 and 1661 cm^{-1} (Fig. 3.2C) with the higher frequency band being considerably more intense. The calculated spectrum for BrMeNQ does indicate two intense bands at 1681 and 1671 cm^{-1} (in agreement with experiment), but these two bands have similar intensity (Fig. 3.3C). The calculated bands at 1681 and 1671 cm^{-1} in the BrMeNQ spectrum are due to pure C_4=O (87%) and C_1=O (83%) stretching vibrations, respectively (Table 3.1). So, the C_4=O mode (the C_4=O group is next to the bromine atom) is 10 cm^{-1} higher in frequency than the C_1=O mode. Similar trends are found for ETMeNQ (see below and Table 3.1). In contrast, calculated frequencies for CMMeNQ show that two C=O stretching modes are similar in frequency giving rise to a single band. For CMMeNQ, however, the C_1=O vibration appears at a slightly higher frequency (Fig. 3.3D and Table 3.1).

The experimental and calculated spectra for 2BrNQ in THF were published previously and C=O bands were observed at 1683 and 1668 cm^{-1} [78]. For BrMeNQ the corresponding bands are at 1674 and 1661 cm^{-1} and are thus downshifted 9/7 cm^{-1}, respectively. So, replacing a hydrogen atom at the 2-position with a methyl group leads to a 9/7 cm^{-1} downshift of the C=O modes.

Computationally we find that the addition of a methyl group in place of a hydrogen atom leads to a 9/3 cm^{-1} downshift, in the C=C_4=O/C_1=O modes, respectively. So, the calculation poorly models the shift of the C_4=O group of 2BrNQ on replacing its hydrogen atom with a methyl group.

For ETMeNQ in THF two intense bands are observed at 1666 and 1647 cm^{-1} (Fig. 3.2E) with similar intensity. The calculated spectrum for ETMeNQ indicates two bands of similar intensity at 1670 and 1653 cm^{-1}, in good agreement with experiment. The calculated bands at 1670 and 1653 cm^{-1} are due to pure C_4=O (84%) and C_1=O (81%) stretching vibrations (Table 3.1). So, the C_4=O mode is 18 cm^{-1} higher in frequency than the C_1=O mode.

The frequency difference between the two C=O bands in the experimental spectra for BrMeNQ and ETMeNQ is also captured well in our calculations. For example, the C_4=O band of BrMeNQ is at a higher frequency than that of ETMeNQ (by 8 cm^{-1}). Computationally the C_4=O mode of BrMeNQ is found 11 cm^{-1} higher than the corresponding band of ETMeNQ. Similar conclusions can be drawn for the C_1=O bands of the two NQs in the calculated and experimental spectra. That is, the C_1=O band of BrMeNQ is at a higher frequency than that of ETMeNQ (by 14 cm^{-1}). Computationally the C_1=O of BrMeNQ is 18 cm^{-1} higher than the corresponding band of ETMeNQ.

For CMMeNQ in THF only a single intense and relatively broad band is observed at 1666 cm^{-1} (Fig. 3.2D). The calculated spectrum for CMMeNQ also indicates only a single band at 1668 cm^{-1}, and so there is good agreement with calculation and experiment on this point. However, the calculated band at 1668 cm^{-1} has contributions from two separate C=O modes (C_1=O (74%) at 1672 cm^{-1} and C_4=O (79%) at 1667 cm^{-1}) (Table 3.1). So, in this case, the C_4=O mode is ~5 cm^{-1} lower in frequency than the C_1=O mode. So, the calculated mode frequencies for CMMeNQ indicate that the presence of the chlorine atom in the chloromethyl substituent does not cause a large frequency splitting between the two carbonyl vibrational modes. Moreover, unlike the case for BrMeNQ and ETMeNQ, the C_1=O (next to the methyl group) vibration of CMMeNQ is calculated to be at a slightly higher frequency (1672 cm^{-1}) than for the C_4=O mode.

3.3.3 Quinonic ring C=C vibrations

For PhQ in THF an absorption band is observed at 1619 cm^{-1} (Fig. 3.2A). A similar band is calculated at 1624 cm^{-1} (Fig. 3.3A) and is due mainly to a C_2=C_3 stretching vibration [ν(C_2=C_3), 68%] (Table 3.1). For 2MNQ in THF a band is observed at 1625 cm^{-1}, upshifted 6 cm^{-1} compared to the corresponding band of PhQ. However, for 2MNQ the C_2=C_3 vibrational mode is calculated

at 1639 cm^{-1} upshifted 15 cm^{-1} compared to the corresponding calculated mode of PhQ (Table 3.1, Fig. 3.3). So, the calculations do not model the frequency difference between the PhQ and 2MNQ C_2=C_3 stretching vibrations very well.

For CMMeNQ in THF a band is observed experimentally at 1622 cm^{-1}, upshifted 3 cm^{-1} compared to the corresponding band of PhQ (Table 3.1)]. For DMNQ in CCl_4 the corresponding band is at 1624 cm^{-1}. however. So, replacing one of the H atoms of the methyl group (in DMNQ) with a chlorine atom seems to make only a minor difference in the frequency of the C_2=C_3 stretching vibration.

In the experimental FTIR spectrum for BrMeNQ in THF the band due to the C_2=C_3 stretching vibration is presumably at 1597 cm^{-1} and is thus downshifted 28 cm^{-1} relative to the corresponding band of 2MNQ. So, exchanging a hydrogen atom for a bromine atom at the 3-position results in this large 28 cm^{-1} downshift. For ETMeNQ in THF, we show that the band at 1591 cm^{-1} in the experimental spectrum is likely due to an aromatic C=C vibration (see below), so the band due to a C_2=C_3 stretching vibration is at 1557 cm^{-1}. This is a very large downshift of 62 cm^{-1} relative to the corresponding band of PhQ. One might not expect such a large difference by exchanging a phytyl chain for an ethyl-thio moiety. The phytyl chain of PhQ is directed out of the plane of the NQ ring after the first carbon atom of the chain, so the suggestion could be that the heavy sulfur atom of ETMeNQ may impact this “kinking” of the side-chain leading to a large alteration in frequency of the C_2=C_3 vibration.

From calculations the $\nu(C_2=C_3)$ modes for BrMeNQ and ETMeNQ are at 1613 and 1565 cm^{-1} (Fig. 3.3), indicating downshifts relative to corresponding PhQ modes of 11 and 59 cm^{-1}, respectively. The former is a considerably smaller downshift than that suggested from experiment while the latter is in line with experiment.

In summary, when the phytyl moiety of PhQ is changed to a hydrogen atom/methyl group/chloromethyl group/bromine atom/ethylthio group the C_2=C_3 mode frequency shifts 6/5/3/-22/-62 cm^{-1}, respectively.

3.3.4 Aromatic ring C=C vibrations

For PhQ in THF/DMNQ in CCl_4/2MNQ in THF an absorption band is observed at 1597/1598/1595 cm^{-1}, respectively (Fig. 3.2 and Table 3.1). Calculations indicate that these bands near 1597 cm^{-1}, are due to $\nu(C=C)_a$ vibrations (Table 3.1).

For BrMeNQ and CMMeNQ in THF bands are observed at 1589 and 1593 cm^{-1}, respectively (Fig. 3.2C and 3.2D). Corresponding bands are calculated at 1597 cm^{-1} for both NQs (Fig. 3.3C and 3.3D). For ETMeNQ, the experimental $\nu(C=C)_a$ band is at 1591 cm^{-1}. A band is calculated at 1596 cm^{-1}, but this band is due to two modes at 1595 [$\nu(C=C)_a$ (40%)] and 1597 cm^{-1} [$\nu(C=C)_a$ (49%)]. For all the quinones, the $\nu(C=C)_a$ mode is downshifted relative to that of PhQ, but the downshift is quite small, as might be expected given that the substitutions are quite distant, at the quinonic part of the NQ ring.

From both calculated and experimental spectra, for PhQ, 2MNQ, BrMeNQ and CMMeNQ the $\nu(C_2=C_3)$ mode is at a higher frequency than the $\nu(C=C)_a$ mode. The reverse is true for ETMeNQ, however.

In summary, all the experimental and calculated spectra show three or four bands in the 1550−1690 cm^{-1} region. The highest frequency bands are due to C_4=O and C_1=O vibrations, or an antisymmetric combination of both. The next two lower intensity bands are due to $\nu(C_2=C_3)$ and $\nu(C=C)_a$ vibrations, with the $\nu(C_2=C_3)$ vibration being higher in frequency than the $\nu(C=C)_a$ vibration except for ETMeNQ. Bands due to $\nu(C=C)_a$ modes are also higher in intensity compared to the bands due to the $\nu(C_2=C_3)$ modes.

3.3.5 Other vibrational modes

PhQ in THF displays an intense band at 1297 cm^{-1} (Fig 3.2A). An intense band is also calculated at 1280 cm^{-1} (Fig. 3.3A) and is due to $\nu(C{-}C)_a$ (10%) and $\nu(C{-}C)_q$ (39%) (Table 3.1). For DMNQ similar conclusions apply with the $\nu(C{-}C)_a/\nu(C{-}C)_q$ band being calculated at 1282 cm^{-1} and found experimentally at 1296 cm^{-1} (Table 3.1).

For 2MNQ in THF no single intense band is observed near 1297 cm^{-1}. Instead, two bands are observed at 1303 and 1268 cm^{-1}. Corresponding bands are calculated at 1294 and 1257 cm^{-1}, respectively. This "splitting" appears to be a characteristic feature for mono-substituted NQ's as such a splitting is present in calculated and experimental spectra for 2ClNQ, 2BrNQ and 2MNQ, but not in spectra for disubstituted NQ's such as Cl_2NQ and Br_2NQ [78], or the other disubstituted NQs considered here (see below).

Similar to the intense band at 1297 cm^{-1} in the PhQ spectrum, BrMeNQ, CMMeNQ and ETMeNQ spectra also display a single intense band at 1280, 1295 and 1283 cm^{-1}, respectively (Fig. 3.2). The calculated spectra agree well with this observation, also indicating a single intense band at 1266, 1279 and 1268 cm^{-1} for BrMeNQ, ETMeNQ and CMMeNQ, respectively (Fig. 3.3). The calculated spectra also capture the correct relative frequencies for the single intense band that is observed experimentally. That is, the peak frequency of the single intense bands is highest for PhQ and CMMeNQ and lower for BrMeNQ and ETMeNQ.

The intense experimental band in the ~1300−1280 cm^{-1} region for the different NQs are due to normal modes that have contributions from several molecular groups (Table 3.1). However, for all five quinones a larger contribution comes from a $\nu(C{-}C)_q$ stretching vibration (Table 3.1).

Most TR FTIR DS experiments on PSI have focused on the 1550-1400 cm^{-1} "anion" spectral region [56]. However, the calculated and experimental spectra presented here indicate that

extending studies to lower frequencies (to ~1250 cm^{-1}) might be useful for the identification of a bands of neutral NQs in the A_1 binding site. The value of such measurements is high when one considers that in the past it has proven difficult to unambiguously identify absorption difference bands associated with the neutral state of quinones incorporated into PSI [65].

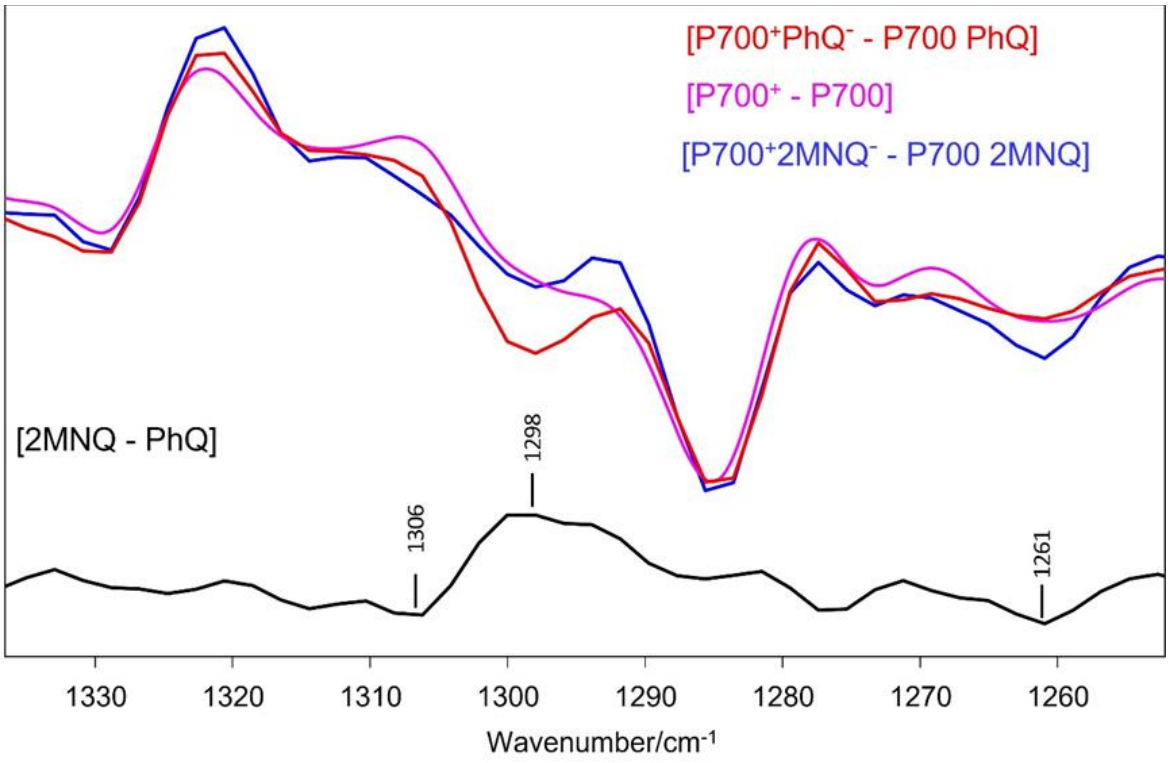

Figure 3.4 Time-resolved step-scan FTIR DS at 77 K obtained using PSI with PhQ (*red*) and 2MNQ (*blue*) incorporated into the A_1 binding site. A TR double difference spectrum obtained by subtracting the PhQ spectrum from the 2MNQ spectrum is also shown (*black*), along with a photoaccumulated ($P700^+$ – P700) FTIR DS (*magenta*).

To test this hypothesis Fig. 3.4 shows preliminary TR FTIR DS collected in the 1350-1250 cm^{-1} spectral region obtained using PSI with PhQ and 2MNQ incorporated into the A_1 binding site. Photoaccumulated ($P700^+$ – P700) FTIR DS are also shown, as are double difference spectra (DDS) constructed by subtracting the PhQ spectrum from the 2MNQ spectrum. Positive/negative bands in the DDS are due to neutral 2MNQ/PhQ, respectively. The spectra in Fig. 3.4 are also

shown in Fig. 3.6 along with appropriate error bars. The spectral features in Gig. 3.4 appear complicated mainly due to P700 and $P700^+$ absorption, although PhQ^- and $2MNQ^-$ could also contribute somewhat. However, a negative band is clearly observed at 1298 cm^{-1} in the TR FTIR DS obtained using PSI with PhQ incorporated. Such a feature is absent in the photoaccumulated FTIR DS and in the TR FTIR DS obtained using PSI with 2MNQ incorporated. This observation provides very strong support for the suggestion that this negative feature is a neutral state PhQ band that is due mostly to a $\nu(C{-}C)_q$ stretching vibration. The feature at 1298 cm^{-1} in the DDS is clearly above the noise level (Fig. 3.6). Furthermore, in the DDS in Fig. 3.4, a negative feature is observed at 1306 and 1261 cm^{-1}, which based on the above discussion and analysis we assign to vibrational modes of neutral 2MNQ in PSI. Admittedly, the band at 1261 cm^{-1} in the DDS is not considerably above the noise level in the experiment (Fig. 3.6).

For a more detailed analysis further TR spectra need to be obtained using PSI with different quinones incorporated. However, we have shown just how useful predictions based on combined experimental and calculated spectra for NQs in solution can be. It was the predictions based on the experimental (and calculated) data that motivated us to investigate the appropriate spectral region in the TR FTIR DS data.

3.4 Conclusions

FTIR absorption spectra for five NQs in THF are presented. Corresponding calculated spectra are also presented along with detailed normal mode assignments for the bands in the spectra. For PhQ in THF a band is observed at 1461 cm^{-1}, which is absent in FTIR spectrum for mono-substituted 2MNQ but appears for all disubstituted NQs, indicating that this band is due to vibrations that are impacted by the substitutions at the 3-position.

The spectra for all five NQs display one or two intense absorption bands in the 1674–1647 cm^{-1} region that are due to either the coupled or separate vibrations of the C=O groups of the NQs. For PhQ, DMNQ and 2MNQ a single band associated with an antisymmetric coupled vibration of both C=O groups is observed. For BrMeNQ/ETMeNQ two bands are observed with the higher/lower frequency band being due to a C_4=O/ C_1=O stretching vibration (the C_1=O group was considered adjacent to the methyl in this study). For CMMeNQ, one relatively broad band is due to the carbonyl stretching modes.

FTIR spectra for all five quinones also display an intense absorption band (two bands for 2MNQ) in the 1297–1283 cm^{-1} region that is due mainly to a $\nu(C–C)_q$ stretching vibration. The spectral features for the different NQs presented here are discussed and it is indicated that these features will prove useful for the interpretation of bands in time resolved FTIR difference spectra that will be obtained in the future for PSI samples with the different NQs incorporated into the A_1 protein binding site.

Supplementary Information

Experimental and Calculated Infrared Spectra of Disubstituted Naphthoquinones

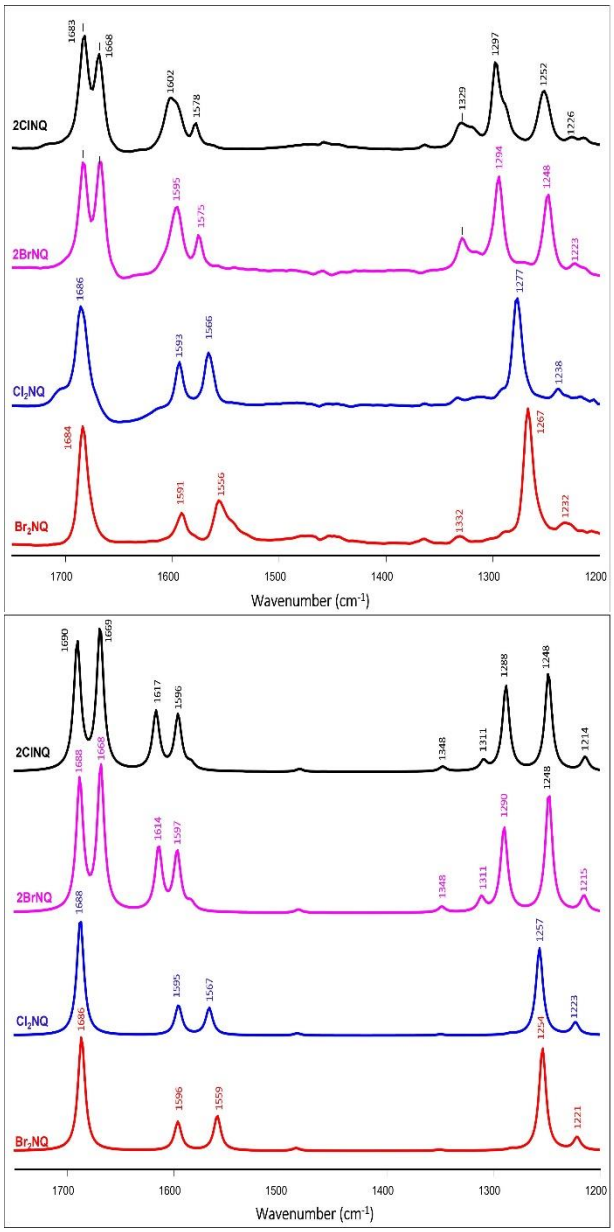

Figure 3.5 Experimental (*top panel*) and calculated (*bottom panel*) IR absorption spectra for 2ClNQ (*black*), 2BrNQ (*magenta*) Cl_2NQ (*blue*) and Br_2NQ (*red*) in THF. The spectra were arbitrarily scaled so that the intensities of the bands in the ~1666 cm^{-1} are similar. Calculated frequencies are scaled by 0.978. Data is modified from that presented in reference [78].

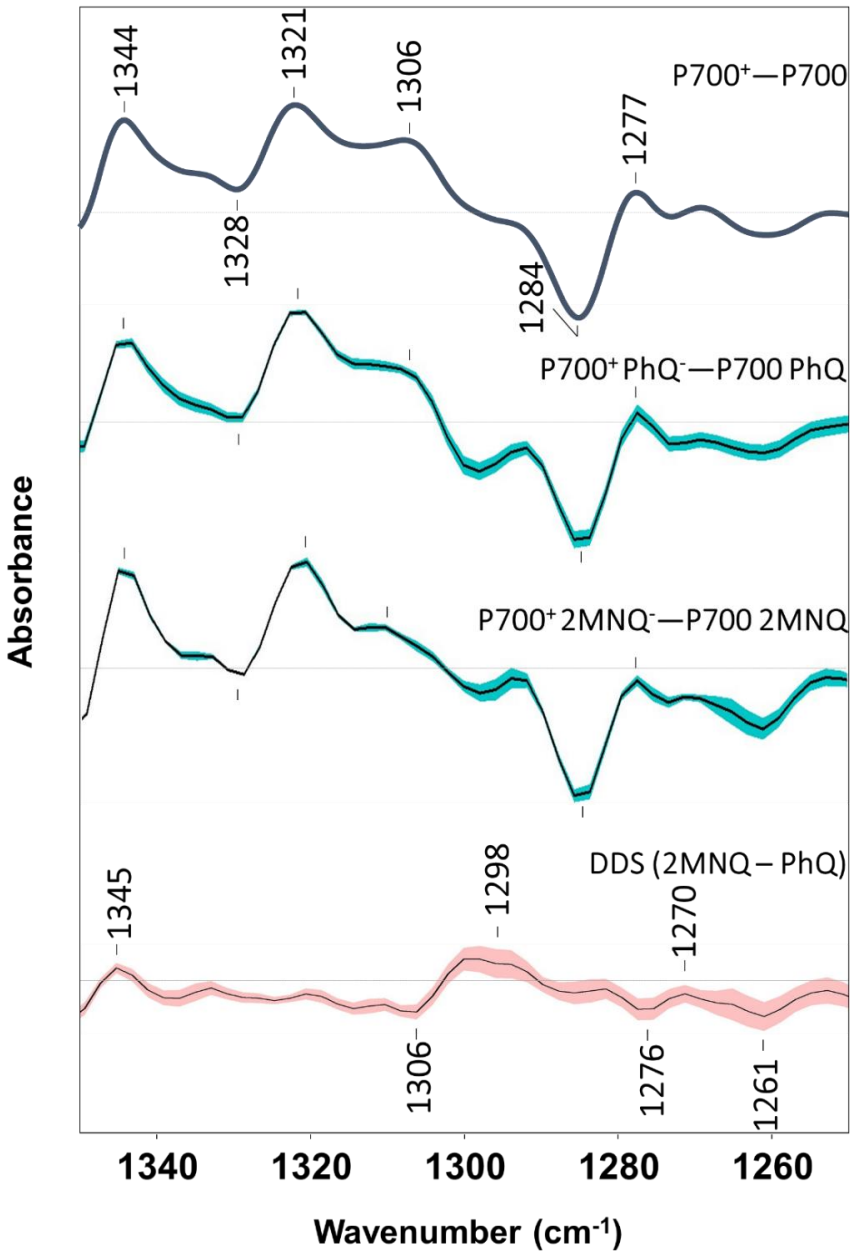

Figure 3.6 Photo-accumulated [$P700^+$ – P700] and time-resolved [$P700^+A_1^-$ – $P700A_1$] FTIR difference spectra in the 1350-1250 cm^{-1} regions obtained at 77 K using photosystem I particles with PhQ and 2MNQ incorporated. Spectra are normalized to the ~1718/1697 cm^{-1} difference band, as described previously [56]. The standard error in the spectra derived from separate measurements [44] are shown as *blue* shade. The double difference spectrum (DDS) is constructed by subtracting the time resolved spectrum for native PSI from the spectrum for PSI with 2MNQ incorporated. The propagated standard error in the DDS is shown in *red* shade. Clearly, the 1306(-)/1298(+) cm^{-1} feature is above the noise level. The noise level in the photoaccumulated [$P700^+$ – P700] spectrum is below the thickness of the line in the figure.

4 TIME-RESOLVED FTIR DIFFERENCE SPECTROSCOPY FOR THE STUDY OF PHOTOSYSTEM I WITH HIGH POTENTIAL NAPHTHOQUINONES INCORPORATED INTO THE A1 BINDING SITE

ABSTRACT

Microsecond time–resolved Fourier transform infrared difference spectroscopy (TR FTIR DS) has been used to study photosystem I (PSI) cyanobacterial photosystem I (PSI) photosynthetic reaction centers from *Synechocystis* sp. PCC 6803 (*S6803*) with four high-potential, 1,4–naphthoquinones (NQs) incorporated into the A_1 binding site. The high–potential NQs are 2–chloro–NQ (2ClNQ), 2–bromo–NQ (2BrNQ), 2,3–dichloro–NQ (Cl_2NQ), and 2,3–dibromo–NQ (Br_2NQ). Native PSI has phylloquinone (PhQ) in the A_1 binding site, and "foreign minus native" double difference spectra (DDS) were constructed by subtracting TR FTIR DS for native PSI from corresponding spectra obtained using PSI with the different quinones incorporated.

To help assess and assign bands in the DS and DDS, density functional theory based vibrational frequency calculations for the different quinones in solvent, or in the presence of a single asymmetric H–bond to either a water molecule or a peptide backbone NH group, were undertaken. Calculated and experimental spectra agree best for the peptide backbone asymmetrically H–bonded system.

By comparing multiple sets of DDS, bands of PhQ^- are identified at 1520, 1494, 1476, 1456 and 1414 cm^{-1}. The 1494 and 1414 cm^{-1} bands are well–known to be due to the $C_1{=}O$ and $C_4{=}O$ stretching vibrations, respectively. The band at 1476 cm^{-1} is assigned to C–H bending modes of the 2–methyl group of PhQ^-. For the bands at 1520 and 1456 cm^{-1}, calculations suggest that they are due to a $C_2{=}C_3$ stretching vibration (in combination with a C–H bending mode) and a near pure C–H bending vibration, respectively. Bands similar to the 1520 and 1456 cm^{-1} bands

of PhQ^- are also identified for the four halogenated NQs. The fact that several bands of PhQ^- are apparent in the DDS indicates that corresponding bands of the foreign incorporated semiquinone anions are shifted compared to that of PhQ^-.

By comparing groups of calculated and experimental spectra the orientation of mono-substituted NQs in the A_1 binding site is assessed. We show that the mono-substituted NQs can occupy the binding site in different orientations, with the C_3 hydrogen atom being both ortho and meta to the H-bonded C_4=O group.

The frequency separation between the $C_1 \cdots O$ and $C_4 \cdots O$ vibrational modes for PhQ^-/$DMNQ^-$/$2MNQ^-$/$2ClNQ^-$/$2BrNQ^-$/Cl_2NQ^-/Br_2NQ^- in the A_1 binding site is 80/69/75/83/83/~60/59 cm^{-1}, respectively. This separation is ~30 cm^{-1} for the neutral state NQs, indicating stronger hydrogen bonding to the C_4=O group in the anion state (for all the different incorporated NQs) compared to neutral state.

4.1 Introduction

In oxygen-evolving photosynthetic organisms, solar energy conversion takes place in two large membrane–spanning protein complexes called photosystem I and II (PSI and PSII)[2] [6]. In both photosystems, the fundamental mechanism of solar energy conversion is light–induced electron transfer (ET) across the thylakoid membrane. In both photosystems, the ET processes exhibit a remarkably high quantum efficiency [11, 12].

[2]**Abbreviations:** 2BrNQ, 2−bromo−NQ; Br_2NQ, 2,3−dibromo−NQ; Cl_2NQ, 2,3−dichloro−NQ; 2ClNQ, 2−chloro−NQ; C=O, carbonyl; Chl *a*, chlorophyll *a*; DAS, decay associated spectrum; DMNQ, 2,3−dimethyl−NQ; DDS, double difference spectrum; DFT, density functional theory; DS, difference spectra/spectrum/spectroscopy; ET, electron transfer; FTIR, Fourier transform infrared; H−bond, hydrogen bond; 2MNQ, 2−methyl−NQ; NQ, 1,4−naphthoquinone; PhQ, phylloquinone (2−methyl−3−phytyl−NQ); PQ, plastoquinone−9; PSI, photosystem I; PSII, photosystem II; RC, reaction center; RT, room temperature (293 K); *S6803*, *Synechocystis* sp. PCC *6803*; THF, tetrahydrofuran; TRSS, time−resolved step−scan; WT, wild type.

ET occurs in a centralized pigment–protein complex called a reaction center (RC). The organization of the ET cofactors in the PSI RC are outlined in Fig. 4.1. The cofactors that participate in ET are termed P700, A_0, A_1, F_X, F_A, and F_B [17]. P700 is a heterodimeric chlorophyll−*a*/ chlorophyll−*a'* (Chl−*a*/Chl−*a*') species. Chl−*a*' is a 13^2 epimer of Chl−*a* [16]. A_0 is a monomeric Chl−*a* molecule. In PSI, the secondary electron acceptor, A_1, is a phylloquinone molecule (PhQ, 2–methyl–3-phytyl–NQ). F_X, F_A, and F_B are iron sulfur [4Fe−4S] clusters. In PSI, the cofactors are arranged two near symmetrical "branches" termed the A– and B– branches. The cofactors on either branch are indicated by a subscript in Fig. 4.1A (e.g. A_{1A}/A_{1B}). In native PSI, following light excitation, an electron is transferred forming the secondary radical pair state, $P700^+A_1^-$ within ~50 picoseconds (ps) [20, 21]. $P700^+A_1^-$ undergoes forward ET to form $P700^+F_X^-$ in ~20 and ~300 nanoseconds (ns) at room temperature (RT, ~293 K). These time constants are thought to represent intrinsic lifetimes of ET on the B and A branches, respectively [27, 28]. Forward ET from F_X^- to the terminal electron acceptors, F_A and F_B occurs on a sub–μs timescale [29]. In isolated cyanobacterial PSI particles, the $P700^+F_{A/B}^-$ terminal radical pair state recombines, *via* repopulation of A_{1A}^- with a time constant of ~50−100 ms [30-35].

At 77 K, ET in PSI becomes heterogeneous. $P700^+A_1^-$ charge recombination occurs in ~35 % of the PSI particles, while ~20 % undergoes $P700^+F_X^-$ charge recombination [22, 36]. Both recombination reactions occur almost exclusively through A_{1A} [37]. In the remainder of the PSI particles $P700^+F_{A/B}^-$ formation is irreversible, resulting in a loss of signal amplitude in repetitive flash experiments [22, 36]. At 77 K, in native cyanobacterial PSI, the $P700^+A_{1A}^-$ state recombines with a time constant of ~350 μs [36, 38]. For PSI with low potential NQs incorporated $P700^+A_{1A}^-$ recombines (at 77 K) in less than 100 μs [22, 35].

Fig. 4.1B shows the structure of PhQ in the A_{1A} binding site, derived from the 2.5 Å X−ray crystal structure of cyanobacterial PSI isolated from *Thermosynechococus elongatus (T. elongatus)* (PDB 1JB0 [16]). Similar structures are obtained from plant and algae PSI [17, 40, 41, 133, 134]. Neutral PhQ in PSI is asymmetrically hydrogen bonded (H-bonded) to the backbone N−H group of LeuA722. H−bonding is to the C_4=O carbonyl group that is adjacent (ortho) to the phytyl chain. The N···O distance is 2.67 Å. Electron paramagnetic resonance (EPR) data supports this asymmetric H−bonding idea for the semiquinone anion [43], as do FTIR studies [44]. The FTIR studies suggest that this H−bond is especially strong, at least for PhQ^- [44]. In spite of this, many of the underlying PhQ pigment−protein interactions, including the exact role of this asymmetric H−bonding are still not well understood [15].

To investigate the molecular properties of PhQ in the A_1 binding site in PSI (and for quinones in protein binding sites in general) one possible way is to study PSI where the native quinone is replaced with a foreign one. This process of foreign quinone incorporation has been simplified with the generation of so−called *menB*$^-$ mutant cells where PhQ biosynthesis has been disrupted. In this study, we used cyanobacterial cells from *Synechocystis* sp. PCC 6803 (*S6803*) in which the *menB* gene is inactivated. In these mutant cells a plastoquinone (PQ) molecule is recruited into the A_1 binding site instead of PhQ [55]. PQ is weakly bound and is easily displaced by incubating PSI particles in the presence of a large molar excess of different NQs [35, 43, 56], including the high potential NQs that are the subject of the current study. This is an ideal minimally disruptive incorporation method and *menB*$^-$ PSI samples with different quinones incorporated have been used in a number of spectroscopic studies [43, 44, 57-62]. These studies have shown that for all non−native incorporated quinones the position and orientation of the C=O groups is essentially the same as it is for PhQ [44].

Recent time resolved step scan (TRSS) FTIR difference spectroscopy (DS) studies of PSI with foreign quinones incorporated, together with QM/MM vibrational frequency calculations have allowed a more detailed understanding of the vibrational properties of quinones in the A_1 binding site in both the neutral and reduced states [44, 63, 64]. One suggestion from these studies is that asymmetric H−bonding to the C_4=O of PhQ is stronger in the anion state compared to the neutral state [44].

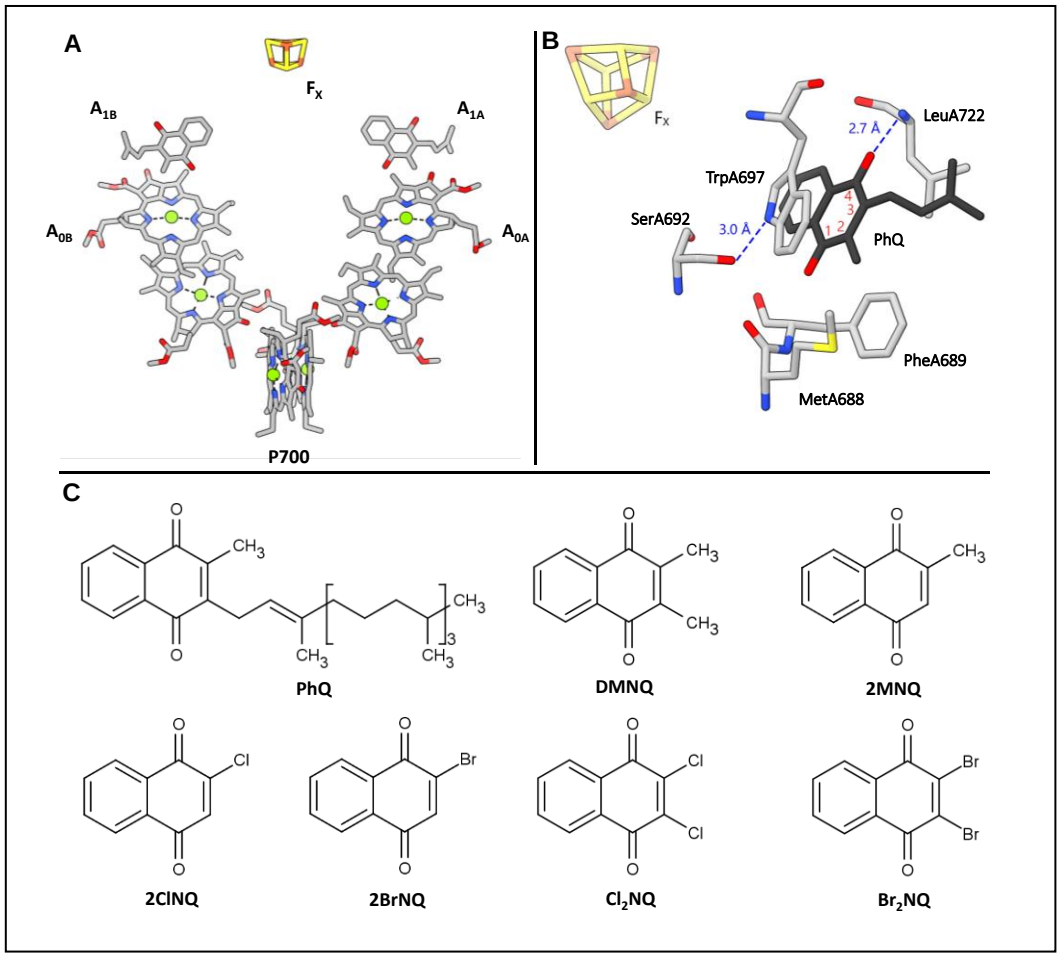

Figure 4.1 (A) Arrangement of ET cofactors in PSI. Structure derived from the 2.5 Å X−ray crystal structure of PSI from *T. elongatus* (PDB file 1JB0 [16]). Subscripts A and B refer to the ET branch. (B) View of PhQ in the A_{1A} binding site. Possible H−bonding interactions are indicated (*dotted*). The numbering scheme for quinonic part of the NQ ring is indicated in *red*. Atom coloring: *black*: carbon atoms of PhQ. Hydrocarbon chain of PhQ and Chl molecules are truncated for clarity in A and B. (C) Structure of the different quinones considered in this manuscript.

Most of the previous FTIR studies focused on the vibrational properties of (relatively) low potential NQs incorporated into PSI. In this manuscript we focus on studies of PSI with a series of high potential halogenated NQs incorporated. There are many reasons for this, one of them being that it is, or will be, possible to study PSI at RT, as microsecond $P700^+A_1^-$ recombination is still the dominant decay pathway at RT in PSI with high potential NQs incorporated [22]. In preparation for these future TRSS FTIR studies we first present here studies at 77 K, focusing on the quinones in the reduced states [1, 57, 63, 65, 66].

In this manuscript, we probe the vibrational properties of four different high potential NQs incorporated into the A_1 protein binding site by obtaining [$P700^+A_1^-$ – $P700A_1$] and [A_1^- – A_1] FTIR DS and "foreign − native" DDS. We show that bands in the DS are unmasked and more easily visualized when multiple DDS can be compared. To aid in spectral interpretation of the demasked bands we also used DFT based vibrational frequency calculations for the different quinones in solvent or in the presence of a single asymmetric H−bond.

4.2 Materials and Methods

Quinones and solvents were obtained from Sigma−Aldrich Inc. (St Louis, MO), and used as received. 2ClNQ was obtained from Pure−Chemistry Scientific (Burlington, MA) and was used as received.

Trimeric PSI particles isolated from *menB*$^-$ mutant cells from *Synechocystis* sp. PCC 6803 (*S6803*) were prepared as described previously [55]. Quinones were introduced into the A_1 binding site by incubating PSI samples in the presence of the quinone of interest. The PSI particle to quinone ratio was approximately 1:500. Quinones were dissolved in dimethyl sulfoxide (DMSO) and added to a suspension of PSI particles in such a way that the volume of the solvent in the

mixture never exceeds 2% of the total volume. Incubation periods of 12−24 hrs. at room temperature (RT, 293 K), with stirring, were typically used.

Following incubation, PSI samples were resuspended in Tris buffer (50 mM Tris buffer with 0.04% n−dodecyl−β−D-maltoside (β−DM)) at pH 8 to make total volume of 1 mL, and then centrifuged at 408,000 g for ~3 hours to produce a soft pellet. Phenazine methosulfate (PMS) (20 μM) and sodium ascorbate (20 mM) were added to the soft pellet (0.1 μL each), which was then squeezed between two circular calcium fluoride (CaF_2) windows. The sample thickness was adjusted so that the optical density of the amide I band (at ~1656 cm^{-1}) was between 0.6 and 1.0. The CaF_2 windows were sealed with vacuum grease and placed in a custom sample holder for measurements at RT. For measurements at low temperature (LT, 77 K) the sample was loaded into a liquid nitrogen cooled cryostat (Cryo Industries of America Inc., Manchester, NH).

FTIR absorption spectra of the different NQs were measured using a Varian 600 UMA FTIR microscope (Varian Inc., MA, USA), utilizing a mercury cadmium telluride (MCT) detector. Spectra were collected at 4 cm^{-1} resolution. The different NQs were dissolved in tetrahydrofuran (THF) at various concentrations, and a small drop (<5 μL) was deposited on a zinc selenide window. An FTIR spectrum of pure THF was also obtained and interactively subtracted from the quinone spectrum.

Static, photo−accumulated [$P700^+$ − P700] FTIR DS were obtained at 77K as described previously using a Bruker Vertex80 FTIR spectrometer equipped with a MCT detector (Bruker Optics, Billerica, MA) [72-75]. Illumination was provided by a 20-mW helium neon laser, expanded to a spot size of ~1 cm at the sample.

Time−resolved step−scan (TRSS) FTIR DS were collected in a manner similar to that described previously [73-76], using the same Bruker Vertex 80 FTIR spectrometer equipped with

a MCT detector. TRSS FTIR DS were collected with 6 µs time resolution over a 3.5 ms time window at 77 K. Data were collected at 4 cm^{-1} spectral resolution in the 1950−1100 cm^{-1} region. Light above 1950 cm^{-1} was blocked by placing 2000−1000 cm^{-1} bandpass filters both before the sample and in front of the MCT detector. The latter also blocks stray laser illumination from reaching the detector. Light below ~1100 cm^{-1} was also blocked by the CaF_2 sample windows, and the windows on the cryostat shroud. Sample excitation was provided by 532 nm laser flash of 5 ns duration from a Minilite Nd:YAG laser (Continuum, San Jose, CA) operating at 10 Hz. Laser flashes with a power of ~0.785 mJ/cm^2 (1 mJ per pulse spread over a circle of diameter of ~1 cm at the sample) were used. TRSS FTIR DS measurements were repeated ~40 times for each PSI sample. At least three independently prepared PSI samples (with the different quinones incorporated) were used, and the result of ~120 full step-scan acquisitions were averaged. The standard error of the three independent spectra obtained for each sample is taken as a measure of experimental variability (noise level) in the measurements and is indicated as error bars on the spectra.

The complete TRSS FTIR DS data set was globally analyzed using Glotaran software [77]. The TRSS FTIR DS were fitted globally to multi−exponential functions and decay−associated spectra (DAS) were constructed. This was done in part to separate spectral features associated with a sample heating artifact caused by the actinic laser flashes used to initiate photochemistry [44].

DFT−based molecular geometry optimization and harmonic normal−mode vibrational frequency calculations were undertaken as described previously [78], using Gaussian16 software (Gaussian Inc. Wallingford, CT) [79]. The phytyl tail of PhQ was truncated to a 5−carbon unit [$CH_2CHC(CH_3)_2$]. Asymmetric H−bonded quinone models were constructed starting from the 2.5 Å X−ray crystal structure of PSI from *T. elongatus*. To construct this model for the other NQs,

PhQ in the A_{1A} binding site was modified without altering the position and orientation of the quinonic ring atoms.

DFT calculations were performed using the B3LYP functional in combination with the 6−31+G(d) basis set [80]. For the anion state of the quinone of interest, the overall charge was assigned as −1. The solvent (THF) was considered using the integral equation formalism of the polarizable continuum model [81] using default parameters in Gaussian16 software. Harmonic, normal mode vibrational frequency calculations result in "stick spectra" (intensities at given frequencies). These stick spectra are convolved with Gaussian functions of 4 cm^{-1} half−width, to produce more realistic looking absorption spectra.

For each molecular model a single scaling factor was calculated by taking the ratio of the calculated and experimental frequencies of the main $C_1 \cdots O$ mode of PhQ^- (at 1495 cm^{-1} [44]). These scaling factors are purely for ease of comparison and are largely irrelevant as it is primarily the shift in the vibrational frequencies for the different quinones that are of interest, and this shift does not depend significantly on the scaling factor.

An assignment of calculated frequencies to molecular groups was based on visual inspection of the calculated atomic displacements associated with the normal modes. The atomic displacements were visualized using GaussView 6 software (Gaussian, Wallingford, CT).

For isolated quinones in solution, potential energy distributions (PEDs) associated with the normal modes are calculated using VEDA [85]. PEDs provide a percentage estimate of how much a specific molecular group contributes to a normal mode.

4.3 Results

4.3.1 TRSS FTIR DS and DDS for PSI with different NQs incorporated

As described previously, PSI samples were prepared for FTIR DS measurements and immediately frozen to 77 K in the dark [53]. FTIR DS for PSI with different halogenated NQs incorporated have not been presented previously, and a paper discussing both the neutral and anion region would become unmanageable. For this reason, we focus here on spectral features in the ~1540−1400 cm^{-1} semiquinone anion spectral region and will defer studies in other spectral regions to another manuscript.

From global analysis of the 77 K TRSS FTIR DS data sets, major decay phases with lifetime of 366/391/239/114/94/78/70 μs were found for PSI with PhQ/DMNQ/2MNQ/2ClNQ/2BrNQ/ Cl_2NQ/Br_2NQ incorporated, respectively. Lifetimes for PSI with the different quinones incorporated were presented previously [35, 38, 59].

The spectra associated with these lifetimes are called decay associated spectra (DAS), and Fig. 4.2 shows DAS for PSI samples with the different quinones incorporated. These DAS correspond to radical pair recombination at 77K and are therefore called [$P700^+A_1^-$ − $P700A_1$] FTIR DAS. In the FTIR DAS in Fig. 4.2 bands are due to $P700^+$/P700, A_1^-/A_1, and protein modes, which are impacted by $P700^+A_1^-$ radical pair formation. A photoaccumulated [$P700^+$ – P700] FTIR DS in the anion region is also shown in Fig. 4.2A.

Prominent positive bands are observed in the [$P700^+A_1^-$ – $P700A_1$] FTIR DAS that are not observed in [$P700^+$ – P700] FTIR DS. These positive bands are attributed mainly to vibrational modes of the semiquinone anion in the A_1 binding site. For example, positive bands at 1495 and 1415 cm^{-1} in [$P700^+A_1^-$ – $P700A_1$] FTIR DAS for PSI with PhQ incorporated (native PSI) have previously been shown to be due to $C_1{=}O$ and $C_4{=}O$ stretching vibrations of PhQ^- [44]. In

[$P700^+A_1^-$ – $P700A_1$] FTIR DAS for PSI with 2MNQ incorporated positive bands are observed at 1506 and ~1432 cm^{-1} and these bands have also previously been shown to be partly due to the $C_1{=}O$ and $C_4{=}O$ stretching vibrations of $2MNQ^-$ [44, 135].

[$P700^+A_1^-$ – $P700A_1$] FTIR DAS contain contributions from multiple species. Often these species display difference features that are considerably more intense than the features (of the quinones) that are of interest. To focus on the analysis of bands associated with the semiquinones often [$P700^+$ – P700] FTIR DS are subtracted from [$P700^+A_1^-$ – $P700A_1$] FTIR DAS to produce a so–called [A_1^- – A_1] FTIR DS. Fig. 4.3 shows [A_1^- – A_1] FTIR DS obtained using PSI with the different quinones incorporated.

[A_1^- – A_1] FTIR DS are relatively free of contributions from P700/$P700^+$ but still contain contributions from protein modes that are impacted by A_1^- formation. To focus on bands associated with the quinones, DDS can be constructed by taking the difference between [A_1^- – A_1] FTIR DS obtained using PSI with two different quinones incorporated. An alternative would be to take the difference between [$P700^+A_1^-$ – $P700A_1$] DAS obtained using PSI with two different quinones incorporated [44, 136]. This latter approach does not require the separate collection of photoaccumulated [$P700^+$ – P700] FTIR DS and is usually preferable although we do find that [$P700^+$ – P700] FTIR DS are near identical for PSI samples with different quinones incorporated. Here we focus on DDS calculated by subtracting the [$P700^+A_1^-$ − $P700A_1$] FTIR DAS for PSI with PhQ incorporated from all the other DAS for PSI with the different quinones incorporated. These DDS could be called “foreign minus native” DDS. Fig. 4.4 shows several “foreign minus native” DDS. In these DDS bands associated with PhQ^- are negative. Since [$P700^+A_1^-$ – $P700A_1$] FTIR DAS for PSI with PhQ incorporated were used to construct all the DDS in Fig. 4.4, negative bands of PhQ^- should be present in all the DDS. Negative bands are observed at 1494 and 1414

cm^{-1} in the DDS in Fig. 4.4 (B, C, D), and so these bands are due to PhQ^{-}. The 1494 cm^{-1} band is not so clear in Fig. 4.4A, E and F. This may be due to both quinones having bands at similar frequencies.

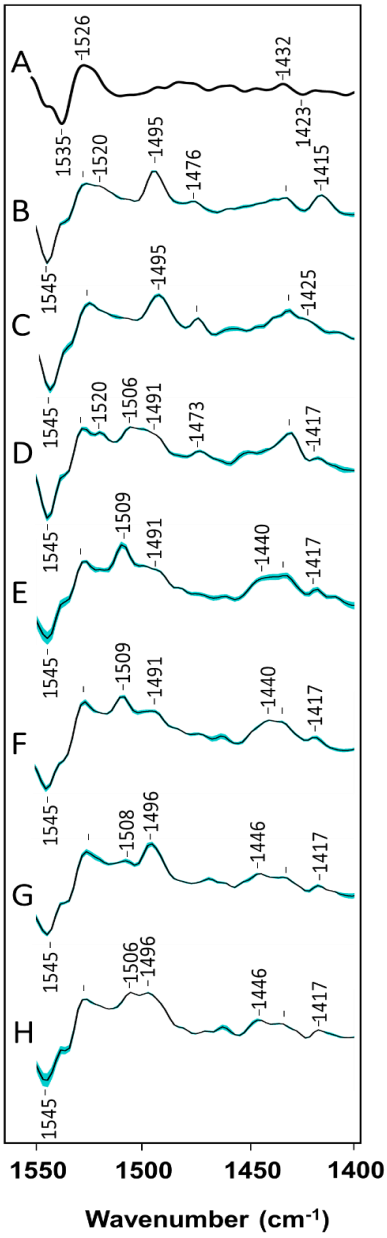

Figure 4.2 Photoaccumulated [$P700^{+}$ – P700] FTIR DS (A) and [$P700^{+}A_1^{-}$ – $P700A_1$] FTIR DAS (B–H) in the 1550–1400 cm^{-1} regions obtained at 77 K using PSI particles with (B) PhQ, (C) DMNQ, (D) 2MNQ, (E) 2ClNQ, (F) 2BrNQ, (G) Cl_2NQ and (H) Br_2NQ incorporated. Spectra are normalized to the ~1718/1697 cm^{-1} difference band. Spectra shown are the average of at least 3 separate experiments. The standard error derived from these separate measurements are also shown (*blue shade*). Photoaccumulated DS have been shown to be nearly identical for PSI with different

quinones incorporated. The photoaccumulated DS shown here is the average from over fifty independent PSI samples with different quinones incorporated.

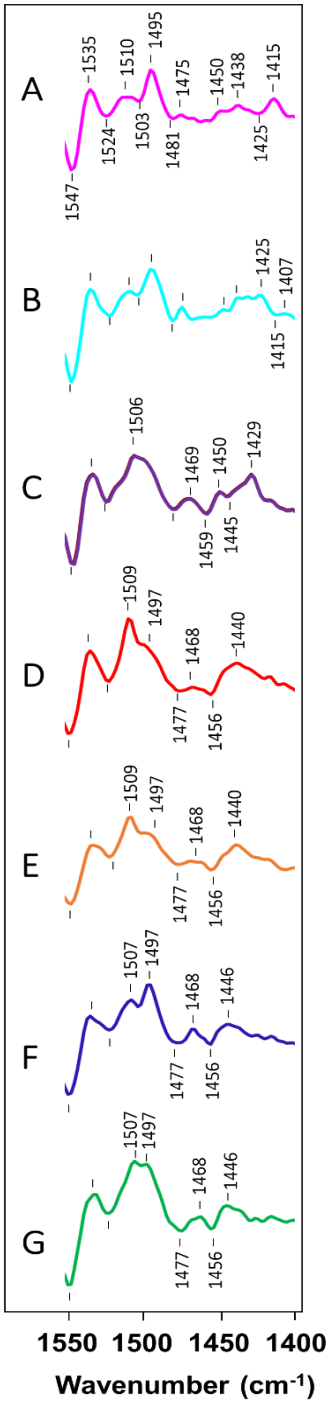

Figure 4.3 [A_1^- – A_1] FTIR DS in the 1550–1400 cm^{-1} region, obtained at 77 K for *menB*⁻ PSI particles with (A) PhQ, (B) DMNQ, (C) 2MNQ, (D) 2ClNQ, (E) 2BrNQ, (F) Cl_2NQ, and (G) Br_2NQ incorporated into the A_1 binding site.

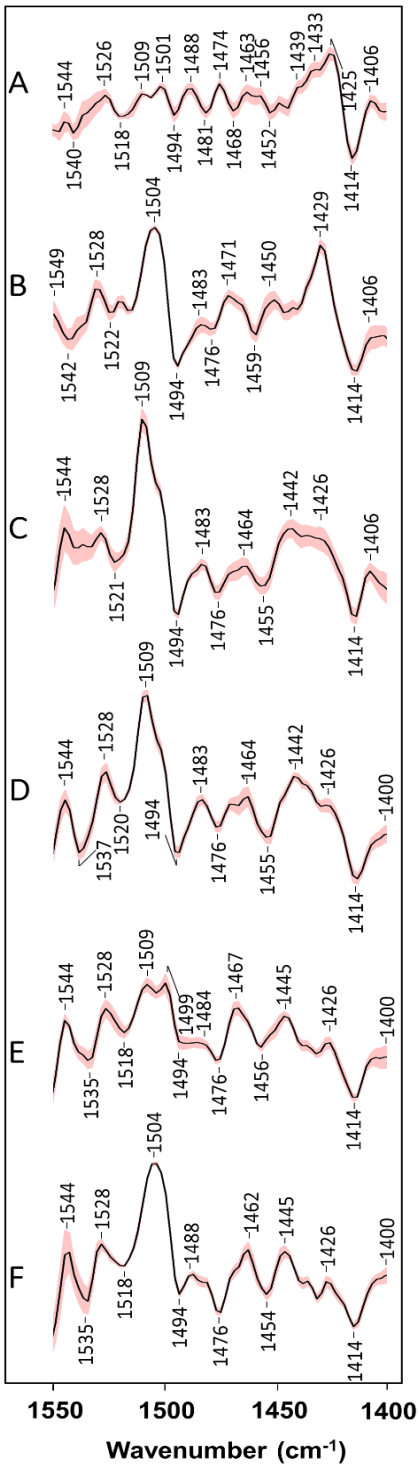

Figure 4.4 Double difference spectra (DDS) in the 1550–1400 cm^{-1} region constructed by subtracting the [$P700^{+}A_1^{-}$ – $P700A_1$] DAS for native PSI from the corresponding DAS for PSI with the indicated quinone incorporated. (A) (DMNQ − PhQ), (B) (2MNQ − PhQ), (C) (2ClNQ − PhQ), (D) (2BrNQ − PhQ), (E) (Cl_2NQ − PhQ) and (F) (Br_2NQ − PhQ). The propagated standard error is shown (*red shade*).

4.3.2 DFT calculated FTIR absorption spectra of NQs

To aid in the analysis and interpretation of the bands in the DS and DDS we have undertaken DFT−based harmonic, normal-mode vibrational frequency calculations for the different semiquinone anions in THF (Fig. 4.8). We have also undertaken calculations for the semiquinones H−bonded to either a water molecule (Fig. 4.9) or to the amide backbone N−H group of a Leu residue (Fig. 4.5/10). The different molecular models are referred to as follows: (Q^{-}+H_2O) for the semiquinones H-bonded to a water molecule; (Q^{-}+Leu) for the model shown in the inset in Fig. 4.5 for the semiquinones H-bonded to a peptide N−H group of a truncated Leu residue. The inset in Fig. 4.5 indicates the molecular model also includes a portion of the backbone from Ala721 and Ser723. When necessary, we will refer to this as (Q^{-}+Leu, model 1 (m_1)). A slightly simpler model with a reduced number of atoms in the protein backbone is considered in Fig 4.10. When necessary, we will refer to this simpler model as (Q^{-}+Leu, model 2 (m_2)). Comparison of the data in Fig. 4.5 and 4.10-14 indicate very similar spectra are calculated for the m_1 and m_2 models.

A model termed (flipped Q^{-}+Leu (f-m_1)) is also considered, where the semiquinone is rotated ~180^{o} along the axis perpendicular to the line joining the C=O groups (quinone is “flipped”). For the three mono substituted NQs, the quinones are “flipped” simply by interchanging the positions of groups attached at C_2 and C_3. Calculated spectra for the “flipped" monosubstituted NQs are shown as *dotted* lines in Fig. 4.5 and 4.10. Composite spectra that are the average of the spectra obtained using the flipped and non-flipped models are also shown in Fig. 4.5 (*grey dotted lines*).

In this study, for PSI with non-native NQs incorporated, we will refer to the H−bonded C=O group as the C_4=O group. We will also refer to the substitutions at C_3 and C_2 as being ortho or meta to the H−bonded C_4=O group, respectively. In some instances, this numbering scheme is

not in keeping with IUPAC numbering, but it will make it simpler to compare normal modes for the different incorporated NQs.

Molecular groups that contribute to the bands in the various calculated spectra are listed in Table 4.8/9/10. The calculated frequencies, intensities, and assignments of the $C_1{=}O$ and $C_4{=}O$ vibrational modes of the semiquinones for the different models are listed in Table 4.4. Key bond lengths and angles obtained from the calculated optimized geometries of the different quinones are listed in Table 4.5.

Fig. 4.6 shows the calculated DDS obtained using the spectra in Fig. 4.5. Comparison of calculated DDS obtained using the flipped and non-flipped models, for the monosubstituted NQs, are shown in Fig. 4.7. The average of the two DDS for the flipped and non-flipped models are also shown in Fig. 4.7. The spectra in Fig. 4.7 are obtained using the (Q^{-}+Leu, model 1), but very similar results are obtained using the slightly simpler (Q^{-}+Leu, model 2) (Fig. 4.11/12/13/14).

Note that for PhQ^{-}, the main $C{=}O$ bands are calculated at 1495 and 1428 cm^{-1}. Experimentally, the bands are at 1494 and 1414 cm^{-1}. So, it may be appropriate to use a separate set of scaling factors for the different spectral regions, but this will not be implemented in this manuscript.

Fig. 4.15 shows a model indicating the calculated bond lengths and angles for reduced PhQ^{-} obtained using the different models. The various bond lengths and angles for the different models are listed in Table 4.5.

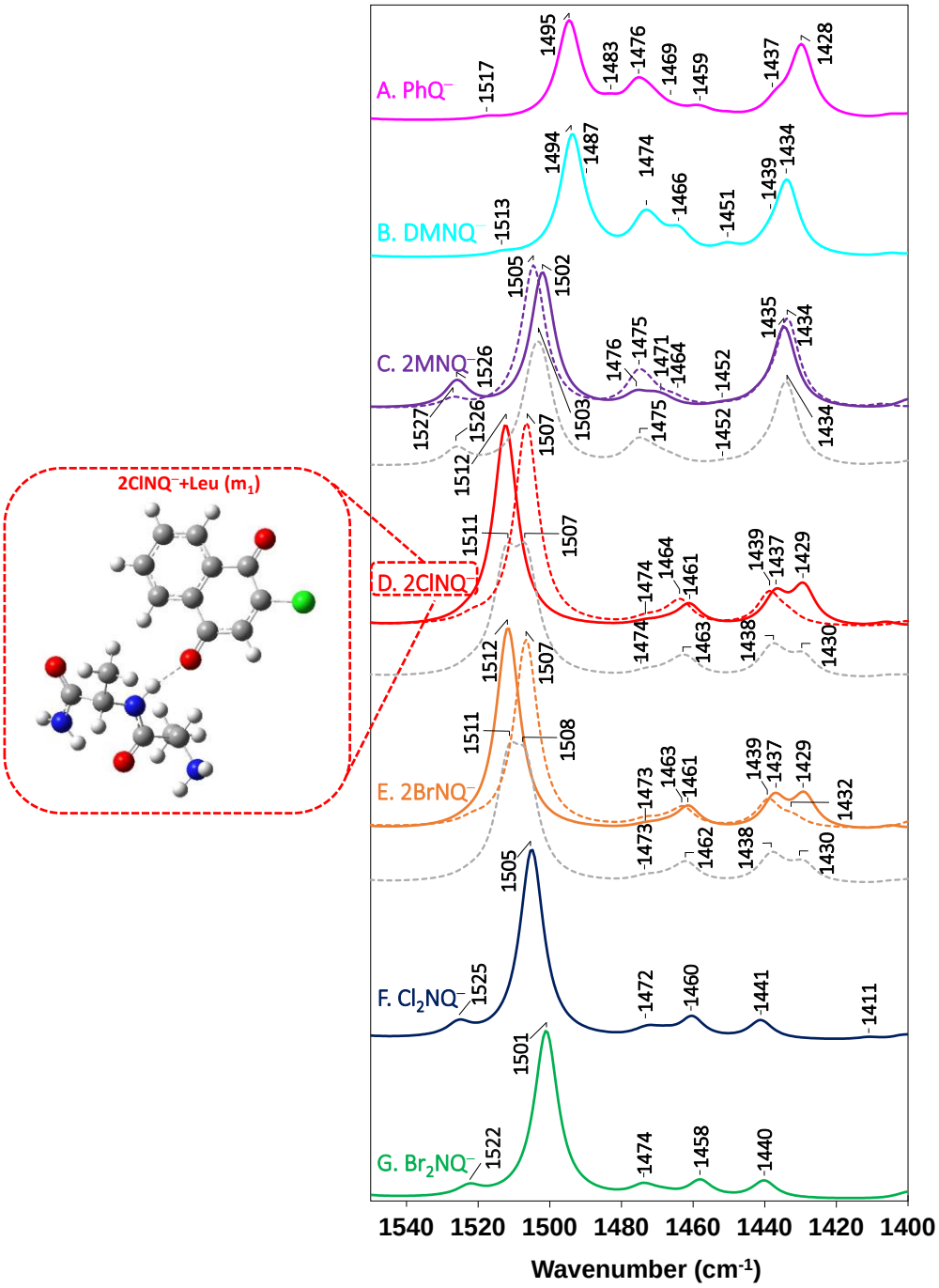

Figure 4.5 Calculated spectra for the semiquinones where the C_4=O group is H–bonded to the backbone of a truncated Leu residue (see inset). (A) PhQ^-, (B) $DMNQ^-$, (C) $2MNQ^-$, (D) $2ClNQ^-$, (E) $2BrNQ^-$, (F) Cl_2NQ^- and (G) Br_2NQ^-. Calculated frequencies are scaled by 0.971. For the monosubstituted NQs, the appropriately color-coded dotted lines show the spectra calculated when the semiquinone is "flipped". The grey dotted lines show the average of the spectra obtained using the flipped and non-flipped models.

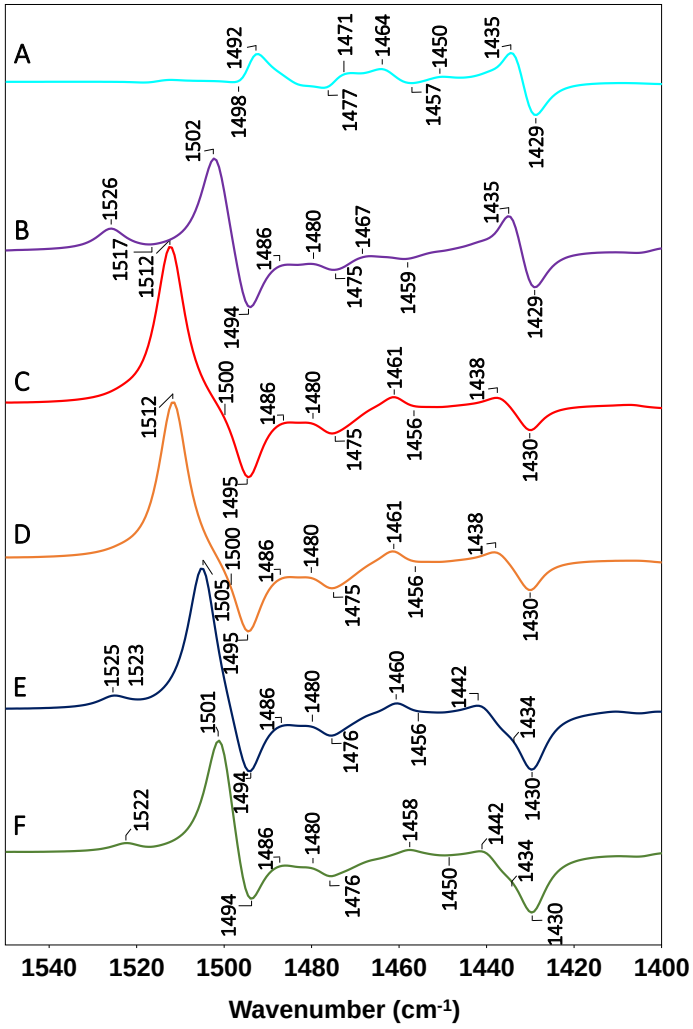

Figure 4.6 Double difference spectra (DDS) constructed using the spectra obtained using the "non-flipped" models in Fig. 4.5. (A) (DMNQ − PhQ), (B) (2MNQ − PhQ), (C) (2ClNQ − PhQ), (D) (2BrNQ − PhQ), (E) (Cl_2NQ − PhQ) and (F) (Br_2NQ − PhQ).

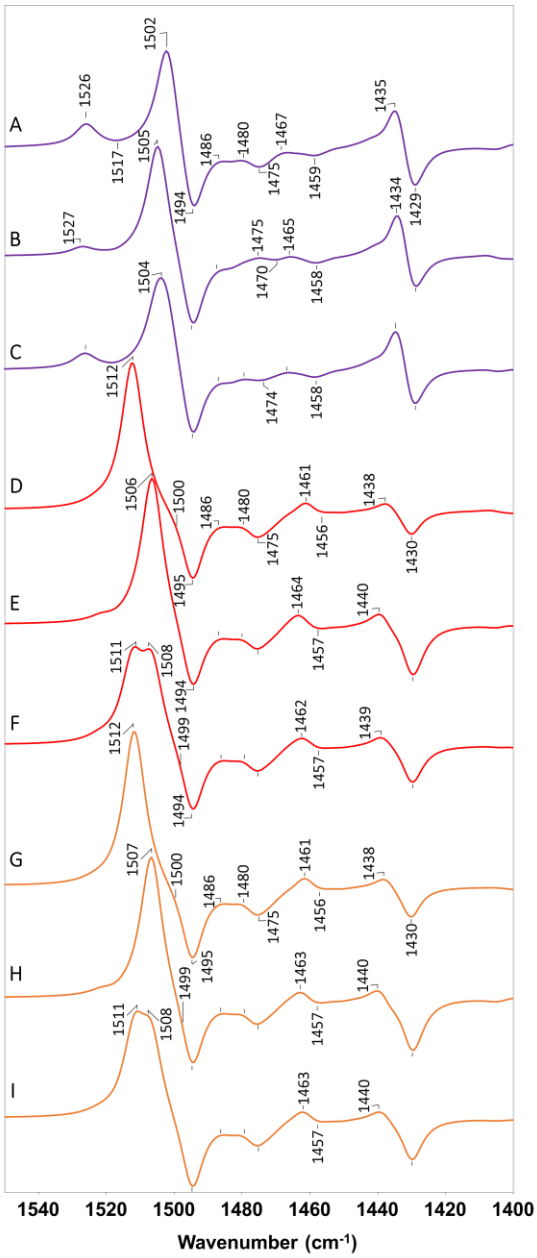

Figure 4.7 DDS constructed using the spectra in Fig. 4.5. Spectra in A-C are for (2MNQ − PhQ) for the (A) non-flipped model, (B) flipped model and (C) the average of the spectra in A and B. Spectra D-F are for (2ClNQ − PhQ) for the (D) non-flipped model, (E) flipped model, and (F) the average of the spectra in D and E. Spectra G-I are for (2BrNQ − PhQ) for the (G) non-flipped model, (H) flipped model, and (I) the average of the spectra in D and E.

4.4 Discussion

4.4.1 Experimentally observed semiquinone bands

Intense IR bands due to the C⋯O modes of the semiquinone anions are found in the ~1550−1400 cm^{-1} region. Spectral contributions from $P700^+$/P700 and other protein modes are weak in this region (Fig. 4.2A) and bands associated with the bound quinone may be more easily visualized (Fig. 4.2B-H). Despite this, bands associated with the bound quinone are best visualized in the DDS (Fig. 4.4). For all DDS shown in Fig. 4.4, FTIR DS obtained using native PSI with PhQ incorporated have been subtracted. Since quinone anion bands are positive in this region, negative bands that appear in the DDS are due to PhQ^-. Off course, bands that appear at a similar frequency in both native PSI and PSI with a foreign quinone incorporated will not show up in the DDS. For example, in the DS for PSI with $DMNQ^-$ or PhQ^- incorporated, a band is observed near 1494 cm^{-1} (compare Fig. 4.3A and B). Consequently, no negative feature is observed near 1494 cm^{-1} in the (DMNQ – PhQ) DDS (Fig. 4.4A).

The DDS in Fig. 4.4B−F clearly indicate (negative) PhQ^- bands at 1494 and 1414 cm^{-1}. These bands are due mainly to C_1⋯O and C_4⋯O stretching vibrations of PhQ^- [44, 65, 135]. The separation between the two C⋯O modes is 80 cm^{-1}, which may in part be due to (relatively) strong H−bonding to the C_4=O group *in the anion state*. [Note that it is probably unwise to make the statement that the 1414 cm^{-1} band is due to a C_4⋯O stretching vibration. More accurately, the band is due to a normal mode that contains contributions from several molecular groups, only one of which is the C_4=O group]. Recently it has been suggested for neutral PhQ in PSI that the C_1=O and C_4=O modes are separated by ~30 cm^{-1} [65]. So, one might argue that H−bonding is strengthened upon anion formation. It is difficult to imagine structural or bioenergetic benefits that could arise from this anion induced H-bond strengthening. For example, Srinivasan et al. have

indicated that PhQ retains its native orientation even in mutant PSI samples where H−bonding to PhQ has been altered [137]. Furthermore, H−bonding is expected to stabilize the semiquinone, leading to a higher (more positive) midpoint potential of PhQ [137, 138] [139, 140]. So, anion induced H−bond strengthening might be expected to be disadvantageous for ET in PSI, which requires the A_1 pigment to operate at a highly negative redox potential.

For PSI with DMNQ incorporated, the semiquinone C⋯O modes give rise to bands at 1495 and ~1432 cm^{-1} (Fig. 4.2C). For PSI with 2MNQ incorporated the semiquinone C⋯O modes give rise to bands at 1506 and 1432 cm^{-1} (Fig. 4.2D). For PSI with 2ClNQ and 2BrNQ incorporated, the C_1⋯O mode gives a very intense band at 1509 cm^{-1} in the DDS, while there appear to be two features at ~1442 and 1426 cm^{-1} (Fig. 4.4C, D), either of which could correspond to the 1415 cm^{-1} band of PhQ^-. For PSI with Cl_2NQ and Br_2NQ incorporated, at least two positive bands appear in the 1509–1496 cm^{-1} range (Fig. 4.4E, F), either of which may correspond to the 1494 cm^{-1} band of PhQ^-. Positive bands also appear near 1445 and 1426 cm^{-1}. Again, either of these bands could correspond to the 1415 cm^{-1} band of PhQ^-. The calculations discussed below may help to address these issues.

The (2MNQ − PhQ), (2ClNQ − PhQ), (2BrNQ − PhQ), (Cl_2NQ − PhQ) and (Br_2NQ − PhQ) DDS all display prominent negative bands at 1494 and 1414 cm^{-1}. As discussed above, this confirms previous work that these bands are due to PhQ^- [44]. The observation of negative bands due to PhQ^- in the DDS indicates that corresponding modes of the non−native semiquinones are shifted relative to PhQ^- in the A_1 binding site.

Five of the DDS exhibit a negative band at 1476 cm^{-1}, which was recently assigned to a PhQ^- C–H bending mode associated with the methyl group at C_2 [56, 65]. Again, this observation from multiple DDS indicate that such a mode is shifted for PSI with foreign quinones incorporated.

Six of the DDS in Fig. 4.4 show negative bands (due to PhQ^-) in the 1517−1522 and 1454−1459 cm^{-1} range. Such PhQ^- features are not obvious in the [$P700^+A_1^-$ − $P700A_1$] (Fig. 4.2B) and [A_1^- – A_1] FTIR DS (Fig. 4.3A). In this manner we demonstrate the potency of using multiple different DDS to uncover "hidden" bands in FTIR DS.

In the (DMNQ – PhQ) DDS most of the features are very weak , indicating that $DMNQ^-$ gives rise to normal modes at the same frequencies to that of PhQ^-. The main difference being that the (predominantly) $C_4{=}O$ mode is upshifted ~11 cm^{-1} to 1425 cm^{-1} for $DMNQ^-$. Replacing the phytyl chain with a methyl group therefore influences predominantly the $C_4{=}O$ mode and not the $C_1{=}O$ mode, which might be expected given the proximity of the phytyl chain (at C_3) to the carbonyl group (at C_4). For $DMNQ^-$, the separation between the $C_1{=}O$ and $C_4{=}O$ modes is ~69 cm^{-1}.

In the ($2MNQ^-$ – PhQ^-) DDS in Fig. 4.4B intense positive bands are observed at 1504 and 1429 cm^{-1} and are assigned to (predominantly) $C_1{=}O$ and $C_4{=}O$ modes of $2MNQ^-$, respectively. These modes are therefore upshifted 10 and 15 cm^{-1}, respectively, for $2MNQ^-$ compared to PhQ^-. The mode separation is 75 cm^{-1}, close to the 80 cm^{-1} found for PhQ^-.

Previous EPR experiments [141] and recent QM/MM vibrational frequency calculations [135], have indicated that the methyl group of 2MNQ is in the same position as it is for PhQ in the A_1 binding site. Therefore, the H atom of 2MNQ is in the position normally occupied by the phytyl chain of PhQ in the A_1 binding site. That is, replacing the phytyl chain of PhQ by a methyl group or a H atom leads to a similar upshift for the $C_4{=}O$ mode. Replacing the phytyl chain by a H atom also causes an upshift of the $C_1{=}O$ mode. This is not the case for replacing the phytyl chain by a methyl group (no upshift is observed).

In *menG* mutant PSI a methyl less PhQ analogue (sometimes called demethyl PhQ) occupies the A_1 binding site. That is, the methyl group of PhQ is replaced with a H atom. In the *menG* mutant the incorporated demethyl-PhQ $C_1{=}O$ mode upshifts ~6 cm^{-1} [142].

In the (2ClNQ – PhQ) and (2BrNQ – PhQ) DDS in Fig. 4.4 an intense band is observed at 1509 cm^{-1},with a shoulder appearing near 1500 cm^{-1}. These two features could indicate a mix of two separately oriented NQ populations. Some with the H atom at the C_2 position and some with it at the C_3 position. If this is the case, then one might suggest that the Cl (or Br) atom does not have a particular affinity for either location (at C_2 or C_3) in the A_1 binding site. However, the positive 1509 cm^{-1} band in the DDS is more intense than this ~1500 cm^{-1} shoulder, which might indicate a population skewed in favor of one orientation over the other.

In the (2ClNQ – PhQ) and (2BrNQ – PhQ) DDS there is a positive feature at 1426 cm^{-1} that would indicate a 12 cm^{-1} upshift of the $C_4{=}O$ mode of $2ClNQ^-$ (or $2BrNQ^-$) relative to PhQ^-. This seems a reasonable upshift for an H atom at C_3, although it is not entirely clear what kind of band shifts to expect for either the $C{=}O$ mode upon incorporating a Cl atom at either the C_2 or C_3 position. In the (2ClNQ – PhQ) and (2BrNQ – PhQ) DDS there is also a positive feature at 1442 cm^{-1} that could indicate a 28 cm^{-1} upshift of the $C_4{=}O$ mode of $2ClNQ^-$ (or $2BrNQ^-$) relative to that of PhQ^-. Again, two features could indicate a mix of two separately oriented NQ populations in PSI. The calculations discussed below might help address this issue. One final point to bear in mind is that the ~1426 cm^{-1} band in the DDS in Fig. 4.4C, D is close to the noise level in the experiment, and it may be reasonable to refrain from attempting to assign this feature. This is not the case for the feature that appears near 1442 cm^{-1}, which is well above the noise level.

The (2MNQ − PhQ) DDS exhibits positive bands at 1528, 1483, and 1471 cm^{-1}, all of which could indicate absorption bands of $2MNQ^-$ which are upshifted ~8, 7 and 15 cm^{-1} relative

to the PhQ^- bands at ~1520, ~1476 and ~1456 cm^{-1}. Similar conclusions apply to the (2ClNQ − PhQ) and (2BrNQ – PhQ) DDS where the positive band near 1483 cm^{-1} is much clearer than in (2MNQ − PhQ) DDS. It seems also that a similar set of positive bands at 1528, 1488 and ~1462 cm^{-1} are observable in the (Cl_2NQ − PhQ) and (Br_2NQ – PhQ) DDS.

In the (Cl_2NQ − PhQ) DDS, the band associated with the $C_1{\cdots}O$ vibration is split into two bands at 1499 and 1509 cm^{-1}. Such a splitting is probably also likely in the (Br_2NQ − PhQ) DDS, but only a single broad positive peak is observed at 1504 cm^{-1}. Both the (Cl_2NQ − PhQ) and (Br_2NQ − PhQ) DDS display a positive band at 1445 cm^{-1}, and a much weaker band at 1426 cm^{-1}. These peaks are similar to that observed in the (2ClNQ − PhQ) and (2BrNQ – PhQ) DDS and both might be assigned to a $C_4{\cdots}O$ vibrational mode of Cl_2NQ^- (or Br_2NQ^-).

4.4.2 Vibrational mode frequency calculations to aid in experimental band assignments

To assign bands in the experimental spectra DFT based vibrational frequency calculations for the semiquinones were undertaken using several different molecular models. In the main manuscript we focus on the (Q^-+Leu model 1 (m_1)), which for $2ClNQ^-$ is shown in the inset of Fig. 4.5. Calculations were also undertaken using a model where the quinone is "flipped" (referred to as (f-m_1)). The average of the spectra obtained using the flipped and non-flipped quinone models is referred to as (avg. m_1). Calculated spectra for the Q^-+Leu (m_1) and Q^-+Leu (m_2) are shown in Fig. 4.5 and 4.10 respectively. DDS calculated using model m_1 are shown in Fig. 4.6.

The most intense band in the calculated spectra occurs in the 1495−1512 cm^{-1} range (Fig. 4.5). For PhQ^-, a vibrational mode is calculated at 1495 cm^{-1} and is due to a $C_1{\cdots}O$ vibration with some coupling to a $C_4{\cdots}O$ stretching and aromatic CH bending modes (see movie titled "1495 mode of PhQ^-" in the SI). The negative 1494 cm^{-1} band in the experimental DDS (Fig. 4.4) is also due to this mode. For $DMNQ^-$/$2MNQ^-$/$2ClNQ^-$/$2BrNQ^-$/Cl_2NQ^-/Br_2NQ^- the corresponding

$C_1{=}O$ mode is calculated to be shifted −1/+7/+17/+17/+10/+6 cm^{-1}, respectively (Fig. 4.5). These shifts compare favorably to the experimentally observed shifts of 0/+10/+15/+15/+5−15/+10 cm^{-1} (Fig. 4.4). The trend in the frequency of the $C_1{=}O$ mode observed experimentally for different quinones in PSI is captured well in the calculated data. This trend is also well captured using the Q^-+Leu (m_2) model (0/+9/+19/+18/+14/+14 cm^{-1}) (Fig. 4.10), the Q^-+H_2O model (0/10/20/20/17/17 cm^{-1}) (Fig. 4.9), and for calculations of the semiquinones in THF (0/10/15/16/14/14 cm^{-1}) (Fig. 4.8). So how the calculated $C_1{=}O$ mode frequencies shift for the different incorporated semiquinones is not a particular valuable probe for assessing which of the molecular models is most appropriate.

The 1494 cm^{-1} band of PhQ^- is clearly visible as a negative band in all the calculated DDS in Fig. 4.6, except for $DMNQ^-$, which has a band at similar frequency to that of PhQ^-.

In the Q^-+Leu (m_1) model for the monosubstituted NQs, $2MNQ^-$/$2ClNQ^-$/$2BrNQ^-$, as mentioned above the $C_1{=}O$ mode is calculated to be shifted +8/+17/+17 cm^{-1} relative to that of PhQ^-, respectively (Fig. 4.7A, D, G). When these monosubstituted NQs are flipped, however, the $C_1{=}O$ mode of $2MNQ^-$/$2ClNQ^-$/$2BrNQ^-$ is shifted +10/+12/+12 cm^{-1} relative to that of PhQ^-, respectively (Fig. 4.7B, E, H). Upon averaging the DDS for the flipped and non-flipped models for the monosubstituted NQs, the $C_1{=}O$ mode for $2MNQ^-$ is upshifted 10 cm^{-1} (Fig. 4.7C). For $2ClNQ^-$ the $C_1{=}O$ band is split into two with peaks at 1511 and 1508 cm^{-1} (upshifted 16 and 13 cm^{-1} relative to that of PhQ^-) (Fig. 4.7F). Similar results are found in the averaged (2BrNQ - PhQ) DDS (Fig. 4.7I). This splitting of the $C_1{=}O$ mode observed in the average calculated (2ClNQ − PhQ) and (2BrNQ − PhQ) DDS is in line with that observed in the experimental DDS (Fig. 4.5), although experimentally the splitting is more asymmetric with the higher frequency peak being more intense. For the averaged calculated (2MNQ − PhQ) DDS (Fig. 4.7C) a splitting of the

positive band (at 1504 cm^{-1}) is less obvious, although in the experimental DDS this positive feature is quite broad (Fig. 4.5C), as it is in the calculated DDS.

Since the average calculated DDS for the monosubstituted NQs are more in line with experiment the suggestion is that the monosubstituted NQs, particularly 2ClNQ and 2BrNQ, are incorporated into the A_1 binding site in both the flipped and non-flipped orientations. This conclusion follows from only a consideration of bands associated with the $C_1{=}O$ modes. Note that the orientation of $2MNQ^-$ in the A_1 binding site has been established using higher-level ONIOM type QM/MM vibrational frequency calculations [143], and a similar set of calculations for $2ClNQ^-$ and $2BrNQ^-$ incorporated into PSI will be undertaken in the near future.

In the Q^-+Leu (m_1) model for PhQ^- there are several modes that contain a contribution from the $C_4{=}O$ stretching vibration. The most intense predominantly $C_4{=}O$ mode is calculated at 1428 cm^{-1} (see movie titled "1428 mode of PhQ^-" in the SI). The calculated separation of the $C_1{=}O$ and $C_4{=}O$ modes of PhQ^- is therefore 67 cm^{-1}. This result is more in line with experiment (80 cm^{-1}) than the separation predicted by the Q^-+H_2O model (59 cm^{-1}) (Fig 4.9 and Table 4.2). As discussed above, the fact that the $C_4{=}O$ mode of PhQ^- is calculated to be at 1428 cm^{-1} (and not 1414 cm^{-1}) poses some problems for a direct comparison of calculated and experimental DDS. Notwithstanding this issue, it may still be reasonable to calculate frequency shifts for corresponding modes of the different NQs.

For $DMNQ^-$/$2MNQ^-$/$2ClNQ^-$/$2BrNQ^-$/Cl_2NQ^-/Br_2NQ^- the corresponding $C_4{=}O$ mode is calculated at 1434/1435/1429/1429/1441/1440 cm^{-1} and is therefore shifted +6/+7/+1/+1/+13/+12 cm^{-1}, respectively, relative to the PhQ^- mode (Fig. 4.5). These results do not agree with the experimentally observed shifts of +11/+15/+12/+12/+31/+30 cm^{-1} (Fig. 4.4). A similar conclusion applies to data calculated using the Q^-+Leu (m_2) model (+2/+3/−1//−1/+8/+9 cm^{-1}) (Fig. 4.10).

The ~1429 cm^{-1} calculated band of PhQ^- is observed as a negative band in all the calculated DDS in Fig. 4.6. So, this mode is clearly shifted for all the NQs relative to PhQ. The 1414 cm^{-1} band of PhQ^- is also observed as a negative feature in all the experimental DDS (Fig. 4.5), so for this particular type of comparison the calculated and experimental DDS agree well.

In the DDS for the monosubstituted NQs, $2MNQ^-/2ClNQ^-/2BrNQ^-$, in the Q^-+Leu (m_1) model (Fig. 4.7A, D, F) the $C_4{\cdots}O$ mode is calculated to upshift +6/+8/+8 cm^{-1} relative to that of PhQ^-, respectively. If the monosubstituted NQs are flipped, however, the $C_4{\cdots}O$ mode is upshifted +6/+10/+10 cm^{-1}. In the averaged DDS the $C_4{\cdots}O$ mode is upshifted 5/9/10 cm^{-1} (Fig. 4.7C, F, I), respectively. It does not appear to be the case from these data that the averaged calculated DDS are more in line with the experimental DDS, than either of the DDS calculated using the flipped and non-flipped models.

The experimental DDS in Fig. 4.4 suggest a PhQ^- band at 1476 cm^{-1}. The calculated DDS in Fig. 4.5 also display a weak negative band at 1476 cm^{-1} that is calculated to be due in part to a $C_4{\cdots}O$ mode (see the movie titled "1476 mode of PhQ^-" in the SI).

The calculation for PhQ^- in Fig. 4.5A indicates very weak bands at 1517 and 1459 cm^{-1}. The 1517 cm^{-1} mode is due to a $\nu(C_2{\cdots}C_3)$ in combination with a δ(CH) vibration, while the 1459 cm^{-1} mode is mainly a δ(CH) vibration (see movie titled "1517 and 1459 mode of PhQ^-" in the SI). These bands are hardly observable in the calculated DDS in Fig. 4.6. These two modes, however, may give rise to the negative bands at ~1520 and ~1456 cm^{-1} in the experimental FTIR DDS (Fig. 4.4).

For $DMNQ^-$ an intense $C_1{\cdots}O$ mode is calculated at 1494 cm^{-1} (Fig. 4.5B), virtually the same as that for PhQ^-. The similarity in the calculated frequency, if translated to experiment, would

predict no feature near 1495 cm^{-1} in the (DMNQ – PhQ) DDS. Such a prediction is in line with the experimental DDS (Fig. 4.4A).

For $DMNQ^-$, however, a predominantly $C_4 \cdots O$ mode is calculated at 1434 cm^{-1} (Fig. 4.5B) upshifted 6 cm^{-1} relative to the corresponding mode of PhQ^-. Experimentally, the upshift is ~11 cm^{-1} (Fig. 4.4A), so the correct trend is predicted but the magnitude of the calculated shift is considerably smaller than that observed.

For $2MNQ^-$, an intense mode is calculated at 1502/1505 cm^{-1} for non-flipped/flipped $2MNQ^-$, respectively (Fig. 4.5C). This mode is also predominantly due to a $C_1 \cdots O$ vibration (with some contribution from CH bending vibrations). This mode is upshifted 7-9 cm^{-1} relative to that of PhQ^- which is comparable with the 10 cm^{-1} observed experimentally.

For $2MNQ^-$ an intense mode is also calculated at ~1435 cm^{-1} for both flipped and non-flopped $2MNQ^-$ (Fig. 4.5C, 4.6B, 4.7A-C) and is primarily due to a $C_4 \cdots O$ vibration. This mode is upshifted 7 cm^{-1} relative to the corresponding PhQ^- mode. Experimentally an upshift of 15 cm^{-1} is observed. So, again, although the calculations correctly indicate the trend, the magnitude of the calculated shift is considerably smaller than that observed experimentally.

For $2MNQ^-$ the calculated separation between the $C_1 \cdots O$ and $C_4 \cdots O$ modes is ~67 cm^{-1}, close to the experimentally observed 75 cm^{-1}.

For $2ClNQ^-$, an intense mode is calculated at 1512 cm^{-1} (Fig. 4.5D). This mode is predominantly due to a $C_1 \cdots O$ vibration with weaker contributions from $C_4 \cdots O$, $C_2 = C_3$ stretching and CH bending vibrations. This mode is upshifted +17 cm^{-1} relative to the corresponding mode of PhQ^- and is also considerably more intense than the corresponding PhQ^- mode. Both the magnitude of the upshift and the intensity increase are in line with experiment.

For flipped $2ClNQ^-$ the $C_1{\cdots}O$ vibration still upshifts to 1507 cm^{-1} (Fig. 4.5D). In the averaged of the two DDS two peaks are observed at 1511 and 1508 cm^{-1} (Fig. 4.7F). In the experimental DDS a positive band is observed at 1509 with a clear shoulder near 1500 cm^{-1} (Fig. 4.4C). These two peaks observed experimentally, along with the two peaks in the calculated average DDS suggest that 2ClNQ may adopt two orientations in the A_1 binding site. Given the higher intensity of the higher frequency component in the experimental DDS (at 1509 cm^{-1}) and taking into account that the higher frequency mode is calculated using a non-flipped model, the likelihood is that non-flipped 2ClNQ is somewhat favored in the A_1 binding site. In summary, 2ClNQ can adopt two different conformations in the A_1 binding site, perhaps slightly favoring a conformation where the Cl atom is adjacent to the C_1=O group (meta to the H-bonded C_4=O group), as shown in the inset in Fig. 4.5. The (2BrNQ – PhQ) and (2BrNQ – PhQ) DDS are very similar. So, the same conclusions also apply to 2BrNQ incorporated into PSI.

For $2ClNQ^-$ a mode is calculated at 1429 cm^{-1} and is primarily due to a $C_4{\cdots}O$ vibration. This mode is upshifted only 1 cm^{-1} relative to the corresponding mode of PhQ^-. This suggests that these features would cancel in a calculated DDS. Given that the PhQ^- mode has a higher intensity (compare Fig. 4.5A and D) a negative feature is observed near 1430 cm^{-1} in the calculated DDS (Fig. 4.6C). In the experimental (2ClNQ – PhQ) DDS (Fig. 4.4C) one hypothesis is that the negative band at 1414 cm^{-1} corresponds to the weak positive band at 1426 cm^{-1}. This 12 cm^{-1} upshift is considerably larger than the 1 cm^{-1} suggested by calculation. It may be the case that the negative 1414 cm^{-1} band corresponds to the positive band at 1442 cm^{-1} in Fig. 4.4C, so the upshift would be 28 cm^{-1}, even more at odds with the calculated data.

Very interestingly, the calculated spectra for the flipped 2ClNQ model shows a single band at 1439 cm^{-1}. However, this band is due to a predominantly C_2=C_3 vibration. The $C_4 \equiv\!\!\equiv O$ vibration appears near 1433 cm^{-1} but it is now much lower in intensity (Table 4.3).

Again, given the fact that the calculations indicate a $C_4 \equiv\!\!\equiv O$ mode of PhQ^- at 1428 cm^{-1} and not 1414 cm^{-1} is likely to pose problems in any calculation of DDS, and it is probably best to hold off on a detailed analysis of the DDS until more detailed QM/MM calculations have been undertaken.

For $2ClNQ^-$ bands are also calculated at 1461 and 1437 cm^{-1} (Fig. 4.5C). The origin of these bands are listed in Table 4.10 but it is not clear how they may relate to experiment. Again, more detailed QM/MM type models may better simulate these aspects of the experimental spectra. Calculated spectra and assignments for $2BrNQ^-$ are similar to that found and discussed for $2ClNQ^-$. This calculated similarity is also found experimentally.

Calculations for Cl_2 and Br_2NQ^- yield very similar results. There is also a high degree of similarity in the experimental DDS. Below we will discuss Cl_2NQ but recognize a similar discussion also follows for Br_2NQ.

For Cl_2NQ^- and Br_2NQ^- an intense vibrational mode calculated at 1505 cm^{-1} and 1501 cm^{-1}, respectively (Fig. 4.5F and G) and is largely due to an antisymmetric coupled $C \equiv\!\!\equiv O$ vibration (with weak contributions from aromatic CH bending and $C_2 = C_3$ stretching modes) (Table 4.3). So, the $C \equiv\!\!\equiv O$ mode of Cl_2NQ^- and Br_2NQ^- is calculated to be upshifted 6-10 cm^{-1} relative to the corresponding mode of PhQ^-, similar to that for $2MNQ^-$ and 7 cm^{-1} lower than that for $2ClNQ^-$ and $2BrNQ^-$. This ordering in the frequency of the modes for the different quinones is the same as that observed experimentally. Experimentally the frequency of the $C \equiv\!\!\equiv O$ mode in the (Cl_2NQ^- – PhQ^-) DDS is difficult to discern exactly but it is likely around 1505 cm^{-1} (Fig. 4.4E).

For Cl_2NQ^-, a vibrational mode is calculated at 1441 cm^{-1} (Fig. 4.6F) and is mainly a $C_4{\cdots}O$ vibration (with contributions from aromatic CH bending vibrations). So, for Cl_2NQ^- the $C_1{\cdots}O$ and $C_4{\cdots}O$ vibrational modes are calculated to be separated by 64 cm^{-1}. However, this putative $C_4{\cdots}O$ vibration is extremely weak compared to the antisymmetric coupled $C{\cdots}O$ vibration, and the calculations suggest that essentially a single $C{\cdots}O$ mode should be easily observed. This calculated prediction could be in line with experiment given the very weak positive band observed at 1426 cm^{-1} in Fig. 4.4 E,F, which may or may not be due to a $C_4{\cdots}O$ vibration.

This type of behavior, where only a single antisymmetric $C{\cdots}O$ vibration is observed experimentally [56] (and computationally [139, 144, 145]) for a bound semiquinone anion is reminiscent of the situation for plastoquinone (PQ) in the Q_A binding site in PSII. Off course, bound PQ in PSII is an asymmetrically substituted benzoquinone (BQ) in a somewhat symmetric H-bonding environment, and here we have a symmetrically substituted NQ (Cl_2NQ or Br_2NQ) in a distinctly asymmetric H−bonding environment. A more detailed QM/MM analysis of both Cl_2NQ in the A_1 binding site and PQ in the Q_A binding site is required.

Computationally, for $2ClNQ^-$ and $2BrNQ^-$ a pair of bands is calculated at 1437 and 1429 cm^{-1}. However, for Cl_2NQ^- and Br_2NQ^- a single band is calculated at 1441 cm^{-1}. This set of features does appear to be preserved in the experimental DDS, where a broad set of positive features is observed with peaks at 1442 and 1426 cm^{-1} in (2ClNQ – PhQ) and (2BrNQ – PhQ) DDS and a predominantly single feature at 1445 cm^{-1} is observed in (Cl_2NQ – PhQ) and (Br_2NQ – PhQ) DDS. This comparison/agreement between calculated and experimental features in four different DDS suggests some validity to the computational approach and the associated calculated normal mode compositions. It is worth noting that such features might also be suggested in calculations using the simpler models, except the two clear bands at 1437 and 1429 cm^{-1} in Fig.

4.5D, E merge into a single broad feature near 1438 cm^{-1} when the (Q^{-}+H_2O) model is used (Fig. 4.9).

4.5 Conclusions

Here we present time resolved FTIR DS and DDS obtained using PSI samples with a series of halogenated NQs incorporated. Comparing these DS and DDS to other previously published DDS, and also by considering corresponding calculated DDS we were able to assess the normal modes of the halogenated NQs in PSI, and from that make inferences on the orientation of the incorporated monosubstituted halogenated NQs in the A_1 binding site.

In this study, we identified two new bands for PhQ^{-} in the anion region (~1520 and ~1456 cm^{-1}). We also identified several bands for the incorporated halogenated NQs for the first time.

For the two mono-substituted halogenated NQs, $2ClNQ^{-}$/$2BrNQ^{-}$, the $C_1{=}O$ vibrational mode appears to contain contributions from two species, which via calculation we suggest is two different orientations for the incorporated NQs. Thus, the Cl or Br atom of the mono-substituted NQs appears not to have a specific preference for being meta or ortho to the H bonded C=O group.

For PSI with all the five NQs (PhQ^{-}, $DMNQ^{-}$, $2MNQ^{-}$, $2ClNQ^{-}$, $2BrNQ^{-}$, Br_2NQ^{-}) incorporated the frequency and intensity of the $C_1{=}O$ mode follows the same pattern in both the experimental and calculated spectra.

From the anion state, it was observed that $C_1{=}O$ and $C_4{=}O$ modes are separated by ~ 76 (±7 cm^{-1}) for all the five NQs which is reduced to ~63 (±3 cm^{-1}) for the two di-substituted halogenated NQs. For neutral PhQ in PSI the C_1=O and C_4=O modes are separated by ~30 cm^{-1}. The reduced frequency separation might indicate that the H-bonding is stronger in the anion state.

Supplementary Information

Time-Resolved Infrared Spectroscopy for the Study of Photosystem I with High Potential Naphthoquinones Incorporated into the A_1 Binding Site

4.S1 Calculated spectra for isolated semiquinones in THF

Calculated spectra for the different NQs in THF are shown in Fig. 4.8. Normal mode assignments are listed in Table 4.1.

For PhQ^- (Fig. 4.8A), the most intense band appears at 1495 cm^{-1}. This band is primarily due to $C_4{=}O$ stretching and methyl CH bending vibrations [$\nu(C_4{=}O)$, 32% + $\delta(CH_2)_{methyl}$, 11%]. For PhQ^- there is also a band at 1492 cm^{-1} appearing as a shoulder which is not visible in the spectra in Fig. 4.8A. This 1492 cm^{-1} mode is due to [$\nu(C_1{=}O)$, 27% + $\delta(CH_2)_{tail}$, 11%].

For $DMNQ^-$ (Fig. 4.8B), the corresponding band is at 1495 cm^{-1} and is due to [$\nu(C{=}O)$, 11% + $\delta(CH_2)_{methyl}$, 11%]. The shoulder at 1482 cm^{-1} is due to [$\delta(CH_2)_{methyl}$, 23%]. For $2MNQ^-$ the corresponding band is at 1505 cm^{-1} and is due to the antisymmetric coupled vibration of both $C{=}O$ groups and C_1-C_2 stretching [$\nu(C_1{=}O)$, 19% + $\nu(C_4{=}O)$, 12%+ $\nu(C_1\text{-}C_2)$, 10%] in Fig. 4.8C. For $2ClNQ^-$/$2BrNQ^-$ (Fig. 4.2 D/E), an intense band is calculated at 1510/1511 cm^{-1} and is also due to the antisymmetric coupled vibration of both $C{=}O$ groups [$\nu(C_1{=}O)$, 35% + $\nu(C_4{=}O)$, 17%/18%]. For both Cl_2NQ^- and Br_2NQ^- (Fig. 4.8 F/G), an intense band is calculated at 1509-/1509 cm^{-1} and is also due to antisymmetric coupled vibration of both $C{=}O$ groups [ν ($C_1{=}O$), 33% + ν ($C_4{=}O$), 33%]$_{AS}$.

For both PhQ^- and $DMNQ^-$, a similar set of features are observed in the 1460-1449 cm^{-1} region where two bands are visible at 1455 ($\pm$1) and 1447-1445 cm^{-1}. The former is due to [$\nu(C_4{=}O)$, 12% + $\delta(HCC)_a$, 19%] for PhQ- and [$\nu(C{=}O)$, 14% + δ(HCC)a, 15%] for $DMNQ^-$, respectively. The later band is due to [$\nu(C_4{=}O)$, 11% + $\delta(CH_2)_{methyl}$, 16% + $\delta(CH_2)_{tail}$, 12%] for

PhQ^- and [$\nu(C_2{=}C_3)$, 15% + $\delta(CH_2)_{methyl}$, 26%] for $DMNQ^-$. For the other quinones, this pair of bands merge into one band in the 1459-1449 cm^{-1} region. The intensity is highest for $2MNQ^-$ (Fig. 4.8 C) and is low for Cl_2NQ^- and Br_2NQ^-. For $2MNQ^-$, the 1448 cm^{-1} band is due to the antisymmetric coupled vibration of both C=O groups [$\nu(C_1{=}O)$, 16% + $\nu(C_4{=}O)$, 17%]. For both $2ClNQ^-$/$2BrNQ^-$ it appears at 1455 ($\pm$1) cm^{-1} which is due to [δ(HCC)a, 32%] and similarly, for Cl_2NQ^-/Br_2NQ^-, it appears at the same location at 1459 ($\pm$1) cm^{-1},due to [ν(C=C), 10% and δ(HCC)a, 33%].

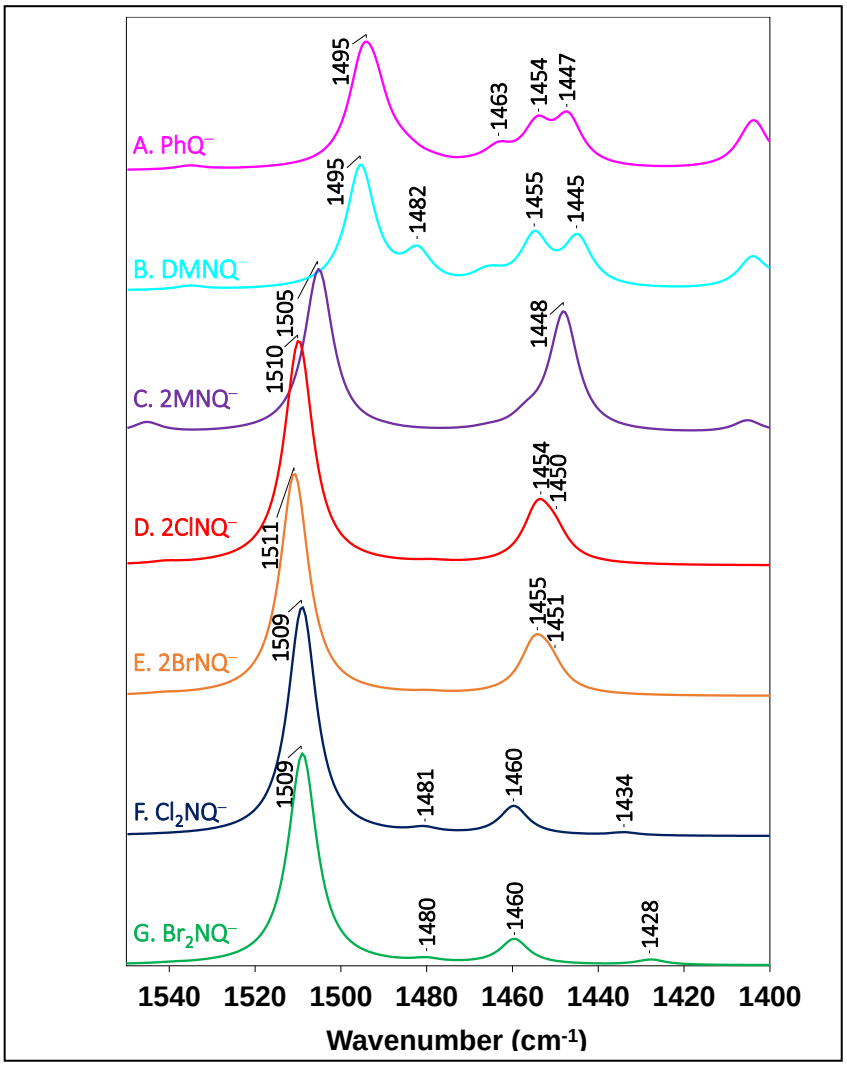

Figure 4.8 Calculated spectra for (A) PhQ^- (pink), (B) $DMNQ^-$ (light blue), (C) $2MNQ^-$ (purple), (D) $2ClNQ^-$ (red), (E) $2BrNQ^-$ (orange), (F) Cl_2NQ^- (blue), and (G) Br_2NQ^- (green) in THF.

Calculated frequencies are scaled by 0.9847 [56, 65, 83, 84, 132]. Spectral range: 1550-1400 cm^{-1}.

Table 4.1 Calculated harmonic normal mode vibrational frequencies (in cm^{-1}) and intensities (in km/mol) of PhQ^-, $DMNQ^-$, $2MNQ^-$, $2ClNQ^-$, $2BrNQ^-$, Cl_2NQ^-, and Br_2NQ^- in THF. Mode assignments and associated potential energy distributions (PEDs) (in % in parenthesis) are listed and were calculated using VEDA software [85]. Calculated frequencies were scaled by 0.9847.

Abbreviations: ν, bond stretching; δ, bending vibration; a, aromatic ring; q, quinone ring; m, methyl; t, phytyl tail, AS, antisymmetric; S, symmetric; H*, Hydrogen atom is at C_3 for $2ClNQ^-$and $2BrNQ^-$.

Quinone	ν Calc. Freq. (Int.)	Mode (PED)
PhQ^-	1495 (461)	$\nu(C_4{=}O)$ (32)+$\delta(CH_2)_m$ (11)
	1492 (263)	$\nu(C_1{=}O)$ (27)+$\delta(CH_2)_t$ (11)
	1463 (84)	$\nu(C_1{=}O)$ (17)+$\delta(CH_2)_t$ (14)
	1454 (200)	$\nu(C_4{=}O)$ (12)+$\delta(HCC)_a$ (19)
	1447 (242)	$\nu(C_4{=}O)$ (11)+$\delta(CH_2)_m$ (16)+$\delta(CH_2)_t$ (12)
$DMNQ^-$	1495 (605)	$\nu(C{=}O)$ (11)+$\delta(CH_2)_m$(11)
	1482 (167)	$\delta(CH_2)_m$ (23)
	1455 (254)	$\nu(C{=}O)$ (14)+$\delta(HCC)_a$ (15)
	1445 (264)	$\nu(C_2 - C_3)$ (15)+$\delta(CH_2)_m$ (26)
$2MNQ^-$	1505 (840)	$[\nu(C_1{=}O)$ (19)+$\nu(C_4{=}O)$ (12)$]_{AS}$+$\nu(C_1 - C_2)$ (10)
	1448 (613)	$[\nu(C_1{=}O)$ (16)+$\nu(C_4{=}O)$ (17)$]_{AS}$
$2ClNQ^-$	1510 (1150)	$[\nu(C_1{=}O)$ (35)+$\nu(C_4{=}O)$ (17)$]_{AS}$
	1454 (267)	$\delta(HCC)_a$ (32)
	1450 (127)	$\nu(C_4{=}O)$ (17)+$\nu(C_2{=}C_3)$ (23)+$\delta(HCC)_a$ (14)
$2BrNQ^-$	1511 (1138)	$[\nu(C_1{=}O)$ (35)+$\nu(C_4{=}O)$ (18)$]_{AS}$
	1455 (234)	$\delta(HCC)_a$ (32)
	1451 (131)	$\nu(C_4{=}O)$ (18)+$\nu(C_2{=}C_3)$ (27)+$\delta(HCC)_a$ (13)
Cl_2NQ^-	1509 (1171)	$[\nu(C_1{=}O)$ (33)+$\nu(C_4{=}O)$ (33)$]_{AS}$
	1481 (25)	$\nu(C_1{=}O)$ (12)+$\nu(C_4{=}O)$ (192)+$\nu(C_2{=}C_3)$ (12)+$\delta(HCC)_a$ (33)
	1460 (148)	$\nu(C{=}C)_a$ (10)+$\delta(HCC)_a$ (33)
	1434 (15)	$\nu(C_2{=}C_3)$ (56)
Br_2NQ^-	1509 (1084)	$[\nu(C_1{=}O)$ (33)+$\nu(C_4{=}O)$ (33)$]_{AS}$
	1480 (18)	$\nu(C_1{=}O)$ (11)+$\nu(C_4{=}O)$ (12)+$\delta(HCC)_a$ (33)
	1460 (129)	$\nu(C{=}C)_a$ (10)+$\delta(HCC)_a$ (33)
	1428 (27)	$\nu(C_2{=}C_3)$ (60)

4.S2 Calculated spectra for semiquinones obtained using the $Q^- + H_2O$ model

Calculated spectra for the different NQs H-bonded to a water molecule are shown in Fig. 4.9. Normal mode assignments are listed in Table 4.2. Inset in Fig. 4.9 shows the molecular model

for 2ClNQ. In this model the Cl atom is meta to the H-bonded C=O group (called the C_4=O group in the main manuscript).

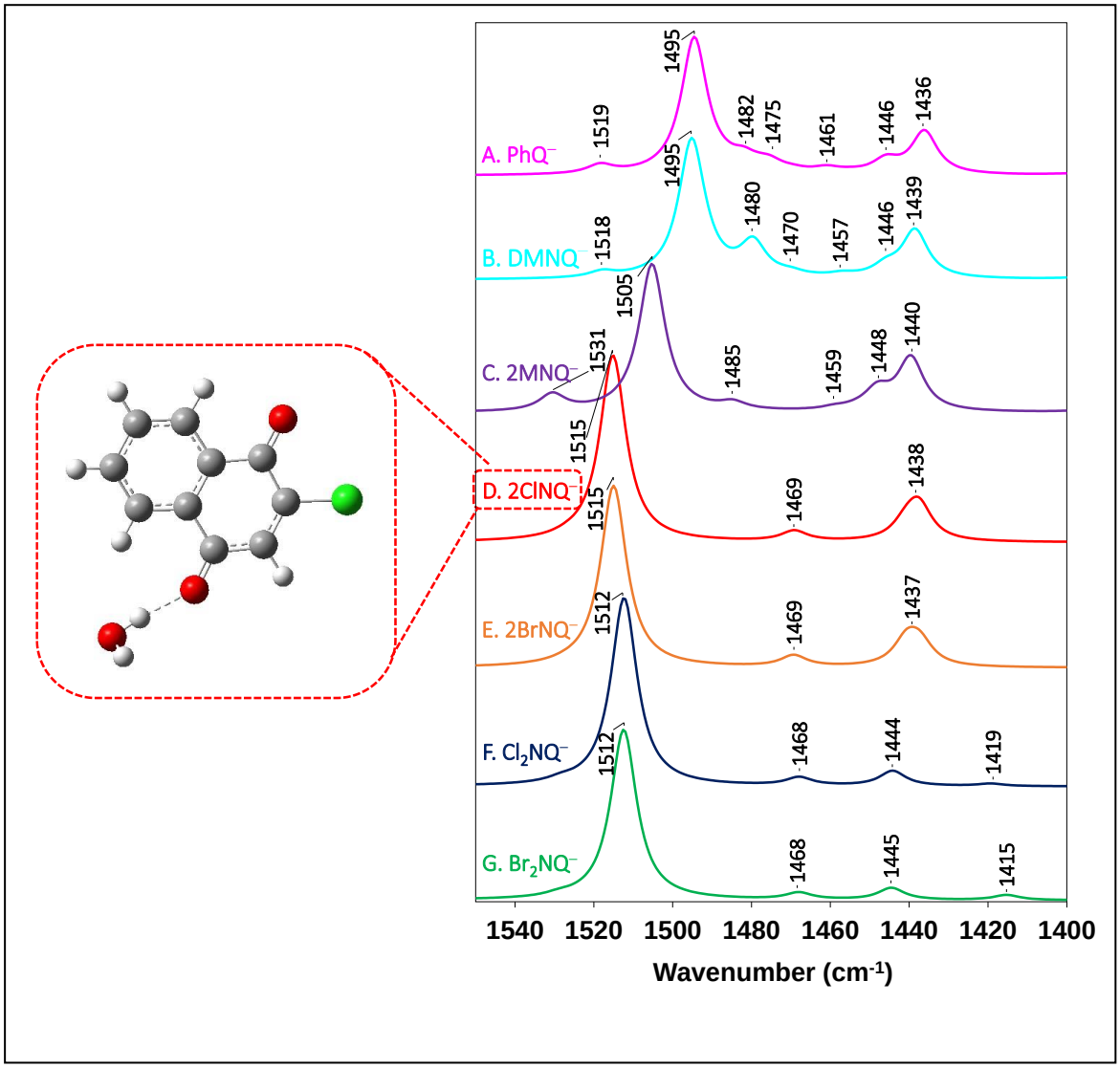

Figure 4.9 Calculated spectra for (A) PhQ^-, (B) $DMNQ^-$, (C) $2MNQ^-$, (D) $2ClNQ^-$, (E) $2BrNQ^-$, (F) Cl_2NQ^-, and (G) Br_2NQ^- obtained using the $Q^- + H_2O$ model. Calculated frequencies are scaled by 0.974. Molecular model shown in the inset.

Table 4.2 Calculated vibrational mode frequencies of PhQ^-, $DMNQ^-$, $2MNQ^-$, $2ClNQ^-$, $2BrNQ^-$, Cl_2NQ^-, and Br_2NQ^- obtained using the $Q^- + H_2O$ model. Frequencies are in cm^{-1}. Intensities in km/mol are listed in parentheses. Calculated frequencies were scaled by 0.974.

Abbreviations: v, bond stretching; *δ*, bending vibration; *a*, aromatic ring; *q*, quinone ring; m, methyl; t, phytyl tail, *AS*, antisymmetric; *S*, symmetric; H*, Hydrogen atom is at C_3 for $2ClNQ^-$ and $2BrNQ^-$.

Quinone	ν Calc. Freq. (Int.)	Mode
PhQ$^-$	1519 (29)	$\nu(C_2{=}C_3)+\delta(CH)_a$
	1495 (457)	$\nu(C_1{=}O)+\delta(CH)_a$
	1482 (39)	$\delta(CH)_m+\nu(C_4{=}O)$
	1475 (26)	$\delta(CH)_t$ (mainly)$+\delta(CH)_m+\nu(C_4{=}O)$
	1461 (15)	$\delta(CH)_m+\nu(C_4{=}O)$
	1446 (44)	$\delta(CH)_a+\delta(CH)_t$
	1436 (144)	$\delta(CH)+\nu(C_4{=}O)$
DMNQ$^-$	1518 (19)	$\nu(C_2{=}C_3)+\delta(CH)_a$
	1495 (457)	$\nu(C_1{=}O)+\delta(CH)_a$
	1480 (112)	$\delta(CH)_m$ attached to $C_2+\nu(C_4{=}O)$
	1470 (12)	$\delta(CH)_m$ attached to both C_2 & C_3
	1457 (10)	$\delta(CH)_m$ attached to both $C_2+\nu(C_4{=}O)$
	1446 (34)	$\delta(CH)_a+\delta(CH)_m$ attached to C_3
	1439 (161)	$\delta(CH)+\nu(C_4{=}O)$
2MNQ$^-$	1531 (56)	$\nu(C_2{=}C_3)+\delta(CH)_a$
	1505 (496)	$\nu(C_1{=}O)+\delta(CH)_a$
	1485 (24)	$\delta(CH)_m$ attached to $C_2+\nu(C_4{=}O)$
	1459 (8)	$\delta(CH)$
	1448 (69)	$\delta(CH)$
	1440 (178)	$\delta(CH)_a+\nu(C_4{=}O)$
2ClNQ$^-$	1515 (627)	$[\nu(C_1{=}O)+\nu(C_4{=}O)]_{AS}+\nu(C_2{=}C_3)$
	1469 (34)	$[\nu(C_1{=}O)+\nu(C_4{=}O)]_S+\nu(C_2{=}C_3)+\delta(CH)_a$
	1441 (52)	$\nu(C_2{=}C_3)+\delta(CH)_a$
	1438 (119)	$\nu(C_2{=}C_3)+\delta(CH)_a+\nu(C_4{=}O)$
2BrNQ$^-$	1515 (610)	$[\nu(C_1{=}O)+\nu(C_4{=}O)]_{AS}+\nu(C_2{=}C_3)$
	1469 (37)	$[\nu(C_1{=}O)+\nu(C_4{=}O)]_S+\nu(C_2{=}C_3)+\delta(CH)_a$
	1441 (86)	$\nu(C_2{=}C_3)+\delta(CH)_a$
	1437 (73)	$\nu(C_2{=}C_3)+\delta(CH)_a+\nu(C_4{=}O)$
Cl$_2$NQ$^-$	1512 (633)	$[\nu(C_1{=}O)+\nu(C_4{=}O)]_{AS}+\nu(C_2{=}C_3)+\delta(CH)_a$
	1468 (27)	$[\nu(C_1{=}O)+\nu(C_4{=}O)]_S+\nu(C_2{=}C_3)+\delta(CH)_a$
	1444 (51)	$\delta(CH)_a$
	1419 (8)	$\nu(C_2{=}C_3)+\delta(CH)_a$
Br$_2$NQ$^-$	1512 (572)	$[\nu(C_1{=}O)+\nu(C_4{=}O)]_{AS}+\nu(C_2{=}C_3)+\delta(CH)_a$
	1468 (23)	$[\nu(C_1{=}O)+\nu(C_4{=}O)]_S+\nu(C_2{=}C_3)+\delta(CH)_a$
	1445 (40)	$\delta(CH)_a$
	1415 (17)	$\nu(C_2{=}C_3)+\delta(CH)_a$

4.S3 Calculated spectra of semiquinones using the Q$^-$ +Leu model (model m2)

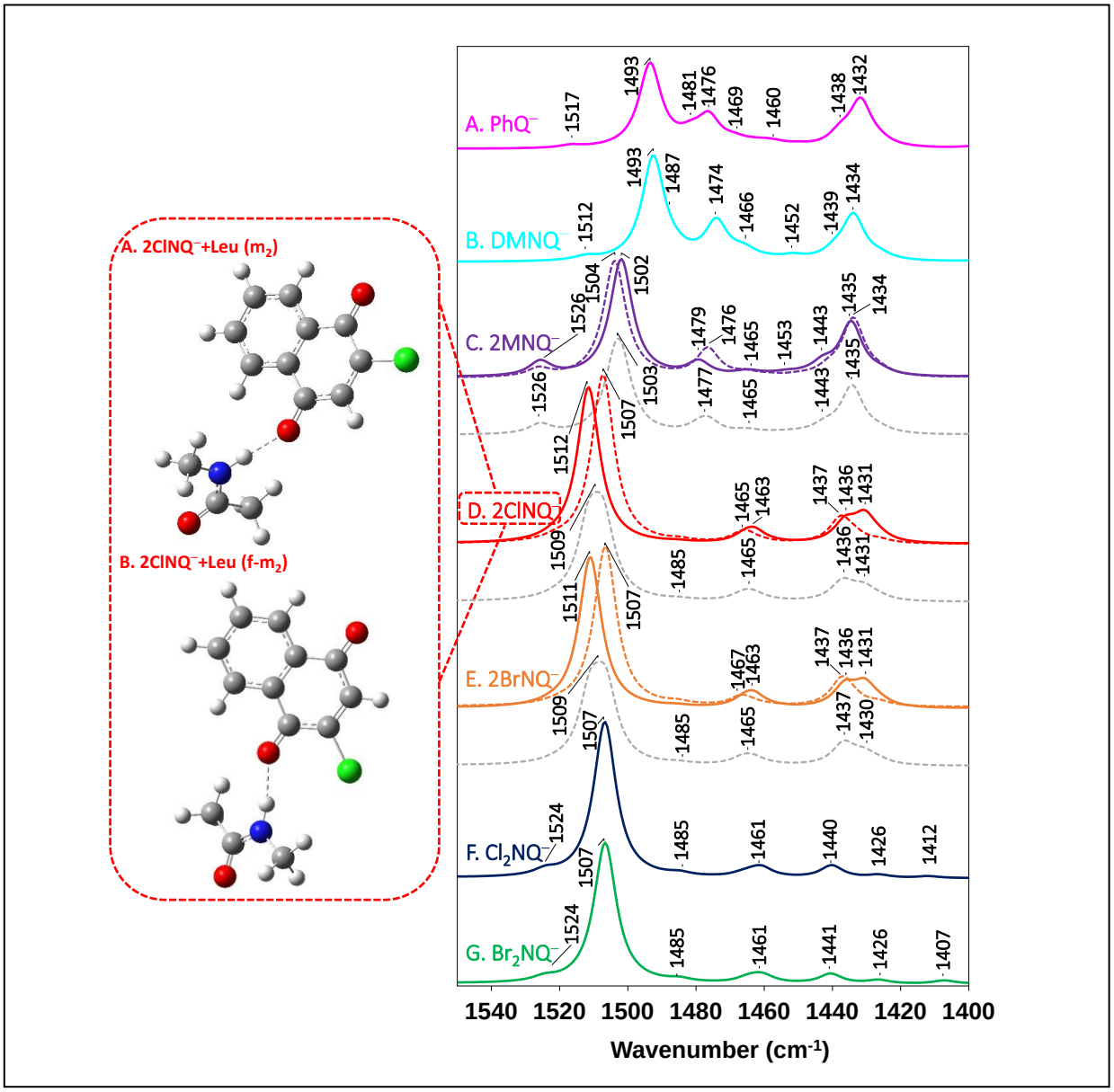

Figure 4.10 Calculated spectra for (A) PhQ^-, (B) $DMNQ^-$, (C) $2MNQ^-$, (D) $2ClNQ^-$, (E) $2BrNQ^-$, (F) Cl_2NQ^-, and (G) Br_2NQ^- obtained using the Q^- +Leu model 2 (m_2). Molecular model for 2ClNQ is shown in A in the inset. In B in the inset the molecular model for the flipped quinone is shown [Q^-+Leu (f-m_2)] the spectra for this flipped model are shown as dotted lines. The average of the spectra for the flipped and non-flipped models is shown in grey dotted lines. Calculated frequencies are scaled by 0.971.

Table 4.3 Calculated vibrational frequencies of PhQ^-, $DMNQ^-$, $2MNQ^-$, $2ClNQ^-$, $2BrNQ^-$, Cl_2NQ^-, and Br_2NQ^- in the Q^- +Leu (m_1, m_2 and f-m_2) models. Frequencies are in cm^{-1}. Intensities in km/mol are listed in parentheses. Calculated frequencies were scaled by a scaling factor of 0.971.

Abbreviations: v, bond stretching; *δ*, bending vibration; *a*, aromatic ring; *q*, quinone ring;

m, methyl; t, phytyl tail, *AS*, antisymmetric; *S*, symmetric; H*, Hydrogen atom is at C_3 for $2ClNQ^-$ and $2BrNQ^-$.

Quinone	ν Calc. Freq. of Q^-+Leu (m_1) (Int.)	ν Calc. Freq. of Q^-+Leu (m_2) (Int.)	ν Calc. Freq. of Q^-+Leu (f-m_1) (Int.)	ν Calc. Freq. of Q^-+Leu (f-m_2) (Int.)	Exp.	Mode
PhQ^-	1517 (9)	1517 (12)			1520 [1517–1522]	$\nu(C_2{=}C_3)+\delta(CH)_{all}$
	1495 (378)	1493 (396)			1494	$[\nu(C_1{=}O)(mainly)+\nu(C_4{=}O)]_{AS}+\delta(CH)_a$
	1476 (98)	1476 (132)			1476	$\delta(CH)_m$ (mainly)+$\nu(C_4{=}O)$
	1459 (27)	1460 (15)			1456 [1454–1459]	$\delta(CH)_{all}$
	1428 (282)	1432 (218)			1414	$\nu(C_4{=}O)+\delta(CH)_{all}$
$DMNQ^-$	1513 (11)	1512 (17)			1526	$\nu(C_2{=}C_3)+\delta(CH)_{all}$
	1494 (470)	1493 (491)			1494	$[\nu(C_1{=}O)(mainly)+\nu(C_4{=}O)]_{AS}+\delta(CH)_{all}$
	1474 (105)	1474 (177)			1474	$\delta(CH)_m$ attached to C_2 (mainly)+$\nu(C_4{=}O)$
	1451 (30)	1452 (18)			1456	$\delta(CH)_m$ attached to both C_2 (mainly) +$\nu(C_4{=}O)$
	1434 (290)	1434 (214)			1425	$\nu(C_4{=}O)+\delta(CH)_{all}$
$2MNQ^-$	1526 (100)	1526 (68)	1527 (34)	1526 (38)	1528	$\nu(C_2{=}C_3)+\delta(CH)_{all}$
	1502 (526)	1502 (557)	1505 (556)	1504 (551)	1504	$[\nu(C_1{=}O)(mainly)+\nu(C_4{=}O)]_{AS}+\delta(CH)_{all}$
	1476 (43)	1479 (66)	1475 (112)	1476 (132)	1483	$\delta(CH)_m$ (mainly)+$[\nu(C_1{=}O)+\nu(C_4{=}O)]_S$
	1452(8)	1453 (12)	1452 (6)	1452 (8)	1471	$\delta(CH)_m$ (mainly)+$\delta(CH)_a$
	1435 (313)	1435 (253)	1434 (345)	1435 (273)	1429	$\nu(C_4{=}O)+\delta(CH)_{all}$
$2ClNQ^-$	1524 (14)	1522 (9)	1522 (21)	1521 (12)	1528	$\nu(C_2{=}C_3)+\delta(CH)_{all}+[\nu(C_1{=}O)+\nu(C_4{=}O)]_S$
	1512 (781)	1512 (740)	1507 (790)	1507 (791)	1509	$[\nu(C_1{=}O)(mainly)+\nu(C_4{=}O)]_{AS}+$ $\nu(C_2{=}C_3)+\delta(CH)_{all}$
	1461(82)	1463 (32) + 1463 (25)	1464 (88)	1465 (39)	1483	$\delta(CH)_a+[\nu(C_1{=}O)+\nu(C_4{=}O)]_S+\nu(C_2{=}C_3)$
	1437 (118)	1436 (91)	1439 (124)	1437 (118)	1442/1464	$\delta(CH)_a$ (mainly)+ $\nu(C_2{=}C_3)$
	1429 (149)	1431 (121)	1433 (32)	1434 (25)	1426	$\nu(C_4{=}O)+\delta(CH)_{all}+\nu(C_2{=}C_3)$
$2BrNQ^-$	1524 (8)	1522 (7)	1522 (18)	1520 (8)	1528	$\nu(C_2{=}C_3)+\delta(CH)_{all}+[\nu(C_1{=}O)+\nu(C_4{=}O)]_S$
	1512 (780)	1511 (715)	1507 (715)	1507 (767)	1509	$[\nu(C_1{=}O)(mainly)+\nu(C_4{=}O)]_{AS}$ $+\nu(C_2{=}C_3)+\delta(CH)_{all}$
	1461(89)	1466 (29) + 1463 (52)	1463 (70)	1467 (38)	1483	$\delta(CH)_a+[\nu(C_1{=}O)+\nu(C_4{=}O)]_S+\nu(C_2{=}C_3)$
	1437 (120)	1436 (97)	1439 (104)	1437 (130)	1442/1464	$\delta(CH)_a$ (mainly)+$\nu(C_2{=}C_3)$
	1429 (128)	1431 (102)	1432 (34)	1434 (22)	1426	$\nu(C_4{=}O)+\delta(CH)_{all}+\nu(C_2{=}C_3)$
Cl_2NQ^-	1525 (51)	1524 (25)			1528	$[\nu(C_1{=}O)$ (mainly)+$\nu(C_4{=}O)]_S+\delta(CH)_a$
	1505 (731)	1507 (737)			1509+1499	$[\nu(C_1{=}O)+\nu(C_4{=}O)]_{AS}$ (mainly) +$\delta(CH)_a+\nu(C_2{=}C_3)$
	1460 (79)	1461 (36)			1484/1467	$\delta(CH)_a$ (mainly)+$\nu(C_4{=}O)+\nu(C_2{=}C_3)$
	1441 (72)	1440 (58)			1445	$\delta(CH)_a+\nu(C_4{=}O)$
Br_2NQ^-	1522 (37)	1524 (20)			1528	$[\nu(C_1{=}O)$ (mainly)+$\nu(C_4{=}O)]_S+\delta(CH)_a$
	1501 (646)	1507 (667)			1504	$[\nu(C_1{=}O)+\nu(C_4{=}O)]_{AS}+\delta(CH)_a+$ $\nu(C_2{=}C_3)$
	1458 (64)	1461 (31)			1488/1462	$\delta(CH)_a$ (mainly)+$\nu(C_4{=}O)+\nu(C_2{=}C_3)$
	1440 (67)	1441 (46)			1445	$\delta(CH)_a+\nu(C_4{=}O)$

Table 4.4 Calculated vibrational frequencies associated with the **C=O** modes of PhQ^-, $DMNQ^-$, $2MNQ^-$, $2ClNQ^-$, $2BrNQ^-$, Cl_2NQ^-, and Br_2NQ^- in the THF, Q+H_2O model, and Q + Leu (m_1, m_2 and m_2 flipped) models. The term "Leu" refers to vibrational modes associated with molecular bonds of the amino acid. Frequencies are in cm^{-1}. Intensities in km/mol are listed in parentheses. Calculated frequencies were scaled by a scaling factor of 0.9847/0.974/0.971 [56, 65, 83, 84, 132] for Q in THF/Q+H_2O/Q+Leu in anion region. *Abbreviations: AS*, antisymmetric.

Quinones	$\nu(C_1{=}O)$ Calculated					$C_1{=}O$ EXP (PSI)	$\nu(C_4{=}O)$ Calculated					$C_4{=}O$ EXP (PSI)
	THF (PED%) (int)	Q+H_2O (int)	Q+Leu (m_1) (int)	Q+Leu (m_2) (int)	Q+Leu (f-m_2) (int)		THF (PED%) (int)	Q+H_2O (int)	Q+Leu (m_1) (int)	Q+Leu (m_2) (int)	Q+Leu (f-m_2) (int)	
PhQ^-	1482[2] (27%) (263)	1495[1] (457)	1495[1] $(378)_{AS}$	1493 $(396)_{AS}$	-	1494[2]	1437 (11%) (242)	1436[1] (144)	1428[1] (282)	1432[1] (218)	-	1414[2]
$DMNQ^-$	1485[2] (11%)(605)	1495 (457)	1494 $(470)_{AS}$	1493 $(491)_{AS}$	-	1494[2]	1445 (14%)(254)	1439 (161)	1434 (290)	1434 (214)	-	1425
$2MNQ^-$	1495 (19%)$(840)_{AS}$	1505 (496)	1502[1] $(526)_{AS}$	1502[1] $(557)_{AS}$	1504 $(551)_{AS}$	1504[2]	1438 (17%)$(613)_{AS}$	1440 (178)	1435[1] (313)	1435[1] (253)	1435 (273)	1429[2]
$2ClNQ^-$	1500 (35%) $(1150)_{AS}$	1515 $(627)_{AS}$	1512 $(781)_{AS}$	1512 $(740)_{AS}$	1507 $(791)_{AS}$	1509[2]	1440 (17%)(127)	1438 (119)	1429 (149)	1431 (121)	1434 (25)	1426
$2BrNQ^-$	1501 (35%)$(1138)_{AS}$	1515 $(610)_{AS}$	1512 $(780)_{AS}$	1511 $(715)_{AS}$	1507 $(767)_{AS}$	1509	1441 (18%)(131)	1437 (73)	1429 (128)	1431 (102)	1434 (22)	1426
Cl_2NQ^-	1499 (33%)$(1171)_{AS}$	1512 $(633)_{AS}$	1505 $(731)_{AS}$	1507 $(737)_{AS}$	-	1499 & 1509 (Split into two)	1450 (8%)(148)	1444 (51)	1441 (72)	1440 (58)	-	1445
Br_2NQ^-	1499 (33%)$(1084)_{AS}$	1512 $(572)_{AS}$	1501 $(646)_{AS}$	1507 $(667)_{AS}$	-	1504	1449 (8%)(129)	1445 (40)	1440 (67)	1441 (46)	-	1445

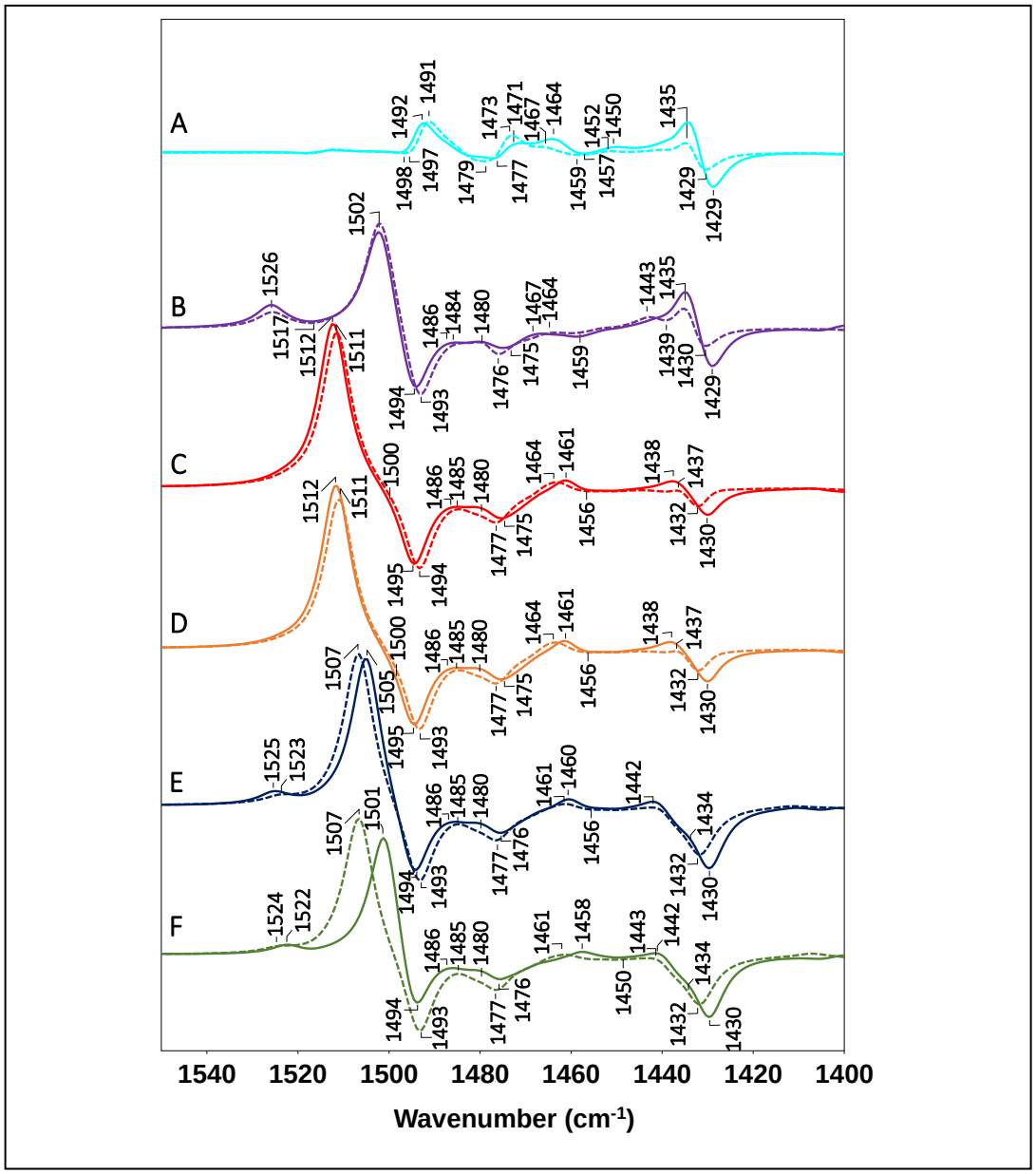

Figure 4.11 Double difference spectra (DDS) constructed by subtracting the calculated spectra for PhQ^{-}+Leu with the indicated quinone. (A) (DMNQ − PhQ), (B) (2MNQ − PhQ), (C) (2ClNQ − PhQ), (D) (2BrNQ − PhQ), (E) (Cl_2NQ − PhQ) and (F) (Br_2NQ − PhQ) in the Q^{-} +Leu model 1 (m_1) (*solid*), Q^{-} +Leu model 2 (m_2) (*dotted*). Calculated frequencies are scaled by 0.971.

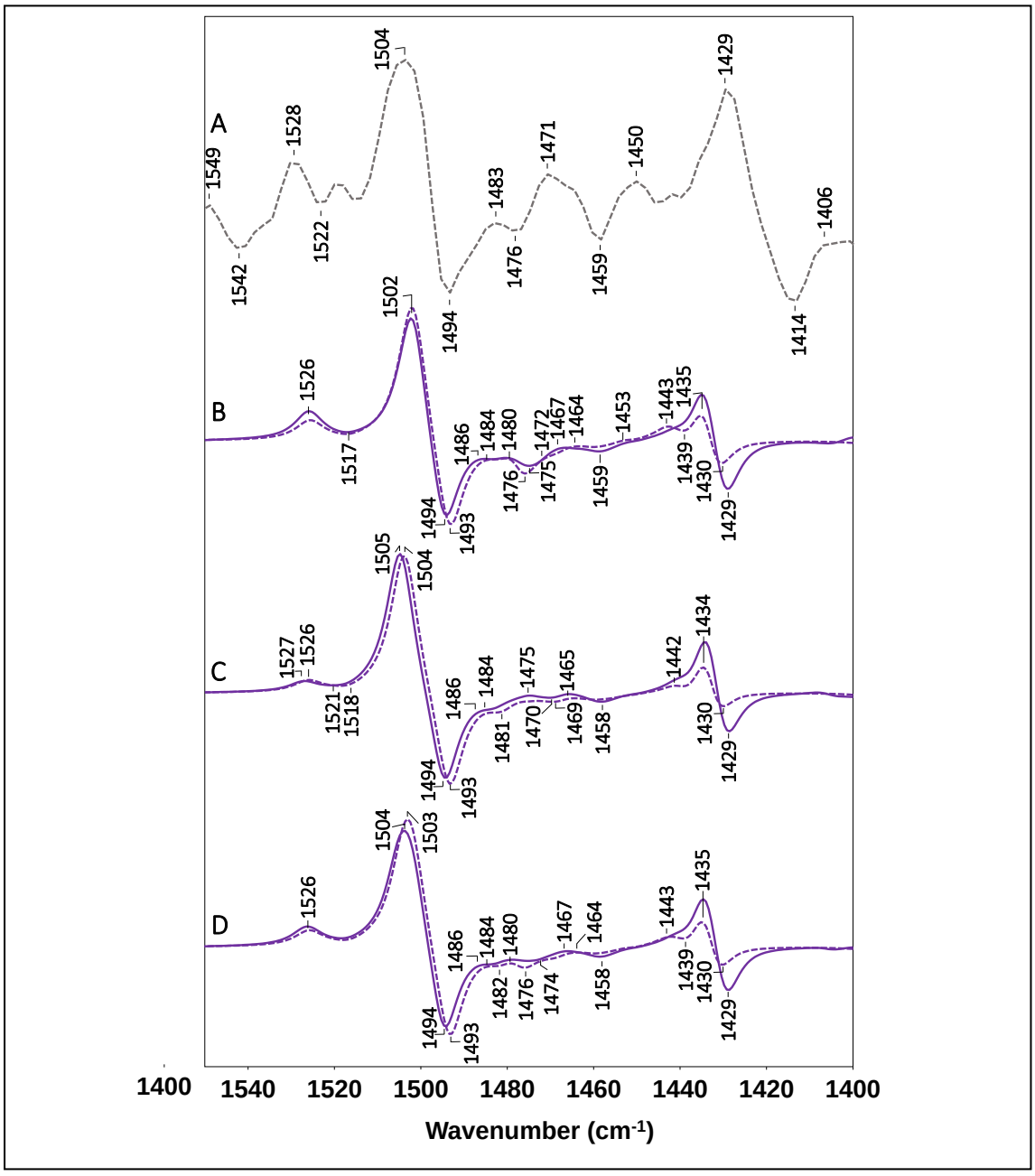

Figure 4.12 Double difference spectra (DDS) for (2MNQ − PhQ) in the 1550−1400 cm^{-1} region. A. Experimental DDS (see Fig. 4.4 in the main manuscript), B. Calculated DDS from Q^- + Leu model 1 (m_1) (*solid*), Q^- + Leu model 2 (m_2) (*dotted*), C. Calculated DDS from Q^- + Leu flipped model 1 (f-m_1) (*solid*), Q^- +Leu flipped model 2 (f-m_2) (*dotted*), and D. Calculated DDS from Q^- + Leu average of m_1 and f-m_1 (*solid*), Q^- + Leu average of m_2 and f-m_2 (*dotted*). Calculated frequencies are scaled by 0.971.

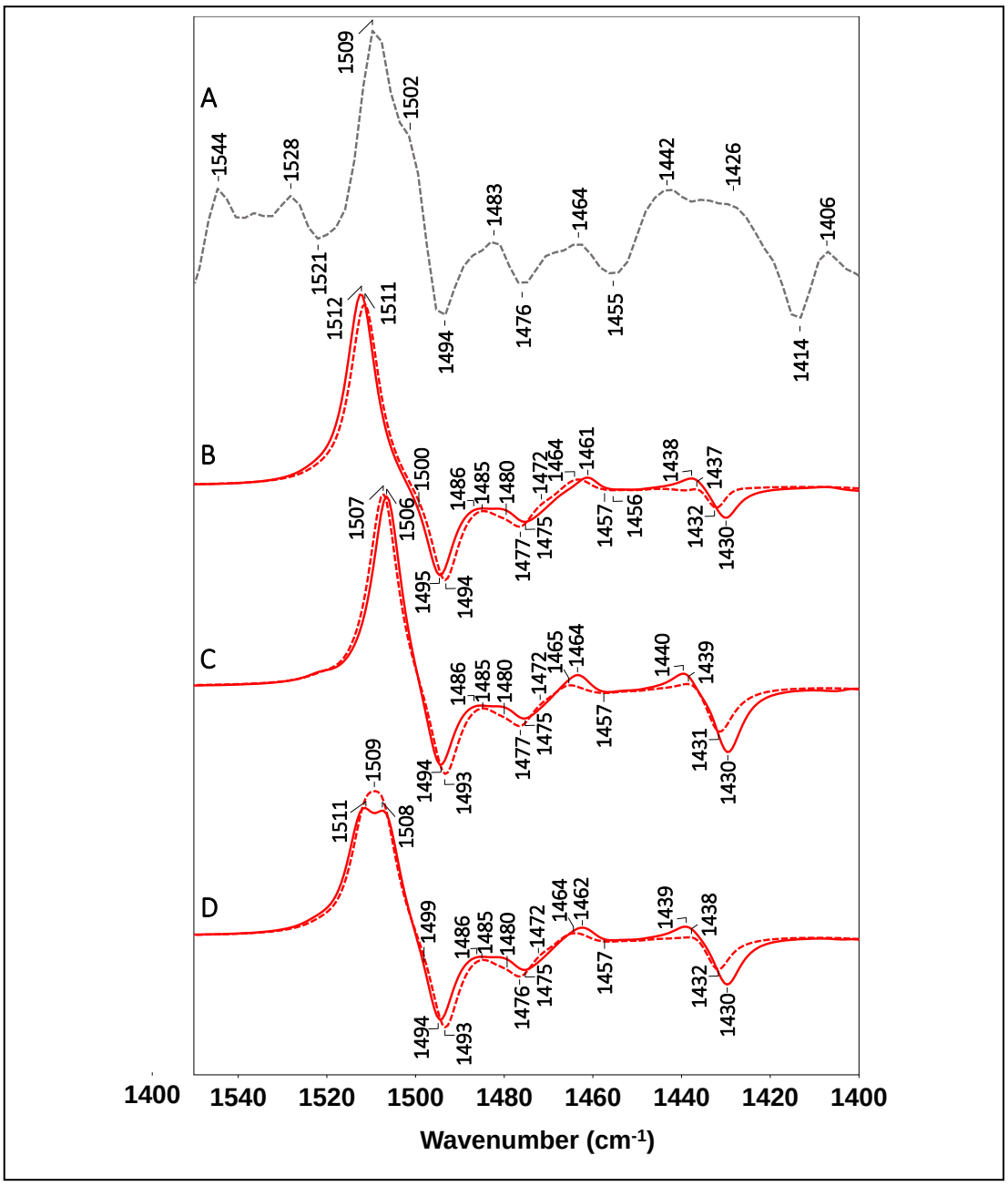

Figure 4.13 Double difference spectra (DDS) for (2ClNQ − PhQ) in the 1550−1400 cm^{-1} region. A. Experimental DDS (see Fig. 4.4 in the main manuscript with the propagated standard error), B. Calculated DDS from Q^-+Leu model 1 (m_1) (*solid*), Q^-+Leu model 2 (m_2) (*dotted*), C. Calculated DDS from Q^-+Leu flipped model 1 (f-m_1) (*solid*), Q^-+Leu flipped model 2 (f-m_2) (*dotted*), and D. Calculated DDS from Q^-+Leu average of m_1 and f-m_1 (*solid*), Q^-+Leu average of m_2 and f-m_2 (*dotted*). Calculated frequencies are scaled by 0.971.

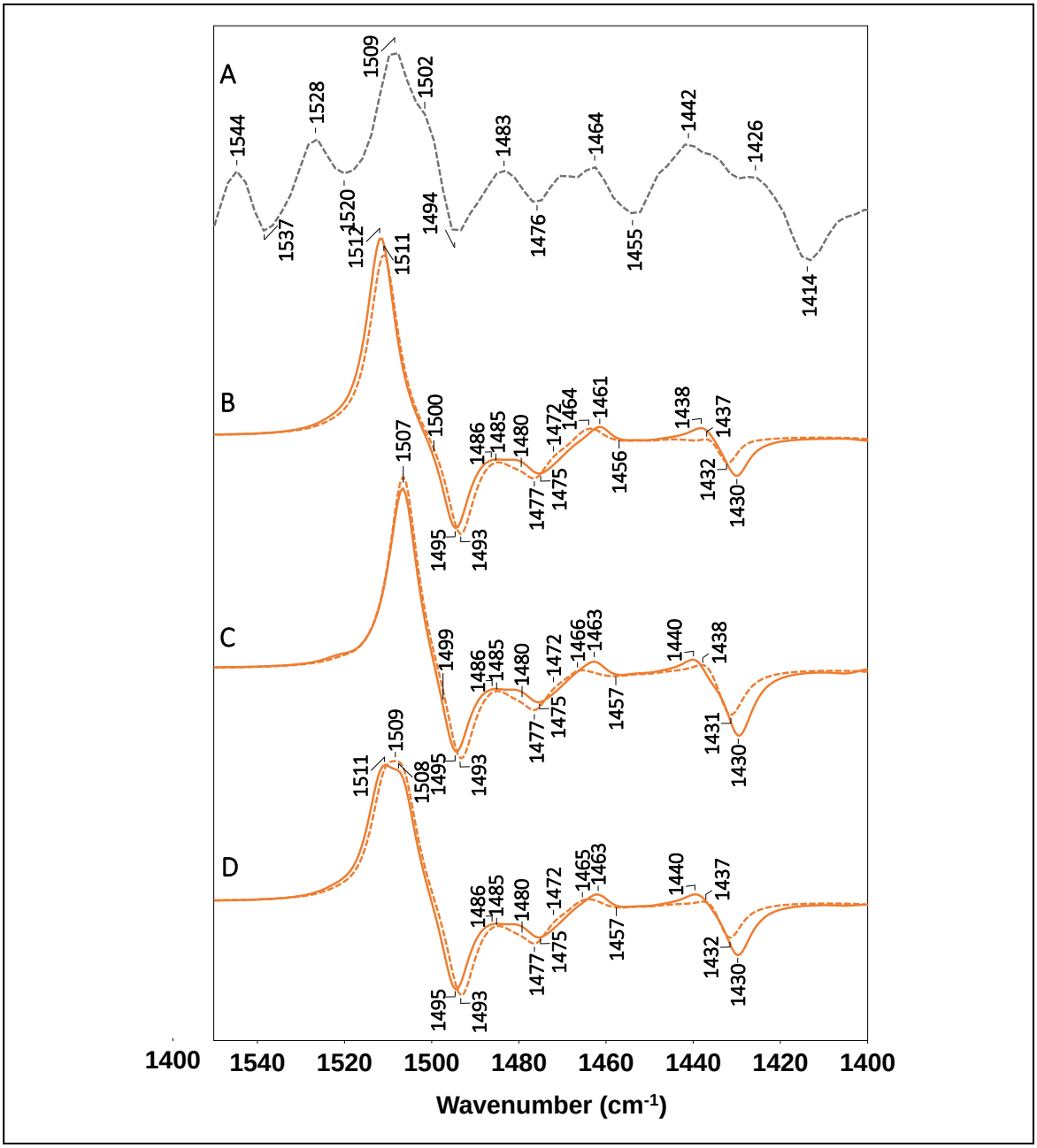

Figure 4.14 Double difference spectra (DDS) for (2BrNQ − PhQ) in the 1550−1400 cm^{-1} region. A. Experimental DDS (see Fig. 4.4 in the main manuscript with the propagated standard error), B. Calculated DDS from Q^-+Leu model 1 (m_1) (*solid*), Q^-+Leu model 2 (m_2) (*dotted*), C. Calculated DDS from Q^-+Leu flipped model 1 (f-m_1) (*solid*), Q^-+Leu flipped model 2 (f-m_2) (*dotted*), and D. Calculated DDS from Q^-+Leu average of m_1 and f-m_1 (*solid*), Q^-+Leu average of m_2 and f-m_2 (*dotted*). Calculated frequencies are scaled by 0.971.

4.S4 Calculated bond lengths and angles obtained from optimized geometries in the different molecular models

DFT based vibrational frequency calculations for all seven quinones in THF [78], in the presence of both a water molecule at the position for leucine residue and a truncated leucine residue where the N−H backbone is H-bonded to the C_4=O group of PhQ [56]. Key bond lengths and angles obtained from the optimized geometry are listed in Table 4.5 (model for reduced PhQ is shown in Fig 4.15) . The one will be described here is for Q+Leu models as the comparison has been made with the QM:MM level of ONION calculation [44, 135] where PhQ is H bonded with Leu residue similar to the one observed in the crystal structure. Various points are significant to consider:

1) Both C⋯O bonds observed in Q+Leu models are very close compared to the QM:MM level of ONION calculation [44, 135] specially the Q+Leu m_2 ones. The C_1⋯O and C_4⋯O bond shorten in m_2 by 0.005/0.004 Å compared to the ones observed from the ONIOM calculation.
2) The distance between the backbone nitrogen atom of LeuA722 and the C_4⋯O carbonyl oxygen atom of PhQ^- is 2.835 Å and 2.526 Å in Q+Leu m_2 and m_1 respectively which is 2.713 Å in the ONIOM model. This indicates that the H-bond length is slightly longer for model 2 but it gets shorter for model 1 optimized structure.
3) Similar bond lengths and angles are calculated for all other six quinones in all the Q+Leu models. This is an indication that replacing the phytl tail of PhQ with a methyl/H-atom/Cl-atom/Br-atom have only a minor impact on the overall orientation of the NQ ring.

4) For PhQ^-, the N-H distance decreases by 0.001 Å when we perform the calculation with a truncated leucine residue as Q+Leu m_2.

5) The angle observed for PhQ^- in these Q+Leu models are also very similar to that found in the ONIOM calculation except the ∠ $N-O_4-C_4-C_3$ which is found to be lengthen by 19° in Q+Leu m_2.

6) All the bond lengths and angles observed in these three Q+Leu models for all quinones are very similar except ∠ $N-O_4-C_4-C_3$ observed in the two di-substituted halogenated quinones which shorten by 150.2° which indicates that when C_3 attached to either Cl or Br atom this angle is becoming so short that may explain why the separation between $C_1 \cdots O$ and $C_4 \cdots O$ vibrational modes of Cl_2NQ^-/Br_2NQ^- are reduced to ~60 cm^{-1} compared to 80 cm^{-1} found for PhQ^-.

Table 4.5 Calculated bond lengths (in Å) and angles (in degrees) for anion PhQ^-, $DMNQ^-$, $2MNQ^-$, $2ClNQ^-$, $2BrNQ^-$, Cl_2NQ^-, and Br_2NQ^-, optimized in THF, Q^-+H_2O and Q^-+Leu models. The X-ray data and the model 2 data for neutral PhQ are also shown. The "A" refers to the various attachments at the C_3 position of the different NQs. For Q^-+Leu model, the values in parentheses are for the Q^-+Leu (m_2) model. For $2MNQ^-$, $2ClNQ^-$ and $2BrNQ^-$, the values in red font are for the "flipped" (f-m_2) models.

Bond/Angle	Q's in THF						
	PhQ^-	$DMNQ^-$	$2MNQ^-$	$2ClNQ^-$	$2BrNQ^-$	Cl_2NQ^-	Br_2NQ^-
$C_1=O$	1.274	1.275	1.274	1.270	1.269	1.262	1.261
$C_4=O$	1.274	1.275	1.274	1.264	1.263	1.262	1.261

Bond/Angle	Q+H_2O						
	PhQ^-	$DMNQ^-$	$2MNQ^-$	$2ClNQ^-$	$2BrNQ^-$	Cl_2NQ^-	Br_2NQ^-
$C_1=O$	1.258	1.267	1.267	1.257	1.256	1.255	1.255
$C_4=O$	1.258	1.278	1.276	1.273	1.272	1.264	1.264
$OH - - O_4$	1.676	1.766	1.761	1.773	1.774	1.791	1.783
$O - - O_4$	2.545	2.750	2.738	2.755	2.751	2.767	2.760
O – H	0.960	0.991	0.992	0.990	0.990	0.987	0.987
∠ $O - O_4 - C_4$	161.8	144.3	147.9	143.6	147.5	149.3	148.2
∠ $O - H - O_4$	148.6	170.8	167.6	170.8	168.9	169.2	170.0
∠ $O - O_4 - C_4 - C_3$	151.4	166.3	179.7	170.0	179.9	180.0	180.0

Bond/Angle	Q+Leu									
	PhQ Xray	PhQ m_2	PhQ^- (ONIOM) [49, 135]	PhQ^- (m_2)	$DMNQ^-$ (m_2)	$2MNQ^-$ (m_2) (f-m_2)	$2ClNQ^-$ (m_2) (f-m_2)	$2BrNQ^-$ (m_2) (f-m_2)	Cl_2NQ^- (m_2)	Br_2NQ^- (m_2)
$C_1{=}O$	1.416	1.229	1.270	1.258 (1.265)	1.265 (1.266)	1.265 (1.266) (1.264)	1.255 (1.256) (1.262)	1.255 (1.256) (1.261)	1.253 (1.254)	1.253 (1.254)
$C_4{=}O$	1.424	1.234	1.284	1.259 (1.280)	1.283 (1.280)	1.281 (1.278) (1.279)	1.277 (1.274) (1.268)	1.277 (1.274) (1.268)	1.269 (1.266)	1.269 (1.266)
$NH\text{-}\,\text{-}O_4$	-	2.053	1.682	1.526 (1.808)	1.766 (1.803)	1.774 (1.804) (1.808)	1.791 (1.822) (1.866)	1.784 (1.822) (1.832)	1.818 (1.876)	1.818 (1.863)
$N\text{-}\,\text{-}O_4$	2.694	3.064	2.713	2.526 (2.835)	2.784 (2.831)	2.789 (2.831) (2.835)	2.807 (2.850) (2.883)	2.802 (2.850) (2.857)	2.845 (2.892)	2.845 (2.880)
N–H	-	1.014 4	1.030	0.999 (1.029)	1.035 (1.029)	1.034 (1.029) (1.029)	1.032 (1.027) (1.026)	1.032 (1.027) (1.026)	1.031 (1.025)	1.031 (1.025)
$\angle N{-}O_4{-}C_4$	145.8	148.3	149.9	158.8 (149.2)	158.3 (149.8)	160.4 (149.8) (148.4)	160.3 (149.7) (148.7)	160.5 (150.6) (151.0)	147.2 (149.4)	147.2 (148.2)
$\angle N{-}H{-}O_4$	-	174.1	179.9	178.2 (175.5)	166.6 (175.7)	166.2 (175.8) (175.8)	167.1 (176.6) (170.7)	167.7 (176.8) (177.4)	174.3 (170.7)	174.3 (171.3)
$\angle N{-}O_4{-}C_4{-}C_3$	142.9	170.1	145.3	161.1 (164.3)	180.0 (151.9)	149.0 (154.7) (148.1)	149.5 (154.1) (8.668)	178.4 (160.9) (155.5)	10.9 (11.39)	10.9 (6.880)
$\angle(C_m\text{-}C_2\text{-}C_1)$	119.0	114.2	116.8	119.8 (115.1)	117.2 (117.1)	117.5 (117.4) (117.5)*	-	-	-	-
$\angle(A\text{-}C_3\text{-}C_4)$	118.5	123.9	116.5	119.8 (115.9)	117.6 (117.4)	115.9 (115.8) (115.9)**	117.2 (117.0) (117.2)	117.0 (116.9) (116.9)	116.3 (116.2)	116.3 (115.6)

*$\angle(C_{methyl}\text{-}C_3\text{-}C_4)$ for flipped model of $2MNQ^-$
**$\angle(A\text{-}C_2\text{-}C_1)$ for flipped model of $2MNQ^-$

4.S5 Calculated optimized geometry of PhQ^{-}+Leu models compared with X-ray crystal structure and ONIOM calculation

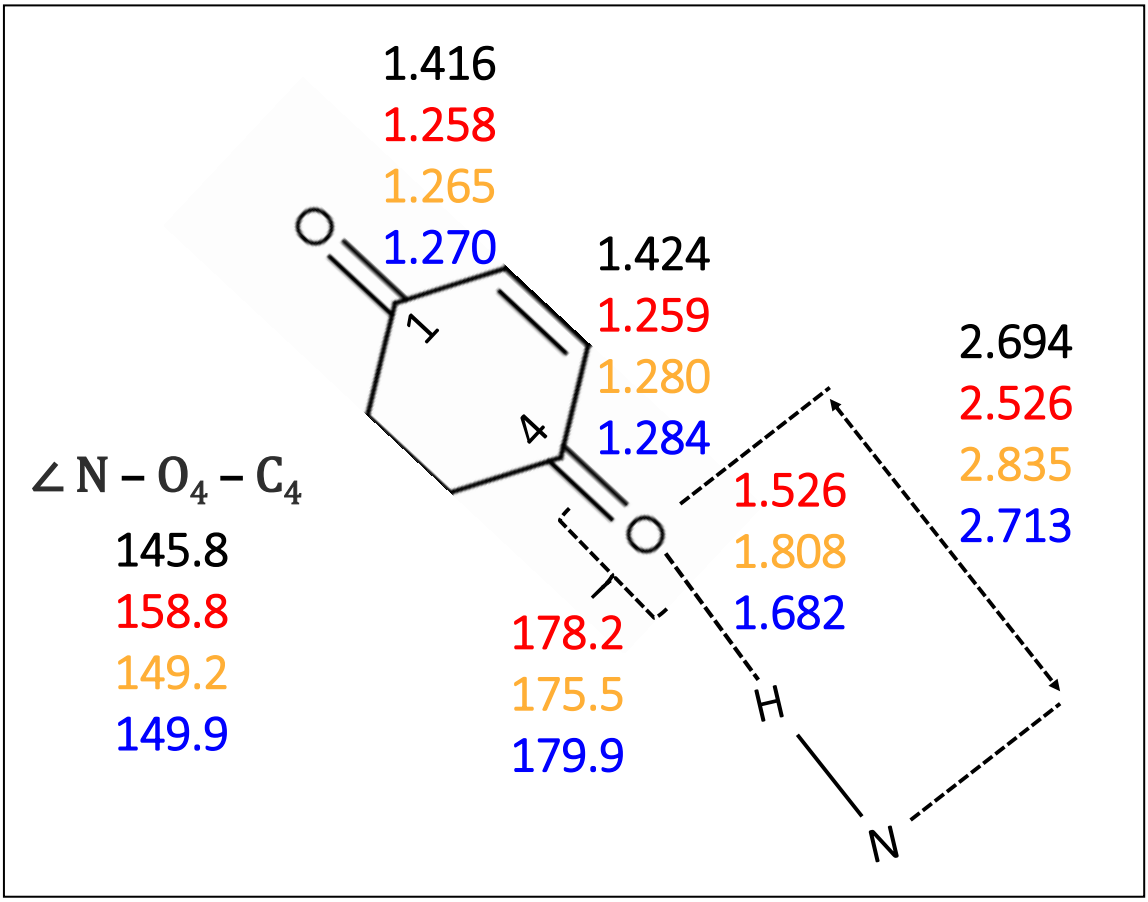

Figure 4.15 Model demonstrating bond lengths and angles calculated for PhQ^{-} (see Table 4.1/4.3). *Black*/*Red*/*Orange*/*Blue*: X-ray/(model m_1)/(model m_2)/(model f-m_2).

5 REVERSIBLE INHIBITION AND REACTIVATION OF ELECTRON TRANSFER IN PHOTOSYSTEM I

ABSTRACT

In photosystem I (PSI) complexes at room temperature electron transfer from A_1^- to F_X is an order of magnitude faster on the B-branch compared to the A-branch. One factor that might contribute to this branch asymmetry in time constants is TrpB673 (*Thermosynechococcus elongatus* numbering), which is located between A_{1B} and F_X. The corresponding residue on the A-branch, between A_{1A} and F_X, is GlyA693. Here microsecond time-resolved step-scan FTIR difference spectroscopy at 77 K has been used to study isolated PSI complexes from wild type and TrpB673Phe mutant (WB673F mutant) cells from *Synechocystis* sp. PCC 6803.

WB673F mutant cells require glucose for growth, and are light sensitive. Photoaccumulated FTIR difference spectra indicate changes in amide I and II protein vibrations upon mutation of TrpB673 to Phe, indicating the protein environment near F_X is altered upon mutation.

In the WB673F mutant PSI samples, but not in WT PSI samples, the phylloquinone molecule that occupies the A_1 binding site is likely doubly protonated following long periods of repetitive flash illumination at room temperature. PSI with (doubly) protonated quinone in the A_1 binding site are not functional in electron transfer. However, electron transfer functionality can be restored by incubating the light treated mutant PSI samples in the presence of added phylloquinone.

5.1 Introduction

In oxygen-evolving photosynthetic organisms solar energy is captured and converted in two large membrane-spanning protein complexes called photosystem I (PSI)[3] and II (PSII) [6]. In both photosystems, light energy is captured in large pigment arrays, which are designed to rapidly transfer the excitation energy to a reaction center (RC) core where the photochemistry takes place [17]. Upon light excitation of special pigments in the RC, electrons are transferred via a series of protein-embedded acceptors, across a biological membrane (thylakoid membrane) [6]. In this manuscript we focus on PSI, where the cofactors operate in a highly reducing regime [32].

The organization of the pigments in PSI, and especially the pigments involved in electron transfer (ET), are highly conserved in higher plants, algae, and cyanobacteria [16, 18, 19, 42, 146, 147]. The PSI complex consists of 11 – 12 protein subunits, with 3 of them (PsaA, PsaB, and PsaC) binding the ET cofactors [16, 18, 19]. The cofactors that participate in ET are termed P700, A_{-1}, A_0, A_1, F_X, F_A, and F_B [17]. P700 is a special pair of chlorophyll *a* and chlorophyll *a*' (Chl *a* and Chl *a*') molecules that are often termed P_B and P_A, respectively. Chl *a*' is a 13^2-epimer of Chl *a* [17]. A_{-1} and A_0 are monomeric Chl *a* species. A_1 is a phylloquinone molecule (2-methyl-3-phytyl-1,4-naphthoquinone, PhQ), or a close analogue [16, 148].

PSI RCs contain two nearly symmetrical branches of ET cofactors, termed the A- and B-branches (Fig. 5.1A). Cofactors in each branch are denoted by an A or B subscript (e.g. A_{1A} and A_{1B}). The two branches emanate from P700 and re-converge at F_X. F_X, F_A and F_B are [4Fe-4S]

[3]**Abbreviations:** BQ, benzoquinone; C=O, carbonyl; Chl *a*, chlorophyll *a*; DAS, decay associated spectrum; DFT, density functional theory; DS, difference spectra/spectrum/spectroscopy; ET, electron transfer; FTIR, Fourier transform infrared; H-bond, hydrogen bond; NQ, naphthoquinone; PhQ, phylloquinone (2-methyl-3-phytyl-1,4-naphthoqiuinone); PSI, photosystem I; PSII, photosystem II; RC, reaction center; *S6803*, *Synechocystis* sp. PCC *6803*; T., *Thermosynechococcus*; TRSS, time-resolved step-scan; WT, wild type.

clusters. F_X is bound to both PsaA and PsaB, while F_A and F_B are bound to the PsaC stromal protein subunit. The geometry of the ET cofactors (minus F_A and F_B) are outlined in Fig. 5.1A.

Following the primary charge separation events, the $P700^+A_1^-$ radical pair is formed within ~50 ps of light excitation of the PSI RC complex [20, 21]. The $P700^+A_1^-$ radical pair state is further stabilized by ET from A_1^- to F_X. At RT, the ET rates are branch specific, with $A_{1A}^- \rightarrow F_X$ occurring in ~300 ns at RT, and $A_{1B}^- \rightarrow F_X$ occurring in ~15 ns [27, 28, 38, 149, 150]. This large difference in the time constants associated with ET down either branch is difficult to rationalize given that the same pigment occupies the A_{1A} and A_{1B} binding sites, and that the environment surrounding the pigments on both branches are near identical. Kinetic models that explain the biphasic nature of the A_1 ET in terms of energetic asymmetries have been proposed previously, however [28, 48, 86].

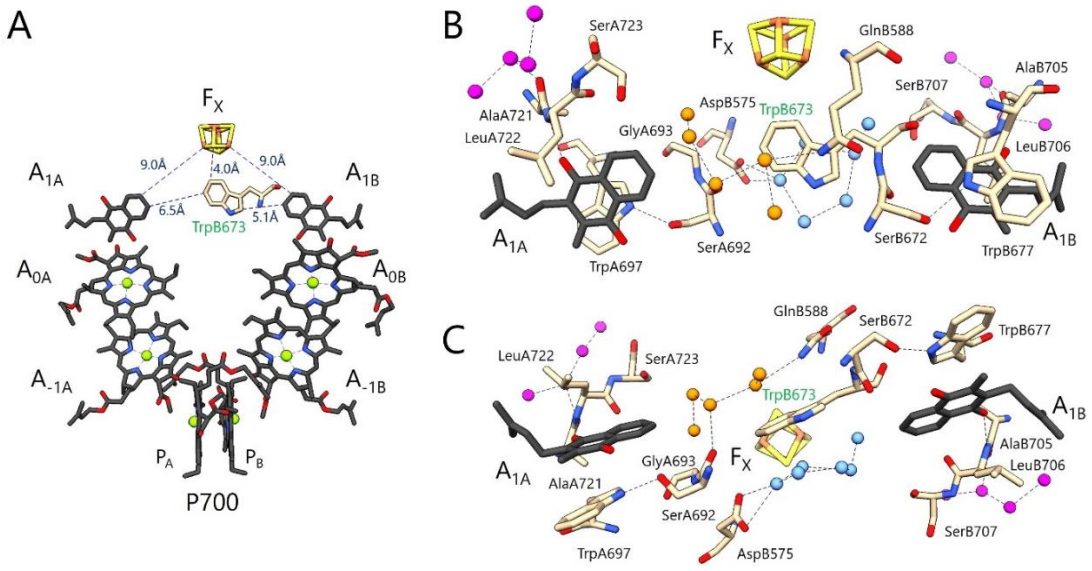

Figure 5.1 A Structural organization of the ET cofactors in PSI. TrpB673 is also shown. Image was derived from 2.5-Å X-ray crystal structure of PSI isolated from *Thermosynechococcus elongatus* (PDB 1JB0) [16]. The terminal acceptors F_A and F_B are not shown. Hydrocarbon tails of PhQ and Chl *a*/*a*' are truncated for clarity. Edge-to-edge distances from TrpB673 to A_{1A}, A_{1B}, and F_X are included (*dotted*) along with the edge-to-edge distances from F_X to A_{1A} and A_{1B}. B Structure showing select amino acid residues and water molecules around A_{1A}, A_{1B}, and F_X. Oxygen atoms of water molecules are enlarged for visualization purpose. Possible H-bonding interactions, ranging from 2.7 Å to 3.4 Å, are depicted as dotted lines. C Alternative view of the

structure in B. Atom coloring: dark grey: carbon atoms of A_1, light khaki: all other carbon atoms, red: oxygen, blue: nitrogen, light green: magnesium, yellow: sulfur, dark yellow: iron, magenta: water molecules behind Ser/Leu/Ala chains on both branches, orange: water molecules between A_{1A} and F_X, and light blue: water molecules between A_{1B} and F_X.

From F_X^-, an electron is further transferred to the terminal electron acceptors F_A and F_B on a sub-μs timescale [29].

In isolated PSI complexes, the $P700^+F_{A/B}^-$ radical pair state recombines in 50 – 100 ms [30, 31, 35]. This recombination proceeds via repopulation of the A_1^- state. This conclusion follows from the observation of a change in recombination rate upon altering the pigment that occupies the A_1 binding site [1, 30, 35, 151, 152].

When the A_1 cofactor is disabled or is no longer functional in its ability to perform forward ET, the $P700^+A_0^-$ radical pair state recombines on a few tens of ns. In a portion of the complexes a decay pathway that involves the P700 triplet state (^{3}P700) is apparent [32, 153, 154]. ^{3}P700 forms in ~10 – 100 ns, and decays in 10 – 20 μs at RT [38, 154]. The formation of ^{3}P700 is thought to occur through a spin flipping mechanism, where the singlet spin configuration of $P700^+A_0^-$ evolves to a triplet configuration via hyperfine interactions [32].

At cryogenic temperatures (~120 K and below), ET in PSI becomes heterogeneous. In ~50% of the PSI complexes the $P700^+F_{A/B}^-$ radical pair state forms irreversibly [22, 36], and does not contribute in repetitive flash measurements. In ~40% of PSI complexes $P700^+A_1^-$ recombines in ~360 μs, and occurs predominantly down the A-branch [22, 36]. In the remaining 10%, $P700^+F_X^-$ forms and then decays in a few ms [22, 36]. In PSI complexes in which the pigment in the A_1 binding site is not functional, ^{3}P700 forms, and at 77 K decays in ~200 – 300 μs [53, 154, 155].

In addition to the functionality of the quinone in the A_1 binding site, recent studies have started to reveal how structural properties may relate to the thermodynamic and energetic

properties of the pigment in the A_1 binding site [1, 86-88]. However, there are many unresolved questions on how different pigment-protein interactions may modulate the functionality of the quinones as ET cofactors in the A_1 binding site [15]. Fig. 5.1B and 5.1C show two views of the environment surrounding the quinones in the A_{1A} and A_{1B} binding sites. Amino acid numbering in this manuscript is for *Thermosynechococcus elongatus* (*T. elongatus*) (PDB 1JB0) [16].

Several molecules in Fig. 5.1B and 5.1C are noteworthy for their potential impact on the functional/structural properties of A_1. A tryptophan residue (TrpA697/TrpB677) is π-stacked with PhQ. The C_4=O group of PhQ is hydrogen bonded (H-bonded) to the backbone of a leucine residue (LeuA722/LeuB706). The C_1=O carbonyl group of PhQ is free from H-bonding, so H-bonding to PhQ in the A_1 binding site is decidedly asymmetrical.

Fig. 5.1B, C indicates clusters of water molecules near PhQ in the A_1 binding site. A series of water molecules located near LeuA722/LeuB706 form a network of H-bonds [water molecule numbering is A5018, A5030, A5031, A5055 for A_{1A}, B5014, B5015, B5037, B5055 for A_{1B}]. These clusters of water molecules have been postulated to have an impact on the redox properties of A_1, and also to contribute to increasing the strength of the asymmetric H-bonding to the C_4=O group of PhQ, at least for PhQ in the A_{1A} binding site [156, 157]. Fig. 5.1 also indicates a cluster of water molecules between the aromatic ring of PhQ and F_X [water molecules numbered A5007, A5015, A5022, A5043, A5049 for A_{1A}, B5018, B5019, B5030, B5055, B5056, B5058 for A_{1B}].

Fig. 5.1 indicates a high degree of structural symmetry between the pigments on the A- and B-branch ET chains. However, TrpB673 breaks this symmetry. The A-branch counterpart of TrpB673 is GlyA693. While TrpB673 is on the PsaB protein subunit, it is spatially located between A_{1A}, A_{1B}, and F_X (Fig. 5.1B, C). Given the unique location of TrpB673 in the ET chain it has been proposed that TrpB673 participates as an intermediate acceptor in ET between A_1 and F_X [158].

Although this hypothesis has since been shown improbable from the perspective of ET theory [34], the role of TrpB673 in ET in PSI is not well understood. An EPR study on PSI complexes from *Chlamydomonas* (*C.*) *reinhardtii* in which Trp was replaced with Gly shows that the mutation alters primarily ET on the B-branch, indicating only an indirect involvement of Trp with the forward ET [159].

Here time-resolved step-scan (TRSS) FTIR difference spectroscopy (DS) at 77 K was used to study a PSI mutant from *S6803* in which TrpB673 was changed to Phe. In this mutant spectral contributions from both $P700^+A_1^-$ and $^3P700$ are found. Adjusting the PSI samples' exposure to actinic illumination at RT, prior to freezing, resulted in different ratio of $P700^+A_1^-$ and $^3P700$ states formed. Furthermore, $^3P700$ state formation was quenched in actinic light exposed PSI mutant samples incubated in the presence of PhQ. This study indicates that the TrpB673 mutation likely disturbs the group of water molecules in the environment near the aromatic ring of PhQ, leading to light-induced phylloquinol ($PhQH_2$) formation, presumably through a double-protonation event induced by the disturbed water molecules. Added PhQ in the buffer is able to displace $PhQH_2$ in the A_1 binding site.

5.2 Materials and Methods

5.2.1 Construction/growth of W673F PSI

The recipient strains were generated by deletion of a portion of the *psaB* gene as described previously [160] with some modifications. The *S6803 psaB* knockout (Δ*psa*B) recipient strain was obtained by the recombinant DNA sequence that was cloned from the 608 bp to 1014 bp on the *psaB* open reading frame, and from 9 to 751 bp after *psaB* with an introduced *Eco*R I restriction site between these two flanking DNA fragments. Then the 1.3 kbp kanamycin resistance cassette gene was added at the *Eco*R I restriction site, which was served for the homologous recombination.

After 9 generations of segregation on BG-11 containing plates, with 20 µg/mL kanamycin antibiotic under very low light intensity, the stable Δ*psa*B strain was obtained and confirmed by PCR analysis. For mutagenesis in the C-terminal region of the PsaB protein, the generated plasmid pBC contains the C-terminal region of the *psa*B gene with resistance genes for ampicillin and chloramphenicol antibiotic and 760 bp region downstream of the *psa*B gene [160], which served as the templates for PCR based site-directed mutagenesis. The site-directed mutated DNA was used to transform the recipient strain Δ*psa*B. The transformation and transformant selection were performed under weak light and heterotrophic growth as described previously [160]. The chloramphenicol resistant colonies were selected and segregated for four generations. The fragment containing the mutated site was amplified by PCR and it was sequenced to ensure the mutation.

The PsaB-W673F mutant, and Δ*psa*B recipient strain were grown in BG-11 medium supplemented with 5 mM glucose with their designed antibiotics. PsaB-W673F was cultured at 30 °C, under low light intensity (<5 µE m^{-2} s^{-1}) while the Δ*psa*B recipient strain is maintained in the dark but supplied with 40 µE m^{-2} s^{-1} light for 10 min every day. Cells were collected during the late exponential growth phase, washed and resuspended in SMN buffer (0.4 M sucrose, 10 mM NaCl, and 10 mM Mops-NaOH, pH 7.0) for further use [160].

5.2.2 Isolation of PSI particles

Thylakoid membranes were prepared from cells in late exponential growth phase as described before [160]. To purify PSI complexes from the thylakoid membranes, the concentration of the thylakoids were adjusted to 0.5 mg/mL Chl in 10 mM Mops-NaOH, pH 7.0 buffer, and solubilized for 2 h at 4 °C by adding n-dodecyl-D-maltopyranoside (DM) to a concentration of 1% (w/v). The solution was centrifuged for 20 min at 15,000 g to remove insoluble debris, and the

supernatant was loaded onto a 10-30% (w/v) sucrose gradient prepared in 10 mM Mops-NaOH pH 7.0 buffer containing 0.05% (w/v) DM. The gradients were centrifuged for 16 – 18 h at 150,000 g at 4 °C, and the lower, dark green band containing PSI trimers was collected. The PSI trimers were concentrated using Pierce concentrators (20,000 molecular weight cut-off membranes (Thermo Scientific)) to a final concentration of ~1 µg/µl Chl, and stored at -80 °C until further use.

5.2.3 Preparation of PSI samples for FTIR DS

20 µL of WB673F PSI particles at Chl-*a* concentration of 1.66 mg/mL were suspended in 980 µL Tris buffer (pH 8.0) with 0.04% DM. The solution was ultra-centrifuged at 408,000 g for 3 h to produce a soft pellet. 0.1 µL each of 20 mM sodium ascorbate and 10 µM phenazine methosulfate were added to the soft pellet to act as exogenous electron donor to $P700^+$. The pellet was squeezed between two CaF_2 windows until the optical density at ~1654 cm^{-1}, corresponding to amide I absorption, was below 1.0. Actinic flashes of ~1 mJ and 5 ns duration at 532 nm were from a Minilite Nd:YAG laser (Continuum, San Jose, CA) operating at 10 Hz. In some experiments samples were exposed to repetitive flashes at RT, prior to freezing to 77 K. Samples were exposed to actinic illumination for 1, 4, or 16 h. For measurement at 77 K, samples were mounted in an Optistat DN-V liquid nitrogen cryostat (Oxford Instrument, United Kingdom). All samples were frozen in the dark regardless of the pre-exposure to actinic flashes at RT.

PhQ was reincorporated into W673F mutant PSI complexes by using the same method as outlined previously to incorporate quinones into PSI that lacked a functional quinone in the A_1 binding site [59]. Briefly, 500x molar excess PhQ, dissolved in ethanol, was added to suspension of PSI particles so that the volume ratio of ethanol in the mixture is below 2%. The mixture was stirred at 277 K for 12 h in the dark, before ultra-centrifugation to form a soft pellet.

5.2.4 FTIR Difference Spectroscopy (DS)

All FTIR DS were collected using a Bruker Vertex80 FTIR spectrometer (Bruker Optics, Billerica, MA). ($P700^+$ – P700) FTIR DS at 77 K were obtained using CW light from a 10 mW helium neon laser, as described previously [76]. Time-resolved step-scan (TRSS) FTIR DS were collected also as described previously [53]. Briefly, time-resolved spectra were collected with 6 μs temporal resolution, over a 3.5 ms time window, in the 1950 – 1100 cm^{-1} spectral range, at 4 cm^{-1} spectral resolution. 2000-1000 cm^{-1} bandpass filters were placed both before and after the sample. The CaF_2 sample compartment windows, and the cryostat shroud windows, also blocked IR light below ~1100 cm^{-1} from reaching the detector. Laser flash of 5 ns duration at 532 nm were from a Minilite Nd:YAG laser (Continuum, San Jose, CA) operating at 10 Hz. At each interferometer step (in step-scan measurements), data from 20 laser flashes were coadded (averaged). Each full step-scan acquisition was repeated ~40 times and all data were averaged to improve the signal-to-noise ratio.

The time-resolved spectra obtained at 77 K were globally analyzed using Glotaran [77], and fitted to a sum of exponential components. The dominant component/phase has a lifetime of ~390 μs and the spectra associated with this lifetime are called decay associated spectra (DAS). Global analysis was primarily used to separate spectral features associated with a heating artifact caused by the actinic laser flashes used to initiate photochemistry [155].

5.3 Results

5.3.1 Characteristics of the W673F mutant PSI

WB673F and WB673A mutant cells require glucose for growth. We failed to isolate PSI complexes from the WB673A mutant cells, however, preventing spectroscopic characterization of WB673A mutant PSI. The WB673F mutation is a more conservative replacement than WB673A,

and the WB673F mutant cells grew well (on glucose under low light), and we were able to prepare PSI trimers from the WB673F mutant strain. Interestingly, the WB673F mutant strain cannot grow photoautotrophically. Further details of the growth rate and other physiological characterizations will be described elsewhere.

In this study, three types of FTIR DS are considered: 1) Photoaccumulated ($P700^+$ – P700) FTIR DS; 2) Time-resolved ($P700^+A_1^-$ – $P700A_1$) FTIR DAS; 3) ($^3P700$ – P700) FTIR DAS. In these FTIR DS and DAS, positive peaks correspond to $P700^+$, $^3P700$ and the A_1^- states, and negative peaks correspond to the P700 and A_1 ground (or neutral) states. All spectra except for ($^3P700$ – P700) DS are normalized to the 1717(+)/1697(–) cm^{-1} difference band appearing in both the photoaccumulated (static) and the time-resolved spectra.

5.3.2 *Photoaccumulated ($P700^+$ – P700) DS at 77 K*

Fig. 5.2 shows ($P700^+$ – P700) FTIR DS collected at 77 K, for PSI from WT and PSI from the WB673F mutant. Two sets of spectra are shown for WB673F PSI (Fig. 5.2B). One sample was exposed to 10 Hz actinic laser flashes for 16 h at RT prior to freezing (Fig. 5.2B, *red*). The other sample was not subjected to actinic illumination at RT, and was frozen in the dark (Fig. 5.2B, *blue*). The samples that were exposed to actinic illumination at RT prior to freezing will be referred to as pre-flashed samples, while samples kept in the dark prior to and during freezing will be referred to as non-flashed samples.

In the ($P700^+$ – P700) FTIR DS for WT PSI (Fig. 5.2A), positive bands are observed at 1754, 1741, 1717, 1688, 1675, 1655, 1622, 1601, 1590, 1567, 1550, 1524, and 1431 cm^{-1}, while negative bands are observed at 1748, 1733, 1697, 1681, 1668, 1637, 1610, 1543. 1535, and 1423 cm^{-1}. These difference features in ($P700^+$ – P700) FTIR DS for cyanobacterial PSI have been discussed in detail before [72, 75, 161].

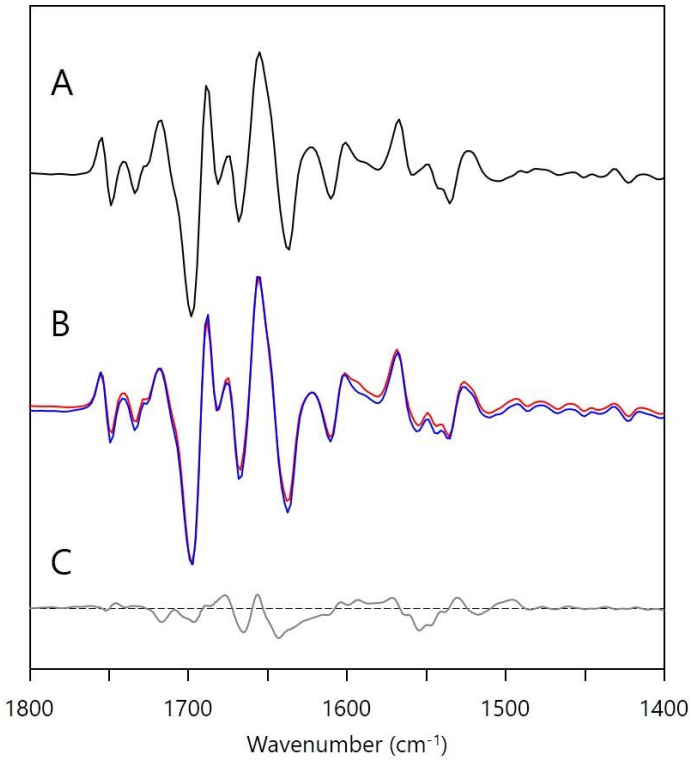

Figure 5.2 Photoaccumulated ($P700^+$ – P700) FTIR DS for (A) WT PSI and (B) WB673F mutant PSI at 77 K. For WB673F mutants PSI, FTIR DS were collected for non-flashed (*blue*) and pre-flashed (532 nm laser flashes for 16 h at 10 Hz) (*red*) samples. The spectra are normalized using the 1717(+)/1697(–) cm^{-1} FTIR difference band. C (WB673F – WT) double difference spectrum (DDS), obtained by subtracting the spectrum in A from the average of the spectra in B.

No significant changes in the ($P700^+$ – P700) FTIR DS are observed for pre-flashed and non-flashed WB673F PSI samples (Fig. 5.2B). However, small changes are observed in the ($P700^+$ – P700) DS for WT and WB673F PSI samples. These small changes are visualized more easily in the (WB673F – WT) double difference spectrum (DDS) (Fig. 5.2C). The most intense features in the DDS in Fig. 5.2C are near ~1650 and ~1550 cm^{-1}. Features near these frequencies are usually associated with amide I and II protein vibrations, respectively. So most likely there is some mutation-induced alteration in the protein environment, presumably near A_1/F_X given that the mutation is near A_1 and F_X. Most likely, the charge on the iron-sulfur clusters have an electrostatic

impact on the protein amide vibrations near A_1 and F_X, and these amide vibrations are modified by the mutation and appear as features in the DDS in Fig. 5.2C.

5.3.3 Time-resolved FTIR DS at 77 K

Fig. 5.3A shows (^{3}P700 – P700) FTIR DAS obtained at 77 K. Time-resolved ($P700^+A_1^-$ – $P700A_1$) FTIR DAS obtained using WT and non-flashed mutant PSI at 77 K are shown in Fig. 5.3B and C, respectively. Time-resolved ($P700^+A_1^-$ – $P700A_1$) FTIR DAS obtained using mutant PSI that has been pre-flashed repetitively at RT with 532 nm laser flashes at 10Hz, for 1, 4, and 16 h are shown in Fig. 5.3D, E and F, respectively.

Low temperature flash-induced absorption changes at 1697 cm^{-1} for the differently illuminated mutant PSI complexes are outlined in Fig. 5.5. At 1697 cm^{-1}, an intense negative band is present in ($P700^+$ – P700) and ($P700^+A_1^-$ – $P700A_1$) FTIR DS, but not in (^{3}P700 – P700) FTIR DS. The transient absorption changes at 1697 cm^{-1} (at 77 K) is therefore associated with $P700^+A_1^-$ charge recombination. Specifically the 1697 cm^{-1} band in Fig. 5.2A and B is well known to be associated with the 13^1-keto C=O group of the P_B pigment of P700 [162, 163]. By fitting the data at 1697 cm^{-1} to two stretched exponential functions and a constant, the lifetime of the major decay phase is calculated to be 389 µs for all off the different PSI complexes. The parameters obtained from fitting the kinetics at 1697 cm^{-1} are listed in Table 5.5.A similar time constant is observed for WT PSI [72].

The time-resolved ($P700^+A_1^-$ – $P700A_1$) FTIR DAS for WT (Fig. 5.3B) and non-flashed mutant (Fig. 5.3C) PSI are similar. In addition to the difference signals associated with $P700^+$/P700 discussed above (Fig. 5.2), the ($P700^+A_1^-$ – $P700A_1$) FTIR DS displays positive bands associated with A_1^- at 1495 and 1415 cm^{-1} due to the C_1=O and C_4=O stretching vibrations of PhQ, respectively [44, 156]. The C_4=O stretching vibration is downshifted relative to the C_1=O vibration

due to H-bonding. The characteristic bands of A_1^- at 1495 and 1415 cm^{-1} are found also in spectra obtained using pre-flashed WB673F PSI (Fig. 5.3D, E).

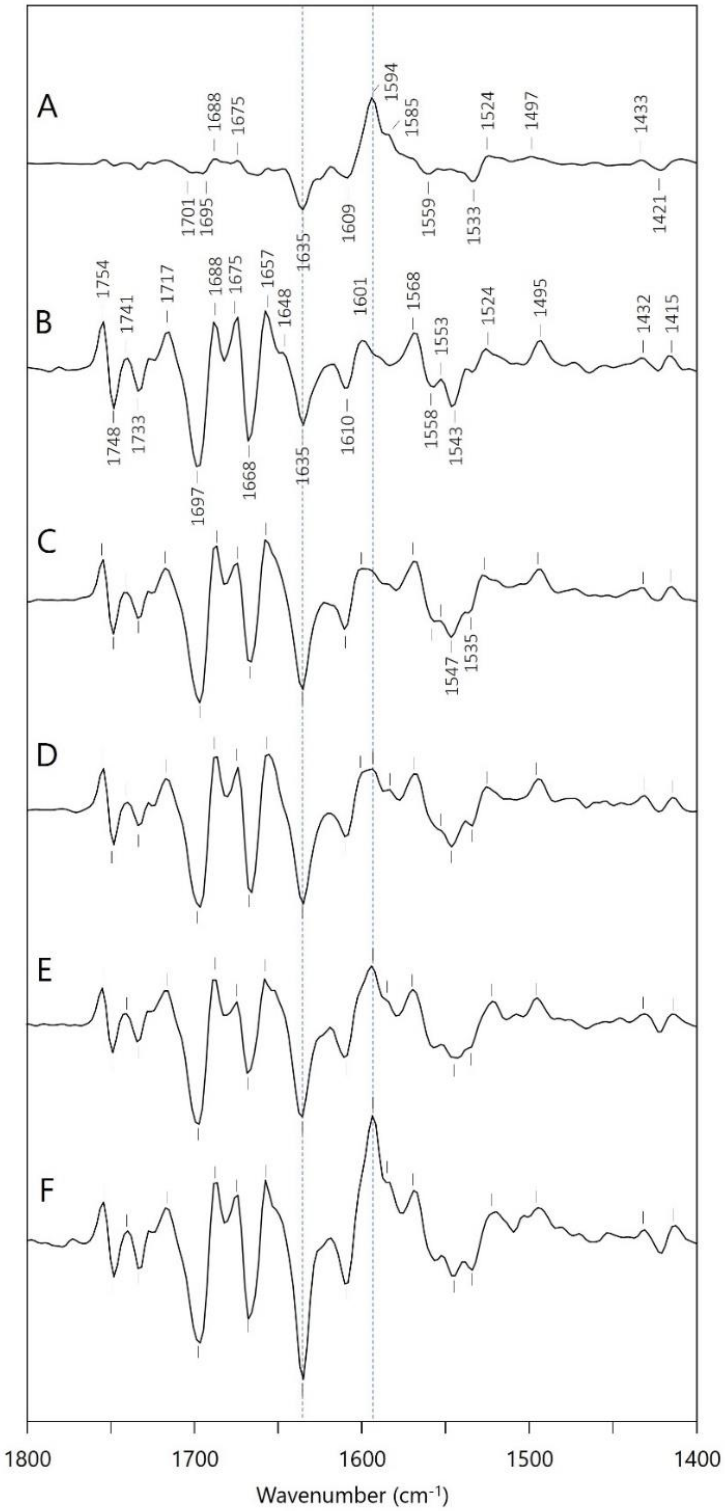

Figure 5.3 A (^{3}P700 – P700) FTIR DS at 77 K, from [53]. B Time-resolved FTIR DAS for WT PSI at 77 K. Time-resolved FTIR DAS for non-flashed (C), 1 h pre-flashed (D), 4 h pre-flashed (E) and 16 h pre-flashed (F) WB673F mutant PSI at 77 K. Vertical dotted lines are shown at 1635 and 1594 cm^{-1}. Time-resolved FTIR DAS (B – F) represent the ~390 µs phase.

The time-resolved ($P700^+A_1^-$ – $P700A_1$) FTIR DS obtained using WT and non-flashed WB673F PSI are very similar (Fig. 5.3B and C) indicating that the mutation does not greatly impact the environment of PhQ in the A_1 binding site, in either the neutral or the anion state. The time-resolved spectra for pre-flashed WB673F PSI (Fig. 5.3D, E and F), however, exhibit clear differences compared to the WT and non-flashed WB673F PSI spectra, most notably near 1635 and 1594 cm^{-1}. For WB673F PSI that was pre-flashed for 1 h (Fig. 5.3D), a positive band is starting to appear at 1594 cm^{-1} with a similar amplitude to the band at 1601 cm^{-1}. In addition, the relative intensity of the negative band at 1635 cm^{-1} increases with respect to the 1697 cm^{-1} band (compare intensity ratios in the spectra in Fig. 5.3B and C). When mutant PSI samples are pre-flashed for 4 h (Fig. 5.3E), these changes at 1635 and 1594 cm^{-1} grow, and after 16 h of pre-flashing the 1635(-) and 1594(+) cm^{-1} bands are now the most prominent bands in the spectrum. These spectral features that grow with the increasing number of flashes at RT prior to cooling are characteristic of features found in the ($^3P700$ – P700) FTIR DS (Fig. 5.3A), where the bleaching at 1635 cm^{-1} is well-known to correspond to the 13^1-keto C=O of the P_A pigment of P700, which downshifts to 1594 cm^{-1} upon $^3P700$ formation [164]. The time-resolved FTIR DAS for pre-flashed WB673F PSI therefore result from a combination of signals found in ($P700^+A_1^-$ – $P700A_1$) and ($^3P700$ – P700) FTIR DS, with the contribution from ($^3P700$ – P700) signals increasing as the number of pre-flashes at RT increases. Note that the $P700^+A_1^-$ and $^3P700$ states decay with similar lifetimes (~360 µs and ~200 – 300 µs, respectively) that cannot easily be separated in the global analysis, so the DAS contains contributions from both states with similar lifetime.

The spectra in Fig. 5.3 indicate $^3P700$ formation in a fraction of WB673F PSI samples only when the samples are exposed to actinic illumination at RT prior to cooling, and the relative fraction depends on the number of pre-flashes at RT. From the relative peak intensities of the 1697

and 1594 cm^{-1} bands (see SI for details), we estimate the relative fraction of WB673F PSI undergoing ^{3}P700 formation is 25, 38, and 58% for 1, 4, and 16 h pre-flashed samples, respectively (Table 5.2). Note that in the time-resolved measurements at 77 K the frozen sample is exposed to repetitive actinic laser flashes at 10 Hz for 5 – 20 h. However, there is no indication for the appearance of a 1635(–)/1594(+) cm^{-1} difference band during the course of measurements at 77 K.

It is well known that ^{3}P700 formation can occur upon $P700^+A_0^-$ charge recombination [122], which is common when the $A_0^- \rightarrow A_1$ forward ET process is inhibited, either because the A_1 binding site is empty [165], or the quinone in the binding site is no longer functional in ET [53, 154, 164]. PhQ is clearly present in the non-flashed mutant PSI samples (anion bands are observed), and it is likely that flash illumination at RT caused some sort of alteration of the PhQ in the A_1 binding site. Given the large number of flashes required this alteration occurs with low yield. Given the location of the mutation, the forward ET from A_1^- to F_X is likely inhibited because A_1 is no longer a functional intermediate in ET. One likely possibility is the light-induced double protonation of PhQ in the mutant PSI samples.

PhQ is clearly observed to be a functional electron acceptor in non-flashed WB673F PSI. Therefore, it is unlikely that the mutation results in an empty A_1 binding pocket. The ^{3}P700 state is observed at 77 K only in the mutant and only under exposure to many hours of actinic laser flashes at 10 Hz, at RT. Therefore, it is likely that the mutation opens up a pathway for movement of water molecules that can lead to protonation of PhQ in the A_1 binding site. Obviously, this is a rare event, as the effects are observed only after thousands of laser flashes.

One might predict that a protonated PhQ in the A_1 binding site will have a lower affinity for the binding site than the native PhQ. So by incubating pre-flashed mutant PSI samples in the presence of PhQ one might find that PhQ could replace the protonated species in the A_1 binding

site, restoring regular ET through A_1, and diminishing triplet state formation. To test this prediction we incubated pre-flashed WB673F PSI samples in the presence of a large molar excess of PhQ. After washing the sample, we undertook time-resolved FTIR experiments on the pre-flashed WB673F PSI samples that had been incubated in the presence of PhQ.

Fig. 5.4 shows time-resolved FTIR DAS obtained using two samples from WB673F mutant PSI where PhQ has been re-introduced (samples were incubated in the presence of a large molar excess of PhQ). Before re-introducing PhQ, both samples were exposed to actinic flashes at RT for ~4 h to disable A_1, so both PSI samples are equivalent to that in Fig. 5.3E. After incubation in the presence of PhQ in the dark for ~12 h, one sample (Fig. 5.4A) was frozen to 77 K in the dark. The other (Fig. 5.4B) was exposed to another series of ~4 h actinic laser flashes at RT before cooling to 77 K. In Fig. 5.4A, the relative amplitude of the 1635 cm^{-1} band and lack of intense band at 1594 cm^{-1} indicates that the ^{3}P700 state is not present. The spectrum in Fig. 5.4A indicates that the ET function of PhQ in the A_1 binding site is recovered simply by adding exogenous PhQ to the PSI samples. On the other hand, Fig. 5.4B shows characteristic features of the (^{3}P700 – P700) FTIR DS, much like in the FTIR DS for pre-flashed WB673F PSI (Fig. 5.3F). Therefore, even after the A_1 function is restored by exogenous PhQ, exposure to repetitive actinic flashes at RT is capable of re-deactivating PhQ in the A_1 binding site. The FTIR DAS in Fig. 5.4 show that the effect of pre-flashing WB673F PSI is reversible. That is, PhQ in the A_1 binding site in the mutant can be disabled through exposure to actinic flashes, and re-enabled when PhQ is re-incorporated by displacing the non-functional quinone in the binding site, and then re-disabled through additional exposure to repetitive laser flash illumination. The likely cause of ^{3}P700 formation in pre-flashed WB673F mutant PSI is a mutant-induced structural modification of the binding site, which allows PhQ protonation to occur, albeit with low yield.

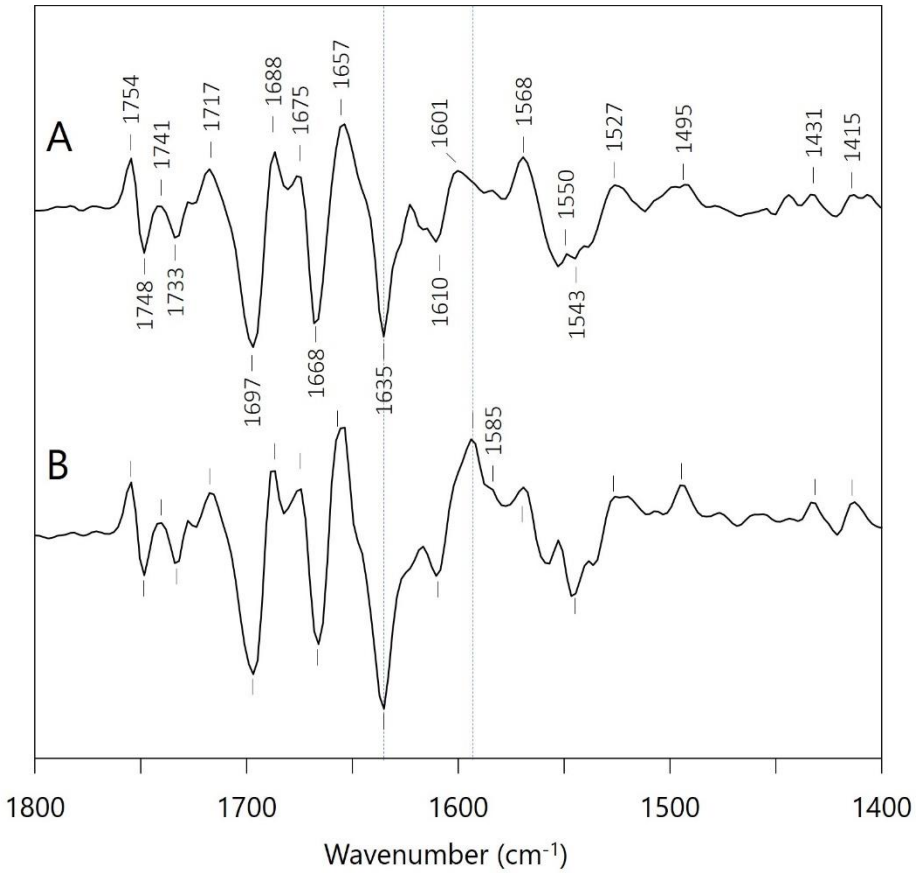

Figure 5.4 Time-resolved ($P700^+A_1^-$ – $P700A_1$) FTIR DAS at 77 K for WB673F mutant PSI with exogenous PhQ added. PhQ was added to WB673F mutant PSI that had been first pre-flashed for 4 h at RT. A WB673F mutant PSI + PhQ, where PSI was cooled in the dark prior to measurement. B Same samples as in A except the WB673F + PhQ PSI was pre-flashed again for 4 h at RT prior to freezing. Dotted *gray* lines are shown at 1635 and 1594 cm^{-1}.

5.4 Discussion

The rate of forward ET from A_1^- to F_X on the B-branch is roughly an order of magnitude larger than for the corresponding ET on the A-branch. Given the similarity in edge-to-edge distances between PhQ on either branch and F_X, the order of magnitude difference in the ET rate is likely due to a difference in midpoint potentials (E_m) between the PhQ's on each branch. Based on kinetic simulations, this difference is approximately ~50 mV [35, 86, 166]. Such a difference in E_m likely results because of a difference in the PhQ's interaction with the surrounding local

environment [167]. Electrostatic calculations have identified structural factors (such as side-chain orientation and protonation states) that could lead to differences in the E_m of PhQ on the A and B branches [50, 167]. However, how pigment-protein interactions impact the functionality of PhQ's as ET cofactors in the A_1 binding sites are still poorly understood. The work presented here suggests that TrpB673, a residue with indole side chain lying at a nexus between A_{1A}, A_{1B}, and F_X, could be important in impeding protonation of PhQ (on perhaps both branches) in PSI, by blocking access of water molecules to PhQ in the A_1 binding site.

5.4.1 Direct impact of WB673F on P700 and A_1

The photoaccumulated ($P700^+$ – P700) FTIR DS and the time-resolved ($P700^+A_1^-$ – $P700A_1$) FTIR DS suggests that the replacement of TrpB673 with Phe does not directly impact P700 or PhQ in the A_1 site as the vibrational frequencies associated with these pigments are unaffected by the mutation. The ($P700^+$ – P700) FTIR DS exhibits weak mutation-induced changes, but these changes are focused mostly in the regions where amide I and amide II protein absorption is expected. Therefore, these weak spectral changes are likely due to mutation-induced modifications in the protein environment surrounding F_X. Since TrpB673 is in the vicinity of A_{1A}, A_{1B}, and F_X cofactors, it is unlikely that P700 will be affected by the mutation. The A_1 pigments on the other hand, are within 4.0-6.5 Å of the indole side chain of TrpB673 (Fig. 5.1A). However, no significant changes are observed in the ($P700^+A_1^-$ – $P700A_1$) FTIR DS either. In particular, the C_1=O and C_4=O modes of A_{1A}^- are found at 1495 and 1415 cm^{-1}, respectively for both WT and mutant PSI. The transient absorption kinetics at 1697 cm^{-1} for PSI at 77 K indicate that $P700^+A_{1A}^-$ charge recombination in mutant PSI has a lifetime of ~390 µs (Fig. 5.5), compared to ~360 µs for WT PSI [59]. Within the noise level of the experiment, the time constants for WT and mutant PSI are the same, suggesting that the midpoint potentials of A_{1A} has not been affected by the mutation.

At 77 K, time-resolved measurements on cyanobacterial PSI from *S6803* probe the A-branch ET process only. As such the measurement does not provide insight to mutation-induced alterations associated with the PhQ on the B-branch.

5.4.2 Quinol formation in WB673F PSI

The time-resolved FTIR DS for pre-flashed WB673F PSI show that the exposure to actinic flashes at RT leads to formation of ^{3}P700 at 77 K, with the relative amplitude of the ^{3}P700 signals increasing as the time associated with pre-flashing increases. Since the ability of PSI samples to form ^{3}P700 can be reversed by addition of exogenous PhQ, and re-created with additional exposure to repetitive flashes at RT, ^{3}P700 formation is likely triggered by the conversion of PhQ in the A_1 binding site to the doubly protonated quinol form ($PhQH_2$).

$PhQH_2$ formation requires two electrons and two protons to be donated to a neutral state quinone [168]. Quinols will not accept any additional electrons (or protons), and can no longer function as ET cofactors. Quinol formation is an essential part of ET in type II RCs, such as PSII and purple bacterial RCs, in which a quinol formation in the Q_B binding site leads to dissociation of the pigment from the binding site, which can then be replaced by a quinone from the membrane pool [99, 169, 170]. However, quinones in the A_1 binding site in PSI (and in the Q_A binding site in type II RCs) function purely as 1-electron intermediaries in ET, and quinol formation would be detrimental to this function. The PSI RC, therefore, is designed to avoid or inhibit quinol formation in the A_1 binding site, even in the presence of nearby clusters of water molecules.

While double-reduction may be achievable through multiple rapid turnovers, double-protonation in PSI is a highly unlikely process, as PhQ in the A_1 binding site lacks a potential proton donor, or a proton transfer pathway to the carbonyl groups of PhQ. $PhQH_2$ formation can

be induced in WT PSI, but usually requires intense illumination in combination with harsh reducing agents while cooling [154, 164, 171-173].

Quinol formation in PSI can, however, be induced without harsh chemical pretreatments, when PhQ in the A_1 binding site is exchanged for a benzoquinone (BQ) [53, 174, 175]. In a process termed photo-inactivation [175], BQ in the A_1 binding site can be converted to benzoquinol (BQH_2) simply be subjecting PSI to a series of 10 Hz actinic laser flashes for 10 – 30 min [175]. In this process, water molecules between A_1 and F_X serve as proton donors [53]. These water molecules cannot donate protons when PhQ occupies the A_1 binding site, and it is the lack of an aromatic ring in the BQ species that opens a pathway for these water molecules to access and protonate BQ in the A_1 binding site. While this mechanism allows for the double-reduction/double-protonation of a BQ, BQH_2 formation in the A_1 site is highly inefficient, requiring thousands of actinic laser flashes at 10 Hz for complete photo-inactivation [53, 175]. It is important to note that the results from these studies of PSI with BQ incorporated, and other previous studies on PSI, indicate that the midpoint potential of the incorporated quinone is not the major factor that enables the double-reduction in A_1. The higher midpoint potentials of BQs, compared to PhQ, make the double-reduction process more thermodynamically favorable. However, previous studies on PSI with higher potential naphthoquinones (NQs) incorporated showed no sign of double-reduction of the NQ in the A_1 binding site. Through these observations, it was suggested that the double-reduction is triggered not by the midpoint potential, but by the structural modification that opens a protonation pathway.

The mechanism underlying $PhQH_2$ formation in WB673F PSI is likely similar to the photo-inactivation process observed for PSI with BQ's incorporated. The lifetime of the $P700^+A_1^-$ state is unaffected (Fig. 5.5, Table 5.1), which suggests that the midpoint potential of A_1 is relatively

unaffected and therefore not the direct cause of double-reduction. A source of protons for the $PhQH_2$ formation is likely the same set of water molecules that are involved in the BQH_2 formation process, given that TrpB673 is located within close proximity to these water molecules (Fig. 5.1B, C). While a similar photo-inactivation mechanism is expected, the yield of the photo-inactivation process is much less efficient for WB673F mutant PSI. For PSI with BQ incorporated, 10 – 30 min of exposure to 10 Hz actinic laser flashes was sufficient to achieve near-complete photo-inactivation. For WB673F mutant PSI, however, 16 h of exposure to actinic laser flash with similar repetition rate and energy only resulted in partial photo-inactivation (Fig. 5.3). Photo-inactivation in the WB673F mutant is considerably more inefficient than the already inefficient process in PSI with BQ incorporated. It seems likely therefore that the aromatic ring of PhQ can still restrict access of the water molecules to protonating the PhQ carbonyl groups. The WB673F mutation likely disrupts the environment of the water network between A_{1A}, A_{1B}, and F_X, such that these water molecules now have some increased capability of protonating PhQ in the A_1 binding site. Since forward ET proceeds predominantly (~95%) down the A-branch at 77 K [22], the water molecules are capable of protonating the A_{1A} PhQ. The very inefficient photo-inactivation process observed here might be partly due to the fact that it is PhQ in the A_{1A} binding site that is being probed, and this PhQ is somewhat distant from TrpB673, making any mutant induced structural alteration of the A_{1A} binding site smaller than for the A_{1B} binding site. If this is the case we would predict B-branch photo-inactivation with much fewer actinic laser flashes than is used here.

While we favor the mechanism described above for $^3P700$ formation, several other scenarios can be hypothesized. It is possible that the WB673F mutation causes an alteration of the branch utilization ratio, and the "disabled" PSI population corresponds to modified B-branch activity. Modification of the A/B-branching ratio in PSI due to specific experimental conditions

such as mutation or removal of ET cofactors, has been reported previously [176, 177]. It is possible that the WB673F mutation increases B-branch utilization, and that it is A_{1B} that is being doubly reduced and protonated through pre-flashing. For this hypothesis to explain the experimental data, however, it must be assumed that the mutation induced rerouting of ET has also modified A_{1B} such that the $P700^+A_{1B}^-$ recombination kinetics and ($P700^+A_{1B}^-$ – $P700A_{1B}$) FTIR DS are now nearly identical to that obtained for A_{1A} in native PSI. While the recombination kinetics and FTIR DS have not been reported for A_{1B} in native PSI at 77 K, the predicted difference in the midpoint potential [86] and previous EPR results for A_{1B} [176, 178, 179] suggest that the kinetic and spectral properties are likely different from those of A_{1A}. The $P700^+A_1^-$ kinetic and spectral properties identified for WB673F PSI in this study, however, indicate that the features observed are characteristic of A_{1A}.

An interquinone ET process, where an electron is transferred from $A_{1B} \rightarrow F_X \rightarrow A_{1A}$ [180], might also help explain mutation induced $^3P700$ formation. In this case one would also have to consider the case where the mutation modifies the midpoint potential of A_{1B} to be more positive than A_{1A}, and then also consider $A_{1A} \rightarrow F_X \rightarrow A_{1B}$ ET. Regardless of the ET direction, we will assume that interquinone ET is the mechanism underlying double reduction. In the first case, where ET proceeds from A_{1B} to A_{1A}, accumulation of doubly-reduced A_{1A} should also result in $P700^+A_{1B}^-$ recombination. In the second case, where ET proceeds from A_{1A} to A_{1B}, $P700^+A_{1B}^-$ recombination is expected in a large fraction of the non-flashed samples. So, in both cases, $P700^+A_{1B}^-$ recombination should be observed in either non-flashed or pre-flashed PSI samples. Such a conclusion is not compatible with the data presented here, where the observed kinetic or spectral features can only be assigned to A_{1A}.

Lastly, it is also possible that the mutation induces heterogeneous binding of PhQ in the A_1 binding site, creating populations with slightly different conformations. The "disabled" fraction, then, is the conformation that allows the double-reduction, while a fraction with active A_1 even after prolonged illumination is the conformation that does not allow the double-reduction. This scenario would explain why the fraction of disabled PSI remains relatively low, even after 16 h of pre-flashing. One limitation in this hypothesis is that while it assumes conformational heterogeneity at room temperature, there is no indication of such a heterogeneity at 77 K. If PhQ is bound in several different conformations in the A_1 binding site, then the semiquinone C=O modes (at 1495 and 1415 cm^{-1}) might be expected to shift in frequency for the different conformations, leading to multiple different bands, or at least some broadening of the main C=O bands. Such features are not observed in the FTIR DS for WB673F PSI (Fig. 5.3).

Confirmation of the double reduction/protonation of PhQ, and the exact mechanism of the process, requires further investigation. One possible approach to confirm the a PhQ protonation process is to repeat the experiments at different pH, as accumulation of $PhQH_2$ via protonation is expected to be accelerated at lower pH. Such a pH induced acceleration was observed in previous work where BQ in the A_1 binding site is doubly protonated [175].

Involvement of B-branch ET, or mutation modified branch utilization, could possibly be investigated using transient absorption spectroscopy at room temperature, with time resolution preferably below 1-2 ns.

5.4.3 The role of WB673 in PSI

Despite the interesting location of TrpB673 at the intersection of the A and B ET branches, the role of TrpB673 in PSI ET is not well understood. It has been suggested that the indole side chain of TrpB673 is involved in ET between A_1 and F_X [158]. This notion is unlikely, however, as

the A_1 – TrpB673 – F_X distances would suggest very rapid ET, much more rapid than the observed A_1^- to F_X ET rates of ~15 and 300 ns [34].

Previously TrpB673 has been replaced by Gly and it was shown that this mutation mainly affected B-branch ET [159]. So TrpB673 could impact the redox properties of A_{1B} (or of both A_{1B} and F_X), and could be involved in modulating the forward ET between A_{1B} and F_X. However, recent calculations have found that TrpB673 does not directly impact on the midpoint potential of A_{1B} [50]. It was suggested, however, that the presence of a bulky side chain introduced a twist in the protein backbone near the A_{1B} site, compared to the A_{1A} site where GlyA693 is found instead of Trp. [167]. For both the A_{1B} and A_{1A} sites, the amino acid adjacent to TrpB673 and GlyA693 is Ser (SerB672 and SerA692, respectively). In the A_{1A} site, SerA692 is oriented to form an H-bond with a nearby cluster of water molecules. In the A_{1B} site, however, because of the different twist in the backbone due to the steric effect of the bulky indole side chain of TrpB673, SerB672 has no partner to form an H-bond with. It is suggested that these differences in the local environment induced by TrpB673 cause a difference in the midpoint potentials between A_{1B} and A_{1A} [167].

Previous computational studies also highlight how the water clusters between A_{1A}, A_{1B}, and F_X contribute to the midpoint potentials of the A_1 pigments. The cluster of water molecules, surrounding TrpB673, are in H-bonding distance to AspB575. While no proton transfer pathway exists beyond AspB575, the interaction may result in protonation of AspB575, which in turn impacts the midpoint potentials of A_1 significantly [167]. If AspB575 remains protonated, the midpoint potentials of A_{1A} and A_{1B} are increased by 106 and 76 mV, respectively, compared to when AspB575 remains ionized [167].

The study presented here shows that the replacement of TrpB673 with Phe results in double-protonation of PhQ in the A_{1A} binding site. The only likely proton donors near PhQ are the

clusters of water molecules indicated in Fig. 5.1 B, C. A cluster of 5 water molecules [A5007, A5015, A5022, A5043, A5049] surround the A_{1A} site and 6 water molecules [B5018, B5019, B5030, B5055, B5056, B5058] for the A_{1B} site. TrpB673 bisects these water clusters. Although a Phe side-chain is likely bulky enough to sustain the original backbone twist, the observed PhQ protonation suggests mutation-induced alteration of these water clusters, which then allows PhQ protonation.

By combining the observations from this study, and the previous study on WB664G mutant PSI [159], and taking into account the computational studies on TrpB673 in PSI [50, 167], the role of TrpB673 in PSI ET can be summarized. The bulky indole side chain of Trp is required to create a backbone twist in the A_{1B} site, that is absent in the A_{1A} site, which contributes to a decrease in the A_{1B} midpoint potential [167]. The twist also allows for TrpB673 to face the direction of the groups of water molecules, and to be inserted between the A_{1A} and A_{1B} water clusters. The inserted TrpB673 stabilizes the water molecules to form fixed H-bond patterns for both the A_{1A} and A_{1B} sites. The presence of these water networks is important in two ways. AspB575 near A_{1A} is within H-bonding distance to one of the water molecules. The interaction of AspB575 with the water is important in controlling the protonation state of AspB575, which alters the midpoint potentials of A_1 by ~100 mV [167]. The fixed H-bonded network of water molecules is also important in preventing the water from accessing PhQ in the A_1 binding site and serving as proton donors. Availability of proton donors enable double-protonation of PhQ to form $PhQH_2$ and effectively disables A_1 as ET cofactor.

5.5 Conclusions

Time-resolved FTIR DS at 77 K has been used to study native and WB673F mutant PSI. The mutation does not directly impact the environment near PhQ in the A_1 binding site (or P700).

However, prolonged exposure to actinic laser flashes at RT results in PhQ protonation in the mutant but not in the WT. PhQ protonation is probed in PSI via ^{3}P700 formation at 77 K. Protonated PhQ ($PhQH_2$) in the mutant A_1 binding site can be reversed by incubating samples in the presence regular PhQ (at RT). Presumably PhQ has a greater affinity for the A_1 binding site compared to the protonated species. We suggest that water clusters near A_{1A}, A_{1B} and F_X are disturbed in the mutant allowing protons access to the PhQ carbonyl groups. TrpB673 plays a structural role in blocking proton access to the A_1 binding site. However, TrpB673 also has an electrostatic impact that could also modulate ET from A_1^- to F_X.

Supplementary Information

Reversible Inhibition and Reactivation of Electron Transfer in Photosystem I

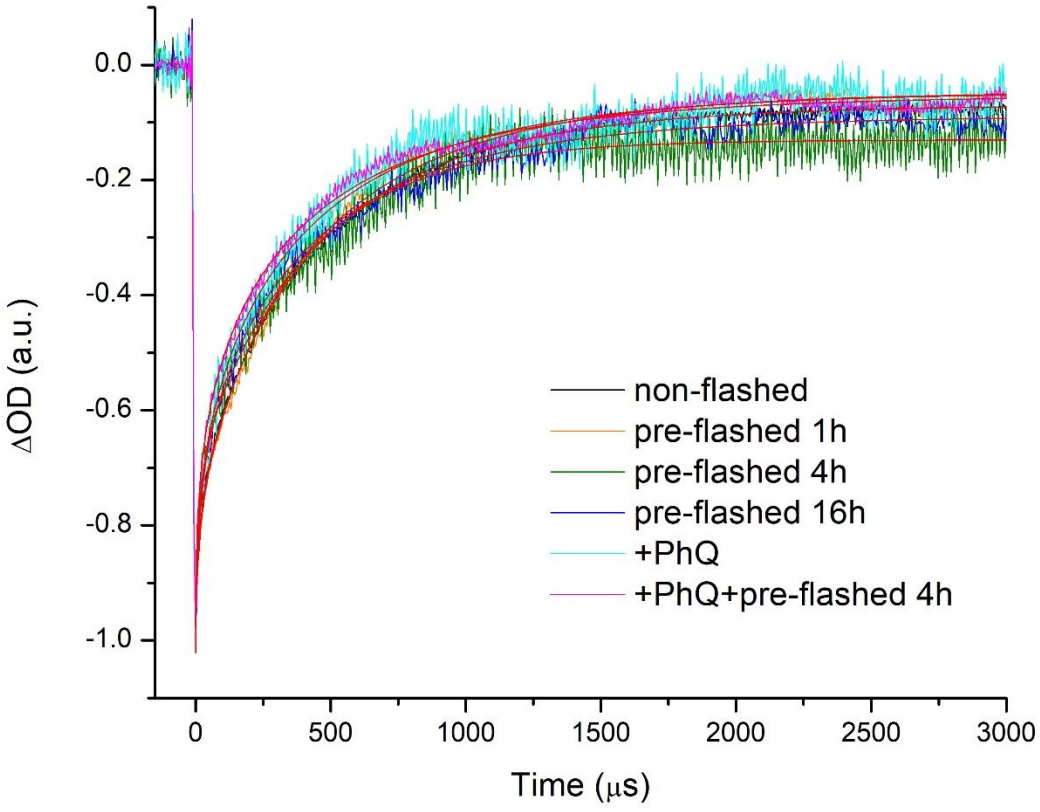

Figure 5.5 Transient absorption kinetics at 1697 cm^{-1} for WB673F PSI at 77 K. The kinetics are for non-flashed WB673F PSI (*black*), 1 h pre-flashed W673F PSI (*orange*), 4 h pre-flashed WB673F PSI (*green*), 16 h pre-flashed WB673F PSI (*blue*), 4 h pre-flashed WB673F PSI with PhQ re-incorporated (*cyan*), and 4 h pre-flashed WB673F PSI with PhQ re-incorporated and pre-flashed for another 4 h (*magenta*). The kinetic traces are globally fitted to two stretched exponential functions and a constant with unshared stretch factors and shared time constants. The time constant of the major decay phase was 389 ± 13 μs. The stretch factor of the major decay phase ranged from 0.75 to 1.00. The fitted functions for each kinetic trace are shown in red.

Table 5.1 Fit parameters obtained from globally fitting the transient absorption kinetics in Fig. 5.5 to two-stretched exponential functions and a constant with unshared stretch factors and shared time constants. The shared time constants were calculated to be t_1 = 389.31 ± 12.80 µs and t_2 = 13.47 ± 2.39 µs. The first time constant (t_1) is in the range expected for the lifetime of the $P700^+A_1^-$ recombination reaction. The time constant, t_2, is in the range expected for the lifetime the heating artifact typically found in time-resolved step-scan FTIR DS experiments on PSI at 77 K. The stretch factors and the signal amplitudes for t_1 and t_2 are listed as β_1 and β_2, and A_1 and A_2, respectively. The non-decaying component is listed as n.d. The absorption changes were normalized at t = 0 prior to fitting.

Samples	n.d. ($x10^{-2}$)	β_1	β_2	A_1 ($x10^{-2}$)	A_2 ($x10^{-2}$)
non-flashed	-6.85	0.81	1.00	-75.75	-14.04
pre-flashed 1h	-4.58	0.79	1.00	-80.10	-13.11
pre-flashed 4h	-13.02	0.99	0.76	-57.36	-27.72
pre-flashed 16h	-8.85	0.79	0.59	-65.72	-26.92
+PhQ	-4.66	0.77	0.41	-66.89	-30.24
+PhQ, pre-flashed 4h	-5.21	0.75	0.43	-61.45	-35.49

Estimating the ^{3}P700 fraction in ($P700^+A_1^-$ – $P700A_1$) FTIR difference spectra obtained using preflashed PSI samples.

Using the normalized DS/DAS in Fig. 5.3, a rough estimate of the relative fraction of PSI particles forming ^{3}P700 can be calculated.

This scaling is accomplished by considering the 1635(–) and 1594(+) cm^{-1} bands in the DS/DAS in Fig. 5.3. The 1635(–) cm^{-1} band is due to the 13^1 keto C=O group of the P_A pigment of P700. This band is present in both (^{3}P700 – P700) and ($P700^+A_1^-$ – $P700A_1$) DS, as it is due to P700 in the ground state. The 1594(+) cm^{-1} band is due to the 13^1 keto C=O group of the P_A pigment of ^{3}P700 and is absent in ($P700^+A_1^-$ – $P700A_1$) DS.

By scaling the (^{3}P700 – P700) DS (Fig. 5.3A) to the WT ($P700^+A_1^-$ – $P700A_1$) DS (Fig. 5.3B) at 1635(–) cm^{-1}, the two DS are normalized to the amount of spectral contributions from P_A. This assumes that the intensity of the 1635(–) cm^{-1} band is the same for both ^{3}P700 and $P700^+$. The scaled (^{3}P700 – P700) and ($P700^+A_1^-$ – $P700A_1$) DS represents spectra in which all of PSI forms either ^{3}P700 or $P700^+$.

In the DAS in Fig. 5.3C – 3F, both ^{3}P700 and P700$^+$ contribute to the spectra. Since the 1594(+) cm^{-1} band is present only in the (^{3}P700 – P700) DS, one can estimate the amount of ^{3}P700 mixed into the DAS by assessing the intensity of this band in the spectra obtained for PSI samples under preflash illumination. To achieve this, we interactively subtracted the (^{3}P700 – P700) DS from the (P700$^+$A$_1^-$ – P700A$_1$) DAS in such a way as to minimize any absorption feature at 1594 cm^{-1} (spectral subtraction to eliminate the 1594 cm^{-1} band). The scaling factor applied to the (^{3}P700 – P700) DS to achieve this result is then used to determine the relative ratio of P700$^+$ to ^{3}P700. For example, if no scaling is required, the ratio of P700$^+$ to ^{3}P700 is 1:1. As a second example, if the (^{3}P700 – P700) FTIR DS needs to be scaled by a factor of 2, then the ratio of P700$^+$ and ^{3}P700 is 1:2.

Using this approach, the relative extent of ^{3}P700 formation in each pre-flashed WB673F mutant PSI sample was estimated, and the results are listed in Table 5.2.

Table 5.2 Scaling factor (s.f.) applied to (^{3}P700 – P700) FTIR DS (Fig. 5.3A) in order to cancel the 1594 cm^{-1} band in pre-flashed mutant PSI (P700$^+$A$_1^-$ – P700A$_1$) DAS (Fig. 5.3C – 3F). The relative fractions undergoing ^{3}P700 formation calculated from the scaling factor are also indicated.

Samples	**s.f.**	**^{3}P700**
pre-flashed 1h	0.34	25.4%
pre-flashed 4h	0.62	38.3%
pre-flashed 16h	1.40	58.3%

The estimates indicated in Table 5.2 are somewhat crude given the assumptions involved in the calculation. The first assumption is that the 1635 cm^{-1} band in (^{3}P700 – P700) DS and (P700$^+$A$_1^-$ – P700A$_1$) DS has equal contributions from P700. This seems reasonable although the extent of underlying spectral contributions from other species is difficult to assess. For example, a very broad positive absorption band associated with a long wavelength electronic transition of

$P700^+$, with a peak near 3000 cm^{-1}, contributes to ($P700^+$ – P700) DS but not ($^3P700$ – P700) DS, and the contribution from this feature at 1635 cm^{-1} is difficult to assess. This feature could possibly be accounted for with appropriate baseline corrections, but that would then involve other assumptions. A second assumption is that the ($^3P700$ – P700) and ($P700^+A_1^-$ – $P700A_1$) DS/DAS are being normalized to total PSI concentration, and that the intensity of 1635 cm^{-1} band is associated with the same neutral P_A in both cases. This is likely not the case, as the $^3P700$ is localized on P_A while $P700^+$ is delocalized over P_B and P_A. It is probably the case that that the 1635 cm^{-1} band is less intense in the ($P700^+A_1^-$ – $P700A_1$) DS than in the ($^3P700$ – P700) DS. Therefore, the fractions indicated in Table 5.2 are probably overestimates, or upper bounds.

6 MONOMERIC AND TRIMERIC CYANOBACTERIAL PSI STUDIED USING TIME-RESOLVED STEP SCAN FOURIER TRANSFORM INFRARED DIFFERENCE SPECTROSCOPY

ABSTRACT

Time-resolved step-scan Fourier transform infrared (FTIR) difference spectroscopy (DS) has been used to study trimeric and monomeric cyanobacterial photosystem I (PSI) samples isolated from *Synechocystis* sp. PCC 6803. Time-resolved $P700^+A_1^-/P700A_1$ and photoaccumulated $P700^+/P700$ FTIR difference spectra were produced for both trimeric and monomeric PSI along with trimeric *menB*$^-$ PSI samples. Native PSI has a phylloquinone (PhQ) (2-methyl-3-phytyl-1,4-naphthoquinone) molecule in the A_1 binding site. *MenB*$^-$ PSI has a plastoquinone molecule (PQ) (2,3-dimethyl-1,4-benzoquinone) in the A_1 binding site.

By subtracting the $P700^+A_1^-/P700A_1$ DS from the $P700^+/P700$ DS, an A_1^-/A_1 FTIR DS was constructed. For trimeric PSI with PhQ incorporated, the A_1^-/A_1 FTIR DS displays bands at 1668 and 1627 cm^{-1} that are likely due to C_1=O and C_4=O stretching vibrations of neutral PhQ, respectively. For the monomeric PSI, either with PhQ incorporated or *menB*$^-$ PSI, the corresponding bands are at 1666 and 1627 cm^{-1}.

In monomeric or trimeric PSI with PhQ incorporated, anion vibration bands are found at 1495 and 1415 cm^{-1}, and are due to $C_1 \cdots O$ and $C_4 \cdots O$ stretching vibrational modes of PhQ^-, respectively. For *menB*$^-$ PSI with PQ in the A_1 binding site, the corresponding semiquinone bands are observed at 1490 and 1419 cm^{-1}.

At 77K, for monomeric and trimeric PSI with PhQ incorporated, $P700^+A_1^-$ radical pair recombination is characterized by a time constant of ~403 and ~431 μs, respectively. For *menB*$^-$ PSI with PQ incorporated, the radical pair recombination time constant is ~193μs [1]. At 298K,

$P700^+F_{A/B}^-$ radical pair recombination time constant for monomeric and trimeric PSI with PhQ incorporated is ~115 and ~154 ms. For *menB*$^-$ PSI with PQ incorporated, the recombination time constant is ~3 ms[1].

6.1 Introduction

In oxygen-evolving photosynthetic organisms, solar energy conversion occurs in two membrane-spanning protein complexes termed photosystem I and II (PSI and PSII)[4] [6]. In both PSI and PSI, light excitation of a special donor species results in the transfer of via a series of pigments across the thylakoid membrane [6]. Light-driven electron transfer (ET) in both photosystems is remarkably efficient [11, 12].

The pigments involved in ET are bound to a set of membrane-spanning proteins in what is called a reaction center (RC). The organization of the ET pigments in the PSI RC is shown in Fig. 6.1A, where electrons are transferred from P700 on one side of the membrane, to F_X on the other side [17]. P700 is thought to be a heterodimer of chlorophyll-*a* (Chl-*a*) and Chl-*a'* molecules [16] . Chl-a' is a 13^2 epimer of Chl-*a* [16]. A_0 is a monomeric Chl-*a* molecule that is considered to be the primary electron acceptor. The secondary electron acceptor A_1 in PSI is a phylloquinone molecule (2-methyl-3-phytyl-1,4-naphthoquinone, PhQ). F_X is an iron sulfur cluster [4Fe-4S]. The cofactors in PSI form two nearly symmetrical "branches" called the A and B-branch. The cofactor subscript in Fig. 6.1 refers to the relevant branch.

Following light excitation of P700 an electron is transferred and the secondary radical pair state $P700^+A_1^-$is formed in less than 50 picoseconds (ps) [20, 21]. Following this an electron is

[4] **Abbreviations:** ; C=O, carbonyl; Chl *a*, chlorophyll *a*; DS, difference spectra/spectrum/spectroscopy; ET, electron transfer; FTIR, Fourier transform infrared; H-bond, hydrogen bond; PhQ, phylloquinone (2-methyl-3-phytyl-NQ); PSI, photosystem I; PSII, photosystem II; RC, reaction center; S6803, *Synechocystis* sp. PCC *6803*; THF, tetrahydrofuran; TRSS, time-resolved step-scan; WT, wild type.

transferred from A_1 to F_X in either 20 or 300 nanoseconds (ns) on the B or A branch, respectively. The branching ratio is species dependent and temperature dependent. In cyanobacterial/green algal PSI the branching ratio is ~85:15/50:50 at room temperature (RT, ~298 K) [25, 27, 181]. At low temperature (LT, 77 K) forward ET is inhibited and $P700^+A_1^-$ recombination occurs with a time constant of ~350 microseconds (□s) [27, 28, 38, 149, 150]. Following the biphasic ET, forward ET from F_X^- to the terminal electron acceptors, F_A and F_B, happens on a sub-μs timeframe [29]. The $P700^+F_{A/B}^-$ radical pair in isolated cyanobacterial PSI particles undergoes charge recombination following ET to the terminal acceptors. With a time constant of ~50 – 100 ms, the recombination reaction happens *via* repopulation of A_{1A}^- [30-35].

ET in PSI becomes heterogeneous at cryogenic temperatures. P700+A1– charge recombination occurs in 35–38% of PSI particles, while $P700^+F_X^-$ charge recombination occurs in 13–21% [22, 36]. In the A-branch, both recombination reactions occur virtually completely through A_1 [37]. The irreversible $P700^+F_{A/B}^-$ state, which manifests as a reduction of signal amplitude in repetitive flash tests [22, 36], is formed by the remaining PSI particles (40–49%). The $P700^+A_{1A}^-$ state recombines with a time constant of 360 μs (micro-second) at 77K in cyanobacterial PSI particles and occurs preferentially down the A-branch [36, 38].

In cyanobacteria, PSI is found mainly in trimeric and slightly in monomeric form [89]. Recent studies has been reported that PSI also appears also in a tetrameric form in some filamentous cyanobacterial species [90, 91]. In mesophilic *Synechocystis* 6803, both trimeric and monomeric structure of PSI have been resolved at atomic level [92, 93]. It seems there are no critical structural changes in monomeric and trimeric PSI. However, the ratio of PSI trimer and monomer varies under different growth conditions, such as light intensity, temperature, and nutrients, etc. [94, 95]. It remains unknown how trimeric PSI is kinetically different than

monomeric PSI which can only be probed by using flash induced/photo-accumulated PSI samples followed by biophysical interrogations. We are interested in asking if there are PSI oligomerization state associated differences of electron transfer kinetics by using TRSS FTIR. Previous x-ray structural studies indicate there are no significant differences between PSI monomer and PSI trimer, however,

In this paper, we isolated and investigated cyanobacterial PSI (*Synechocystis* sp. PCC 6803 (*S6803*) using µs time-resolved step-scan FTIR difference spectroscopy (TRSS FTIR DS) at 77 K. The investigation was for both the neutral and anion states with three different PSI complexes Comparison has been performed between trimeric and monomeric native and non-native PSI (mutant cells, hereafter called *menB*$^{-}$ PSI). For wild type (WT) trimeric and monomeric PSI, phylloquinone (PhQ) (2-methyl-3-phytyl-1,4-naphthoquinone) molecule is occupied in the A_1 binding site and for the trimeric *menB*$^{-}$ PSI in which the *menB* gene is inactivated, PhQ synthesis is inhibited, and a plastoquinone molecule (PQ) (2,3-dimethyl-1,4-benzoquinone) is found to occupy the A_1 binding site instead of PhQ [55] (see Fig. 6.1 for molecular structures). In addition, we investigate the $P700^{+}F_{A/B}^{-}$ radical pair recombination time constant at RT and $P700^{+}A_1^{-}$ radical pair recombination time constant at LT for monomeric and trimeric PSI with PhQ incorporated at 298 K and compared the data with previous studies on trimeric PSI with PhQ and PQ incorporated. Previously studies are conducted on all these PSI complexes but to clarify some ambiguities on some bands in both neutral and anion spectral regions and comparisons have been made between WT trimeric and monomeric PSI and trimeric *menB*$^{-}$ PSI complexes from same *Synechocystis* sp. PCC 6803 (*S.6803)*. For observing bands associated to $P700^{+}$/P700 and neutral and reduced quinone bands, [$P700^{+}$ – P700] FTIR DS, [$P700^{+}A_1^{-}$ – $P700A_1$] DS and [A_1^{-} – A_1] FTIR DS are calculated.

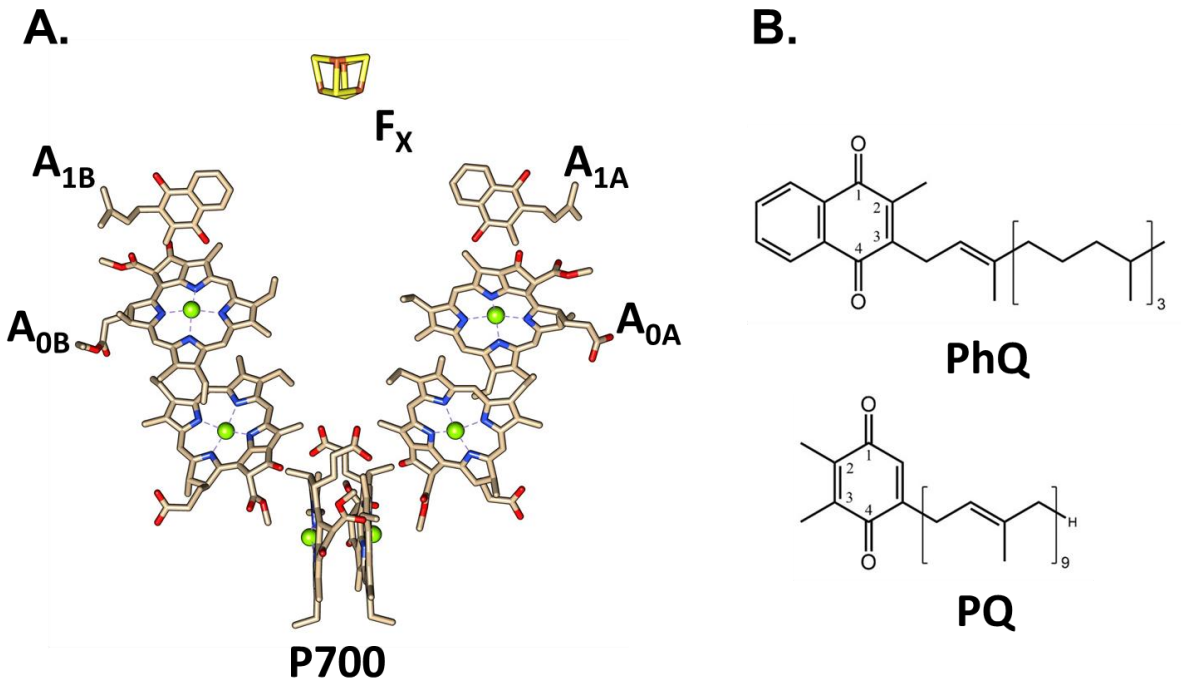

Figure 6.1 A. Arrangement of ET cofactors in PSI. Structure was derived from the 2.5 Å X-ray crystal structure of PSI from *Thermosynechococcus elongatus (T. elongatus)* (PDB file 1JB0 [16]) *(left)*. Structures of 2-methyl-3-phytyl-1,4-naphthoquinone (PhQ), and (2,3-dimethyl-1,4-benzoquinone) (PQ) *(right)*. Hydrocarbon chains of PhQ and Chl molecules are truncated for clarity. Subscripts A and B refer to the ET branch. B. Structures of 2-methyl-3-phytyl-1,4-naphthoquinone (PhQ), plastoquinone-9 (PQ).

6.2 Materials and Methods

Trimeric and monomeric PSI particles were prepared as described previously [182] after removal of PSII in a *Synechocystis* sp. PCC 6803 (*S.6803)* strain (HT-3) in which CP47 is C-terminally His_6-tagged [183]. Briefly, a bead-beater was used to break the cells under ice-bath to avoid temperature changes incurred by using French method. PSII was removed [184] by using Ni-NTA affinity column and the flowthrough was saved and diluted 5X before loading onto a sucrose gradient which was ultracentrifuged at 4° C for 18 hours. The lower and upper green bands were for trimeric and monomeric PSI [182]. The green bands were collected and save in -80°C until use. Absence of PSII in the isolated PSI samples was verified using 77 K fluorescence

spectrophotometry. Trimeric PSI particles isolated from *menB*$^{-}$ mutant cells from *Synechocystis* sp. PCC 6803 (*S6803*) were prepared as described previously [55].

Visible absorption spectra of PSI samples (see Fig. 6.2 (A,B,C)) and Chl-*a* concentration of PSI samples were obtained using a Shimadzu UV-1700 PharmaSpec UV-Visible spectrophotometer with 0.2 nm sampling interval. For FTIR spectroscopy PSI samples were centrifuged at 408,000g for 4 hours to obtain a soft pellet. The supernatant from this centrifugation was discarded but its absorption spectrum is shown in Fig. 6.2D. The soft pellet was placed on a calcium fluoride (CaF_2) window and 1 µL of phenazine methosulfate (PMS) (20 µM) and sodium ascorbate (20 mM) were added. The liquid was allowed to partially dry for 5 minutes, and then the sample was squeezed between two CaF_2 windows. The CaF_2 windows were sealed using vacuum grease. The sample thickness was adjusted to achieve an optical density close to 1.0 for the amide I band at ~1656 cm^{-1} (see Fig. 6.3 (A,B,C)). Samples were placed in a liquid nitrogen cooled cryostat (Cryo Industries of America Inc., Manchester, NH) for measurements at 77 K.

TRSS FTIR DS and photo-accumulated [$P700^{+}$ – P700] FTIR DS were obtained using a Bruker Vertex80 FTIR spectrometer (Bruker Optics, Billerica, MA) equipped with a mercury cadmium telluride (MCT) detector (Kolmar), as described previously [72-75]. In photoaccumulation measurements actinic illumination was from a 633 nm helium-neon laser at max 20mW output power(JDS Uniphase, Carlsbad, CA), enlarged to a spot size of 1 cm at the sample.

TRSS FTIR DS measurements with ~ 6.5 µs time resolution were undertaken at 77K. Spectra were collected in the 1950 – 1100 cm^{-1} range at 4 cm^{-1} resolution. Bandpass filters (2000 – 1000 cm^{-1}) were placed in front of the sample and in front of the MCT detector. The latter prevents stray actinic laser light from reaching the detector. The CaF_2 sample windows, as well as

the windows on the cryostat shroud, also block IR light below ~1100 cm^{-1}. Samples were excited with 532 nm laser pulses (~ 5 ns) at 10 Hz from a Minilite Nd:YAG laser (Continuum, San Jose, CA). A laser pulse intensity of ~ 0.785 mJ/cm^2 (1 mJ per pulse dispersed over a 1 cm diameter circle at the sample) was used.

Transient absorption changes are analyzed at 77K, and the lifetime associated with $P700^+A_1^-$ charge recombination is determined PSI samples using TR– FTIR measurements and flash induced absorption changes (kinetics) are analyzed at 810nm at 298K, and the lifetime associated with $P700^+F_{A/B}^-$ charge recombination is determined for PSI samples using pump-probe measurements.

6.3 Results and Discussions

6.3.1 Visible absorption spectra of PSI from S6803

Fig. 6.2, shows visible absorption spectra obtained for trimeric and monomeric PSI solution samples as received before wash at RT. A spectrum for trimeric *menB*$^-$ PSI is also shown in similar condition. All spectra show a Q_y absorption peak between 678–680 nm. Interestingly, the monomeric, but not the trimeric PSI samples display an absorption band at ~ 623 nm. As mentioned in the methods section, the visible absorption was measured for the supernatant obtained for monomeric WT PSI sample after 4 hours centrifugation. The peak at ~ 623 nm was observed that suggests the monomeric WT PSI sample contains contaminated phycobilin protein (Fig. 6.2D). This protein fell off during centrifugation as the peak corresponds to it reduces to a significant order of magnitude in the spectrum observed for WT monomeric PSI (Fig. 6.2B). All four spectra were normalized at 439 nm peak.

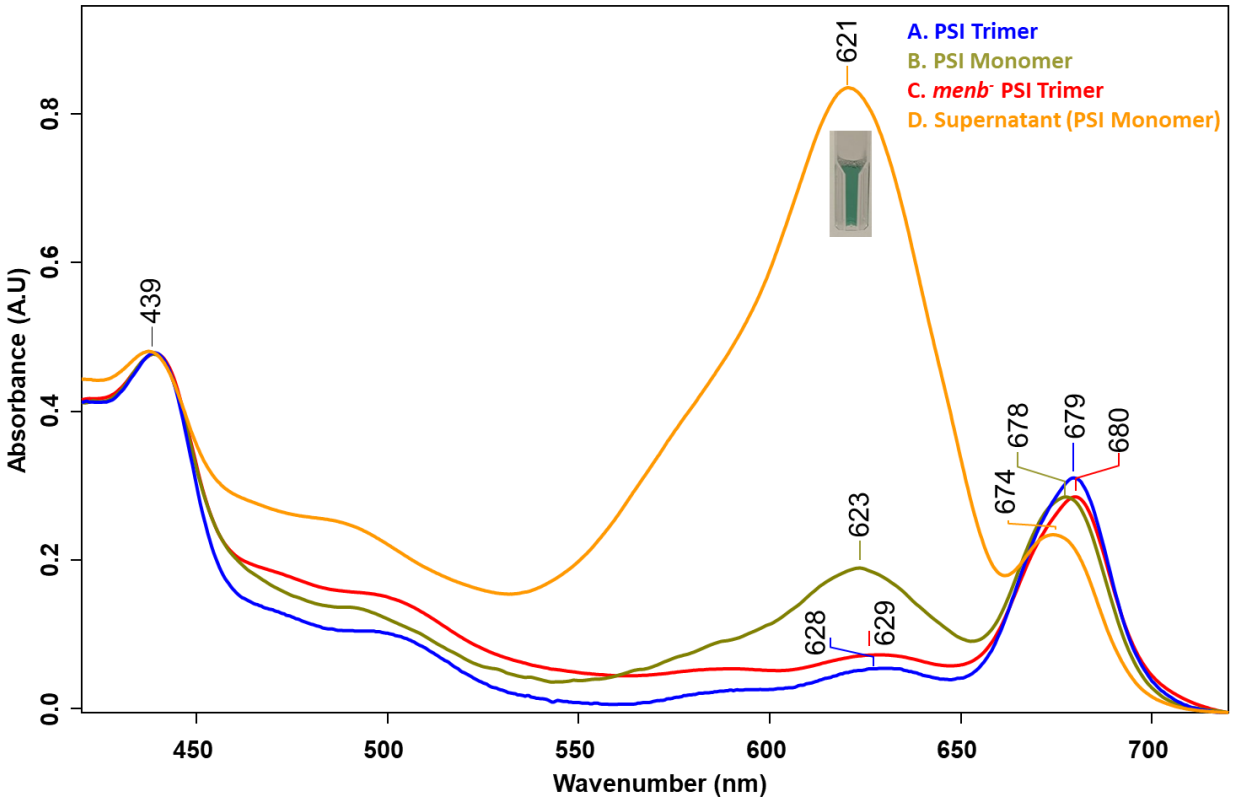

Figure 6.2 Visible absorption spectra of A. PSI Trimer (*blue*), B. PSI Monomer (with phycobiliproteins) (*gold*), C. *menB*⁻ PSI Trimer (*red*), and D. Supernatant from PSI Monomer after centrifugation (*orange*). Inset bluish solution sample in cuvette shows the supernatant collected from monomeric PSI after 4 hours of ultra-centrifugation. Normalized at 439 nm.

6.3.2 FTIR absorption spectra

FTIR absorption spectra in the 4000-1400 cm^{-1} spectral range for the three PSI complexes are shown in Fig. 6.3. Bands at 1656/1548 cm^{-1} are the well-known amide I/II bands. Bands at 2926/2855 cm^{-1} are due to CH_2 and CH_3 bands associated with lipids and protein. The broad band near 3400 cm^{-1} is associated with water O−H stretching and protein (Amide A) N−H stretching vibrations. The shape of this band is distorted due to very intense water absorption. A weaker water absorption band is observed near 2200 cm^{-1}. CO_2 absorption bands are observed near 2350 cm^{-1} in one of the spectra. CO_2 bands usually appear when spectra are measured using a poorly purged (or unpurged) spectrometer.

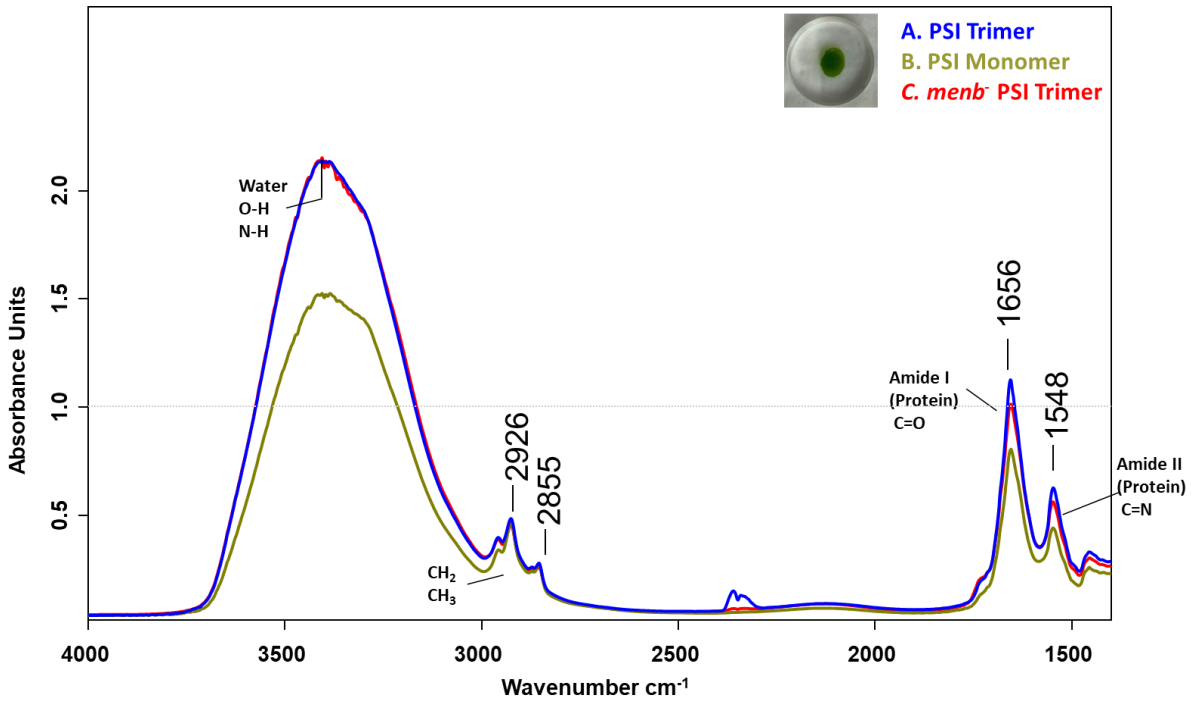

Figure 6.3 FTIR absorption spectra of trimeric A. WT *S6803*$_T$ (*blue*), B. WT *S6803*$_M$ (*gold*), C. *menB*$^-$ *S6803*$_T$ (*red*). Inset FTIR thin film shows how the FTIR sample looks like for the PSI particles prepared from PSI pellet and squeezed between two CaF_2 windows after 4 hours of ultra-centrifugation.

6.3.3 Photo-accumulated [P700$^+$−P700] FTIR DS of PSI S.6803

Fig. 6.4 shows [P700$^+$−P700] FTIR DS collected at 77K (*solid*) and 298K (*dotted*), for trimeric and monomeric PSI with PhQ in the A_1 binding site and trimeric *menB*$^-$ PSI with PQ in the binding site in *blue*, *gold*, and *red* font respectively in the 1800−1400 cm^{-1} spectral region. In all the spectra, bands due to P700 will exhibit negative intensity and P700$^+$ will exhibit positive intensity. All spectra are normalized from at 1723(+)/1696(−) cm^{-1} to make the P700 intensity the same for all four spectra. [P700$^+$−P700] FTIR DS for both trimeric and monomeric WT PSI and trimeric *menB*$^-$ PSI are very similar in the 1760−1600 cm^{-1} spectral region except mainly one negative band at around 1636 cm^{-1}. This trend is valid for both the LT and RT DS. This suggests that any interpretation of the difference bands in terms of precise bonding interactions is likely to be valid for both the WT PSI and *menB*$^-$ PSI at 77K and 298K. For WT and *menB*$^-$ S. 6803 particles

at LT (Fig. 6.4 and Table 6.1A), the 1756(+)/1748(−) and 1740(+)/1733(−) cm^{-1} difference bands were assigned to an upshift of the 13^3 ester C=O groups of the Chls of P700 upon cation formation [75, 161, 185]. According to a previous study, the two bands could indicate a dimeric nature for P700 due to absorption at two different frequencies, which results from different environmental perturbations on each of the Chl's of P700 [186]. Similar features were observed at RT (Fig. 6.4 and Table 6.1B) which appear at 1754(+)/1748(−) and 1742 (+)/1733(−) cm^{-1} for these PSI samples. Hastings et al. [185] suggested that the higher-frequency ester C=O mode is most likely to be free of H-bonding, i.e., the 1756(+)/1748(□) cm^{-1} at LT and 1754(+)/1748(□) cm^{-1} at RT difference bands are due to the 13^3 ester C=O group of Chl a on PsaB, while the 1740(+)/1733(□) cm^{-1} for LT and 1742 (+)/1733(−) cm^{-1} for RT bands are due to the 13^3 ester C=O group of Chl a' on PsaA (Fig. 6.4, Table 6.1), which is H-bonded, via a water molecule, to TyrA, SerA, or/and ThrA. However, a study conducted by Sivakumar et al. [72] in 2005, stated that ~1754(+)/~1748(−) cm^{-1} band cannot be due to a protein mode as this DS band is observed in the $[A_1^- - A_1]$ difference spectra (DS) (Fig. 6.5). In contrast we argue that these DS bands are due to 13^3 ester C=O group of Chl a on PsaB as these appeared at the same position for all three PSI samples with either PhQ or PQ incorporated.

The negative 1697/1698 cm^{-1} bands observed in spectra for both WT and *menB*$^-$ PSI at LT/RT (Fig. 6.4) respectively, are due to 13^1 keto C=O mode of one or both of the Chl-*a* molecules that are postulated to make up P700 [164, 185, 187]. Study conducted by Breton et al. and Hastings et al. [136, 164] suggest that the 1697(−) cm^{-1} band at LT and 1698(−) cm^{-1} band at RT result from a single Chl a keto C=O mode of a Chl a on PsaB, that upshifts to 1717(+) and 1719(+) cm^{-1} respectively for LT and RT upon cation formation (Fig. 6.4 and Table 6.1). A suggestion came into account by Hamacher et al. [187] that both 13^1 keto C=O modes of both Chls of P700

contribute to the ~1697(−) cm^{-1} band at LT and RT where that one C=O group upshifts to ~1718 cm^{-1} is likely due to the 13^1 keto C=O mode of Chl a on PsaB while the other downshifts to ~1686 cm^{-1} due to the 13^1 keto C=O mode of Chl a′ on PsaA, which is H-bonded to ThrA739 upon cation formation. Though this piece of information is not directly from experimental data, it indeed brings some light to analyze this phenomenon. In fact, this hypothesis helps resolve the discrepancies between FTIR and EPR data, as it suggests quite an asymmetry in the charge distribution over the Chls of P700. This hypothesis could also indicate that much of the charge on P700+ is located on PsaB (as this mode upshifts upon cation formation), in agreement with magnetic spectroscopic data. Furthermore, given the above hypothesis, the similarity in the frequency of the C=O modes in the ground state indicates that ThrA provides a relatively weak H−bond [185]. By fitting the data at 1697 cm^{-1} at LT to single stretched exponential function with unshared stretch factor and shared time constant, the lifetime of the major decay phase is calculated to be ~431 μs for WT trimeric PSI and ~403 μs for WT monomeric PSI (Fig. 6.7). Previous studies by Agarwala et al. [74] and Makita et al. [1] suggest the similar lifetime for WT trimeric PSI from the same strain of *S6803*. The lifetime for trimeric *menB*$^-$ PSI with PQ was studied by Makita et al. [1] and found to be ~193 μs. By fitting the data for RT recombination kinetics to single stretched exponential function with unshared stretch factor and shared time constant, the lifetime of $P700^+F_{A/B}^-$ radical pair is found to be ~154 ms for WT trimeric PSI and ~115 ms for WT monomeric PSI (Fig. 6.8). Previously conducted study by Makita et al. [1] suggest the similar lifetime for WT trimeric PSI at RT along with the lifetime for trimeric *menB*$^-$ PSI with PQ which was found to be ~ 3 ms. For both the LT and RT, the recombination rate is higher for WT trimeric PSI compared to the monomeric one which is the indication that midpoint potential for monomeric PSI would be lower but very close to PhQ which is around -465 mV.

Another negative band at LT for trimeric and monomeric PSI and trimeric *menB*$^{-}$ PSI at 1636 and 1638 cm^{-1} and for RT at 1640 cm^{-1} for all these three PSI, are due to 13^{1} keto C=O group of the other Chl a on PsaA of P700 which upshift to 1655 cm^{-1} at LT and 1654 cm^{-1} at RT upon cation formation for all these PSI samples [164] (Fig. 6.4, *Solid and dotted* and Table 6.1). Thus the 13^{1} keto C=O group of P_A/P_A^+ is downshifted ~60 cm^{-1} compared to P_B/P_B^+, indicating that the 13^{1} keto C=O of both P_A and P_A^+ is very strongly H-bonded to ThrA [75, 164].

Both the 13^{1} keto C=O modes of P_A and P_B under both temperatures are upshifted about 20 cm^{-1} upon cation formation with similar intensity indicating that the cation charge is evenly distributed or delocalized over both the P_A and P_B pigments of P700 [164]. This statement is not in well agreement with conclusions drawn from EPR measurements, which, however, indicate the charge is predominantly localized on the P_B pigment [188].

In IR absorption spectra in Fig. 6.3, the band at 1548 cm^{-1} and in FTIR DS in Fig. 6.4, the set of features at ~1536 (−)/1549(+) cm^{-1} are due to amide II protein absorption bands which are associated to NH bending modes of the protein backbone [189]. The contribution from the Amide I absorption bands are associated with peptide C=O stretching vibrations which are mainly observed between the 1660–1645 cm^{-1} region for α-helices [189]. The bands observed for parallel and anti-parallel β-sheet structures are observed at lower (1630 cm^{-1}) and higher (1690 cm^{-1}) frequencies respectively [189, 190].

Upon comparing the static measurements for all these three PSI samples at LT and RT, it was found that the major bands in photo-accumulated [P700^{+} – P700] FTIR DS having no significant changes except few bands actually have ($\pm$2) cm^{-1} up or down shifted due to having either monomeric/trimeric PSI with PhQ or PQ incorporated.

Table 6.1 C=O modes frequencies (in cm^{-1}) of the P_A and P_B pigments of P700 of the WT monomeric and trimeric PSI and *menb*$^-$ trimeric PSI from *S6803* at 77K.

Band Assignments	P700	Band Assignments	P700$^+$
13^3 -methylester C=O of P_A	1733 (–)	13^3 -methylester C=O of P_A^+	1740 (+)
13^3 -methylester C=O of P_B	1748 (–)	13^3 -methylester C=O of P_B^+	1756 (+)
13^1 -keto C=O of P_A	~1636 (–)	13^1 -keto C=O of P_A^+	1655 (+)
13^1 -keto C=O of P_B	1697 (–)	13^1 -keto C=O of P_B^+	1717 (+)

Table 6.2 C=O modes frequencies (in cm^{-1}) of the P_A and P_B pigments of P700 of the WT monomeric and trimeric PSI and *menb*$^-$ trimeric PSI from *S6803* at 298K.

Band Assignments	P700	Band Assignments	P700$^+$
13^3 -methylester C=O of P_A	1733 (–)	13^3 -methylester C=O of P_A^+	1742 (+)
13^3 -methylester C=O of P_B	1748 (–)	13^3 -methylester C=O of P_B^+	1754 (+)
13^1 -keto C=O of P_A	1640 (–)	13^1 -keto C=O of P_A^+	1654 (+)
13^1 -keto C=O of P_B	1698 (–)	13^1 -keto C=O of P_B^+	1719 (+)

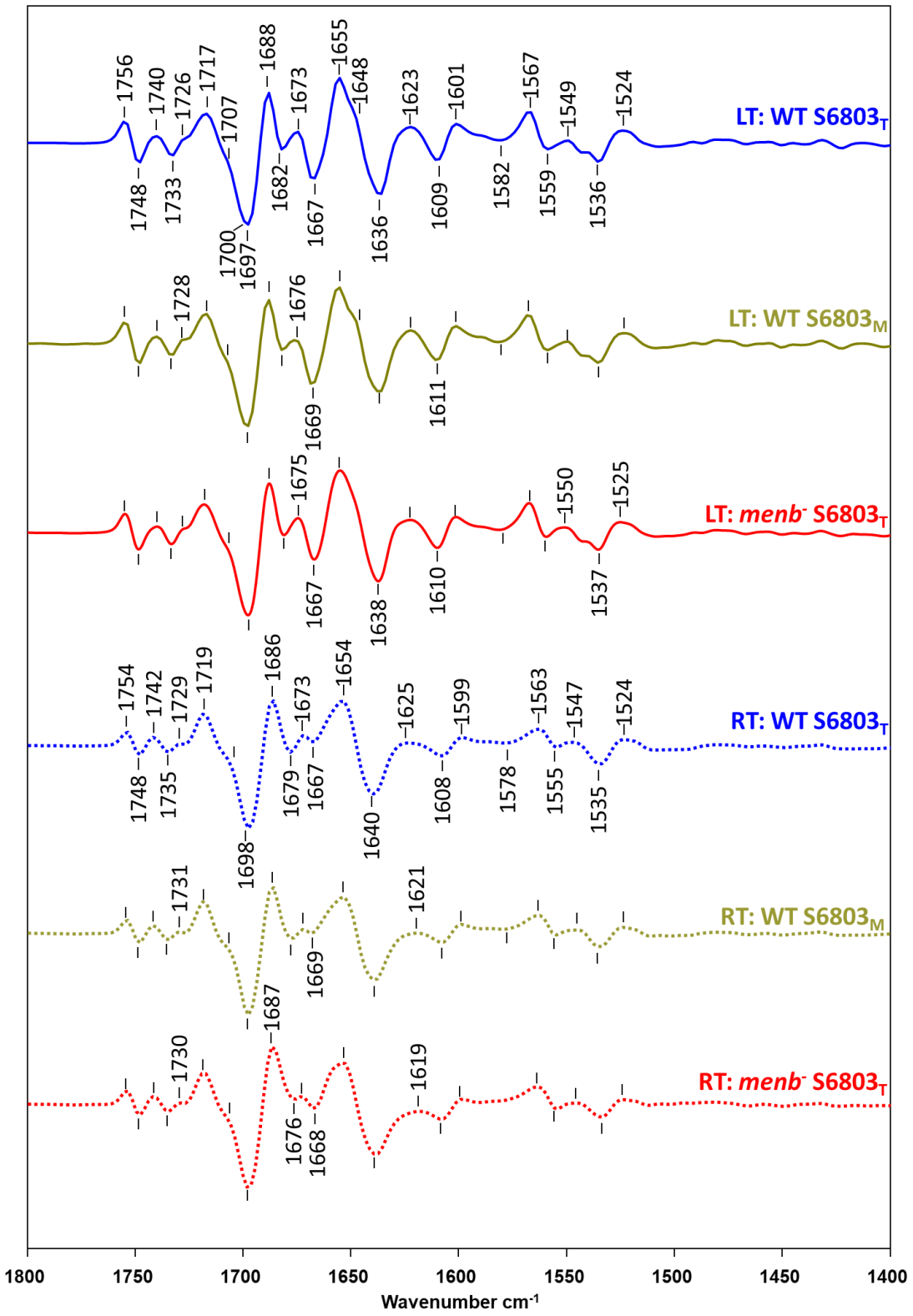

Figure 6.4 Photo-accumulated [$P700^+$ – P700] FTIR DS in the 1800-1400 cm^{-1} regions obtained at 77K (*Solid*) and 298K (*dotted*) using A. WT *S6803*$_T$ (*blue*), B. WT *S6803*$_M$ (*gold*), C. *menB*$^-$ *S6803*$_T$ (*red*). Normalized at 1723 and 1695 cm^{-1}.

6.3.4 (P700$^+$A$_1^-$ – P700A$_1$) DS of PSI from S6803

Fig. 6.5 shows time-resolved [P700$^+$A$_1^-$/P700A$_1$] FTIR DS obtained for monomeric and trimeric PSI with PhQ incorporated and trimeric *menB*$^-$ PSI with PQ incorporated. The bands between 1760–1600 cm^{-1} assigned as neutral bands mainly correspond to the vibrational modes due to P700$^+$/P700 and nearby pigments and protein impacted by P700$^+$A$_1^-$ radical pair formation. The bands between 1550–1400 cm^{-1} have relatively small contributions from P700$^+$/P700. In this less crowded region, [P700$^+$A$_1^-$/P700A$_1$] FTIR DS exhibit prominent positive bands which are absent in P700$^+$/P700 DS. These bands are attributed to the vibrational modes of the anionic quinones in the A$_1$ binding site [191].

An intense negative band at 1697 cm^{-1} is present in both [P700$^+$−P700] FTIR DS (Fig. 6.4) and [P700$^+$A$_1^-$/P700A$_1$] FTIR DS (Fig. 6.5), which is associated with P700$^+$A$_1^-$ charge recombination. Specifically, the 1697($\pm$1) cm^{-1} band in Fig. 6.4 and Table 6.1 is well known to be associated with the 13^1 keto C=O group of the P$_B$ pigment of P700 [136, 164]. To further analyze the bands associated with the semiquinones, [A$_1^-$ – A$_1$], difference spectra (DS) were performed. Fig. 6.6 shows [A$_1^-$ – A$_1$] FTIR DS that are calculated by subtracting [P700$^+$ – P700] FTIR DS from [P700$^+$A$_1^-$ – P700A$_1$] DS. All [P700$^+$ – P700] FTIR DS and [P700$^+$A$_1^-$ – P700A$_1$] DS spectra are normalized from at 1723(+)/1696(−) cm^{-1} to make this difference intensity the same for all spectra before producing [A$_1^-$ – A$_1$] FTIR DS.

The time-resolved (P700$^+$A$_1^-$ – P700A$_1$) FTIR DS for WT trimeric (Fig. 6.5, *blue*) and monomeric (Fig. 6.5, *gold*) PSI are similar between the 1760-1600 cm^{-1} neutral spectral region except few minor changes in terms of intensity and ratio. One major change was observed in terms of intensity of positive bands at 1656 cm^{-1}, i.e., the intensity is more prominent for the monomeric PSI sample compared to trimeric one. A minor difference was observed at 1689 and 1675 cm^{-1}in

terms of the ratio for the bands, i.e., the 1689 cm^{-1} band is slightly higher in intensity compared to 1675 cm^{-1} for trimeric PSI. This phenomenon, however, is reversed for monomeric PSI. Another change observed for the intense negative band at 1698 cm^{-1} for trimeric sample downshifted 1 cm^{-1} to 1697 cm^{-1} for monomeric sample, whereas the corresponding positive band upon cation formation at 1716 cm^{-1} for trimeric sample upshifted 2 cm^{-1} to 1718 cm^{-1} for monomeric sample. The changes observed between the two trimeric PSI samples with PhQ (Fig. 6.5, *blue*) and PQ (Fig. 6.5, *red*) are mainly between the 1690–1635 cm^{-1} spectral region. The sets of features for WT trimeric PSI at 1689(+)/1683(–)/1668(–) cm^{-1} I are downshifted 2 cm^{-1} to 1687(+)/1681(–)/1666(–) cm^{-1} for trimeric *menB*$^{-}$ PSI, whereas the difference features for WT PSI at 1656(+)/1635(–) cm^{-1} are their upshift of 2/3 cm^{-1} to 1658(+)/1638 (–) cm^{-1} for *menB*$^{-}$ PSI. Previous study by Makita et al. [65] suggests that the 1668(–)/1635(–) cm^{-1} bands are tentatively assigned to the C_1=O and C_4=O stretching vibrations (Fig. 6.5 and Table 6.2). These assignments indicate a 30 cm^{-1} separation between the C_1=O and C_4=O modes.

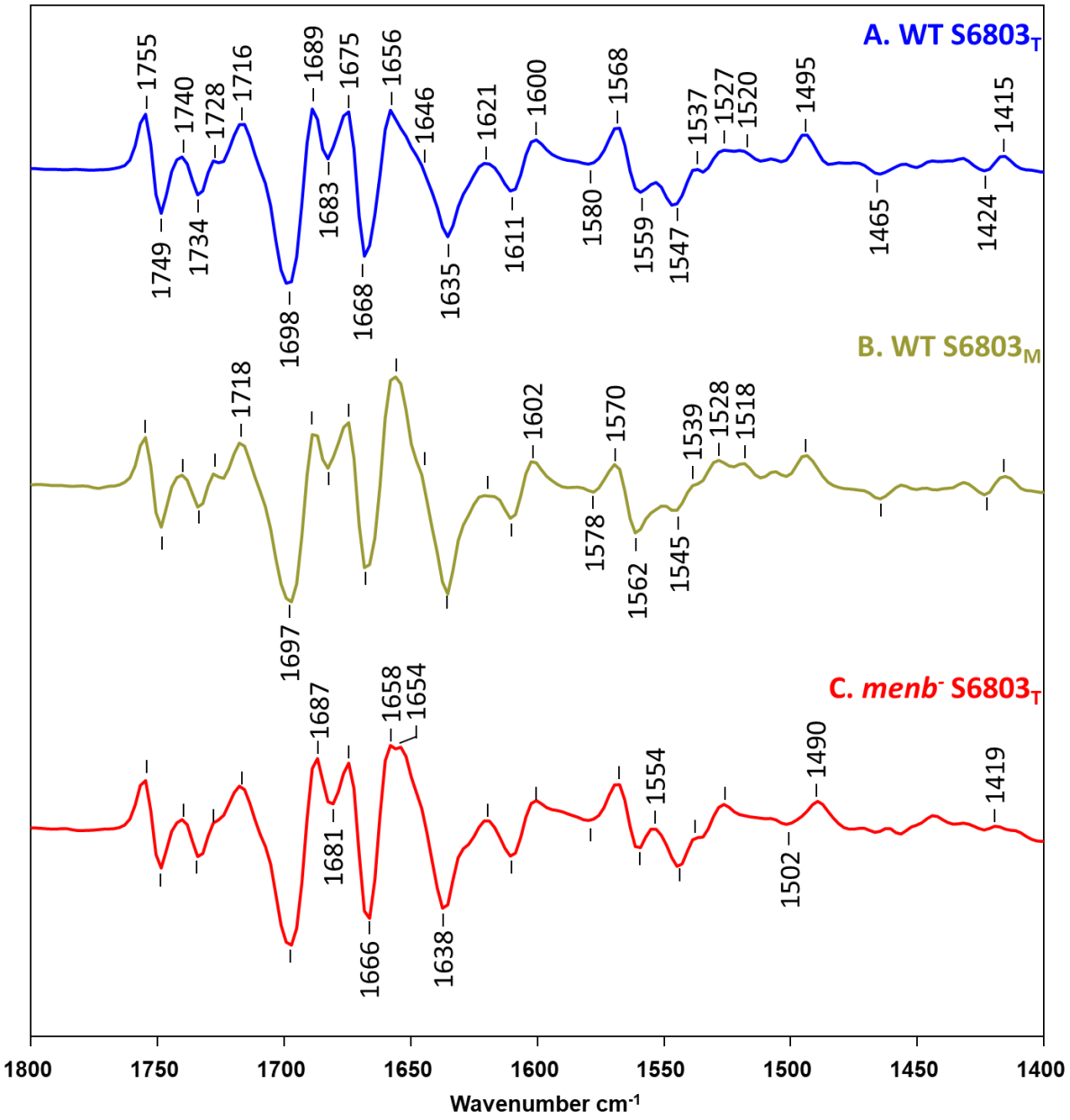

Figure 6.5 Time-resolved [$P700^{+}A_1^{-}$ – $P700A_1$] FTIR DS in the 1800-1400 cm^{-1} regions obtained at 77K for A. WT *S6803*$_T$ (*blue*), B. WT *S6803*$_M$ (*gold*), C. *menB*$^{-}$ *S6803*$_T$ (*red*). Normalized at 1723 and 1695 cm^{-1}.

In the time-resolved ($P700^{+}A_1^{-}$ – $P700A_1$) FTIR DS in Fig. 6.5, the anion spectral region between 1550–1400 cm^{-1} displays positive bands associated with A_1^{-} at 1495 and 1415 cm^{-1} due to the C_1 ⎓ O and C_4 ⎓ O stretching vibrations of PhQ^{-} (Table 6.2), respectively [44, 135]. The C_4⎓ O stretching vibrations are downshifted relative to the C_1 ⎓ O vibration due to H-bonding.

The characteristic bands of A_1^- at 1495 and 1415 cm^{-1} also found in spectra of monomeric PSI with PhQ (Fig. 6.5 *gold*) incorporated indicate that the monomeric PSI does not impact the environment of PhQ in the A_1 binding site (Fig. 6.5 *blue*), in either the neutral or the anion state. The time resolved spectra for trimeric *menB*$^-$ PSI with PQ incorporated (Fig. 6.5 *red*) exhibit clear differences compared to the WT PSI spectra. Among the two positive bands for PhQ^- at 1495 and 1415 cm^{-1}, the band due to $C_1 \overset{\cdots}{=} O$ stretching vibrations is downshifted 5 cm^{-1} to 1490 cm^{-1} and the band due to $C_4 \overset{\cdots}{=} O$ stretching vibrations is upshifted 4 cm^{-1} to 1419 cm^{-1} upon having PQ in the binding site (Table 6.2). Such an assignment suggests that the $C_1 \overset{\cdots}{=} O$ and $C_4 \overset{\cdots}{=} O$ stretching modes are separated by 71–80 cm^{-1}, compared to ~30 cm^{-1} in the neutral state (Table 6.2). As the separation in anion state is more than doubled compared to the neutral state, so the suggestion is that hydrogen bonding is weaker for the neutral state compared to the anion state, indicating radical-induced proton dynamics associated with the quinone in the A_1 binding site in PSI.

6.3.5 (A_1^- – A_1) FTIR DS for PSI from S6803

To further aid in the identification of neutral and anion states quinone bands, [A_1^- – A_1] FTIR DS (Fig. 6.6) is constructed. $P700/P700^+$ contributions are relatively absent from [A_1^- – A_1] FTIR DS (Fig. 6.6), although contributions from protein modes influenced by A_1 production are still present. Fig. 6.6 shows [A_1^- – A_1] FTIR DS with PhQ incorporated in WT trimeric/monomeric PSI (Fig. 6.6, *blue/gold*) and PQ incorporated in *menB*$^-$ PSI ((Fig. 6.6, *red*).

Neutral state bands

Multiple difference features are observed in the neutral quinone spectral region (~1700 – 1600 cm^{-1}) in (A_1^- – A_1) DS. For PhQ, in (A_1^- – A_1) DS, intense negative bands can be identified at 1748, 1691, 1668, 1654, and 1627 cm^{-1} in the neutral quinone region (Fig. 6.6 *blue*). However, similar sets of negative bands are also observed in (A_1^- – A_1) DS for the rest of the two PSI

complexes (Fig. 6.6). This region coincides with the range of amide I band, any changes experienced by the nearby amino acids due to the anion formation are also expected to produce difference features in this range. Furthermore, $P700^+$ and P700 exhibit many intense bands in this range, so, differences between the statically collected ($P700^+$ – P700) DS and the time-resolved counterpart, (A_1^- – A_1) DS are expected to reflect these features as well. In such a scenario, it is nearly impossible to assign the neutral bands for quinones from this DS. One possible solution is to produce DDS (Double Difference Spectra) to cancel out all the bands not resulting from quinones but from having less sets of measurements. It is, however, very difficult to produce such spectra in this study, which makes the spectra smaller and noisier. However, we are indeed able to assign the neutral bands for all three PSI complexes by referring to a recent study by Makita et al. [65].

Ester and keto C=O bands

In WT trimeric PSI [A_1^- – A_1] FTIR DS (Fig. 6.6 *blue*), a difference band is clearly observed at 1755(+)/1748(–) cm^{-1} which is unaffected for both the WT monomeric PSI and trimeric *menB*$^-$ PSI (Fig. 6.6 *gold* and *red*). This band is associated with the 13^3 ester C=O vibrational mode of a Chl a pigment (Table 1) that is impacted by the negative charge on the quinone. Given its proximity to A_1 and a previous study, the pigment is most likely the A_0 [72]. As we already observed the contribution of A_0 to this DS, we conclude that the positive band at 1710 cm^{-1} for both the PhQ spectra is due to 13^1 keto C=O of A_0 [65] which is upshifted 2 cm^{-1} to 1712 cm^{-1} upon having PQ in the binding site.

C_1=O and C_4= O modes of neutral PhQ, PQ

In the neutral region, the $C_1 = O$ stretching mode for trimeric and monomeric PSI with PhQ incorporated and trimeric PSI with PQ incorporated are observed at 1668/1666/1666 and the

$C_4 = O$ stretching mode are at 1627 cm^{-1} for all three samples (Fig. 6.6 *blue, gold, red* respectively). However, for WT monomeric PSI, this 1627 cm^{-1} band is split into two bands at 1635 and 1627 cm^{-1}. The neutral region bands associated with $C_1 = O$ and $C_4 = O$ modes are in well agreement with several previous studies [72, 78, 192]. In one study [72], the $C_1 = O$ band appearing at about 1656 cm^{-1} has ~10 cm^{-1} downshift. The $C_4 = O$ band is observed with a downshift of ~8 cm^{-1} at 1627 cm^{-1} when compared to another research [65], in which the band appears at 1635 cm^{-1}.

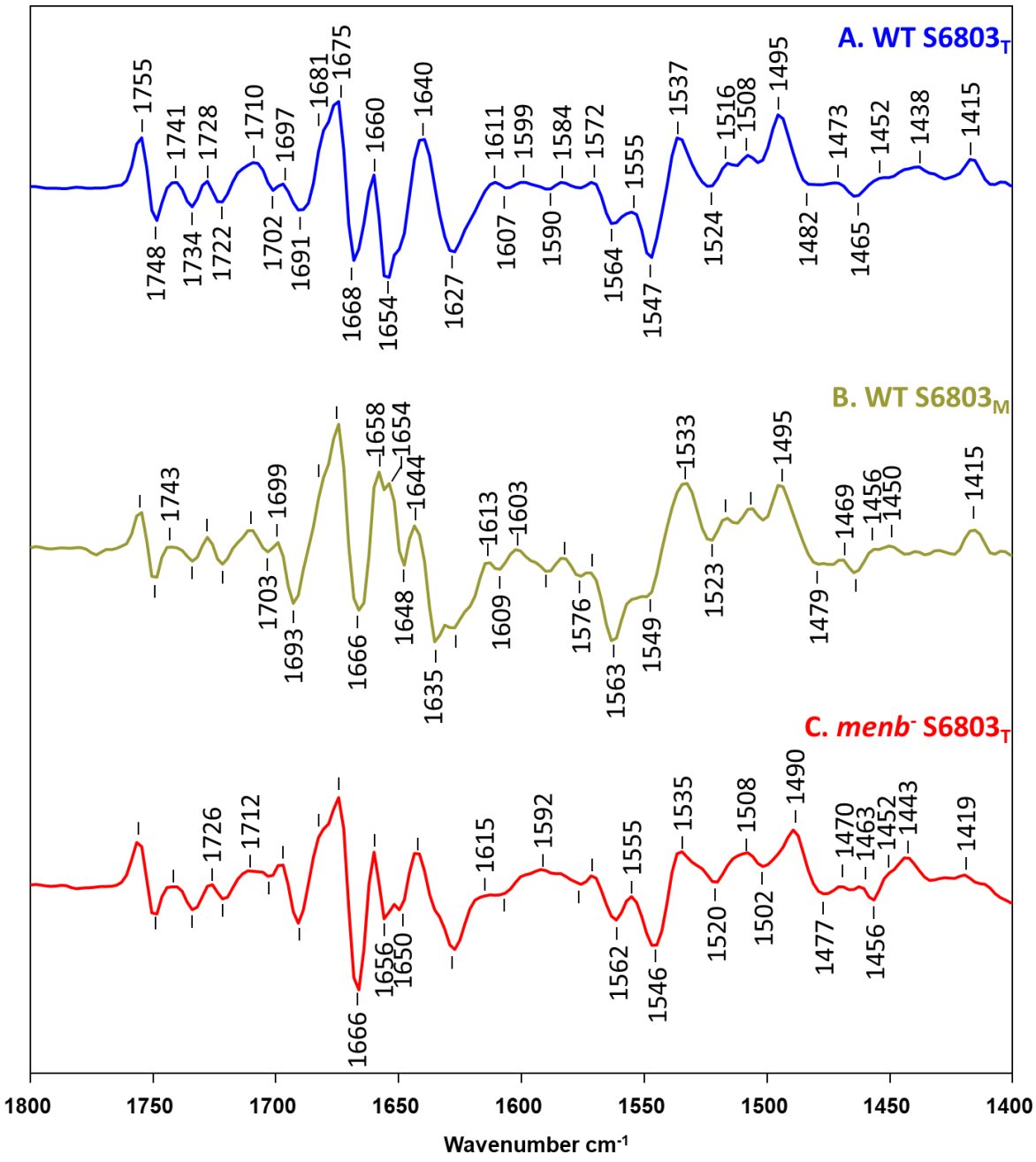

Figure 6.6 [$A_1^- - A_1$] FTIR DS in the 1800-1400 cm^{-1} regions obtained at 77K for A. WT *S6803*$_T$ (*blue*), B. WT *S6803*$_M$ (*gold*), C. *menB*$^-$ *S6803*$_T$ (*red*). Normalized at 1723 and 1695 cm^{-1}.

Other neutral bands

Previous studies [44, 72, 136] using DDS suggested that a negative band at 1657–1648 cm^{-1} is a candidate for the C_1=O vibration of PhQ, however, those studies did not consider the possibility of removing artifactual contributions to the spectra from sample heating [44]. Even

though a band at 1657–1654 cm^{-1} was suggested to be due to neutral PhQ in the literature, we, however, cannot assign this with full confidence, simply because heating usually gives rise to large absorption changes in the amide I region, near 1656 cm^{-1}. The band appeared at WT trimeric/monomeric/*menB*$^-$ PSI at 1654/1648/~1656 splits to two bands at 1656,1650 cm^{-1}. Another minor broad positive band was identified as neutral PhQ mode at 1600 ($\pm$) cm^{-1} in the [$P700^+A_1^-$ – $P700A_1$] FTIR DS of WT trimeric PSI (Fig. 6.5, *blue*) which is appeared at 1611 cm^{-1} in the [A_1^- – A_1] FTIR DS (Fig. 6.6, *blue*) which is upshifted 2 and 5 cm^{-1} to 1613 and 1615 cm^{-1} for WT monomeric and *menB*$^-$ trimeric PSI respectively (Fig. 6.6, *gold, red*). Previous three-level QM/MM calculation has predicted a minor band in this region (calculated at 1614 cm^{-1}) due to C_2=C_3 stretching for neutral PhQ [44].

Amide bands

An intense difference is visible for both the trimeric PSI at 1691(−)/1675(+) cm^{-1} with a shoulder at 1681 cm^{-1} in the PSI [A_1^- – A_1] FTIR DS (Fig. 6.6 *blue, red*). The negative band at 1691 cm^{-1}, however, upshifted to 1693 cm^{-1} for monomeric PSI (Fig. 6.6 *gold*). As this difference feature is nearly at the similar position in all these three DS, we conclude that this feature is most likely due to an amide I protein vibration, but not due to the quinone in the binding site. Similar observation has been made for another difference feature at 1547(−)/1537(+) cm^{-1} for WT trimeric PSI which is shifted little bit at 1549(−)/1533(+) cm^{-1} for WT monomeric PSI and 1546(−)/1535(+) cm^{-1} for *menB*$^-$ trimeric PSI. Previous study [65] indeed confirmed that this difference feature is associated with an amide II protein vibration which is in great agreement with the band observed from Fig. 6.3. A negative band was observed at 1668 cm^{-1} in WT trimeric PSI (Fig. 6.6 *blue*) which is downshifted 2 cm^{-1} to 1666 cm^{-1} for other two PSI complexes. It seems that this feature is associated with an amide I protein vibration, in agreement well with a previous

study [65]. Please note that the band appeared in all these PSI IR absorption spectra at 1656 cm^{-1} in Fig. 6.3.

Anion state bands

The anionic semiquinone bands are expected in the ~1520 –1400 cm^{-1} range of [A_1^- – A_1] FTIR DS (Fig. 6.6). Between this region, the spectral contributions by $P700^+$/P700 is relatively small in PSI. In this less-clouded ~1520 – 1400 cm^{-1} region, both [$P700^+A_1^-$ – $P700A_1$] (Fig. 6.5) and [A_1^- – A_1] (Fig. 6.6) DS exhibit prominent positive bands that are absent in [$P700^+$ – P700] DS. These bands are attributed to the vibrational modes of the anionic quinones in the A_1 binding site [191]. Detailed analysis and discussion of these bands are presented in the later sections.

C_1 ⋯O and C_4⋯ O modes of anion PhQ^-, PQ^-

From the [A_1^- – A_1] FTIR DS, the bands associated to C_1⋯O stretching mode for trimeric (Fig. 6.6 *blue*) and monomeric (Fig. 6.6 *gold*) PSI with PhQ incorporated and trimeric PSI with PQ (Fig. 6.6 *red*) incorporated are observed at 1495/1495/1490 cm^{-1} and the C_4⋯O stretching mode are at 1415/1415/1419 cm^{-1} respectively in the anion region. In a previous study of monomeric and trimeric WT PSI [72], the C_1⋯O and C_4⋯O stretching mode are stated to be observed at 1495/1414 cm^{-1} respectively in the anion region from [A_1^- – A_1] FTIR DS (Table 2). Similarly, from this study we observed that C_1⋯O and C_4⋯O stretching modes in the anion region for monomeric and trimeric WT PSI appeared at the same position, but in comparison with the previous study by Sivakumar et al. [72] the band for C_4⋯O stretching mode is upshifted about 1 cm^{-1}.

Other anion bands

In the [A_1^- – A_1] FTIR DS (Fig. 6.6) , a less pronounced band is observed at 1473 cm^{-1} for WT trimeric PSI which is shifted -4 cm^{-1} for WT monomeric PSI to 1469 cm^{-1} and downshifted 3

cm^{-1} for trimeric PSI with PQ (Fig. 6.6 *red*) to 1470 cm^{-1}. This band came into light from a recent study in 2020 by Makita et al. [65] where the band appeared at 1476 cm^{-1} in the DDS. More recent studies involving QM/MM higher level calculations that consider the effects of surrounding protein environment has predicted that this band is composed mostly of CH_3 bending mode at C_2 position [156].

Table 6.3 C=O modes frequencies (in cm^{-1}) for the neutral and anion states of the WT monomeric and trimeric PSI and *menb*$^-$ trimeric PSI from *S6803* at 77K.

Neutral	***WT S6803$_T$***	***WT S6803$_M$***	***menb$^-$ S6803$_T$***
$C_1 = O$	1668	1666	1666
$C_4 = O$	1635	1635	1638
C=O Band Separation (in cm^{-1})	33	31	28
Anion	***WT S6803$_T$***	***WT S6803$_M$***	***menb$^-$ S6803$_T$***
$\mathbf{C_1 \cdots O}$	1495	1495	1490
$\mathbf{C_4 \cdots O}$	1415	1415	1419
$\mathbf{C \cdots O}$ Band Separation (in cm^{-1})	80	81	71

6.4 Conclusions

Two native PSII complexes (trimeric and monomeric) and one non-native trimeric PSI complex were used in this study to create [$P700^+$ – P700], [$P700^+A_1^-$ – $P700A_1$] and [A_1^- – A_1] FTIR DS to identify the anion and neutral quinone bands. In the anion region, no notable difference is observed between WT trimeric and monomeric PSI, consistent with a previous structural studies of monomeric PSI (Netzer-EL 2019 Frontier in Plant Science), however, we indeed found that the $C_1 \cdots O$ stretching mode is downshifted to 1490 cm^{-1} and $C_4 \cdots O$ stretching mode is upshifted to 1419 cm^{-1} ((Fig. 6.6) when A_1 binding site is occupied by PQ.

In the neutral region, due to spectral range overlap with the highly absorbing amide I and intense difference features from $P700^+$/P700, as well as protein-heating artifact with microsecond lifetime, the [$P700^+A_1^-$ – $P700A_1$] and [A_1^- – A_1] FTIR DS is highly impacted and as a result not all the bands were visible from this study. This problem could be solved by producing DDS by

subtracting [$P700^+A_1^-$ – $P700A_1$] DS of one species from the [$P700^+A_1^-$ – $P700A_1$] DS from species. We could not complete such analysis here due to not having plenty of datasets, and by doing so the spectra become smaller and noisier. Even after that, we are still able to observe all the major bands at the neutral region those are due to the $C_1 = O$ and $C_4 = O$ stretching modes that are appeared at 1668/1666/1666 and 1627 cm^{-1} respectively for trimeric and monomeric PSI with PhQ incorporated and trimeric PSI with PQ incorporated.

In the neutral region, the $C_1 = O$ and $C_4 = O$ stretching modes are separated by 30 cm^{-1} which is considerably less than the 71–80 cm^{-1} found for similar modes of trimeric and monomeric PhQ− and trimeric PQ−. This is the indication that the hydrogen bonding is weaker for the neutral state compared to the anion state, indicating radical-induced proton dynamics associated with the quinone in the A_1 binding site in PSI.

The life time of $P700^+F_{A/B}^-$ radical pair at RT and $P700^+A_1^-$ radical pair at LT for monomeric/trimeric PSI with PhQ incorporated are observed to be ~115 ms/~154 ms and ~403 μs/~431 μs from this study which are in great agreement with the previous study of trimeric PSI by Makita et al. [1]. For both the LT and RT, the recombination rate is higher for WT trimeric PSI compared to the monomeric one which is the indication that midpoint potential for monomeric PSI would be lower but very close to PhQ which is around -465 mV. Previous research on PSI trimer and monomer in *Synechocystis* 6803 didn't find significant structural differences between them, partly due to their limited structural resolution. However, our interrogations on PSI by using TRSS FTIR give more dynamic picture of their functionality in their different oligomerization states. Even the differences are small, they indeed represent their functional differences.

Supplementary Information

Monomeric and Trimeric Cyanobacterial PSI Studied Using Time-Resolved Step Scan Fourier Transform Infrared Difference Spectroscopy

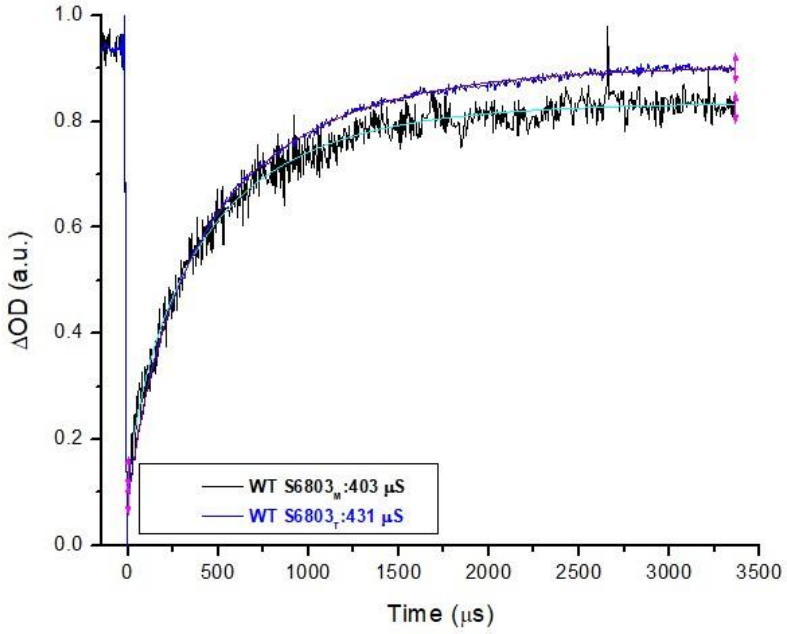

Figure 6.7 Transient absorption kinetics at 1697 cm^{-1} for trimeric (*blue*) and monomeric (*black*) PSI with PhQ at 77K. The kinetic traces are independently fitted to single stretched exponential function with unshared stretch factor and shared time constant. The time constant of the fit was ~431 μs for WT trimeric PSI and ~403 μs for WT monomeric PSI. The fitted functions for each kinetic trace are shown in solid red and cyan for trimeric and monomeric PSI respectively.

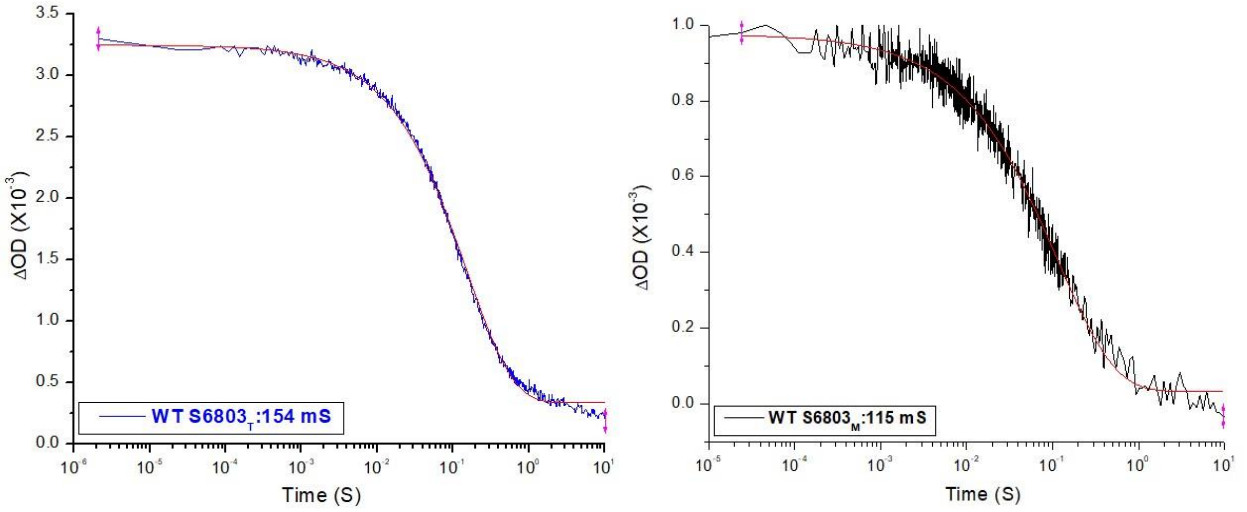

Figure 6.8 RT recombination kinetics at 810 nm for trimeric (*left*) and monomeric (*right*) PSI with PhQ. Data was collected over several time windows and is plotted here on a logarithmic timescale. Fitted curves are also shown. . The kinetic traces are independently fitted to single stretched exponential function with unshared stretch factor and shared time constant. The time constant of the fit was ~154 ms for WT trimeric PSI and ~115 ms for WT monomeric PSI. The fitted functions for each kinetic trace are shown in solid red.

7 DISSERTATION SUMMARY AND FUTURE RESEARCH

7.1 Summary and Conclusions

This dissertation presents studies of the bioenergetics of photosynthetic reaction center (RC) including the vibrational properties of quinones using FTIR DS in combination with DFT based vibrational frequency calculations. In the native system, phylloquinone molecule (PhQ, 2–methyl–3-phytyl–NQ) occupies the A_1 (secondary electron acceptor) binding site. To investigate the molecular properties of PhQ or other non-native quinones in the A_1 binding site in PSI, one possible way is to study PSI where the native quinone is replaced with a foreign one using *menB*$^-$ mutant cells where PhQ biosynthesis has been disrupted. To carry out this research, cyanobacterial cells from *Synechocystis* sp. PCC 6803 (*S6803*) is used in which the *menB* gene is inactivated where plastoquinone (PQ) molecule is occupied into the A_1 binding site instead of PhQ [55]. In this mutated PSI, PQ is weakly bound and is easily replaced by overnight incubating PSI particles in the presence of a large molar excess of different NQs [35, 43, 56]. This is an ideal and minimally disruptive incorporation method, where *menB*$^-$ PSI samples with different quinones incorporated being used in several spectroscopic studies [43, 44, 57-62]. These studies have shown that for all non−native incorporated quinones the position and orientation of the C=O groups is essentially the same as it is for PhQ [44].

In order to fully understand the energetics and the molecular mechanisms of a specific electron acceptor (in our study it is A_1, only two A_1 per RC) in the binding site of the huge protein complex, spectroscopic techniques with high temporal and spectral resolutions are required. As a result, in this dissertation, TRSS time-resolved step-scan (TRSS) FTIR difference spectroscopy (DS) at 77 K were used to study the binding site of Trimeric PSI with 10 different NQs, monomeric PSI with native PhQ and a PSI mutant in which TrpB673 was changed to Phe. To help assess and

assign bands in the difference and double difference spectra, density functional theory based vibrational frequency calculations for the different quinones in solvent, or in the presence of a single asymmetric H–bond to either a water molecule or a peptide backbone NH group, were undertaken. Recent studies using resolved step scan (TRSS) FTIR DS of PSI with foreign quinones incorporated, together with QM/MM vibrational frequency calculations, have allowed a more detailed understanding of the vibrational properties of quinones in the A_1 binding site in both the neutral and reduced states [44, 63, 64]. One suggestion from these studies is that asymmetric H–bonding to the C_4=O of PhQ is stronger in the anion state compared to the neutral state [44].

This chapter will provide the summary of the previous chapters including the quinones in solution and in the binding site of PSI along with the DFT based vibrational calculations. This chapter will conclude with a proposal of the future research, supported by preliminary data.

In the first two chapters of the published works (chapter 2 and 3) we present FTIR absorbance spectra for four halogenated NQs, 2-chloro-1,4-naphthoquinone (2ClNQ), 2-bromo-1,4-naphthoquinone (2BrNQ), 2,3-dichloro-1,4-naphthoquinone (Cl_2NQ) and 2,3-dibromo-1,4-naphthoquinone (Br_2NQ) as well as three mythyl substituted NQs, 2-bromo-3-methyl-1,4-naphthoquinone (BrMeNQ), 2-chloromethyl-3-methyl-1,4-naphthoquinone (CMMeNQ) and 2-ethylthio-3-methyl-1,4-naphthoquinone (ETMeNQ) in tetrahydrofuran (THF). The FTIR spectra of the substituted naphthoquinones (NQs) were compared to FTIR spectra of 2-methyl-3-phytyl-1,4-naphthaquinone (phylloquinone (PhQ)) and 2-methyl-naphthoquinone (2MNQ). To aid in the assignment of bands in the experimental spectra, density functional theory (DFT) based vibrational frequency calculations for all the substituted NQs were undertaken. By calculating normal mode potential energy distributions, unambiguous quantitative band assignments were made. The calculated and experimental spectra together make predictions about what may be observable in

time resolved FTIR difference spectra obtained using PSI with the different NQs incorporated. Time resolved FTIR difference spectra are presented that support these predictions. From this study, for PhQ in THF a band is observed at 1469 cm^{-1}, which is absent in FTIR spectra for the other quinones, indicating that this band is due to vibrations associated with the phytyl tail of PhQ. The spectra for all nine NQs display one or two intense absorption bands in the 1684–1647 cm^{-1} region that are due to either the coupled or separate vibrations of the C=O groups of the NQs. For PhQ, DMNQ and 2MNQ a single band associated with an antisymmetric coupled vibration of both C=O groups is observed. For 2ClNQ/2BrNQ in THF this band is split into two bands, the higher/lower frequency band being due to the C_1=O/C_4=O stretching vibration, respectively. For BrMeNQ/ETMeNQ, two bands are observed with the higher/lower frequency band being due to a C_4=O/ C_1=O stretching vibration (the C_1=O group was considered adjacent to the methyl in this study). For CMMeNQ, one relatively broad band is due to the carbonyl stretching modes. FTIR spectra for all nine quinones also display an intense absorption band (two bands for 2MNQ2ClNQ/2BrNQ) in the 1297–1267 cm^{-1} region that is due mainly to a $\nu(C–C)_q$ stretching vibration. The spectral features for the different NQs presented here are discussed and it is indicated that these features will prove useful for the interpretation of bands in time resolved FTIR difference spectra that will be obtained in the future for PSI samples with the different NQs incorporated into the A_1 protein binding site.

Following the work presented in chapter 2 and 3, in chapter 4 microsecond TR FTIR DS has been used to study PSI photosynthetic reaction centers with four high-potential, 1,4-naphthoquinones incorporated into the A_1 binding site which are 2–chloro–NQ (2ClNQ), 2–bromo–NQ (2BrNQ), 2,3–dichloro–NQ (Cl_2NQ), and 2,3–dibromo–NQ (Br_2NQ). Most of the previous FTIR studies focused on the vibrational properties of (relatively) low potential NQs

incorporated into PSI. This chapter focuses on studies of PSI with a series of high potential halogenated NQs incorporated. There are many reasons for this; one of them being that it is, or will be, possible to study PSI at RT, as microsecond $P700^+A_1^-$ recombination is still the dominant decay pathway at RT in PSI with high potential NQs incorporated [22]. In preparation for these future TRSS FTIR studies, we first present here studies at 77 K, focusing on the quinones in the reduced states [1, 57, 63, 65, 66]. Preliminary data on one of these four halogenated NQs are presented at RT. "Foreign minus native" double difference spectra (DDS) were constructed by subtracting difference spectra for native photosystem I (with phylloquinone in the A_1 binding site) from corresponding spectra obtained using photosystem I with the different quinones incorporated.

In this study, comparing these DS and DDS to other previously published DDS and also considering corresponding calculated DDS we were able to assess the normal modes of the halogenated NQs in PSI, and from that make inferences on the orientation of the incorporated monosubstituted halogenated NQs in the A_1 binding site. We identified two new bands for PhQ^- in the anion region (~1520 and ~1456 cm^{-1}). We also identified several of the bands for the incorporated halogenated NQs for the first time. For the two mono-substituted halogenated NQs, $2ClNQ^-$/$2BrNQ^-$, the $C_1{=}O$ vibrational mode appears to contain contributions from two species, which via calculation we suggest that there are two different orientations for the incorporated NQs. Thus, the Cl or Br atom of the mono-substituted NQs appears not to have a specific preference for being meta or ortho to the H bonded C=O group. For PSI with all the five NQs (PhQ^-, $DMNQ^-$, $2MNQ^-$, $2ClNQ^-$, $2BrNQ^-$, Br_2NQ^-) incorporated, the frequency and intensity of the $C_1{=}O$ mode followed the same pattern in both the experimental and calculated spectra. From the anion state, it was observed that $C_1{=}O$ and $C_4{=}O$ modes are separated by ~ 76 (±7 cm^{-1}) for all the five NQs which are reduced to ~63 (±3 cm^{-1}) for the two di-substituted halogenated NQs. For neutral PhQ

in PSI the C_1=O and C_4=O modes are separated by ~30 cm^{-1}. The reduced frequency separation might indicate that the H-bonding is stronger in the anion state.

In chapter 5, like chapter 4, TRSS FTIR DS is used at 77K to study native and WB673F mutant PSI. The study presented here shows that the replacement of TrpB673 with Phe results in double-protonation of PhQ in the A_{1A} binding site. The only likely proton donors near PhQ are the clusters of water molecules indicated in Fig. 5.1 B, C. TrpB673 bisects these water clusters. Although a Phe side-chain is likely bulky enough to sustain the original backbone twist, the observed PhQ protonation suggests mutation-induced alteration of these water clusters, which then allows PhQ protonation. By combining the observations from this study, and the previous study on WB664G mutant PSI [159], and taking into account the computational studies on TrpB673 in PSI [50, 167], the role of TrpB673 in PSI ET can be summarized. The bulky indole side chain of Trp is required to create a backbone twist in the A_{1B} site, that is absent in the A_{1A} site, which contributes to a decrease in the A_{1B} midpoint potential [167]. The twist also allows for TrpB673 to face the direction of the groups of water molecules, and to be inserted between the A_{1A} and A_{1B} water clusters. The inserted TrpB673 stabilizes the water molecules to form fixed H-bond patterns for both the A_{1A} and A_{1B} sites. The presence of these water networks is important in two ways. AspB575 near A_{1A} is within H-bonding distance to one of the water molecules. The interaction of AspB575 with the water is important in controlling the protonation state of AspB575, which alters the midpoint potentials of A_1 by ~100 mV [167]. The fixed H-bonded network of water molecules is also important in preventing the water from accessing PhQ in the A_1 binding site and serving as proton donors. Availability of proton donors enable double-protonation of PhQ to form $PhQH_2$ and effectively disables A_1 as ET cofactor.

In this study, we suggest that the mutation does not directly impact the environment near PhQ in the A_1 binding site (or P700). However, prolonged exposure to actinic laser flashes at RT results in PhQ protonation in the mutant but not in the WT. PhQ protonation is probed in PSI via ^{3}P700 formation at 77 K. Protonated PhQ ($PhQH_2$) in the mutant A_1 binding site can be reversed by incubating samples in the presence regular PhQ (at RT). Presumably PhQ has a greater affinity for the A_1 binding site compared to the protonated species. We suggest that water clusters near A_{1A}, $A_{1B,}$ and F_X are disturbed in the mutant allowing protons access to the PhQ carbonyl groups. TrpB673 plays a structural role in blocking proton access to the A_1 binding site. However, TrpB673 also has an electrostatic impact that could also modulate ET from A_1^- to F_X.

Similarly in chapter 6, TRSS FTIR DS and construction of DDS and DS are used to study two native PSI complexes (trimeric and monomeric) and one non-native trimeric PSI complex to identify the anion and neutral quinone bands. In addition, we investigate transient absorption changes, which are analyzed at 77K, and the lifetime associated with $P700^+A_1^-$ charge recombination is determined for the PSI samples using TR−FTIR measurements and flash induced absorption changes (kinetics). These changes are analyzed at 810nm at 298K, and the lifetime associated with $P700^+F_{A/B}^-$ charge recombination is determined for PSI samples using pump-probe measurements.

The study suggest that in the anion region, no notable difference is observed between WT trimeric and monomeric PSI, consistent with a previous structural studies of monomeric PSI (Netzer-EL 2019 Frontier in Plant Science), however, we indeed found that the $C_1{=}O$ stretching mode is downshifted to 1490 cm^{-1} and $C_4{=}O$ stretching mode is upshifted to 1419 cm^{-1} ((Figure 6) when A_1 binding site is occupied by PQ.

In the neutral region, due to spectral range overlap with the highly absorbing amide I and intense difference features from $P700^+/P700$, as well as protein-heating artifact with microsecond lifetime, the [$P700^+A_1^-$ – $P700A_1$] and [A_1^- – A_1] FTIR DS is highly impacted and as a result not all the bands were visible from this study. This problem could be solved by producing DDS by subtracting [$P700^+A_1^-$ – $P700A_1$] DS of one species from the [$P700^+A_1^-$ – $P700A_1$] DS from species. We could not complete such analysis here due to not having enough datasets, and by doing so, the spectra also become smaller and noisier. Even after that, we are still able to observe all the major bands at the neutral region those are due to the $C_1 = O$ and $C_4 = O$ stretching modes that appear at 1668/1666/1666 and 1627 cm^{-1}, respectively for trimeric and monomeric PSI with PhQ incorporated and trimeric PSI with PQ incorporated. In the neutral region, the $C_1 = O$ and $C_4 = O$ stretching modes are separated by 30 cm^{-1}, which is considerably less than the 71–80 cm^{-1} found for similar modes of trimeric and monomeric PhQ− and trimeric PQ−. This is the indication that the hydrogen bonding is weaker for the neutral state compared to the anion state, indicating radical-induced proton dynamics associated with the quinone in the A_1 binding site in PSI.

The life time of $P700^+F_{A/B}^-$ radical pair at RT and $P700^+A_1^-$ radical pair at LT for monomeric/trimeric PSI with PhQ incorporated are observed to be ~115 ms/~154 ms and ~403 µs/~431 µs from this study, which are in great agreement with the previous study of trimeric PSI by Makita et al. [1]. For both the LT and RT, the recombination rate is higher for WT trimeric PSI compared to the monomeric one, which indicates that midpoint potential for monomeric PSI would be lower but very close to PhQ which is around -465 mV. Previous research on PSI trimer and monomer in *Synechocystis* 6803 didn't find significant structural differences between them, partly due to their limited structural resolution. However, our interrogations on PSI by using TRSS FTIR

give more dynamic picture of their functionality in their different oligomerization states. Even the differences are small, they indeed represent their functional differences.

7.2 Future Research

Observations of the protein-quinone interaction in A_1 binding site of PSI using FTIR DS under natural conditions (at RT) are highly important as this is the more physiological condition in which the photosynthesis naturally occurs. However, all previous works to study A_1 binding site of PSI using FTIR DS are undertaken at LT (77K). No works have been done on the PSI binding site at RT. The main reason behind this was, the lowest potential reports would suggest the ET from A_1^- to F_X is a highly exergonic, or a thermodynamically downhill reaction. So, due to its downhill nature at low redox potential, at room temperature, it is hard to study $P700^+A_1^-$ charge recombination as it is very short-lived, and for the reduced potential quinones like PhQ, the recombination rate is ~300 nanoseconds (ns) at room temperature (RT, ~293 K). Charge recombination reactions can be observed if the forward electron transfer to the next series of electron acceptors is blocked, and this becomes possible when the binding site of PSI is incorporated by the high redox potential halogenated NQs (the LT data are discussed in chapter 4). This NQs made is possible to study A_1 at RT as $P700^+A_1^-$ recombination is on a microsecond scale, and µs-TRSS-FTIR DS can be used to study these high potential NQs at the binding site. Fig. 7.1 shows a set of preliminary data of [$P700^+A_1^-$ – $P700A_1$] FTIR DS in *pink* (*top*) for PhQ, in *green* (*bottom*) for Br_2NQ and [$P700^+$ – P700] FTIR DS in *red* at RT. The spectra in the Fig 7.1(A) seems to be same for both [$P700^+A_1^-$ – $P700A_1$] and [$P700^+$ – P700] FTIR DS, even though the spectrum for PhQ has the contribution from the quinones in the binding site. It seems that at RT, for the reduced potential quinones like PhQ, we cannot see any changes associated with the PhQ in the binding site, and the bands are overlapping with the bands from P700 in the static light-

dark spectrum in *red*. Changes are clearly visible when the binding site is occupied by one of the high potential halogenated NQs like Br_2NQ (Fig. 7.1(B)) in *green*. Similarly, comparison has been made between the $[P700^+A_1^- - P700A_1]$ FTIR DS for Br_2NQ (*green*) and $[P700^+ - P700]$ FTIR DS (*red*). In this case, we can observer the changes due to the Br_2NQ in the binding site between the 1550-1400 cm^{-1}, region which is defined as the anion region where the contributions are mainly due to the quinones in the A_1 binding site. These results open a new platform to study the other high potential NQs like 2ClNQ, 2BrNQ, and Cl_2NQ in the binding site to better understand the functionality of the quinone in the A_1 binding site along with how structural properties may relate to the thermodynamic and energetic properties of the pigment in the A_1 binding site along with how different pigment-protein interactions may modulate the functionality of the quinones as ET cofactors in the A_1 binding site.

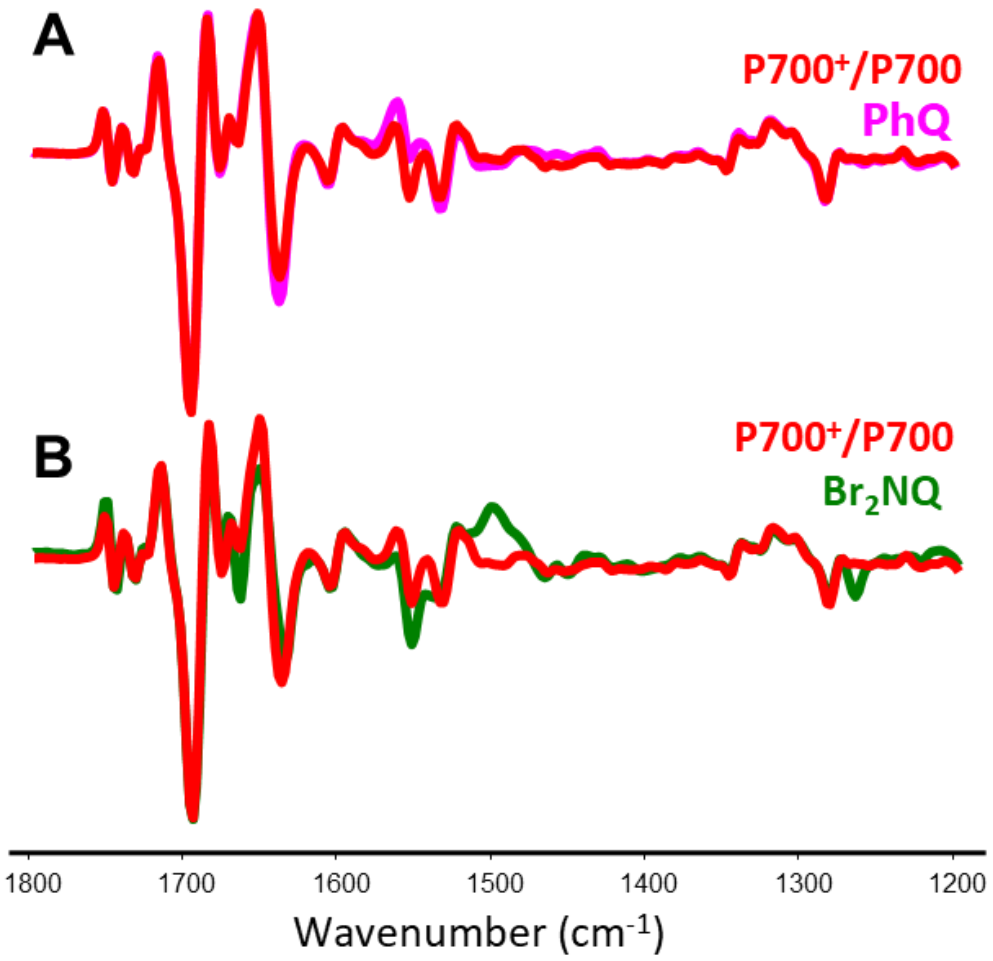

Figure 7.1 Photoaccumulated [$P700^+$ – P700] FTIR DS (*red*) and [$P700^+A_1^-$ – $P700A_1$] FTIR DAS in the 1800–1200 cm^{-1} regions obtained at ~293 K using PSI particles with (A) PhQ (*pink*), and (B) Br_2NQ (*green*) incorporated. Spectra are normalized to the ~1718/1697 cm^{-1} difference band. Spectra shown are the average of at least 3 separate experiments. The photoaccumulated DS shown here is the average from over fifty independent PSI samples with different quinones incorporated.

Another great possibility for study would be to investigate A_1 binding site of PSI with benzoquinones (BQs) incorporated and perform TRSS measurements at LT. Because nature makes use of it so, it would a very useful thing to know their structure/orientation and functionality in great details. Incorporation of different quinones allow easy modifications of the driving force associated with ET. By establishing ET rates and associated driving force in PSI with different

quinones incorporated, Marcus curve can be generated. Even with high potential NQs, reaction rates still reside in the inverted region. BQs were initially incorporated into the A_1 binding site to overcome this problem, as the range of *in vitro* midpoint potentials for BQs are more positive (spans over 800 mV) than that for commercially available high potential NQs and AQs (in the ~500 mV range). However, the reaction rate for PQ_9 [1], does not seem to follow the trend built by all the other NQs and AQs. Given the environmental difference that BQs experience in the A_1 binding site, it is likely that the midpoint potentials of BQs are influenced differently than NQs and AQs are, and/or the ET parameters, such as the reorganization energy, are modified. Given these conditions, construction of the Marcus curve that includes both the normal and inverted regions may be possible with BQs in the A_1 binding site. Few recent studies on some of the BQs ($DMBQ^-$, PQ^-, and Cl_4BQ^-) were published in 2018 [53, 56] at LT (77K) but many others are left behind to be studied. When studying these BQs analogue, one important thing needs to be kept in mind that, the sample needs to be cooled down to 77K and all the steps must be flowed in dark to prevent the degradation of the sample. In addition to that, collection of the kinetics on different benzoquinones (BQs) at LT and RT may be very useful to observe their decay lifetime. However, this study may not be possible at RT with TRSS FTIR DS as repeated flash on this sample at RT will deactivate the A_1 binding site and form triplet state [53, 74]. One solution would be studying these BQs at RT using one flash measurement using Joliot Type pump-probe Spectrometer (JTS).

The last potential future study could be on the improvement or development of multi layered (QM+MM) calculations to interpret the bands in both anion and neutral regions. The work presented here has shown the DFT–based harmonic, normal–mode vibrational frequency calculations for the different semiquinone anions in THF, H–bonded to either a water molecule or to the amide backbone N–H group of a Leu residue (chapter 4) to aid in the analysis and

interpretation of the bands in the DS and DDS. However, a more detailed QM/MM analysis of all these NQs in the A_1 binding site and PQ in the Q_A binding site is required to assign the bands more accurately and precisely.

REFERENCES

1. Makita, H. and G. Hastings, *Inverted-region electron transfer as a mechanism for enhancing photosynthetic solar energy conversion efficiency.* Proceedings of the National Academy of Sciences, 2017. **114**(35): p. 9267-9272.
2. Nations, U. *World population to reach 8 billion on 15 November 2022*. 2022; Available from: https://www.un.org/en/desa/world-population-reach-8-billion-15-november-2022.
3. Balzani, V., A. Credi, and M. Venturi, *Photochemical Conversion of Solar Energy.* 2008. **1**(1-2): p. 26-58.
4. Cogdell, R.J., et al., *Solar fuels and inspiration from photosynthesis.* Journal of Photochemistry and Photobiology A: Chemistry, 2018. **353**: p. 645-653.
5. Morton, O., *Solar energy: a new day dawning? Silicon Valley sunrise.* Nature, 2006. **443**(7107): p. 19-22.
6. Walker, D., *Energy, plants and man*. 2nd ed., with amendments. ed. 1993, Brighton, East Sussex: University Science Books.
7. van Grondelle, R., et al., *Energy transfer and trapping in photosynthesis.* Biochimica et Biophysica Acta (BBA) - Bioenergetics, 1994. **1187**(1): p. 1-65.
8. Blankenship, R.E. and H. Hartman, *The origin and evolution of oxygenic photosynthesis.* Trends in Biochemical Sciences, 1998. **23**(3): p. 94-97.
9. Blankenship, R.E., *Origin and Early Evolution of Photosynthesis.* Photosynthesis Research, 1992. **33**(2): p. 91-111.
10. Iverson, T.M., *Evolution and unique bioenergetic mechanisms in oxygenic photosynthesis.* Curr Opin Chem Biol, 2006. **10**(2): p. 91-100.
11. Nelson, N. and C.F. Yocum, *Structure and Function of Photosystems I and II.* Annual Review of Plant Biology, 2006. **57**(1): p. 521-565.
12. Nelson, N. and A. Ben-Shem, *The complex architecture of oxygenic photosynthesis.* Nat Rev Mol Cell Biol, 2004. **5**(12): p. 971-982.
13. Lawlor, D.W., *Ke, B. Photosynthesis: photobiochemistry and photobiophysics*, in *Ann Bot*. 2003. p. 106.
14. Friebe, V.M. and R.N. Frese, *Photosynthetic reaction center-based biophotovoltaics.* Current Opinion in Electrochemistry, 2017. **5**(1): p. 126-134.
15. Srinivasan, N. and J.H. Golbeck, *Protein–cofactor interactions in bioenergetic complexes: The role of the A1A and A1B phylloquinones in Photosystem I.* Biochimica et Biophysica Acta (BBA) - Bioenergetics, 2009. **1787**(9): p. 1057-1088.
16. Jordan, P., et al., *Three-dimensional structure of cyanobacterial photosystem I at 2.5A resolution.* Nature, 2001. **411**(6840): p. 909-917.
17. Fromme, P., P. Jordan, and N. Krauss, *Structure of photosystem I.* Biochimica et Biophysica Acta (BBA) - Bioenergetics, 2001. **1507**(1-3): p. 5-31.
18. Malavath, T., et al., *Structure and function of wild-type and subunit-depleted photosystem I in Synechocystis.* Biochim Biophys Acta Bioenerg, 2018. **1859**(9): p. 645-654.
19. Mazor, Y., et al., *Structure of the plant photosystem I supercomplex at 2.6 Å resolution.* Nature Plants, 2017. **3**: p. 17014.
20. Hastings, G., et al., *Universality of Energy and Electron Transfer Processes in Photosystem I.* Biochemistry, 1995. **34**(47): p. 15512-15522.
21. Hastings, G., et al., *Observation of the Reduction and Reoxidation of the Primary Electron Acceptor in Photosystem I.* Biochemistry, 1994. **33**(11): p. 3193-3200.

22. Makita, H. and G. Hastings, *Directionality of electron transfer in cyanobacterial photosystem I at 298 and 77 K.* FEBS Letters, 2015. **589**(13): p. 1412-1417.
23. Bautista, J.A., et al., *Biochemical and Biophysical Characterization of Photosystem I from Phytoene Desaturase and Zeta-Carotene Desaturase Deletion Mutants of Synechocystis Sp. PCC 6803: evidence for PsaA- and PsaB-side electron transport in cyanobacteria.* Journal of Biological Chemistry, 2005. **280**(20): p. 20030-20041.
24. Santabarbara, S., et al., *Directionality of Electron-Transfer Reactions in Photosystem I of Prokaryotes: Universality of the Bidirectional Electron-Transfer Model.* The Journal of Physical Chemistry B, 2010. **114**(46): p. 15158-15171.
25. Xu, W., et al., *Electron Transfer in Cyanobacterial Photosystem I: II. determination of forward electron transfer rates of site-directed mutants in a putative electron transfer pathway from A0 through A1 to FX.* Journal of Biological Chemistry, 2003. **278**(30): p. 27876-27887.
26. Cohen, R.O., et al., *Evidence for Asymmetric Electron Transfer in Cyanobacterial Photosystem I: Analysis of a Methionine-to-Leucine Mutation of the Ligand to the Primary Electron Acceptor A0.* Biochemistry, 2004. **43**(16): p. 4741-4754.
27. Guergova-Kuras, M., et al., *Evidence for two active branches for electron transfer in photosystem I.* Proceedings of the National Academy of Sciences, 2001. **98**(8): p. 4437-4442.
28. Agalarov, R. and K. Brettel, *Temperature dependence of biphasic forward electron transfer from the phylloquinone(s) A1 in photosystem I: only the slower phase is activated.* Biochimica et Biophysica Acta (BBA) - Bioenergetics, 2003. **1604**(1): p. 7-12.
29. Byrdin, M., et al., *Assignment of a kinetic component to electron transfer between iron–sulfur clusters FX and FA/B of Photosystem I.* Biochimica et Biophysica Acta (BBA) - Bioenergetics, 2006. **1757**(11): p. 1529-1538.
30. Shinkarev, V.P., et al., *Modeling of the P700+ charge recombination kinetics with phylloquinone and plastoquinone-9 in the A1 site of photosystem I.* Biophysical journal, 2002. **83**(6): p. 2885-2897.
31. Jordan, R., U. Nessau, and E. Schlodder, *Charge Recombination Between the Reduced Iron-Sulphur Clusters and P700+*, in *Photosynthesis: Mechanisms and Effects*, G. Garab, Editor. 1998, Springer Netherlands. p. 663-666.
32. Brettel, K., *Electron transfer and arrangement of the redox cofactors in photosystem I.* Biochimica et Biophysica Acta (BBA) - Bioenergetics, 1997. **1318**(3): p. 322-373.
33. Vassiliev, I.R., et al., *Near-IR absorbance changes and electrogenic reactions in the microsecond-to-second time domain in Photosystem I.* Biophysical Journal, 1997. **72**(1): p. 301-315.
34. Moser, C. and P.L. Dutton, *Application of Marcus Theory to Photosystem I Electron Transfer*, in *Photosystem I*, J. Golbeck, Editor. 2006, Springer Netherlands. p. 583-594.
35. Makita, H. and G. Hastings, *Modeling electron transfer in photosystem I.* Biochimica et Biophysica Acta (BBA) - Bioenergetics, 2016. **1857**(6): p. 723-733.
36. Schlodder, E., et al., *Temperature dependence of forward and reverse electron transfer from A1-, the reduced secondary electron acceptor in photosystem I.* Biochemistry, 1998. **37**(26): p. 9466-76.
37. Redding, K., A. van der Est, and J.H. Golbeck, *The Directionality of Electron Transport in Photosystem I: Photosystem I.* 2006, Springer Netherlands. p. 413-437.

38. Makita, H., N. Zhao, and G. Hastings, *Time-resolved visible and infrared difference spectroscopy for the study of photosystem I with different quinones incorporated into the A1 binding site.* Biochimica et Biophysica Acta (BBA) - Bioenergetics, 2015. **1847**(3): p. 343-354.
39. Arnoux, P., et al., *A structural basis for the pH-dependent xanthophyll cycle in Arabidopsis thaliana.* 2009. **21**(7): p. 2036-2044.
40. Busch, A. and M.J.B.e.B.A.-B. Hippler, *The structure and function of eukaryotic photosystem I.* 2011. **1807**(8): p. 864-877.
41. Ben-Shem, A., F. Frolow, and N.J.N. Nelson, *Crystal structure of plant photosystem I.* 2003. **426**(6967): p. 630-635.
42. Antoshvili, M., et al., *Structure and function of photosystem I in Cyanidioschyzon merolae.* Photosynthesis Research, 2018.
43. Pushkar, Y.N., et al., *Asymmetric Hydrogen-Bonding of the Quinone Cofactor in Photosystem I Probed by 13C-Labeled Naphthoquinones.* The Journal of Physical Chemistry B, 2004. **108**(27): p. 9439-9448.
44. Makita, H., et al., *Quinones in the A1 binding site in photosystem I studied using time-resolved FTIR difference spectroscopy.* Biochimica et Biophysica Acta (BBA) - Bioenergetics, 2017. **1858**(9): p. 804-813.
45. Brettel, K. and W. Leibl, *Electron transfer in photosystem I.* Biochimica et Biophysica Acta (BBA) - Bioenergetics, 2001. **1507**(1-3): p. 100-114.
46. Nakamura, A., et al., *Species Dependence of the Redox Potential of the Primary Electron Donor P700 in Photosystem I of Oxygenic Photosynthetic Organisms Revealed by Spectroelectrochemistry.* Plant and Cell Physiology, 2011. **52**(5): p. 815-823.
47. Ptushenko, V., et al., *Semi-continuum electrostatic calculations of redox potentials in photosystem I.* Photosynthesis Research, 2008. **97**(1): p. 55-74.
48. Santabarbara, S., P. Heathcote, and M.C.W. Evans, *Modelling of the electron transfer reactions in Photosystem I by electron tunnelling theory: The phylloquinones bound to the PsaA and the PsaB reaction centre subunits of PS I are almost isoenergetic to the iron–sulfur cluster FX.* Biochimica et Biophysica Acta (BBA) - Bioenergetics, 2005. **1708**(3): p. 283-310.
49. Iwaki, M. and S. Itoh, *Reaction of Reconstituted Acceptor Quinone and Dynamic Equilibration of Electron Transfer in the Photosystem I Reaction Center.* Plant and Cell Physiology, 1994. **35**(7): p. 983-993.
50. Ishikita, H. and E.-W. Knapp, *Redox Potential of Quinones in Both Electron Transfer Branches of Photosystem I.* Journal of Biological Chemistry, 2003. **278**(52): p. 52002-52011.
51. Setif, P. and H. Bottin, *Identification of electron-transfer reactions involving the acceptor A1 of photosystem I at room temperature.* Biochemistry, 1989. **28**(6): p. 2689-2697.
52. Vos, M.H. and H.J. van Gorkom, *Thermodynamical and structural information on photosynthetic systems obtained from electroluminescence kinetics.* Biophysical Journal, 1990. **58**(6): p. 1547-1555.
53. Makita, H. and G. Hastings, *Photosystem I with benzoquinone analogues incorporated into the A1 binding site.* Photosynth Res, 2018. **137**(1): p. 85-93.
54. Agarwala, N., et al., *Reversible inhibition and reactivation of electron transfer in photosystem I.* Photosynthesis Research, 2020. **145**(2): p. 97-109.

55. Johnson, T.W., et al., *Recruitment of a Foreign Quinone into the A1 Site of Photosystem I: I. Genetic and Physiological Characterization of Phylloquinone Biosynthetic Pathway Mutants in Synechocystis sp. PCC 6803.* Journal of Biological Chemistry, 2000. **275**(12): p. 8523-8530.
56. Makita, H. and G. Hastings, *Time-resolved step-scan FTIR difference spectroscopy for the study of photosystem I with different benzoquinones incorporated into the A1 binding site.* Biochimica et Biophysica Acta (BBA) - Bioenergetics, 2018. **1859**(11): p. 1199-1206.
57. Mula, S., et al., *Incorporation of a high potential quinone reveals that electron transfer in Photosystem I becomes highly asymmetric at low temperature.* Photochemical & Photobiological Sciences, 2012. **11**(6): p. 946-956.
58. van der Est, A., et al., *Incorporation of 2,3-Disubstituted-1,4-Naphthoquinones into the A1 Binding Site of Photosystem I Studied by EPR and ENDOR Spectroscopy.* Applied Magnetic Resonance, 2010. **37**(1-4): p. 65-83.
59. Makita, H. and G. Hastings, *Time-resolved visible and infrared absorption spectroscopy data obtained using photosystem I particles with non-native quinones incorporated into the A1 binding site.* Data in Brief, 2016. **7**: p. 1463-1468.
60. Johnson, T.W., et al., *Recruitment of a Foreign Quinone into the A1 Site of Photosystem I: in vivo Replacement of Plastoquinone-9 by Media-Supplemented Naphtoquinones in Phylloquinone Biosynthetic Pathway Mutants of Synechocystis sp. PCC 6803.* Journal of Biological Chemistry, 2001. **276**(43): p. 39512-39521.
61. Zybailov, B., et al., *Recruitment of a Foreign Quinone into the A1 Site of Photosystem I: II. Structural and Functional Characterization of Phylloquinone Biosynthetic Pathway Mutants by Electron Paramagnetic Resonance and Electron-Nuclear Double Resonance Spectroscopy.* Journal of Biological Chemistry, 2000. **275**(12): p. 8531-8539.
62. Mezzetti, A. and W. Leibl, *Time-resolved infrared spectroscopy in the study of photosynthetic systems.* Photosynthesis Research, 2016: p. 1-24.
63. Breton, J., et al., *Binding sites of quinones in photosynthetic bacterial reaction centers investigated by light-induced FTIR difference spectroscopy: Binding of chainless symmetrical quinones to the QA site of Rhodobacter sphaeroides.* Biochemistry, 1994. **33**(41): p. 12405-12415.
64. Hellwig, P., *Infrared spectroscopic markers of quinones in proteins from the respiratory chain.* Biochimica et Biophysica Acta (BBA) - Bioenergetics, 2015. **1847**(1): p. 126-133.
65. Makita, H. and G. Hastings, *Time-resolved FTIR difference spectroscopy for the study of quinones in the A1 binding site in photosystem I: Identification of neutral state quinone bands.* Biochimica et Biophysica Acta (BBA) - Bioenergetics, 2020. **1861**(5): p. 148173.
66. Cyran, J.D., J.M. Nite, and A.T. Krummel, *Characterizing Anharmonic Vibrational Modes of Quinones with Two-Dimensional Infrared Spectroscopy.* The Journal of Physical Chemistry B, 2015. **119**(29): p. 8917-8925.
67. Davis, R., et al., *Fourier transform infrared (FT-IR) spectroscopy: a rapid tool for detection and analysis of foodborne pathogenic bacteria.* 2010. **2**: p. 1582-1594.
68. Stuart, B., *Infrared Spectroscopy*, in *Kirk-Othmer Encyclopedia of Chemical Technology*.
69. Giechaskiel, B. and M. Clairotte, *Fourier Transform Infrared (FTIR) Spectroscopy for Measurements of Vehicle Exhaust Emissions: A Review.* 2021. **11**(16): p. 7416.

70. Makita, H., *Time Resolved Absorption Spectroscopy for the Study of Electron Transfer Processes in Photosynthetic Systems*, in *Physics and Astronomy*. 2012, Georgia State University.
71. Griffiths, P.R. and J.A. de Haseth, *Fourier Transform Infrared Spectrometry*, in *Fourier Transform Infrared Spectrometry*. 2007, John Wiley & Sons, Inc.
72. Sivakumar, V., R. Wang, and G. Hastings, *A1 Reduction in Intact Cyanobacterial Photosystem I Particles Studied by Time-Resolved Step-Scan Fourier Transform Infrared Difference Spectroscopy and Isotope Labeling†.* Biochemistry, 2005. **44**(6): p. 1880-1893.
73. Hastings, G., K.M. Priyangika Bandaranayake, and E. Carrion, *Time-Resolved FTIR Difference Spectroscopy in Combination with Specific Isotope Labeling for the Study of A1, the Secondary Electron Acceptor in Photosystem 1*. Biophysical Journal, 2008. **94**(11): p. 4383-4392.
74. Agarwala, N., et al., *Reversible inhibition and reactivation of electron transfer in photosystem I.* Photosynth Res, 2020.
75. Hastings, G., et al., *Fourier transform visible and infrared difference spectroscopy for the study of P700 in photosystem I from Fischerella thermalis PCC 7521 cells grown under white light and far-red light: Evidence that the A–1 cofactor is chlorophyll f.* Biochimica et Biophysica Acta (BBA) - Bioenergetics, 2019. **1860**(6): p. 452-460.
76. Wang, R., et al., *FTIR Difference Spectroscopy in Combination with Isotope Labeling for Identification of the Carbonyl Modes of P700 and P700+ in Photosystem I.* Biophysical Journal, 2004. **86**(2): p. 1061-73.
77. Snellenburg, J.J., et al., *Glotaran: a Java-based Graphical User Interface for the R-package TIMP*. Journal of Statistical Software, 2012. **49**(3): p. 1-22.
78. Agarwala, N., et al., *Calculated and Experimental Infrared Spectra of Substituted Naphthoquinones.* Frontiers in Science, Technology, Engineering and Mathematics (FSTEM), 2019. **3**(2): p. 71-80.
79. M. J. Frisch, G.W.T., H. B. Schlegel, G. E. Scuseria, M. A. Robb, J. R. Cheeseman, G. Scalmani, V. Barone, G. A. Petersson, H. Nakatsuji, X. Li, M. Caricato, A. Marenich, J. Bloino, B. G. Janesko, R. Gomperts, B. Mennucci, H. P. Hratchian, J. V. Ortiz, A. F. Izmaylov, J. L. Sonnenberg, D. Williams-Young, F. Ding, F. Lipparini, F. Egidi, J. Goings, B. Peng, A. Petrone, T. Henderson, D. Ranasinghe, V. G. Zakrzewski, J. Gao, N. Rega, G. Zheng, W. Liang, M. Hada, M. Ehara, K. Toyota, R. Fukuda, J. Hasegawa, M. Ishida, T. Nakajima, Y. Honda, O. Kitao, H. Nakai, T. Vreven, K. Throssell, J. A. Montgomery, Jr., J. E. Peralta, F. Ogliaro, M. Bearpark, J. J. Heyd, E. Brothers, K. N. Kudin, V. N. Staroverov, T. Keith, R. Kobayashi, J. Normand, K. Raghavachari, A. Rendell, J. C. Burant, S. S. Iyengar, J. Tomasi, M. Cossi, J. M. Millam, M. Klene, C. Adamo, R. Cammi, J. W. Ochterski, R. L. Martin, K. Morokuma, O. Farkas, J. B. Foresman, and D. J. Fox, *Gaussian 09, Revision D.01*. 2013, Gaussian, Inc., Wallingford CT, 2016.
80. Bandaranayake, K.M.P., et al., *Modeling the A(1) binding site in photosystem - I. Density functional theory for the calculation of "anion-neutral" FTIR difference spectra of phylloquinone.* Vibrational Spectroscopy, 2006. **42**(1): p. 78-87.
81. Tomasi, J., et al., *Molecular properties in solution described with a continuum solvation model.* 2002. **4**(23): p. 5697-5712.

82. Irikura, K.K., et al., *Uncertainties in scaling factors for ab initio vibrational zero-point energies.* The Journal of Chemical Physics, 2009. **130**(11): p. 114102.
83. Irikura, K.K., R.D. Johnson, and R.N. Kacker, *Uncertainties in Scaling Factors for ab Initio Vibrational Frequencies.* The Journal of Physical Chemistry A, 2005. **109**(37): p. 8430-8437.
84. Andersson, M.P. and P. Uvdal, *New Scale Factors for Harmonic Vibrational Frequencies Using the B3LYP Density Functional Method with the Triple-ζ Basis Set 6-311+G(d,p).* The Journal of Physical Chemistry A, 2005. **109**(12): p. 2937-2941.
85. Jamróz, M.H., *Vibrational Energy Distribution Analysis (VEDA): Scopes and limitations.* Spectrochimica Acta Part A: Molecular and Biomolecular Spectroscopy, 2013. **114**: p. 220-230.
86. Santabarbara, S., A.P. Casazza, and G. Hastings, *Modelling electron transfer in photosystem I: limits and perspectives.* Physiologia Plantarum, 2019. **166**(1): p. 73-87.
87. Cherepanov, D.A., et al., *Electron–Phonon Coupling in Cyanobacterial Photosystem I.* The Journal of Physical Chemistry B, 2018. **122**(33): p. 7943-7955.
88. Milanovsky, G.E., et al., *Kinetic modeling of electron transfer reactions in photosystem I complexes of various structures with substituted quinone acceptors.* Photosynthesis Research, 2017. **133**(1): p. 185-199.
89. Rögner, M., et al., *Mono-, di- and trimeric PS I reaction center complexes isolated from the thermophilic cyanobacterium Synechococcus sp.: Size, shape and activity.* Biochimica et Biophysica Acta (BBA) - Bioenergetics, 1990. **1015**(3): p. 415-424.
90. Jordan, P., et al., *Three-dimensional structure of cyanobacterial photosystem I at 2.5 Å resolution.* 2001. **411**(6840): p. 909-917.
91. Watanabe, M., et al., *Attachment of phycobilisomes in an antenna–photosystem I supercomplex of cyanobacteria.* 2014. **111**(7): p. 2512-2517.
92. Malavath, T., et al., *Structure and function of wild-type and subunit-depleted photosystem I in Synechocystis.* 2018. **1859**(9): p. 645-654.
93. Netzer-El, S.Y., I. Caspy, and N.J.F.i.p.s. Nelson, *Crystal structure of photosystem I monomer from Synechocystis PCC 6803.* 2019: p. 1865.
94. Ivanov, A.G., et al., *Iron deficiency in cyanobacteria causes monomerization of photosystem I trimers and reduces the capacity for state transitions and the effective absorption cross section of photosystem I in vivo.* 2006. **141**(4): p. 1436-1445.
95. Salomon, E. and N.J.P.p. Keren, *Manganese limitation induces changes in the activity and in the organization of photosynthetic complexes in the cyanobacterium Synechocystis sp. strain PCC 6803.* 2011. **155**(1): p. 571-579.
96. Nohl, H., W. Jordan, and R.J. Youngman, *Quinones in Biology: Functions in electron transfer and oxygen activation.* Advances in Free Radical Biology & Medicine, 1986. **2**(1): p. 211-279.
97. de Wijn, R. and H.J. van Gorkom, *Kinetics of Electron Transfer from QA to QB in Photosystem II.* Biochemistry, 2001. **40**(39): p. 11912-11922.
98. Breton, J., et al., *Binding sites of quinones in photosynthetic bacterial reaction centers investigated by light-induced FTIR difference spectroscopy: assignment of the interactions of each carbonyl of QA in Rhodobacter sphaeroides using site-specific 13C-labeled ubiquinone.* Biochemistry, 1994. **33**(48): p. 14378-14386.

99. Saito, K., A.W. Rutherford, and H. Ishikita, *Mechanism of proton-coupled quinone reduction in Photosystem II.* Proceedings of the National Academy of Sciences of the United States of America, 2013. **110**(3): p. 954-959.
100. Zhu, Z. and M.R. Gunner, *Energetics of Quinone-Dependent Electron and Proton Transfers in Rhodobacter sphaeroides Photosynthetic Reaction Centers.* Biochemistry, 2005. **44**(1): p. 82-96.
101. Hou, H.J.M. and D. Mauzerall, *The A-FX to FA/B Step in Synechocystis 6803 Photosystem I Is Entropy Driven.* Journal of the American Chemical Society, 2006. **128**(5): p. 1580-1586.
102. Beulens, J.W.J., et al., *The role of menaquinones (vitamin K2) in human health.* British Journal of Nutrition, 2013. **110**(8): p. 1357-1368.
103. Kishi, S., et al., *Redox potentials of ubiquinone, menaquinone, phylloquinone, and plastoquinone in aqueous solution.* Photosynthesis Research, 2017. **134**(2): p. 193-200.
104. Coates, C.S., et al., *The Structure and Function of Quinones in Biological Solar Energy Transduction: A Cyclic Voltammetry, EPR, and Hyperfine Sub-Level Correlation (HYSCORE) Spectroscopy Study of Model Naphthoquinones.* The Journal of Physical Chemistry B, 2013. **117**(24): p. 7210-7220.
105. Breton, J. and E. Nabedryk, *Protein-quinone interactions in the bacterial photosynthetic reaction center: light-induced FTIR difference spectroscopy of the quinone vibrations.* Biochimica et Biophysica Acta (BBA) - Bioenergetics, 1996. **1275**(1): p. 84-90.
106. Makita, H. and G. Hastings, *Directionality of electron transfer in cyanobacterial photosystem I at 298 and 77K.* FEBS Letters, 2015. **589**(13): p. 1412-1417.
107. Hastings, G., *FTIR Studies of the Intermediate Electron Acceptor A_1*, in *Photosystem I: The Light Driven Plastocyanin:Ferredoxin Oxidoreductase.*, J. Golbeck, Editor. 2006, Springer: Dordrecht. p. 301-318.
108. Frisch, M.J., et al., *Gaussian 16 Rev. B.01*. 2016: Wallingford, CT.
109. Tomasi, J., et al., *Molecular properties in solution described with a continuum solvation model.* Physical Chemistry Chemical Physics, 2002. **4**(23): p. 5697-5712.
110. Breton, J., et al., *The binding sites of quinones in photosynthetic bacterial reaction centers investigated by light-induced FTIR difference spectroscopy: assignment of the Q_A vibrations in Rhodobacter sphaeroides using ^{18}O- or ^{13}C-labeled ubiquinone and vitamin K_1.* Biochemistry, 1994. **33**(16): p. 4953-4965.
111. Frisch, J.B.F.a.Æ., *Exploring Chemistry with Electronic Structure Methods*. 3rd ed ed. Exploring Chemistry with Electronic Structure Methods, ed. I. Gaussian. 2015, Wallingford, CT: Gaussian, Inc.
112. Bandaranayake, K.P., et al., *Modeling the A1 binding site in photosystem: I. Density functional theory for the calculation of "anion− neutral" FTIR difference spectra of phylloquinone.* Vibrational Spectroscopy, 2006. **42**(1): p. 78-87.
113. Trumpower, B., *Function of quinones in energy conserving systems*. 2012: Elsevier.
114. Ke, B., *Photosynthesis: Photobiochemistry and Photobiophysics*. 2001, Dordrecht ; Boston: Kluwer Academic Publishers.
115. Srinivasan, N. and J.H. Golbeck, *Protein-cofactor interactions in bioenergetic complexes: The role of the A(1A) and A(1B) phylloquinones in Photosystem I.* Biochimica et Biophysica Acta (BBA) - Bioenergetics, 2009. **1787**(9): p. 1057-1088.

116. Breton, J. and E. Nabedryk, *Protein-quinone interactions in the bacterial photosynthetic reaction center: Light-induced FTIR difference spectroscopy of the quinone vibrations.* Biochimica et Biophysica Acta, 1996. **1275**(1-2): p. 84-90.
117. de Wijn, R. and H.J. van Gorkom, *Kinetics of electron transfer from Q(a) to Q(b) in photosystem II.* Biochemistry, 2001. **40**(39): p. 11912-22.
118. Breton, J., et al., *Binding Sites of Quinones in Photosynthetic Bacterial Reaction Centers Investigated by Light-Induced FTIR Difference Spectroscopy: Assignment of the Interactions of Each Carbonyl of QA in Rhodobacter sphaeroides Using Site-Specific 13C-Labeled Ubiquinone.* Biochemistry, 1994. **33**(48): p. 14378-14386.
119. Saito, K., A.W. Rutherford, and H. Ishikita, *Mechanism of proton-coupled quinone reduction in Photosystem II.* Proc Natl Acad Sci U S A, 2013. **110**(3): p. 954-9.
120. Zhu, Z.Y. and M.R. Gunner, *Energetics of quinone-dependent electron and proton transfers in Rhodobacter sphaeroides photosynthetic reaction centers.* Biochemistry, 2005. **44**(1): p. 82-96.
121. Hou, H.J.M. and D. Mauzerall, *The A(-)F(x) to F-A/B step in Synechocystis 6803 photosystem I is entropy driven.* Journal of the American Chemical Society, 2006. **128**(5): p. 1580-1586.
122. Golbeck, J.H. and D.A. Bryant, *Photosystem I, in Current topics in bioenergetics.* Academic Press: New York, 1991. **16**: p. 83-177.
123. Beulens, J.W., et al., *The role of menaquinones (vitamin K(2)) in human health.* Br J Nutr, 2013. **110**(8): p. 1357-68.
124. Wraight, C.A. and M.R. Gunner, *The Acceptor Quinones of Purple Photosynthetic Bacteria — Structure and Spectroscopy*, in *The Purple Phototrophic Bacteria*, C.N. Hunter, et al., Editors. 2009, Springer Netherlands: Dordrecht. p. 379-405.
125. Breton, J., *Efficient exchange of the primary quinone acceptor Q_A in isolated reaction centers of Rhodopseudomonas viridis.* Proc. Natl. Acad. Sci. USA, 1997. **94**(21): p. 11318-11323.
126. Mezzetti, A. and W. Leibl, *Time-resolved infrared spectroscopy in the study of photosynthetic systems.* Photosynth Res, 2017. **131**(2): p. 121-144.
127. Santabarbara, S., A.P. Casazza, and G. Hastings, *Modelling electron transfer in photosystem I: limits and perspectives.* Physiologia Plantarum, 2019. **0**(0).
128. Frisch, M., et al., *Gaussian 16 Rev. B. 01 (Wallingford, CT, 2016).*
129. Hunter, A.D., *ACD/ChemSketch 2.0 (freeware)*. 2020, Advanced Chemistry Development, Inc.: Toronto, ON, Canada.
130. Hanwell, M.D., et al., *Avogadro: an advanced semantic chemical editor, visualization, and analysis platform.* Journal of Cheminformatics, 2012. **4**.
131. Breton, J., et al., *The Binding Sites of Quinones in Photosynthetic Bacterial Reaction Centers Investigated by Light-Induced FTIR Difference Spectroscopy: Assignment of the QA Vibrations in Rhodobacter sphaeroides Using 18O- or 13C-Labeled Ubiquinones and Vitamin K1.* Biochemistry, 1994. **33**(16): p. 4953-4965.
132. Irikura, K.K., et al., *Uncertainties in scaling factors for ab initio vibrational zero-point energies.* 2009. **130**(11): p. 114102.
133. Wang, J., et al., *Structure of plant photosystem I−light harvesting complex I supercomplex at 2.4 Å resolution.* 2021. **63**(7): p. 1367-1381.
134. Pi, X., et al., *Unique organization of photosystem I–light-harvesting supercomplex revealed by cryo-EM from a red alga.* 2018. **115**(17): p. 4423-4428.

135. Rohani, L., et al., *Calculated vibrational properties of semiquinones in the A(1) binding site in photosystem I.* Biochim Biophys Acta Bioenerg, 2019. **1860**(9): p. 699-707.
136. Hastings, G., *Vibrational spectroscopy of photosystem I.* Biochim Biophys Acta, 2015. **1847**(1): p. 55-68.
137. Srinivasan, N., et al., *Role of the Hydrogen Bond from Leu722 to the A1A Phylloquinone in Photosystem I.* Biochemistry, 2009. **48**(15): p. 3315-3324.
138. Feldman, K.S., D.K. Hester Ii, and J.H. Golbeck, *A relationship between amide hydrogen bond strength and quinone reduction potential: Implications for photosystem I and bacterial reaction center quinone function.* Bioorganic & Medicinal Chemistry Letters, 2007. **17**(17): p. 4891-4894.
139. Ashizawa, R. and T. Noguchi, *Effects of hydrogen bonding interactions on the redox potential and molecular vibrations of plastoquinone as studied using density functional theory calculations.* Physical Chemistry Chemical Physics, 2014. **16**(24): p. 11864-11876.
140. Ivancich, A., et al., *Effects of hydrogen bonds on the redox potential and electronic structure of the bacterial primary electron donor.* Biochemistry, 1998. **37**(34): p. 11812-20.
141. Pushkar, Y.N., et al., *Orientation and Protein−Cofactor Interactions of Monosubstituted n-Alkyl Naphthoquinones in the A1 Binding Site of Photosystem I.* The Journal of Physical Chemistry B, 2002. **106**(46): p. 12052-12058.
142. Bandaranayake, K., R. Wang, and G. Hastings, *Modification of the Phylloquinone in the A_1 Binding Site in Photosystem I Studied Using Time-Resolved FTIR Difference Spectroscopy and Density Functional Theory.* Biochemistry, 2006. **45**(13): p. 4121-4127.
143. Rohani, L. and G. Hastings, *Assessment of the orientation and conformation of pigments in protein binding sites from infrared difference spectra.* Biochim Biophys Acta Bioenerg, 2021. **1862**(4): p. 148366.
144. Berthomieu, C., et al., *Characterization by FTIR spectroscopy of the photoreduction of the primary quinone acceptor QA in photosystem II.* FEBS Letters, 1990. **269**(2): p. 363-367.
145. Takano, A., et al., *Herbicide effect on the hydrogen-bonding interaction of the primary quinone electron acceptor QA in photosystem II as studied by Fourier transform infrared spectroscopy.* Photosynthesis Research, 2008. **98**(1): p. 159-167.
146. Suga, M., et al., *Structure of the green algal photosystem I supercomplex with a decameric light-harvesting complex I.* Nature Plants, 2019. **5**(6): p. 626-636.
147. Qin, X., et al., *Structure of a green algal photosystem I in complex with a large number of light-harvesting complex I subunits.* Nature Plants, 2019. **5**(3): p. 263-272.
148. Ozawa, S., et al., *5'-Monohydroxyphylloquinone is the Dominant Naphthoquinone of PSI in the Green Alga Chlamydomonas reinhardtii.* Plant and Cell Physiology, 2012. **53**(1): p. 237-243.
149. Joliot, P. and A. Joliot, *In Vivo Analysis of the Electron Transfer within Photosystem I: Are the Two Phylloquinones Involved?* Biochemistry, 1999. **38**(34): p. 11130-11136.
150. Setif, P. and K. Brettel, *Forward electron transfer from phylloquinone A1 to iron-sulfur centers in spinach photosystem I.* Biochemistry, 1993. **32**(31): p. 7846-7854.
151. Lüneberg, J., et al., *Spectroscopic characterization of PS I core complexes from thermophilic Synechococcus sp: Identical reoxidation kinetics of A−1 before and after removal of theiron-sulfur-clusters FA and FB.* FEBS Letters, 1994. **338**(2): p. 197-202.

152. Shen, G., et al., *Assembly of photosystem I. II. Rubredoxin is required for the in vivo assembly of FX in Synechococcus sp. PCC 7002 as shown by optical and EPR spectroscopy.* Journal of Biological Chemistry, 2002.
153. Webber, A.N. and W. Lubitz, *P700: the primary electron donor of photosystem I.* Biochimica et Biophysica Acta (BBA) - Bioenergetics, 2001. **1507**(1): p. 61-79.
154. Schlodder, E.P., A; Cetin, M. *Triplet states in photosystem I complexes from Synechococcus elongatus*. in *12th International Congress on Photosynthesis*. 2001. Brisbane, Australia.
155. Makita, H. and G. Hastings, *Time-Resolved Step-Scan FTIR Difference Spectroscopy for the Study of the P700 Triplet State in Photosystem I.* Frontiers in Science, Technology, Engineering and Mathematics, 2019. **3**.
156. Rohani, L., et al., *Calculated vibrational properties of semiquinones in the A1 binding site in photosystem I.* Biochimica et Biophysica Acta (BBA) - Bioenergetics, 2019. **1860**(9): p. 699-707.
157. Karyagina, I., et al., *Contributions of the Protein Environment to the Midpoint Potentials of the A1 Phylloquinones and the FX Iron−Sulfur Cluster in Photosystem I.* Biochemistry, 2007. **46**(38): p. 10804-10816.
158. Ivashin, N. and S. Larsson, *Electron transfer pathways in photosystem I reaction centers.* Chemical Physics Letters, 2003. **375**(3): p. 383-387.
159. Ali, K., et al., *Bidirectional electron transfer in photosystem I: Replacement of the symmetry-breaking tryptophan close to the PsaB-bound phylloquinone (A1B) with a glycine residue alters the redox properties of A1B and blocks forward electron transfer at cryogenic temperatures.* Biochimica et Biophysica Acta (BBA) - Bioenergetics, 2006. **1757**(12): p. 1623-1633.
160. Xu, W., et al., *Electron transfer in cyanobacterial photosystem I - I. Physiological and spectroscopic characterization of site-directed mutants in a putative electron transfer pathway from A(0) through A(1) to F-x.* Journal of Biological Chemistry, 2003. **278**(30): p. 27864-27875.
161. Breton, J., *FTIR Studies of the Primary Electron Donor, P700*, in *Photosystem I*, J. Golbeck, Editor. 2006, Springer Netherlands. p. 271-289.
162. Breton, J., *FTIR Studies of the Primary Electron Donor, P700*, in *Photosystem I: The Light Driven Plastocyanin:Ferredoxin Oxidoreductase.*, J. Golbeck, Editor. 2006, Springer: Dordrecht. p. 271-289.
163. Hastings, G., *Vibrational spectroscopy of photosystem I.* Biochimica et Biophysica Acta (BBA) - Bioenergetics, 2015. **1847**(1): p. 55-68.
164. Breton, J., E. Nabedryk, and W. Leibl, *FTIR Study of the Primary Electron Donor of Photosystem I (P700) Revealing Delocalization of the Charge in P700+ and Localization of the Triplet Character in 3P700.* Biochemistry, 1999. **38**(36): p. 11585-11592.
165. Sieckmann, I., et al., *Transient electron paramagnetic resonance of the triplet state of P700 in photosystem I: Evidence for triplet delocalization at room temperature.* Biochemistry, 1993. **32**(18): p. 4842-4847.
166. Santabarbara, S. and A.P. Casazza, *Kinetics and Energetics of Phylloquinone Reduction in Photosystem I: Insight From Modeling of the Site Directed Mutants.* Frontiers in Plant Science, 2019. **10**: p. 852.

167. Kawashima, K. and H. Ishikita, *Structural Factors That Alter the Redox Potential of Quinones in Cyanobacterial and Plant Photosystem I.* Biochemistry, 2017. **56**(24): p. 3019-3028.
168. Gunner, M.R., J. Madeo, and Z. Zhu, *Modification of quinone electrochemistry by the proteins in the biological electron transfer chains: examples from photosynthetic reaction centers.* Journal of Bioenergetics and Biomembranes, 2008. **40**(5): p. 509.
169. Okamura, M.Y., et al., *Proton and electron transfer in bacterial reaction centers.* Biochimica et Biophysica Acta (BBA) - Bioenergetics, 2000. **1458**(1): p. 148-163.
170. Joliot, P. and A. Joliot, *Cyclic electron flow in C3 plants.* Biochimica et Biophysica Acta (BBA) - Bioenergetics, 2006. **1757**(5–6): p. 362-368.
171. Frank, H.A., M.B. McLean, and K. Sauer, *Triplet states in photosystem I of spinach chloroplasts and subchloroplast particles.* Proceedings of the National Academy of Sciences, 1979. **76**(10): p. 5124.
172. Gast, P., et al., *Evidence for a new early acceptor in Photosystem I of plants. An ESR investigation of reaction center triplet yield and of the reduced intermediary acceptors.* Biochimica et Biophysica Acta (BBA) - Bioenergetics, 1983. **722**(1): p. 163-175.
173. Rutherford, A.W. and P. Sétif, *Orientation of P700, the primary electron donor of Photosystem I.* Biochimica et Biophysica Acta (BBA) - Bioenergetics, 1990. **1019**(2): p. 128-132.
174. Lefebvre-Legendre, L., et al., *Loss of Phylloquinone in Chlamydomonas Affects Plastoquinone Pool Size and Photosystem II Synthesis.* Journal of Biological Chemistry, 2007. **282**(18): p. 13250-13263.
175. McConnell, M.D., et al., *Double Reduction of Plastoquinone to Plastoquinol in Photosystem 1*. Biochemistry, 2011. **50**(51): p. 11034-11046.
176. Poluektov, O.G., J. Niklas, and L.M. Utschig, *Spin-Correlated Radical Pairs as Quantum Sensors of Bidirectional ET Mechanisms in Photosystem I.* The Journal of Physical Chemistry B, 2019. **123**(35): p. 7536-7544.
177. Badshah, S.L., et al., *Mutations in algal and cyanobacterial Photosystem I that independently affect the yield of initial charge separation in the two electron transfer cofactor branches.* Biochimica et Biophysica Acta (BBA) - Bioenergetics, 2018. **1859**(1): p. 42-55.
178. Poluektov, O.G. and L.M. Utschig, *Directionality of Electron Transfer in Type I Reaction Center Proteins: High-Frequency EPR Study of PS I with Removed Iron–Sulfur Centers.* The Journal of Physical Chemistry B, 2015. **119**(43): p. 13771-13776.
179. Berthold, T., et al., *Exploring the Electron Transfer Pathways in Photosystem I by High-Time-Resolution Electron Paramagnetic Resonance: Observation of the B-Side Radical Pair P700+A1B– in Whole Cells of the Deuterated Green Alga Chlamydomonas reinhardtii at Cryogenic Temperatures.* Journal of the American Chemical Society, 2012. **134**(12): p. 5563-5576.
180. Santabarbara, S., et al., *Interquinone Electron Transfer in Photosystem I As Evidenced by Altering the Hydrogen Bond Strength to the Phylloquinone(s).* The Journal of Physical Chemistry B, 2010. **114**(28): p. 9300-9312.
181. Xu, W., et al., *Electron transfer in cyanobacterial photosystem I: I. Physiological and spectroscopic characterization of site-directed mutants in a putative electron transfer pathway from A0 through A1 to FX*. 2003. **278**(30): p. 27864-27875.

182. Sun, J., et al., *Isolation and functional study of photosystem I subunits in the cyanobacterium Synechocystis sp. PCC 6803*, in *Methods in Enzymology*. 1998, Academic Press. p. 124-139.
183. Bricker, T.M., et al., *Isolation of a highly active Photosystem II preparation from Synechocystis 6803 using a histidine-tagged mutant of CP 47.* Biochimica et Biophysica Acta (BBA) - Bioenergetics, 1998. **1409**(1): p. 50-57.
184. Kashino, Y., et al., *Proteomic analysis of a highly active photosystem II preparation from the cyanobacterium Synechocystis sp. PCC 6803 reveals the presence of novel polypeptides.* 2002. **41**(25): p. 8004-8012.
185. Hastings, G., et al., *Primary Donor Photo-Oxidation in Photosystem I: A Re-Evaluation of (P700+ − P700) Fourier Transform Infrared Difference Spectra.* Biochemistry, 2001. **40**(43): p. 12943-12949.
186. Hastings, G. and V. Sivakumar, *A Fourier transform infrared absorption difference spectrum associated with the reduction of A1 in photosystem I: are both phylloquinones involved in electron transfer?* Biochemistry, 2001. **40**(12): p. 3681-9.
187. Hamacher, E., et al., *Characterization of the primary electron donor of photosystem I, P700, by electrochemistry and Fourier transform infrared (FTIR) difference spectroscopy.* 1996. **52**(1): p. 107-121.
188. Lubitz, W., *EPR Studies of the Primary Electron Donor P700 in Photosystem*, in *Photosystem I*. 2006, Springer. p. 245-269.
189. Surewicz, W. and H. Mantsch, *Infrared absorption methods for examining protein structure*, in *Spectroscopic methods for determining protein structure in solution*. 1996, VCH Publishers, Inc.: New York. p. 135-162.
190. Susi, H. and D.M. Byler, *[13] Resolution-enhanced fourier transform infrared spectroscopy of enzymes*, in *Methods in Enzymology*. 1986, Academic Press. p. 290-311.
191. Hastings, G., *Fourier Transform Infrared Studies of the Secondary Electron Acceptor, A1*, J.H. Golbeck, Editor. 2006, Springer Netherlands. p. 413-437.
192. Agarwala, N., L. Rohani, and G. Hastings, *Experimental and calculated infrared spectra of disubstituted naphthoquinones.* Spectrochimica Acta Part A: Molecular and Biomolecular Spectroscopy, 2022. **268**: p. 120674.